Technical Report

DNA-TR-95-59-V2

Advanced Simulator Power Flow Technology/Advanced Radiation Simulation Volume 2: MHD Modeling of POS and Power Flow

Approved for public release; distribution is unlimited

Technical Report
September 1999

Prepared for:
Defense Threat Reduction Agency
45045 Aviation Drive
Dulles, VA 20166-7517

DNA001-93-C-0229

Donald Parks, Phil Coleman, Randy Ingermanson,
Paul Steen, John Thompson, and Jack Waltrous

Prepared by: Maxwell Technologies Systems Division, Inc.
8888 Balboa Avenue
San Diego, CA 92123-1506

DESTRUCTION NOTICE:

Destroy this report when it is no longer needed. Do not return to sender.

PLEASE NOTIFY THE DEFENSE THREAT REDUCTION AGENCY, ATTN: ADP, 45045 AVIATION DRIVE, DULLES, VA 20166-7517, IF YOUR ADDRESS IS INCORRECT, IF YOU WISH IT DELETED FROM THE DISTRIBUTION LIST, OR IF THE ADDRESSEE IS NO LONGER EMPLOYED BY YOUR ORGANIZATION.

DISTRIBUTION LIST UPDATE

This mailer is provided to enable DTRA to maintain current distribution lists for reports. (We would appreciate you providing the requested information.)

- ❑ Add the individual listed to your distribution list.
- ❑ Delete the cited organization/individual.
- ❑ Change of address.

Note:
Please return the mailing label from the document so that any additions, changes, corrections or deletions can be made easily. For distribution cancellation or more information call DTRA/ADM (703) 325-1036.

NAME: _____

ORGANIZATION: _____

OLD ADDRESS	NEW ADDRESS
_____	_____
_____	_____
_____	_____

TELEPHONE NUMBER: ( ) _____

DTRA PUBLICATION NUMBER/TITLE	CHANGES/DELETIONS/ADDITIONS, etc.) *(Attach Sheet if more Space is Required)*
_____	_____
_____	_____
_____	_____

DTRA or other GOVERNMENT CONTRACT NUMBER: _____

CERTIFICATION of NEED-TO-KNOW BY GOVERNMENT SPONSOR (if other than DTRA):

SPONSORING ORGANIZATION: _____

CONTRACTING OFFICER or REPRESENTATIVE: _____

SIGNATURE: _____

DEFENSE THREAT REDUCTION AGENCY
ATTN: ADM
45045 AVIATION DRIVE
DULLES, VA 20166-7517

DEFENSE THREAT REDUCTION AGENCY
ATTN: ADM
6810 TELEGRAPH ROAD
ALEXANDRIA, VA 22310-3398

REPORT DOCUMENTATION PAGE

Form Approved
OMB No. 0704-0188

1. AGENCY USE ONLY (Leave blank)	2. REPORT DATE	3. REPORT TYPE AND DATES COVERED
	September 1999	Technical 931001–961030

4. TITLE AND SUBTITLE

Advanced Simulator Power Flow Technology/Advanced Radiation Simulation Volume 2 – MHD Modeling of POS and Power Flow

5. FINDING NUMBERS

C-DNA-001-93-C-0229
PE-4662
PR-AB
TA-AJ
WU-DH00011

6. AUTHOR

Donald Parks, Phil Coleman, Randy Ingermanson, Paul Steen, John Thompson, and Jack Watrous

7. PERFORMING ORGANIZATION NAME(S) AND ADDRESS(ES)

Maxwell Technologies Systems Division, Inc.
8888 Balboa Avenue
San Diego, CA 92123-1506

8. PERFORMING ORGANIZATION REPORT NUMBER

SSS-DTR-94-14855

9. SPONSORING/MONITORING AGENCY NAME(S) AND ADDRESS(ES)

Defense Special Weapons Agency
6801 Telegraph Road
Alexandria, VA 22310-3398
EST/Ware

10. SPONSORING/MONITORING AGENCY REPORT NUMBER

DNA-TR-95-59-V2

11. SUPPLEMENTARY NOTES

This work was sponsored by the Defense Special Weapons Agency under RDT&E RMC Code B 4662 D GE 00011 3300 A AB 25904D

12a. DISTRIBUTION/AVAILABILITY STATEMENT

Approved for public release; distribution is unlimited

12b. DISTRIBUTION CODE

13. ABSTRACT (Maximum 200 words)

This is the second of 3 volumes describing work for the Advanced Simulator Power Flow Technology/Advanced Radiation Simulation Program. This volume, for FY95, deals with analytical, computational and experimental studies of power flow in vacuum feed and switch regions of pulsed power, inductive energy store systems. The first section analyzes by means of a two-dimensional MHD code the evolution of density of the opening switch plasma in the Hawk generator and its dependence on electrode geometry. The following three sections describe the Mach2 MHD code and its application to the design of a novel switch configuration and to the simulation of ACE-4 flashboard experiments. In Sections 5 and 6 the Mach2 code is discussed, including the search for algorithms for the electron Hall effect. In Section 7 the two-dimensional Delta MHD code is described with its analysis of Tandem Puff experiments on ACE 4. Section 8 addresses the new user-friendly, SPICE-MIRIAD based circuit code. Sections 9 and 11, respectively, report improvements to the fast running two-dimensional snowplow model. And Section 10 reports the results from measurements and analysis of current losses in convolutes measured on the ACE 4 coaxial configuration. The contract option work is discussed in the Executive Summary.

14. SUBJECT TERMS

Pulsed Power
Plasma Opening Switch
Aboveground Simulation
Inductive Energy Store

15. NUMBER OF PAGES

159

16. PRICE CODE

17. SECURITY CLASSIFICATION OF REPORT	18. SECURITY CLASSIFICATION OF THIS PAGE	19. SECURITY CLASSIFICATION OF ABSTRACT	20. LIMITATION OF ABSTRACT
UNCLASSIFIED	UNCLASSIFIED	UNCLASSIFIED	SAR

NSN 7540-01-280-5500

Standard Form 298 (Rev. 2-89)
Prescribed by ANSI Sta. 239-18
298-102

EXECUTIVE SUMMARY

Volume 2 describes work performed in Fiscal Year 1995 (FY 95) under contract DNA001-93-C-0229, the second year of a three-year program titled *Advanced Simulator Power Flow Technology for Advanced Radiation Simulation.* The first Volume for FY94 was issued as DNA-TR-95-59.

The objective of the program is to model, design and validate means for achieving more efficient power transfer from the capacitor prime energy storage systems up to and including the dynamic radiation source of the simulator. This report deals primarily with analytical, computational and experimental studies related to this objective, focusing primarily on power flow in the plasma opening switch (POS) and in the vacuum feed region separating switch and load regions in pulsed power, inductive energy store systems and, to a lesser degree, on the performance of PRS loads configured in tandem with a switch.

Experiments on the Hawk generator have demonstrated the sensitivity of switch performance to electrode geometry. Specifically, the experiments studied the effect of an anode extension of the POS region (see Figure 1-5) on switch performance. In Section 1 we apply the two-dimensional x-y geometry code DELTA to analyze the motion of a switch plasma during a power pulse and its dependence on geometry. The most distinctive feature of these calculations is the accumulation of plasma along electrode surfaces. The axial motion of these plasmas inhibits the thinning of the switch plasma as it moves past the anode extension into the region with large radial gap. The greater thinning rate that occurs without the extension would presumably lead to a more rapid development of voltage and better current transfer.

The MHD codes currently in use at Maxwell do not accurately represent the physical mechanisms that would allow us to predict switch voltage and current transfer to a load. The electron magnetohydrodynamic Hall effect would allow voltage to develop as the plasma thinned in the course of its evolution under pulsed power. Whether this effect alone is sufficient to account for observed voltages in microsecond conduction time switches is unknown. It is quite possible, but by no means certain, that locally unbalanced charges or other physical effects not accounted for in quasineutral theories dominate the opening phase of a POS. Algorithms to accurately represent the Hall effect are currently under development for the Mach2 code (Section 6) and will be a focus of activity in the final year of this contract and hopefully lead to answers to these unresolved questions.

Initially, the Mach2 code was acquired and implemented to take advantage of its capability to perform calculations in axisymmetric geometry. The description of Mach2, its installation and its validation for POS problems is discussed in Section 2. Its primary applications have been to the design of plasma opening switches and to the analysis of plasma electron densities measured by means of laser interferometry.

The Catcher's Mitt is the name given to the POS design undertaken with the Mach2 code. The idea behind the Catcher's Mitt is to push the plasma into a cavity at the end of the conduction phase (Section 3, Figures 3-3 and 3-11). The mass remaining in the untrapped plasma should have a low density compatible with rapid opening to high voltage. Experiments on ACE 4 did not yield the expected behavior. In fact, the switch did not perform as well as simpler switch designs without the Catcher's Mitt. The failure of the concept further supported a long held idea that plasma remaining or created in the original volume occupied by the switch plasma shunted current through this volume. This idea is being pursued experimentally and theoretically in the final year of the contract.

A primary purpose of the modeling effort is to compare simulation results with measurements and thereby gain a better understanding of the nature and properties of the switch plasma. This

purpose has been largely achieved in the measurement and computation of electron line densities and magnetic fields in a freely expanding flashboard-produced plasma, and of electron line densities during the conduction phase of a power pulse.

The comparison between density probe responses and magnetic field probes responses indicates that the simulation matches the magnetohydrodynamics of the freely flowing plasma quite well. A self consistent treatment of ionization, for example, Saha ionization, is required to attain this agreement. The comparison also points to significant cooling and a change of mean charge state from near two to about one as the plasma moves away from the flashboard surface. The precise mechanisms that determine the plasma temperature and density adjacent to the flashboard are not well understood. In the calculations these quantities are specified as boundary values and adjusted to produce agreement with the corresponding values measured near the surface. Nevertheless, the model is substantially validated for a given set of flashboards which perform with good reproducibility through about two hundred shots.

The plasma from the flashboards is no longer freely expanding as it passes through an anode structure and into the region between anode and cathode of the pulsed power diode. The second set of comparisons between calculated and measured plasma properties therefore involve the evolution of line densities in this region prior to and during the power pulse. The measurements show a buildup of density on the cathode surface both before and during the conduction phase, an increase of ionization in the middle of the gap during the first two thirds or so of the conduction process, followed by a rapid decrease of line density in the last few hundred nanoseconds preceding opening. All of these features are reproduced by the Mach2 code and the mechanisms modeled within it. The Saha ionization captures the increase of line density observed in the early part of the power pulse, while the hydro features of the model capture the pushing of plasma into the electrodes and the consequent diminution of line density in the middle of the gap late in the conduction phase. Given the density of the plasma at the onset of pulsed power, the Mach2 model of conduction is well validated for microsecond switches.

In contrast to the microsecond conduction process, there is no well validated first principles or semi-empirical model of the opening process. Accounting for the electron hydrodynamic Hall effect presents not only the prospect of calculating voltage and load current transfer from first principles, but also of conduction in short conduction time switches (in the few hundred nanosecond regime) dominated or significantly affected by this Hall effect. At present the effort is focused on the development of an algorithm based on upwind differencing schemes. The results of this effort will be more fully reported in the final report associated with this contract.

The remaining two-dimensional code development under this contract has been accomplished to support experiments based on the tandem puff concept (Section 7). The tandem puff involves a POS in parallel with a plasma radiating source (PRS). At one extreme the POS is remains well separated from the PRS and opens in the manner of a conventional switch, thereby transferring current to the load. At the opposite extreme the switch is close to the PRS puff gas, mingles with it during the conduction process, and commutates the current without passing through a distinct opening phase. Naturally, the tandem puff may be arranged to operate anywhere between these two extremes.

The analysis of the tandem puff configuration was performed with the two-dimensional MHD code, DELTA. To enable this analysis DELTA was extended to incorporate axisymmetric geometry and non-equilibrium rate processes for calculating ionic state populations and emission of radiation in the approximation that the radiating plasma is optically thin. The experimental configuration contained B-dot probes at various locations between the POS and the PRS, as well as radiation diagnostics for measuring total radiation and radiation with energies greater than 1 kV. The experimental configuration permitted axially resolved measurements of time of onset of emission of photons with energies above 1 kV.

Initial calculations of the experimental configuration were performed to compare time of arrival of current at the B-dot probes and time of onset of radiation of energetic (>1 keV) photons from the neon and argon puff gas loads. In the interests of efficiency these initial computations were carried out with an ideal gas model ignoring the effects of ionization, excitation and radiation. Their main purpose was to use the time of arrival of signal at the B-dot probes to establish the initial density in the POS plasma. Then the computed times at which high temperatures were attained on axis could be calculated and compared with the observed time of radiation onset. This time would vary with the puff gas injection time, a variable not only of the experiment but also of the model, which modeled the entire process of puff gas injection, POS conduction and PRS pinch. In general the calculated and measured timing data were in good agreement, especially with regard to axial variation of signal onset (zippering).

Detailed calculations of radiation energy and spectral output were performed utilizing the full atomic kinetics and radiation capabilities of the code. Generally the computed results for the >1 keV radiation were larger than the measured results, especially for argon. Measurement gave less than 1 kJ for argon: computed values were about 8 kJ. For neon the measured values were in the range from about 3 to 20 kJ; the corresponding theoretical value was about 30 kJ, assuming that the full generator current passed through the load. The most obvious uncertainty in comparing theory with experiment is the amount of current that is actually conducted through the load. Without a knowledge of this current the theoretical models cannot be considered validated.

Section 8 describes work begun on a general circuit code, SPOCK, which will incorporate some of the most useful features of modern software technology. Underlying the code is the industry standard circuit code SPICE developed over the last 20 years at the University of California at Berkeley. SPICE comes with a clumsy user interface and only rudimentary plotting facilities. It defines a large number of devices including resistors, capacitors, inductors, transmission lines, current and voltage sources, ideal switches, diodes and an array of semiconductor components that are not of interest to the pulsed power community.

New components lacking in SPICE that are under development by us include POS's, PRS's, MITL's, bremsstrahlung diodes and plasma filled diodes. SPOCK will incorporate a SPICE preprocessor with a graphical user interface for easy setup of circuits. It will incorporate the MIRIAD technology developed at S-Cubed over the last several years. MIRIAD is facile in the integration of many codes and allows quick setup of parameter studies.

Section 8 describes the various new models of interest in the pulsed power community which have already been put into SPOCK along with some simple test applications. New devices and models can be added to the code with only a small incremental effort. In contrast, adding new devices to our previous circuit code caused sharply increased code complexity. Ease of modifying SPOCK is made possible by the techniques of object oriented programming, a methodology for managing complexity.

Section 9 describes improvements to our two-dimensional Snowplow model, a model for the rapid calculation of two-dimensional effects in opening switch and radiating source plasmas. Previously the code solved only mass and momentum conservation equations. Addition of energy conservation equations permits us to estimate heretofore inaccessible features of snowplowed plasmas, such as their temperature and thickness.

Section 10 reports measurements and analysis of current losses associated with the convolute transition between the radial triplate feed and coaxial sections of the ACE-4 coaxial configuration. The losses are associated with the breakdown at high voltage of the cathode surfaces in the neighborhood of magnetic nulls. Specifically, with a large inductance downstream of the convolute in the ACE-4 coaxial configuration, but with no POS in place, large inductive voltages developed at the position of the convolute and about fifty percent of the generator current leaked

across the convolute. The lost current appeared consistent with a Child-Langmuir current over the entire area of cathode between convolute posts. That the magnetic fields in the vicinity of the convolute posts should be so ineffective in limiting the current losses is somewhat surprising. With a POS located downstream of the convolute no current loss was observed at the convolute, an observation which is consistent with inferred voltages at the convolute lying below breakdown thresholds.

The final power flow issue confronted in this report is the power loss in electrodes where currents converge to levels of megaamps per centimeter before passing through a load. Section 10 describes a simple analytic model for estimating electrode power losses in such highly converged currents for arbitrary current waveforms. The validity of the model is established by comparison with full magnetohydrodynamic calculations of losses in the resistively heated, ablating surface material.

Work performed under the option to this contract concerns the thermostructural response of four composite materials tested in the proton beam of the SABRE accelerator at Sandia National laboratories. This work is described under separate cover in the Maxwell S-Cubed report SSS-DTR-95-15191, "Thermostructural Response Testing of Composite Materials in the SABRE Ion Beam Facility," September 1995, by Russ Wilson, Joe Sallay, Mel Rice, Gerry Gurtman and Gary Steckel.

CONVERSION FACTORS FOR U.S. CUSTOMARY TO METRIC (SI) UNITS OF MEASUREMENT

To Convert From	To	Multiply By
angstrom	meters (m)	1.000 000 x E -10
atmosphere (normal)	kilo pascal (kPa)	1.013 25 x E +2
bar	kilo pascal (kPa)	1.000 000 x E +2
barn	meter^2 (m^2)	1.000 000 x E -28
British thermal unit (thermochemical)	joule (J)	1.054 350 x E +3
cal (thermochemical)/cm^2	mega joule/m^2 (MJ/m^2)	4.184 000 x E -2
calorie (thermochemical)	joule (J)	4.184 000
calorie (thermochemical)/g	joule per kilogram (J/kg)*	4.184 000 x E +3
curies	gig becquerel (Gbq)+	3.700 000 x E +1
degree Celsius	degree kelvin (K)	$t_K = t°_C = 273.15$
degree (angle)	radian (rad)	1.745 329 x E -2
degree Fahrenheit	degree kelvin (K)	$t_K = (t°_F + 459.67)/1.8$
electron volt	joule (J)	1.602 19 x E -19
erg	joule (J)	1.000 000 x E -7
erg/second	watt (W)	1.000 000 x E -7
foot	meter (m)	3.048 000 x E -1
foot-pound-force	joule (J)	1.355 818
gallon (U.S. liquid)	meter^3 (m^3)	3.785 412 x E -3
inch	meter (m)	2.540 000 x E -2
jerk	joule (J)	1.000 000 x E +9
joule kilogram (J/kg) (radiation dose absorbed)	gray (Gy)*	1.000 000
kilotons	terajoules	4.183
kip (1000 lbf)	newton (N)	4.448 222 x E +3
kip/inch^2 (ksi)	kilo pascal (kPa)	6.894 757 x E +3
ktap	newton-second/m^2 (N-s/m^2)	1.000 000 x E +2
micron	meter (m)	1.000 000 x E -6
mil	meter (m)	2.540 000 x E -5
mile (international)	meter (m)	1.609 344 x E +3
ounce	kilogram (kg)	2.834 952 x E -2
pound-force (lbf avoirdupois)	newton (N)	4.488 222
pound-force inch	newton-meter (N•m)	1.129 848 x E -1
pound-force/inch	newton/meter (N•m)	1.751 268 x E +2
pound-force/foot^2	kilo pascal (kPa)	4.788 026 x E -2
pound-force/inch^2 (psi)	kilo pascal (kPa)	6.894 757
pound-mass (lbm avoirdupois)	kilogram (kg)	4.535 9024 x E -1
rad (radiation dose absorbed)§	gray (Gy)*	1.000 000 x E -2
roentgen§	coulomb/kilogram (C/kg)	2.579 760 x E -4
shake	second (s)	1.000 000 x E -8
slug	kilogram (kg)	1.459 390 x E -1
torr (mm Hg, O• C)	kilo pascal (kPa)	1.333 22 x E -1

* The gray (Gy) is the accepted SI unit equivalent to the energy imparted by ionizing radiation to a mass and corresponds to one joule/kilogram.

\+ The becquerel (Bq) is the SI unit of radioactivity; 1 Bq = 1 event/s.

TABLE OF CONTENTS

TABLE OF CONTENTS (Continued)

FIGURES

FIGURES (Continued)

FIGURES (Continued)

FIGURES (Continued)

FIGURES (Continued)

FIGURES (Continued)

TABLES

SECTION 1

MHD ANALYSIS OF HAWK ANODE GEOMETRY VARIATION RESULTS

Experiments performed on ACE 4 (Section 3) show that the axially integrated electron density near the middle of the anode-cathode gap can decrease rapidly with time during the last half of the conduction phase. Further, it is observed that in general, the more the density decreases, the greater is the voltage generated after the conduction phase. The experiments also indicate that the electrode geometry substantially influences the magnitude of this voltage.

In the process of trying to understand the influence of electrode geometry on the performance of ACE 4, we have examined some related results from Hawk. One series of HAWK shots were taken for three different HAWK geometries.[1] In all three cases, the cathode was solid metal so that no plasma could flow out of it, and the main anode consisted of a series of bars between which plasma could flow freely. In this 8-cm long injection region, the anode-cathode (A-K) gap was 2 cm, while the anode opened out to a distance of 4 cm from the cathode downstream of the injection region. The differences between the three cases was in the separation of these two regions. In the first case, the injection region was immediately adjacent to the downstream "open" region. In the second region, there was an intermediate 2 cm long region, in which the anode remained 3 cm from the cathode, but was solid instead of open; that is, no plasma could flow out through it. In the third case, the length of this intermediate region was increased to 6 cm. These three geometries are diagrammed in Figure 1-1.

When otherwise identical shots were taken for these three geometries, an obvious trend was observed. The shots with no anode extension gave good switch voltages and load currents, while the 2 cm anode extension gave significantly degraded performance, and the 6 cm extension showed even worse degradation. Since this trend is in the same direction as some of our results in ACE 4, we desired to understand these results as completely as possible.

One of our tools most directly applicable to studying these results was our 2-D triangular hydrodynamic DELTA code. While this code has the capability of performing MHD calculations, for technical reasons this capability at the time of these calculations was implemented only in an X-Y coordinate system, not in an R-Z one. (This limitation has now been removed - see Section 7). This was a significant drawback, as it precluded a quantitative simulation of the actual machine because the radial effects of HAWK's coaxial geometry could not be taken into account. Nevertheless, we proceeded to do simulations in the X-Y geometry, hoping to see qualitative effects which would provide insight into possible causes of the observed trend.

To economize our use of computer time, we did two simulations: one with no anode extension and one with a 2 cm extension. The mesh with no extension is shown in Figure 1-2.

In these simulations, the bottom edge of the mesh, representing the solid cathode, has a "slip" boundary condition, meaning that the plasma cannot have a velocity component into or out of the cathode, but can flow freely along it without frictional drag. The open portion of the anode extends between the right end of the small "notch" on the left and the bottom end of the long "notch" which descends from the top edge near the center of the mesh. That is, it is the boundary between the yellow and brown regions shown in Figure 1-2. In order to make the current flow along this anode while still allowing hydrodynamic effects above and below it, the anode region itself is made very highly conductive (with about the conductivity of stainless steel). In addition, the magnetic field is excluded from the region above the anode (i.e., above the top edge of the left-most "notch"). This forces the entire current to flow in the anode. Since the anode is interior to the mesh, the plasma mass can flow freely through it. The magnetic field rises linearly along the left-hand edge of the A-K gap (the line labeled "15" in Figure 1-2) at a rate of 2.42×10^{10}

Gauss/second, and satisfies the natural boundary condition $\hat{n} \bullet \vec{\nabla} B = 0$ along all metal mesh boundaries.

The initial plasma density distribution is slightly complex. In the vacuum regions (shown in white in Figure 1-2), a nominal initial number density of 10^{12} particles/cm^3 is assumed. In the A-K gap plasma region (shown in yellow), the initial number density varies between 2 x 10^{15}/ cm^3 at the anode or cathode to 10^{15}/cm^3 midway between the two as a smooth cosine wave. In the plasma region above the anode (shown in brown), the initial number density is a constant 2 x 10^{15}/ cm^3. An additional complication is that the plasma has an initial velocity of 3 x 10^6 cm/sec in the downward direction, corresponding to an injection velocity from the flashboards. (This is also the velocity with which flashboard plasma is injected into the mesh from the inflow boundary which is shown in blue in Figure 1-2 along the upper left side of the mesh.) The effect of this initial velocity is that the initial density distribution, in the absence of magnetic field, would simply slide downward at this speed and pile up at the cathode. Finally, the initial temperature of the plasma is taken to be 1 eV, and a condition is imposed at all the solid metal surfaces such that the temperature of the plasma immediately adjacent to these surfaces may not exceed 2 eV. This is intended to simulate cooling of the plasma at these surfaces, as discussed in previous reports.[2]

The results from these calculations were as follows. Initially, the snowplow front pushed into the plasma fastest down the center of the A-K gap, since the density was at a local minimum there. As the vertical location of this density minimum continued to drift downward during the course of the calculation, after about 400 ns the downstream plasma no longer showed a local minimum. However, the initial shape of the front led to "thinning," which pushed the swept-up plasma away from the center and toward the anode and cathode region. The plasma stagnated when swept against the cold cathode, while at the anode, it simply flowed through and into the field-free exterior region. The effect of this was that penetration continued fastest in the center of the gap even without the local minimum, leading to a "bow shock" type of profile. After about 800 ns, the density profile was as seen in Figure 1-3. Note that, at this time, there is no significant difference seen between the case with no anode extension and the case with the 2 cm extension, as the front has not yet reached that region. Accordingly, we show only one of the two cases here.

The point of main significance here is that, near the anode, the plasma is being pushed by the magnetic field primarily rightwards, but also upwards. This becomes significant when the plasma begins to move into the open downstream region.

This process is shown in the following figures. Figures 1-4, 1-6, 1-8, and 1-10 show progressive development of the plasma density contours at 20 ns intervals as the plasma moves out into the open region for the case of no anode extension, while Figures 1-5, 1-7, 1-9, and 1-11 show the same for the case with a 2 cm extension.

Figures 1-4 and 1-5 show the plasma density at the time when the plasma is just starting to move into the open region. Note that this time is not the same for both cases, as the plasma had a longer distance to travel with an extended anode.

A few points to note about these plots: First, in both cases, the density does not vary greatly along the snowplow front until the front very nearly approaches either the cathode or anode. (This is, of course, an artifact of our X-Y calculational geometry; there would be variation in the true R-Z geometry.) Second, the solid anode extension of what we called the "Gap" case has accreted a layer of compressed plasma similar to (but much less dense than) the layer seen along the cathode in both cases. This of course does not occur in the "No Gap" case because there is no solid anode surface upon which to accumulate a surface plasma. Figures 1-6 and 1-7 show the density contours 20 ns later.

At this time, a noticeable difference between the two cases is starting to appear. In the case with no anode extension, a distinct density "valley" is starting to form just right of where the front touches the anode. In other words, following the path of the front from cathode to anode while examining the density along it will yield a nearly constant density until just before reaching the anode, at which point the density will dip sharply and then rise again. (Note that the contours are logarithmically spaced, so that the density in the "valley" is about one-fourth to one-fifth of the density along the central portion of the front.) This does not appear in the case with the anode extension, because the plasma which accreted along the solid anode region slides down the anode to fill in the density valley before it has a chance to form. Accordingly, the density along the front is much more nearly constant with an anode extension than without it. Figures 1-8 and 1-9 show density contours at a time 40 ns from the onset of expansion into the open downstream region.

At this time, the valley formed in the snowplow front in the no-extension case has become quite pronounced. Specifically, at its lowest point the front density is now less than 2×10^{-8} grams/cm^3, which was the initial plasma mass density in the center of the A-K gap. This density is low enough that the magnetic field is beginning to push through the front, as can be seen by the outward bulge of the front at this point. Meanwhile, the extended-anode case is also beginning to develop a low-density point, but in its case, the minimum density occurs precisely at the anode, rather than at a two-sided valley. It has not yet shown signs of upward motion.

Figures 1-10 and 1-11 show the density contours at a time when the plasma has expanded upwards to the limits of the open region. This occurs 60 ns from the time just prior to expansion.

At this time, the low-density front regions of both configurations have been pushed directly upward until they have collided with the top boundary of the open downstream region. Since we have no opening model in this simulation, the front plasma has remained highly conductive throughout this entire period, with the resistivity taken to be Spitzer throughout. In reality, it is quite possible that an erosion gap or some other mechanism would allow the field to penetrate through the snowplow front at or before this point. In any event, in a true R-Z geometry the details of the vertical expansion would almost certainly differ from those shown here, due to the 1/r reduction in both the plasma density and the magnetic field strength. For both those reasons, we did not continue the calculation beyond this point. Several differences in the two cases suggest avenues of further exploration. First, the formation of a plasma layer along the solid anode that subsequently fills in the forming "valley" in the front could act to delay the onset of opening in this case. Second, the formation of a minimum-density point directly alongside the anode rather than some distance away from it, might also serve to degrade the switch opening, as surface ablation, cooling or some other effect might impede the opening mechanism in this case. However, for further investigation we need to consider a model for switch opening, and to accurately represent the true plasma conditions for input to that model we will need a true R-Z MHD code.

To this end we have acquired and implemented the Mach 2 code, described in Section 2.1. To take advantage of the greater geometric capability of the triangular mesh DELTA code, we have also made the modifications required to solve MHD problems in R-Z geometry, as described in Section 2.

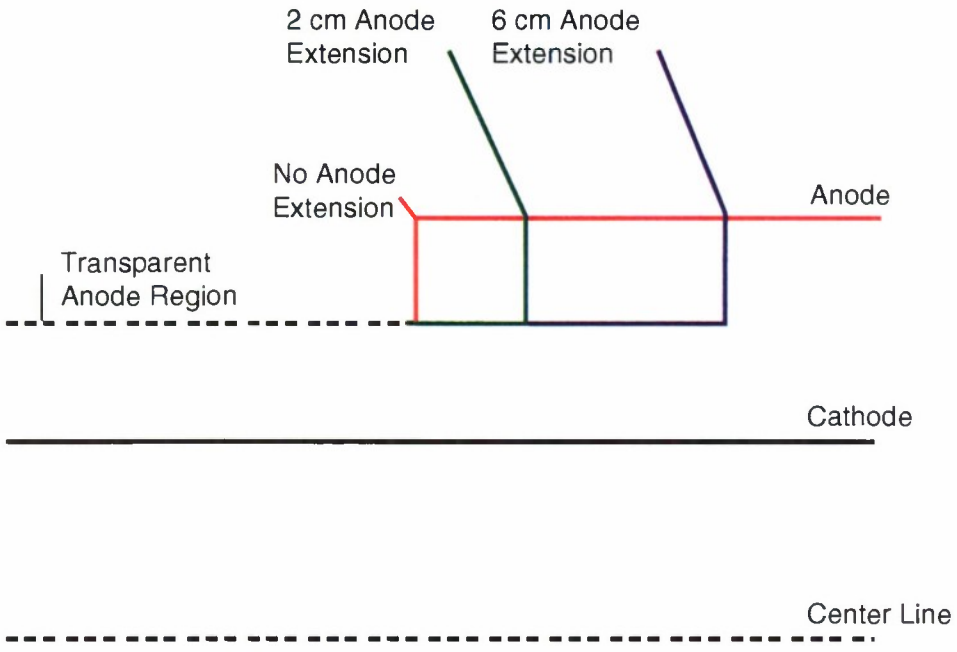

Figure 1-1. Three HAWK Anode Geometries.

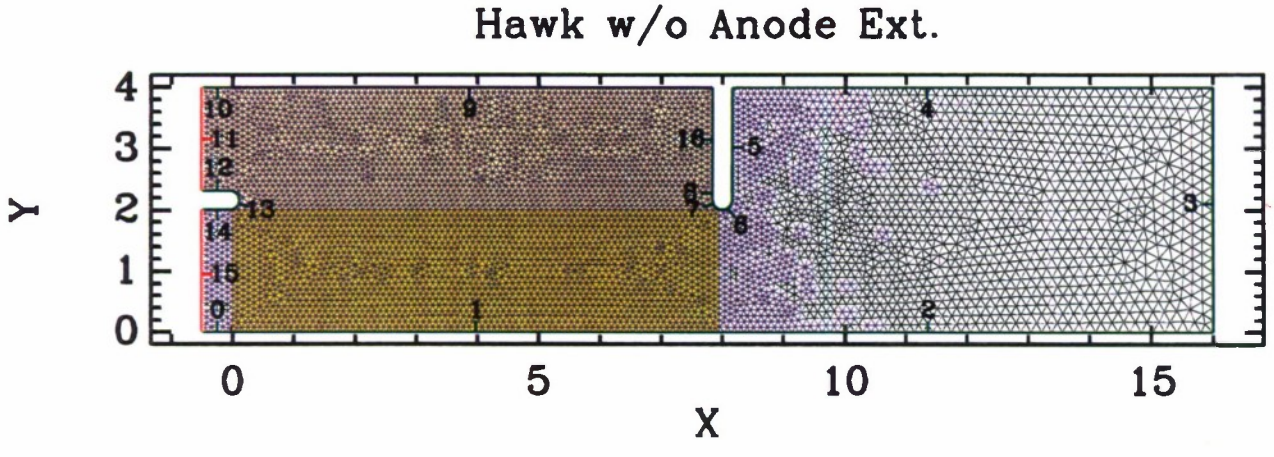

Figure 1-2. Triangular DELTA mesh for HAWK simulation.

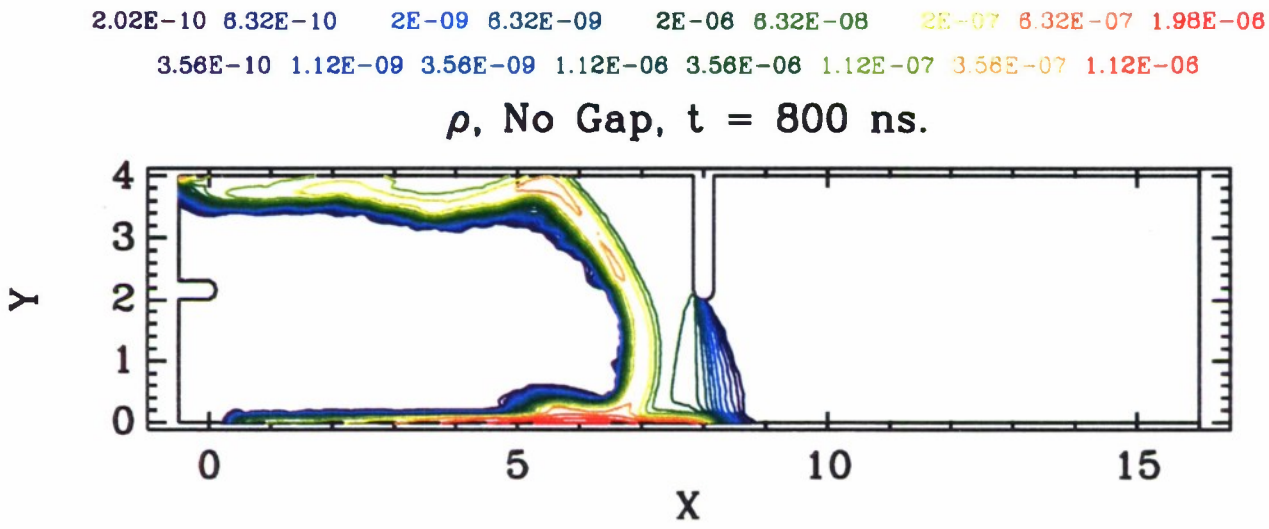

Figure 1-3. Plasma mass density just before the end of the switch.

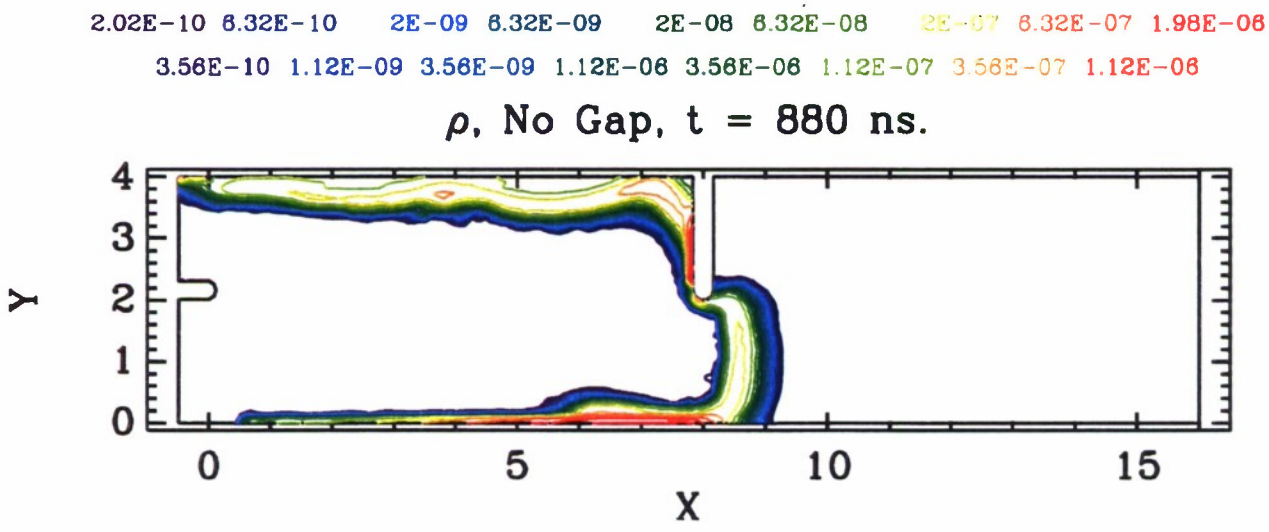

Figure 1-4. Just before expansion without extension.

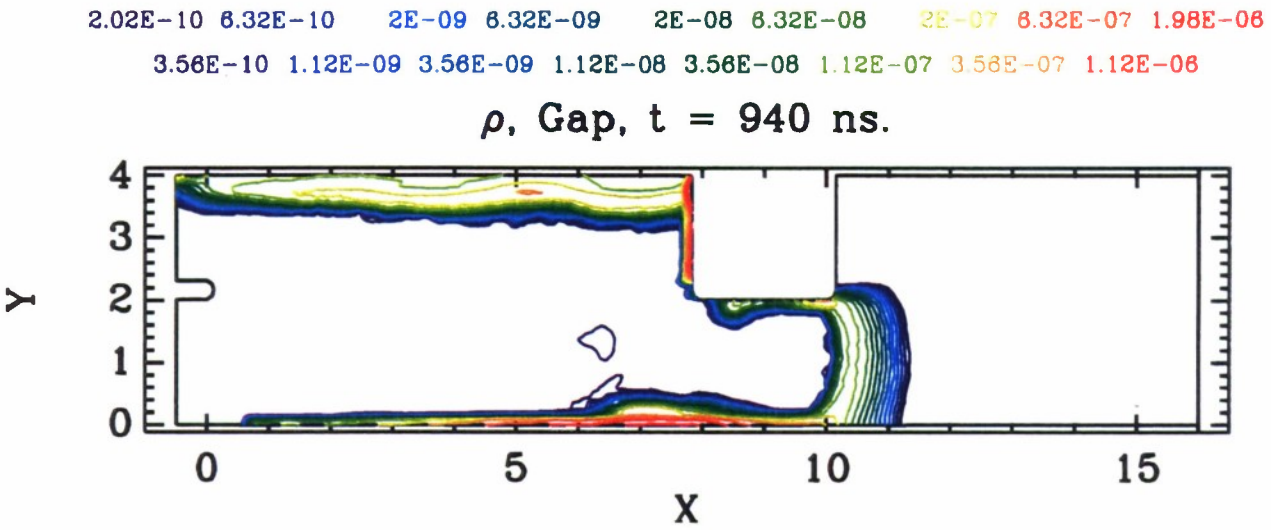

Figure 1-5. Just before expansion with 2 cm extension.

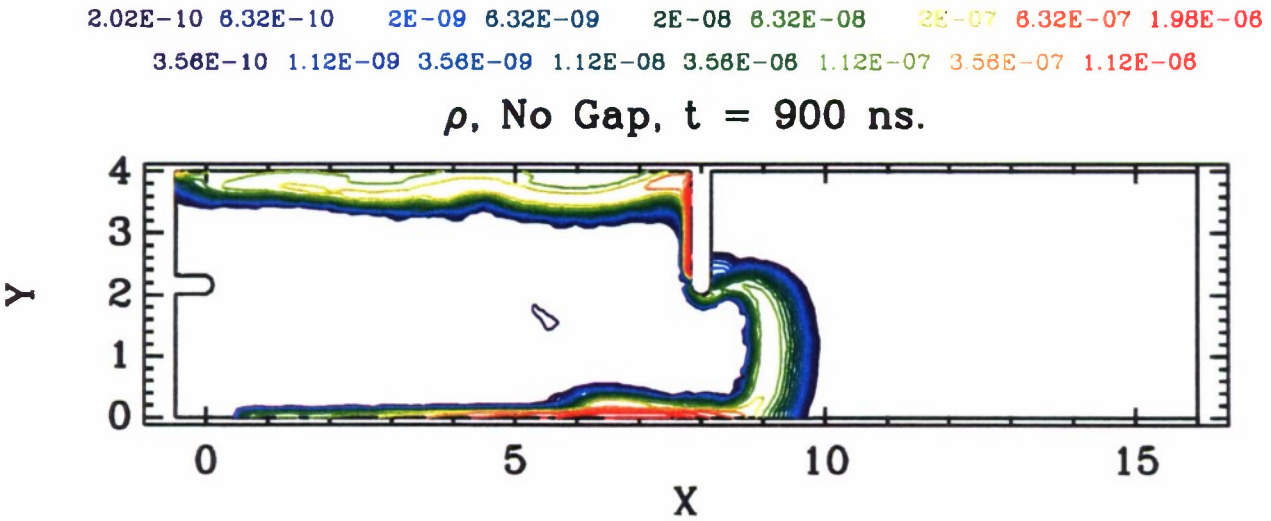

Figure 1-6. Beginning of expansion without extension.

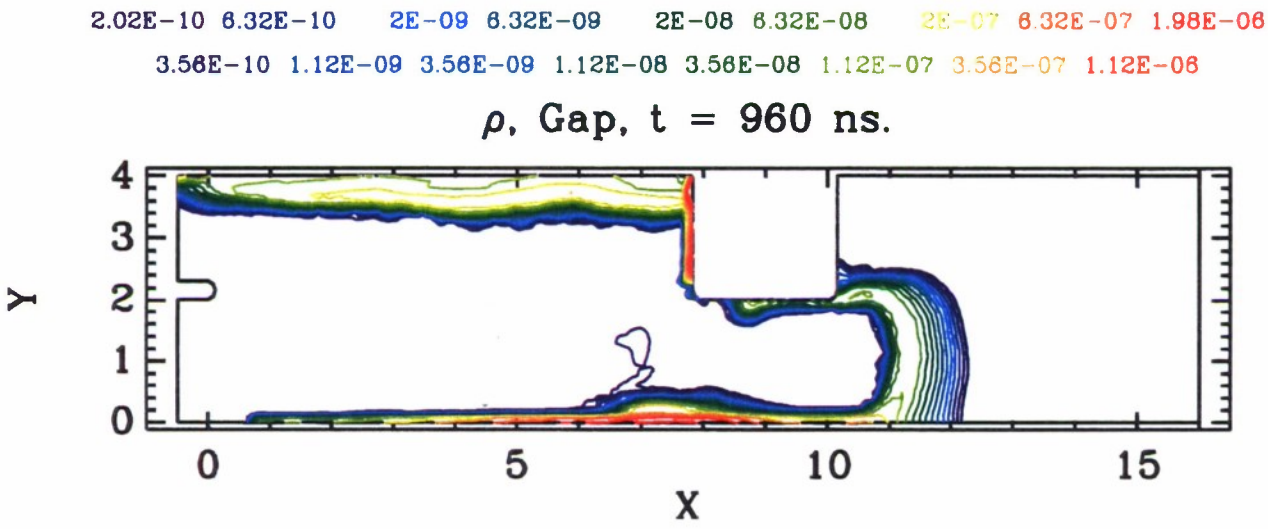

Figure 1-7. Beginning of expansion with 2 cm extension.

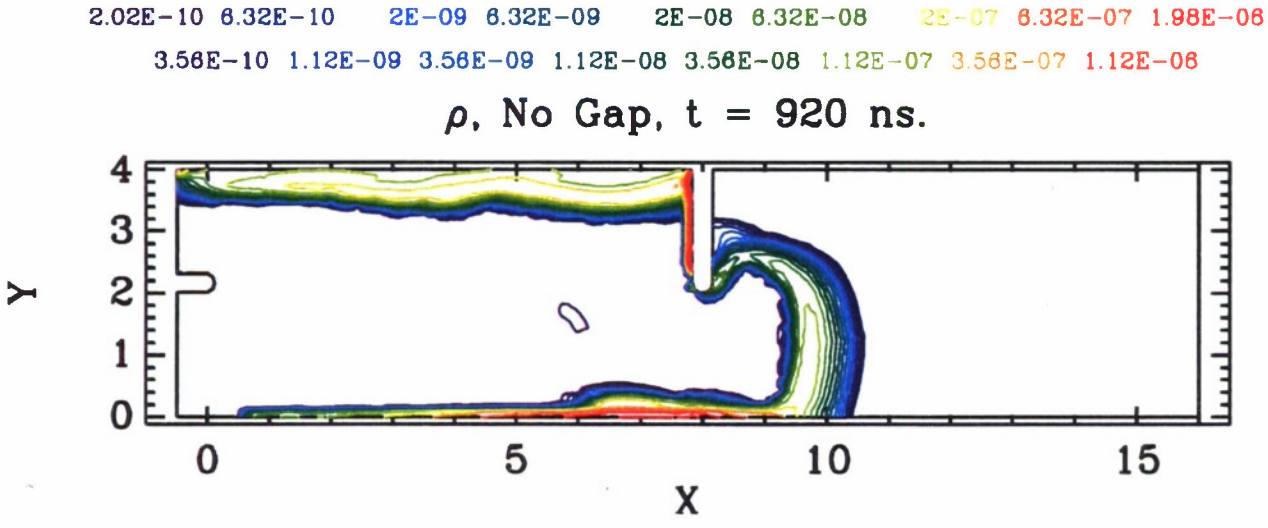

Figure 1-8. Beginning of valley formation without extension.

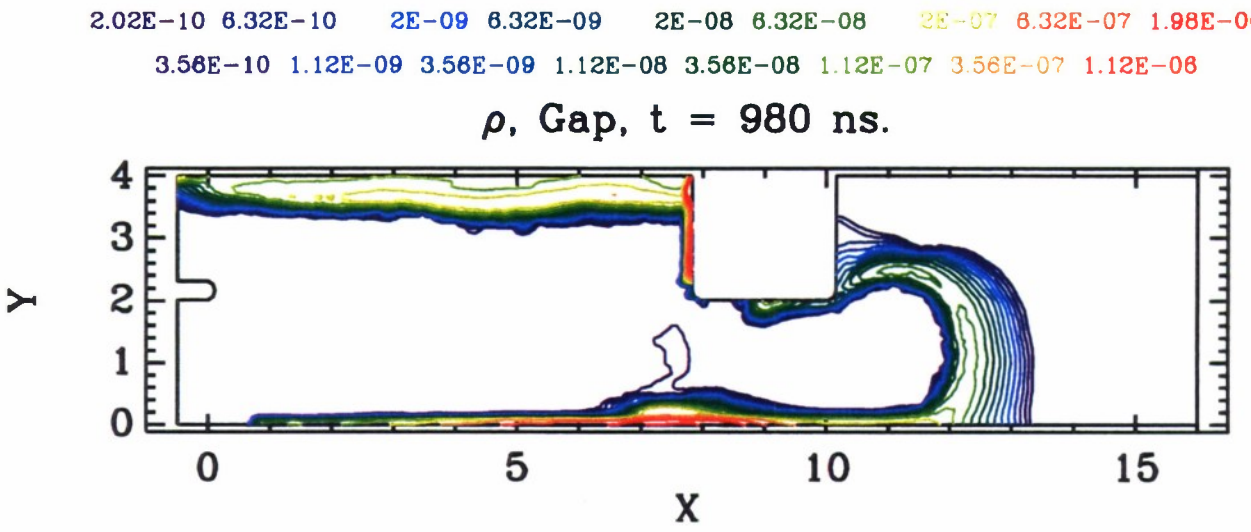

Figure 1-9. Beginning of valley formation with 2 cm extension.

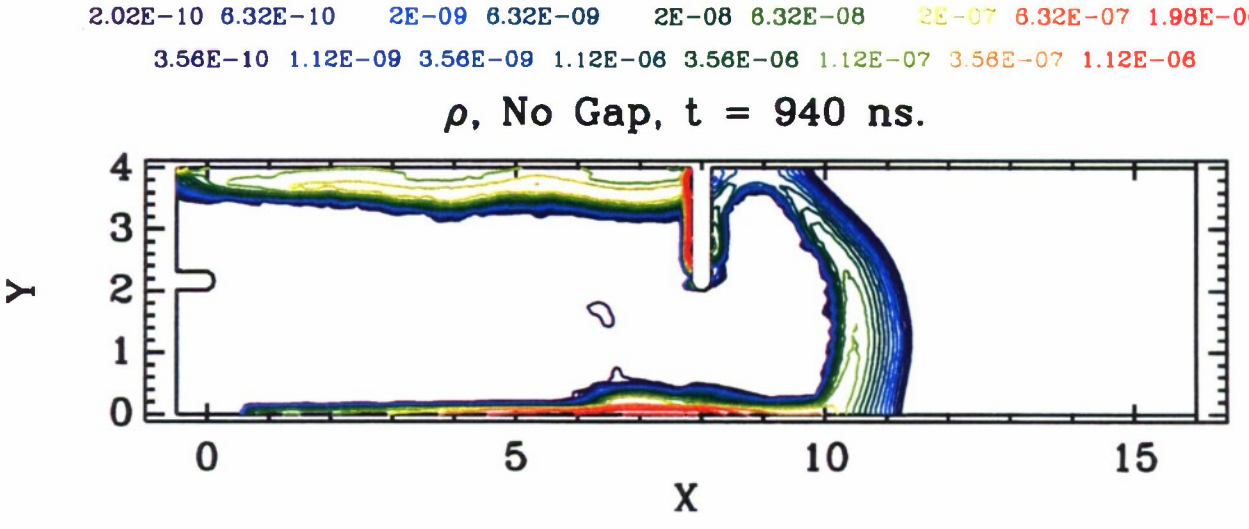

Figure 1-10. Vertical expansion without extension.

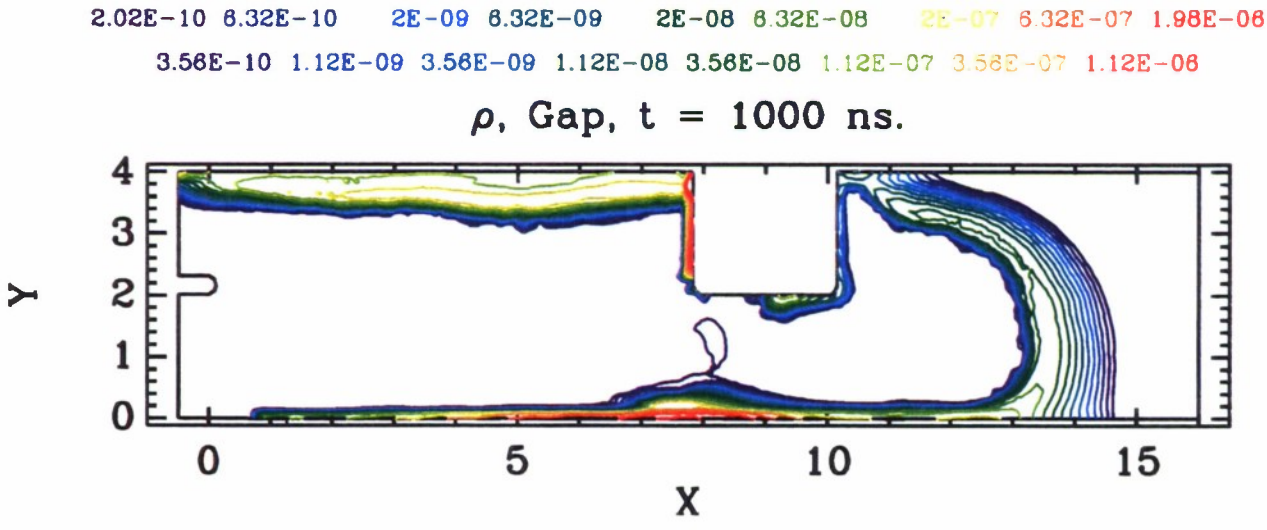

Figure 1-11. Vertical expansion with 2 cm extension.

SECTION 2

MACH2 CODE

2.1 DESCRIPTION OF MACH2.

In January of 1995, S-Cubed took steps to acquire Mach2. This section provides a brief description of that code and why it is considered a valuable addition to DNA's capabilities.

Mach2 is a two-dimensional magnetohydrodynamic (MHD) code which incorporates the arbitrary Lagrangian-Eulerian (ALE) gridding technique on a grid of arbitrary quadrilaterals. The core of the code comes from the YAQUI and MOQUI codes written in the mid-70's by Jerry Brackbill of Los Alamos National Laboratory. In the mid-80's, Phillips Laboratory (then the Air Force Weapons Laboratory) contracted with Mission Research Corporation to create a production code out of YAQUI capable of dealing with complex geometries.

The geometric flexibility of Mach2, incorporated through a multiblock architecture, makes the code extraordinarily useful for modeling important aspects of real experiments, but beyond this, Mach2 has a wealth of physical models and boundary conditions. Mach2 may include in a calculation all three vector components of both fluid velocity and magnetic field. Finite electrical conductivity can be included; the user may choose from a variety of resistivity models, including Spitzer, several types of anomalous, and electron-neutral collisions. Heat diffusion can also be included in a calculation; the provision exists for including the magnetic inhibition of electron heat conduction on the Spitzer model for thermal conductivity. Detonation effects can be modeled; a dynamic burn model with flexible initiation options has been calibrated against data for PBX-9501 and PBX-N110. Laser interaction with a plasma can be modeled, as can self-generated magnetic fields VIA the thermo-electric effect. Elastic/plastic deformations of a solid can be modeled. The plasma can be characterized either by a single temperature, or by separate ion and electron temperatures. Plasma radiation can be treated within the framework of the single-group radiation diffusion model (appropriate for optically thick plasmas) or with an optically thin radiation model. For the equation of state, the user may choose from an ideal gas equation of state, a Gruneisen equation of state, or the SESAME tabular equations of state. Numerous options exist for adaptive grid control. This allows the user to direct the code to concentrate grid points on features of interest, such as magnetic field gradients, density peaks, or temperature gradients. Boundary conditions exist which permit the user to control the flow of material and magnetic field into the simulation domain in a wide variety of ways.

Since its creation, Mach2 has been used on a wide variety of problems: plasma flow switches; z-pinches and cascading gas puffs; rail-guns; laser-target interactions and the "aneurysm" effect; compact toroid generation, evolution and acceleration; explosively-driven magnetocummulative generators; magnetized-target ICF; imploding liners; electric propulsion; the magnetically controlled plasma opening switch, the magnetized plasma opening switch, and the standard plasma opening switch.

The acquisition of Mach2 has significantly enhanced S-Cubed's modeling capabilities. While the DELTA code has recently been extended to be able to perform resistive MHD in cylindrical geometry, that code has neither the extensive collection of physics models, nor the extensive validation against experimental results that Mach2 enjoys. However, Mach2 is not considered a replacement for DELTA; DELTA is a useful and powerful code, and in fact, has strengths where Mach2 has weaknesses. For example, the multiblock architecture of Mach2 is such as to allow geometries which are topologically either simply or singly connected; DELTA does not suffer from such a restriction. DELTA is equipped with a graphical user interface which allows the user to grid-up new problems very efficiently; in contrast, Mach2 is driven with namelist input which

forces the user into an oft-times tedious iterative edit-and-execute mode for creating grids for new problems. Thus, the availability of both codes is a significant asset for S-Cubed.

2.2 MACH2 INSTALLATION.

Mach2 is distributed without charge by Phillips Laboratory to government employees and qualified contractors. As of January 1995, Mach2 had been configured to run on several different Cray computers (including the YMP at Los Alamos), Sun workstations, and the IBM 6000. While using Mach2 on the DNA Cray is an important mode of our operation, we also strongly desired to be able to run it on the available S-Cubed workstations, which are Silicon Graphics Indigos (SGI). Thus, the first order of business after acquiring the Mach2 tar file from Phillips was to make the code modifications necessary for it to compile and execute on the SGI. This task took several weeks to accomplish. The primary obstacle was the frequent occurrence of very out-dated FORTRAN handling of character variables, but there were a large number of unrelated minor details as well. A complete record of the changes and fixes required to get Mach2 compiled and running was maintained, and is available to anyone else who needs to go through this process.

With this task finished in mid-February, we have adopted a mode of work in which the tasks of new problem set-up, running small or low priority jobs, and post-processing are performed on an SGI R3000; jobs of moderate size or intermediate priority are run on an SGI R4000; and jobs or large size or high priority are run on the DNA Cray at Los Alamos.

2.3 VALIDATION AGAINST SIMPLE SNOWPLOW MODEL.

The first task set for application of Mach2 was to investigate the predictions of an idealized one-dimensional snowplow calculation. The calculation gives the trajectory of the snowplow as well as the temperature of the plasma swept up by the snowplow. Previous attempts to compare the analytic prediction of plasma temperature with simulation results from the DELTA code has led to concerns over whether DELTA was calculating the temperature correctly.

The highly idealized problem consists of an infinite half-space filled with plasma of uniform density and infinite electrical conductivity. The plasma is treated as an ideal g-law gas with g = 5/3. Ionization and other processes which absorb energy are neglected. At time t=0, electrical current begins to flow on the plasma/vacuum interface. The current increases linearly in time. This creates a magnetic pressure which accelerates the plasma/vacuum interface into the plasma-filled region. Under the snowplow model, one imagines that as this interface moves into the plasma, it collects plasma into an infinitely thin layer of infinite density. For this model, the trajectory of the plasma/vacuum interface, or snowplow, is

$$x(t) = \dot{B}t^2 / (48\pi\rho_o)^{1/2} \text{ (cgs units)} \qquad (2.1)$$

where $\dot{B}$ is the rate at which the magnetic field in the vacuum increases and ρ_o is the mass density of the undisturbed plasma. Under the assumption that the excess of work done by the magnetic field over kinetic energy goes into internal energy, we obtain a prediction for the temperature of the swept-up plasma:

$$T(t)(eV) = 8.33\times10^{-12}(L/T_c)^2(t/T_c)^2 \text{ (cgs units)} \qquad (2.2)$$

where L is the distance the snowplow has moved from time t=0 to time t=T_c. With the following choices of parameters: L = 8 cm, $\dot{B} = 2.42 \times 10^{10}$ Gauss/s, $\rho_o = 2\times10^{-8} gm/cm^3$; the conduction time T_c is 757 ns and the temperature at that time is 930 eV.

A Mach2 simulation was designed to run with the same parameter values. The first attempt was with an Eulerian calculation, i.e., a calculation in which the numerical grid remained static. The observation from this simulation was that the temperature in the highest density portion of the swept-up mass was only 4-5 eV. With a more highly resolved grid, the temperature in the shock front was higher, but never did it approach the 930 eV predicted by theory. The observation that higher spatial resolution tended to produce temperatures which were in better agreement with theory prompted the execution of simulations performed with a Lagrangian grid. In that case, the amount of mass contained in any given cell remains constant, and the cell deforms according to the instantaneous hydrodynamic velocity. Figures 2-1 and 2-2 show the results from such a calculation.

Figure 2-1 shows the trajectories of the cell boundaries. This calculation was actually for a 16 cm long plasma, and the comparison is to be made between theory and the state of the plasma calculated at the time at which the snowplow has traversed 8 cm.

Figure 2-2 shows the temperature history from each computational cell. Note that the trajectory plot shows that the region from x=0 to x=8 cm was initially spanned by 16 zones of equal width. As the snowplow accelerates into the plasma, a thin, high density region is indeed formed, as the trajectory plot shows. The temperature history plot shows that a cell's temperature undergoes an abrupt increase as the front approaches, then continues with a more gentle increase in temperature. The maximum temperature achieved at the time at which the snowplow has tranversed 8 cm is approximately 600 eV. While this is quite a bit higher than that obtained in the coarsely resolved Eulerian calculations, it is still lower by more that 50% than the analytic prediction.

The reason for this discrepancy becomes clear upon further comparison of the zone trajectory plot with the premise of the analytic model; recall that the latter assumed that once contacted by the snowplow front, plasma becomes part of an infinitely thin, infinitely dense layer. Such a situation cannot be realized in the simulation, and it, in fact, is behaving in a completely different manner. The plasma which is swept-up by the snowplow forms a dense layer of growing thickness. This situation has analogies to the structure of an atmosphere gravitationally bound to a planet. Thus, part of the energy which under the snowplow model goes into thermal energy, is used in the simulation for maintaining this growing "atmospheric" layer, and the peak temperature is consequently lower than that predicted. The situation was thus one wherein the analytic model made certain assumptions that simply would not occur in the simulation.

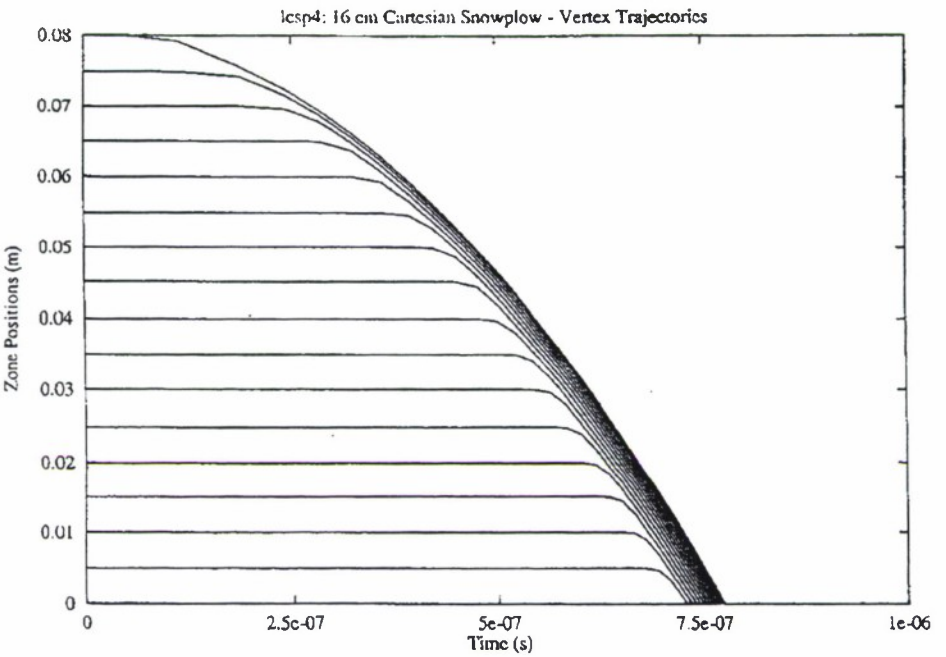

Figure 2-1. Trajectories of cell boundaries in Mach2 calculations.

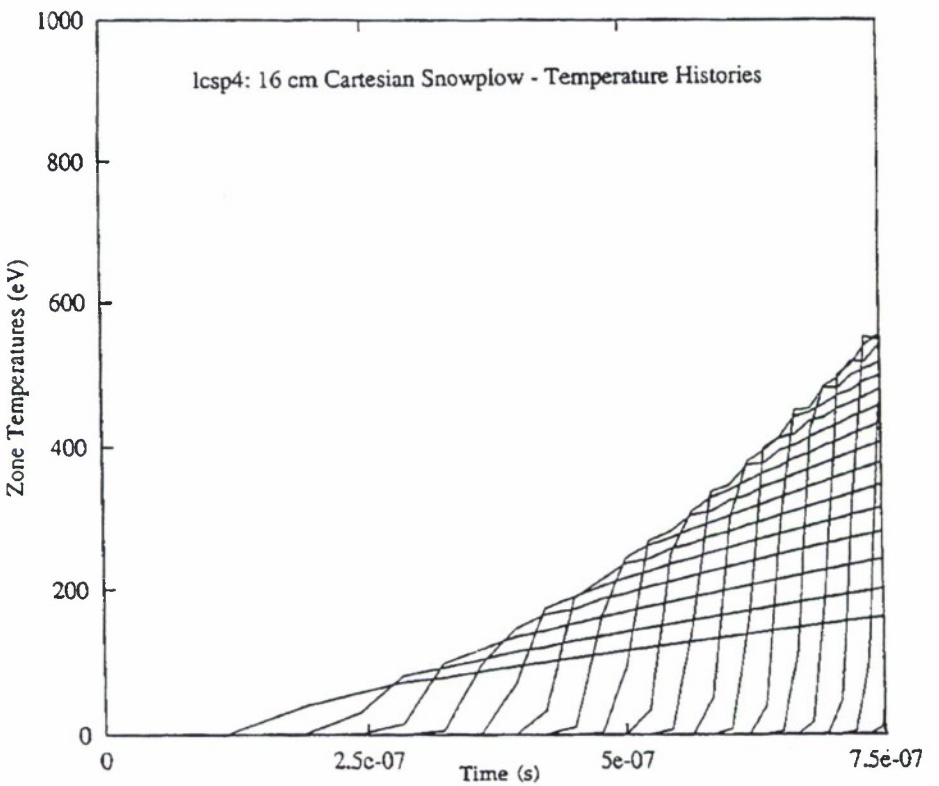

Figure 2-2. Temperature history of each computational cell in Mach2 calculations.

SECTION 3

CATHER'S MITT DESIGN CALCULATIONS

3.1 CONCEPT.

The Cather's Mitt concept was developed in the December-January timeframe in response to difficulties with the ACE 4 experiment. In the attempt to reproduce experimental results obtained during the summer of 1994, ACE 4 experimentalists observed that the flashboards were behaving in a significantly different manner than they had been during the near forgotten balmy days of summer past, despite the fact that the setup was identical to that used previously. This prompted concern since past observations, simulations, and theory had indicated that the behavior of the switch was to some degree dependent upon the radial distribution of plasma from the flashboards.

The rationale for the Cather's Mitt can be expressed by analogy. In electronics, if one were to design an electrical circuit whose proper behavior were dependent upon the value of a particular resistor, and that value had to be known to three significant figures, one would merely need to obtain a resistor of the correct rating - a requirement readily satisfied by a trip to Radio Shack. On the other hand, if the proper behavior of the circuit depended upon the value of the beta of a transistor, and again, this value had to be correct to three significant figures, one would be faced with a serious difficulty. The beta of a transistor is not a well-characterized parameter - it can be measured accurately, but transistor manufacturers do not attempt to produce transistors with precise values of beta. Thus, the electronics engineer designs his circuit so that it is not strongly sensitive to the precise value of beta. It was this design strategy that the Cather's Mitt was intended to follow. Rather that be tied strongly to the precise distribution of plasma across the A-K gap, the hope was to find some perturbation of the electrode geometry that would result in a decreased sensitivity to the plasma distribution.

In addition to decreasing sensitivity to plasma distribution, the Cather's Mitt offers a solution to the problem of excess mass. A plasma opening switch can be a long-conduction-time switch for multi-mega-ampere current levels only if it has sufficient mass to hold off the current while it builds to the desired level. But once the switch has opened, the large inventory of plasma instantly becomes a liability - the plasma can conspire to reclose the switch before appreciable load voltages develop. The Cather's Mitt offers some possibility of containing a significant portion of the switch plasma inventory.

Early conceptual calculations used the Cartesian version of DELTA/MHD to explore the efficacy of a geometric perturbation which has since come to be known as the Cather's Mitt. This geometry involves an abrupt increase in anode radius just beyond the end of the nominal switch region. Within this expanded A-K gap resides an L-shaped protrusion, shown in Figure 3-3. Much of the plasma from the switch region flows downstream into the trap made by this protrusion. Often, a small portion of the switch plasma flows around the outside of this structure and forms a low density plasma switch. The purpose of the design calculations to be presented below is to examine in far greater detail the nature of the interaction of the switch plasma with the electrode structure.

3.2 DENSITY PROFILE USED.

Figure 3-1 shows the various radial density profiles used in the design effort. These profiles were extracted from the large body of experimental measurements of flashboard-only shots. They are intended to be representative of the range of possible profiles one might encounter experimentally. In all simulations that are carried out the initial density profile is axially uniform over a 20 cm length and vanishes outside this interval. The plasma is taken to be an ideal $g = 5/3$ gas with the degree of ionization fixed at one.

The calculations were driven with current obtained from an RLC circuit model in which the lumped circuit parameters were chosen to mimic the ACE 4 current drive. This required a capacitance of 18 μF, an inductance of 125 nH, and a resistance of 0.012 Ohms. The initial voltage on the capacitor is reduced to 80% of the value actually used in the experiment in order to account for current which flows through the inactive 600 nH leg of the machine. Figure 3-2 gives the resulting current for one particular calculation. The current for other simulations is essentially the same, with minor differences due to the differences in how the switch plasma inductively loads the circuit.

The various profiles used in this design study can be characterized by the conduction time they produce when driven by the current described above. A two-component number is used to denote the various profiles - the part preceding the period is the ACE 4 shot number, the second part is the time in tenths of microseconds from when the flashboards were fired. Thus, profile 1466.30 comes from shot number 1466 and occurs 3.0 μs after the flashboards are fired. Table 3-1 summarizes the conduction times for the profiles shown in Figure 3-1.

Table 3-1. Conduction times for the density profiles used in the Cather's Mitt design study.

Profile	Conduction Time (ns)
1211.35	1560
1478.35	ill-defined
1478.55	1340
1466.30	1380

3.3 EFFECTS OF VARIOUS GEOMETRY CHANGES.

Figure 3-3 shows the computational grid used for this design study. The design study followed the approach of filling in a matrix of cases wherein each alteration to the geometry is tested with each of the various density profiles. Alterations to the geometry are either simple parametric variations or are suggested by specific simulation results. The parameters which were varied in the design study were (1) the width of the Cather's Mitt opening, (2) depth of the Cather's Mitt, and (3) the axial displacement between the leading edge of the Cather's Mitt and the point at which the anode radius abruptly increases.

Mach2 protocol allows that the results from different runs be maintained in separate directories under the UNIX operating system. This requires that each run be assigned a unique name. For the Cather's Mitt design study, the runs were named according to the form CMdsXn, where "CMds" stands for "Cather's Mitt design study," X = A, B, C, ... corresponding to the geometry, and n = 1, 2, 3, ... corresponding to the density profile used as the initial condition or perhaps to some other change made in the simulation. Table 3-2 shows the matrix. Not all spaces in the matrix were filled in. This was the result of conclusions drawn from calculations performed earlier in the given series indicating that nothing further could be reasonably expected from the given geometry. Geometry A in the table is omitted as that series was a shakedown of some of the aspects of the calculation approach. Geometry D has several calculations performed with the same profile; this was due to an attempt to correct some aspects of the simulation. The profile denoted "1220" was from ACE 4 shot 1220 and had been used in some earlier work. It was not used to any great degree in this effort, other than as an available profile with which to help shakedown the calculation procedure.

Table 3-2. Calculation matrix for Cather's Mitt design study.

Profile	Geometry: A	B	C	D	E	F	G	H
1211.35		5	—	4*	3	2	1	3
1478.35		2	—	1**				
1478.55		4	1	2,3,5	2	1		
1220	1-5	1						
1466.3							2	2

Table 3-3 indicates the relation between the upper case geometry designation letter and the actual geometry. The "opening" is defined as the radial separation between the inner lip of the leading edge of the Cather's Mitt and the unperturbed, coaxial section of the cathode. The "depth" is defined as the axial separation between the leading edge of the Cather's Mitt structure and its backplate. The axial separation between the Cather's Mitt leading edge and the point at which the anode radius abruptly increases was 2 cm for most of the simulations. A separation distance of 4 cm was explored briefly, but as described below, did not present any advantages which would have justified a more detailed examination.

Table 3-3. Geometries for the Cather's Mitt design study.

Series	Opening (cm)	Depth (cm)
A	2.5	4.0
B	2.5	4.0
C	3.5	8.0
D	3.5	8.0
E	2.5	8.0
F	3.0	12.0
G	2.5	14.0

The primary common problem observed in the simulations was the containment of the plasma which was caught by the Cather's Mitt. In many cases, a secondary switch would form on the exterior of the Cather's Mitt structure, which would then proceed to thin rapidly, or the switch would act like a plasma flow switch, opening as it moved past the abrupt increase in anode radius. If in these cases, the plasma which was caught in the Cather's Mitt had simply disappeared, the result would be very promising. However, it was often the case that this caught plasma reappeared, flowing back out of the Cather's Mitt, and threatening to cause a restrike.

The design study indicated that there is little to be gained from increasing the width of the Cather's Mitt opening. Increasing the width of the opening allowed the expanding switch plasma to acquire greater radial momentum. The greater the radial momentum of the plasma, the more problematic the interaction of the plasma with the Cather's Mitt structure appeared to be, at least with respect to the containment properties of the structure. This difference is illustrated in Figures 3-4 (a, b) and Figures 3-5 (a, b). Figures 3-4 (a, b) are taken from run CMdsE2, in which density profile 1478.55 was used in a geometry wherein the opening of the Cather's Mitt was 2.5 cm. Figures 3-5 (a, b) come from run CMdsD5, which used the same density profile, but had a geometry wherein the opening of the Cather's Mitt was 3.5 cm. The density distributions found

in these two simulations at any time prior to interaction with the Cather's Mitt should be identical to one another.

As shown in Figures 3-4 (a) and 3-5 (a), the results at this time are indeed quite similar, but they are not identical. The discrepancy is found at the point where plasma has just begun to accelerate around the corner made by the abrupt increase in anode radius. It is due to a difference in the computational grid. The grids used in these two simulations are identical to one another in the switch region. In the Cather's Mitt region, the two simulations use the same number of cells and use the same points as block corner points. This results in a slightly different grid spacing, and this is most pronounced in the region in the vicinity of the anode corner.

Figures 3-4 (b) and 3-5 (b) show the pronounced difference that results as the plasma interacts with the Cather's Mitt structure. Of particular interest is the difference in the distribution of plasma along the inner surface of the coaxial portion of the mitt structure. Figure 3-4 (b) shows a thin plasma layer in comparison to the widely dispersed plasma seen in Figure 3-5 (b). The difference comes from the greater radial momentum acquired by the plasma before interacting with the mitt. With a 3.5 cm wide opening, the radial momentum the plasma acquires before striking the mitt causes it to rebound violently from the inner surface of the mitt once interaction does occur. This is considered to be a negative effect as that plasma then tends to dwell in the mouth of the Cather's Mitt where it could foster a restrike event.

For a reason similar to that which disfavors an increase in the width of the Cather's Mitt, an increase in the distance between the leading edge of the Cather's Mitt and the exit of the nominal switch region is not desirable. Increasing that distance merely allows the plasma to acquire greater momentum which then makes the interaction of plasma and mitt structure more problematic. Increasing the separation while keeping a fairly narrow opening resulted in little plasma entering the Cather's Mitt, a result which defeats the purpose of the Mitt. Increasing the separation while simultaneously increasing the width of the opening, while not examined specifically in the simulations, would certainly result in an extremely violent interaction of caught plasma with the mitt structure, and would most likely lead to rapid expulsion of the caught plasma out of the Mitt.

Of the width of the opening, the separation distance between leading edge and anode corner, and the depth, the latter parameter had the greatest positive effect over the containment of the caught plasma. But rather than truly helping to better contain the caught plasma, increasing the Cather's Mitt depth is merely a delaying tactic. This is illustrated by comparing the results from two simulations which differ from one another only in the Cather's Mitt depth. Runs CMdsE3 and CMdsG1 both used the initial density profile 1211.35, a leading edge/anode corner separation distance of 2 cm, and an opening width of 2.5 cm. But CMdsE3 used a depth of 8 cm while CMdsG1 used a depth of 14 cm. The initial density profile is such that plasma is pushed directly into the backplate of the Cather's Mitt, as opposed to being pushed into either the inner or outer coaxial surfaces. As illustrated in Figures 3-6 (a, b, c), this produces a splash-back. The rebounding plasma quickly moves back out of the Cather's Mitt, possibly causing a restrike. The rapidity with which the plasma rebounds from the Cather's Mitt is the worst problem - this allows far too little time for any effective power transfer to the load to take place. Figures 3-7 (a, b, c) illustrate the same sort of effect for a Cather's Mitt with a 14 cm depth, 6 cm deeper than that shown in Figures 3-6 (a, b, c). Again, plasma splashes off the backplate of the Cather's Mitt to cause a restrike. In this case, several more tens of nanoseconds are required for the restrike to occur than with the 8 cm deep mitt, but this is still probably not adequate for effective power transfer to the load.

These observations lead to a three-fold modification to the basic design. First, the depth was increased to 16 cm. More significantly, the backplate was angled inward to direct spashing plasma radially inward toward the third modification - a recessed section of the cathode. Figure 3-8 shows these modifications in a plot of the simulation grid. This is an imperfect depiction of the geometry

as the horizontal scale differs from the vertical scale. Figures 3-9 (a, b) illustrate the interaction of switch plasma with this electrode structure in a simulation which used profile 1211.35 as the initial switch density distribution. In this case, it is the recess in the cathode which plays the primary role. It accepts the plasma which has been flowing along the cathode, providing an out-of-the way place for that plasma to accumulate. Comparison of Figure 3-9 (a) with Figures 3-6 (a) and 3-7 (a) shows that the inner structure of the Cather's Mitt does not affect the formation of the secondary switch.

Figures 3-10 (a, b, c, d) show the effect of this improved plasma trap design on density profile 1466.30. This profile is unusual in that it tends to promote motion of plasma toward the cathode. In particular, it results in nearly all of the switch plasma being directed into the Cather's Mitt. In this case, the recess and the inwardly-angled backplate work together to trap the switch plasma in a clockwise circulation pattern in the recessed region. With this particular profile, in which the opening is observed to occur at about 1380 ns, the advanced trap provides a period of at least 150 ns, and probably significantly longer, before any danger of restrike from back-splashing plasma occurs.

3.4 EXPERIMENTAL RESULTS AND CONCLUSIONS.

Tests of the Cather's Mitt concept were conducted in the ACE 4 configurations depicted in Figure 3-11. Results from the tests are given here for three values of gap size defined as the distance from the tip of the Cather's Mitt to the nearest point on the anode. This is indicated in Figure 3-12, which also shows the lines of sight for the chordal interferometry used to measure time integrated electron densities in the secondary switch region B. For the chordal interferometry, a ribbon laser beam is split into nine beams, each approximately 1mm in size. The beams are labeled 1 through 9, beam 1 being closest to the generator. Beams 1 through 5 are separated by 1.5 mm, beams 5 through 9 by 3 mm. The locations and labels of current monitors are shown in Figures 3-11 and 3-12.

Table 3-4 summarizes the matrix of shots for data to be presented here. The variables in the matrix are the gap size d and the injection time delay between the firings of the flashboards and the Marx generator. For the "no mitt" case, the mitt was removed to permit axial interferometry of the injected switch plasma.

The locations of the axial inferometric lines of sight relative to the cathode and anode in the primary POS region are summarized in Figure 3-13.

Table 3-4. Shot MATRIX in 1400 series for Cather's Mitt experiments.

Geometry	Relative Plasma Injection Delay	Marx Delay Relative to Flashboards
	2.5 ms	**6.0 ms**
No Mitt	1414	1421
2 cm gap	1432	1433
3 cm gap	1441	1438
4 cm gap	1452	1450

The data taken with axial interferometry and B-dot probes are shown in Figures 3-14 through 3-19. The current and voltage results deduced from the B-dot probes can be compared with the corresponding data taken while the Cather's Mitt was in place. (The axial interferometry results do not offer a basis for comparison however since the primary switch region is inaccessible to our interferometry set up with the Cather's Mitt in place). Before comparing currents and voltages in the two configurations, we digress briefly to point out some features of the data obtained without the Mitt.

Figure 3-14 shows line density measurements in the POS taken before firing the ACE 4 Marx banks. Figure 3-15 shows the corresponding data in the case with pulsed power. Figure 3-16 shows the ratio of measured line density with pulsed power to that without pulsed power. In all cases measured line density is converted to density by dividing by 20 cm, the nominal switch length. Observe the rapid decrease in density beginning at about 2.7 μs, shortly after the onset of generator current, followed by a rapid increase after the minimum in the probe signal just before 3.0 μs. The rapid decrease is observed in many shots and is attributed to the pushing of plasma to the electrodes under the magneto-hydrodynamic action of the magnetic field penetrating into the POS gap. Prior to this density decrease the probes in the case with pulsed power tend to track the corresponding ones in the case without pulsed power. The later rapid increase in density is also a recurring feature of measurements with pulsed power, representing an ionization phenomenon and/or motion of plasmas from the vicinity of an electrode toward the center of the A-K gap.

Figure 3-17 shows current and voltage traces overlaid by a plot of the density obtained by axial probe 3. To fit the density onto the figure it has been multiplied by the factor 10^{-9}. The voltage wave form is obtained by inductively correcting the voltage measured near the insulator stack. The correction is made using an assumed constant inductance in the region between the stack and the downstream end of the POS. This overestimates the correction because of the early exclusion of magnetic field between the actual current path in the POS and the load-side end of the POS. Hence, the negative voltage between $t = 0$ and $t \sim 500$ ns. The maximum voltage of about 800 kV is achieved at ~0.58 μs.

One feature of Figure 3-17 that is not completely understood is the approximately 40 ns offset between the density minimum at probe 3 and the rise of current in the current probe IBR1 just on the load side of the switch region. The "density" is obtained by dividing the observed line integrated density by 20 cm; since the sensitivity limit of the interferometer is $\sim 10^{15}/cm^2$, the density at the probe location could be as high as $5 \times 10^{14}/cm^3$ for a snowplowed plasma having a width of 2 cm. Perhaps density probe number 6, which shows a "zero" density extending several tens of nanoseconds after that of probe 3 is a better indicator of when and where opening occur.

Another noteworthy feature of Figure 3-17 is the difference between the measured voltage and that calculated from multiplying the 100 nH vacuum inductance of the load with the time derivatives $\dot{I}$ at the various downstream locations. The maximum $L\dot{I}$ obtained in this manner is about 2 MV using IBR1, compared with a measured value of 800 kV, suggesting that plasma pushed into the inductor shields a substantial fraction of the 100 nH from the magnetic field. The small but finite levels of current in the other downstream probes support this surmise.

The downstream current monitors IBR1-5 appear to detect current sequentially, starting with IBR1 nearest the switch. IBR2 seems to follow IBR1, although for reasons not at all understood it swings negative before turning positive. This may be a result of probe damage or of asymmetries in the current flow. Probes 4 and 5 start up at about the same time, apparently within a few tens of nanoseconds of the IRT and other probes within the inductor, and just before the most steeply rising part of the voltage curve. This coincidence of onset of current in various downstream anode probes is generally indicative of switch opening as well as current transfer.

Figures 3-18 and 3-19 show densities with and without pulsed power, respectively, for a delay time of 6 μs. In contrast to shot 1414, shot 1421 shows no evidence of plasma expulsion with pulsed power, but does show an apparently strong increase of electron density with pulsed power. This is probably indicative of increased ionization during the power pulse. Figure 3-20 shows onset of current in the downstream probes and the development of voltage 1 μs following the start of generator current. In this case the maximum in the voltage, ~400 kV, of Figure 3-19 is only about one-half of that achieved for the shorter 2.5 ms delay time, Figure 3-17.

With voltage as a standard, the Cather's Mitt did not perform well. The data in Figures 3-21 to 3-25, corresponding to various values of delay times and mitt tip-anode gap sizes given in Table 3-4, support this conclusion. These figures also show current measured at the indicated positions and densities measured by chordal interferometry in the secondary switch region shown in Figure 3-12. The density in the figures is obtained by averaging the line densities over the nine downstream probes and dividing by 20 cm, the assumed value of the chordal length through the plasma. The density has been scaled by a factor of 5×10^{-10} in Figures 3-21 to 3-25.

In general, the measured densities in the secondary switch region exhibit a plateau region, or at least a region of diminished time derivative relative to the derivatives at times preceding and following the plateau time interval.

Judging by separations in time of the curves in Figures 3-26 and 3-27 in the rising signal region that precedes the plateau corresponding to a 6 ms delay time, the plasma in the secondary switch region is moving with an axial speed of $\sim 10^8$ cm/sec. Plasma speeds corresponding to the 2.5 ms delay time are more uncertain because of signal fluctuations, as shown in Figure 3-18, but also appear to be about 10^8 cm/sec.

Except in the plateau region, the line density observed in the secondary switch region increases continuously with time, at least for several hundred nanoseconds. The only evidence that density eventually begins to decrease occurs in Figure 3-21, and then only about 600 ns after electrons are first detected in the region. If only a fast moving ($\sim 10^8$ cm/sec) narrow ring (2 ~3 cm in width in the axial direction) entered the catchers mitt at the end of the conduction phase, we might expect that the chordal measurements in the secondary switch would generate a signal that would first rise and then decrease after about 30 ns. The absence of such a signature suggests that plasma moves continuously into the secondary switch region following the first arrival of plasma at the Cather's Mitt. This continuous injection may result from the drift of plasma that is continuously pushed into the anode vanes during the conduction phase. It is also possible that plasma pushed into region B of Figure 3-12 stagnates on the anode structure and remains in the chordal line of sight.

From the IBRX and generator current traces, assuming that the current probes are not shorted out by plasma, a greater portion of the ~2.6 MA generator current is conducted in the primary switch region at late times than in the secondary switch region. Presumably plasma left behind in the primary switch region fills the anode-cathode gap. This would not be the case had the concept underlying the Cather's Mitt design been realized.

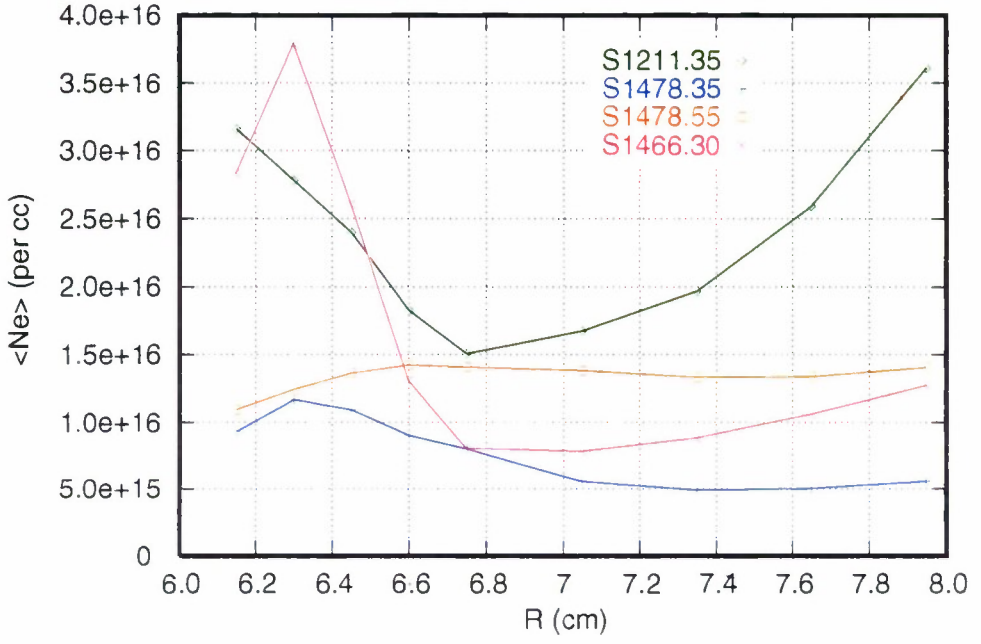

Figure 3-1. Radial density profiles used in Cather's Mitt design studies. See text for discussion of legend in body of figure.

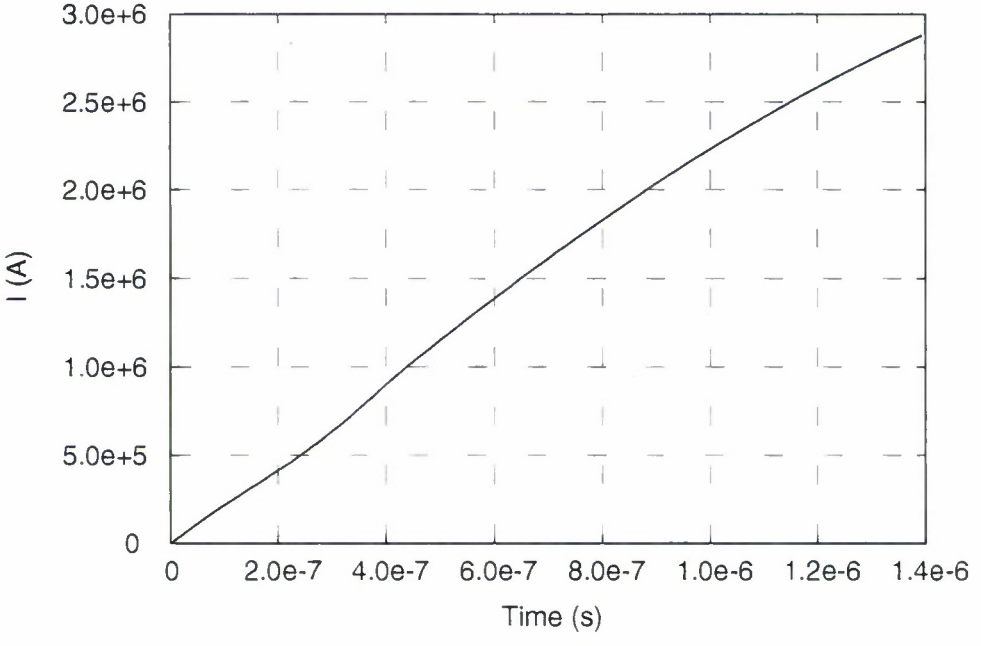

Figure 3-2. Current wave form used in one simulation of Cather's Mitt performance. The current wave forms for all calculations are nearly the same.

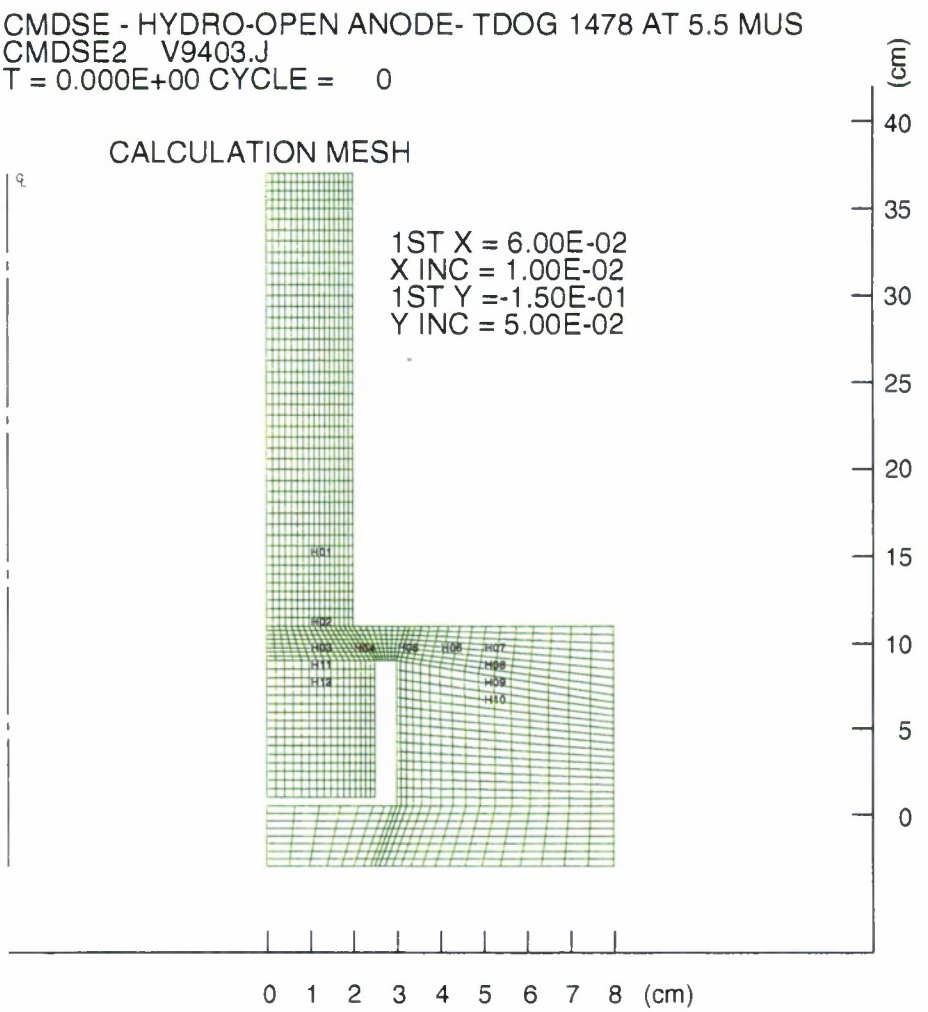

Figure 3-3. Computational grid used in the design study of initial Catcher's Mitt concept.

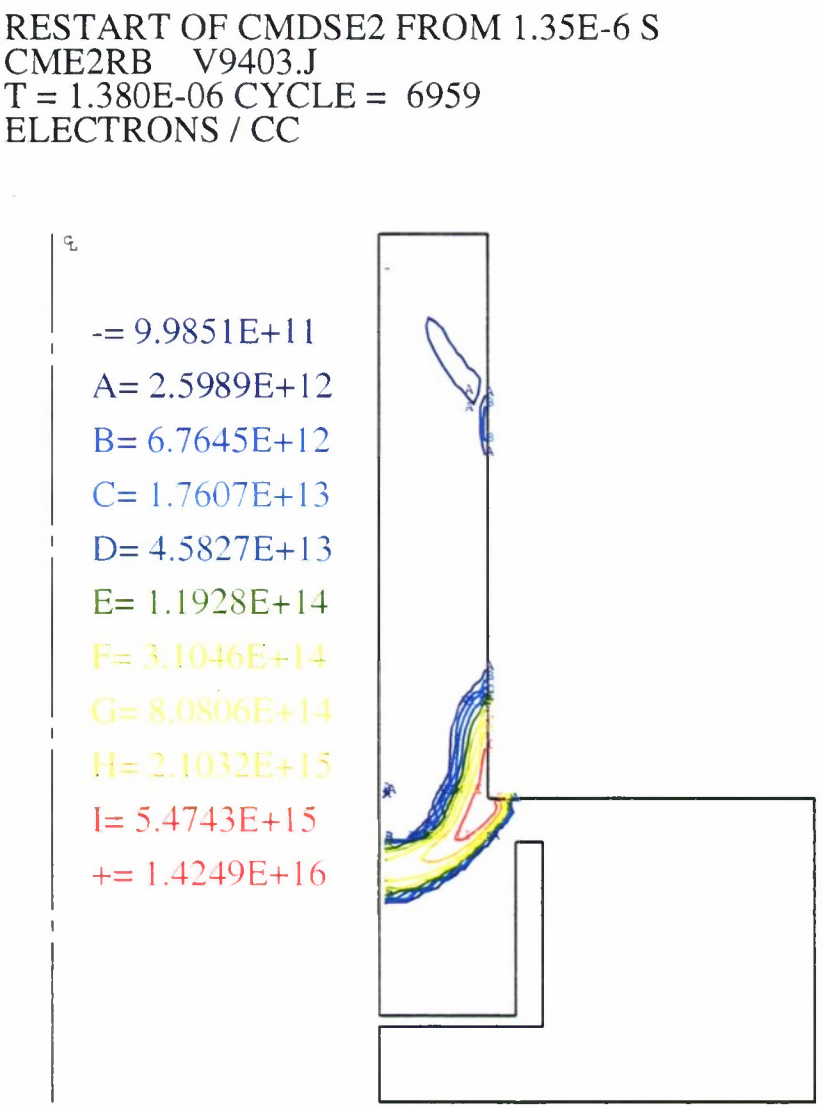

(a) t = 1.38 μs

Figure 3-4. Density contours following onset of current for case E2 (see text).

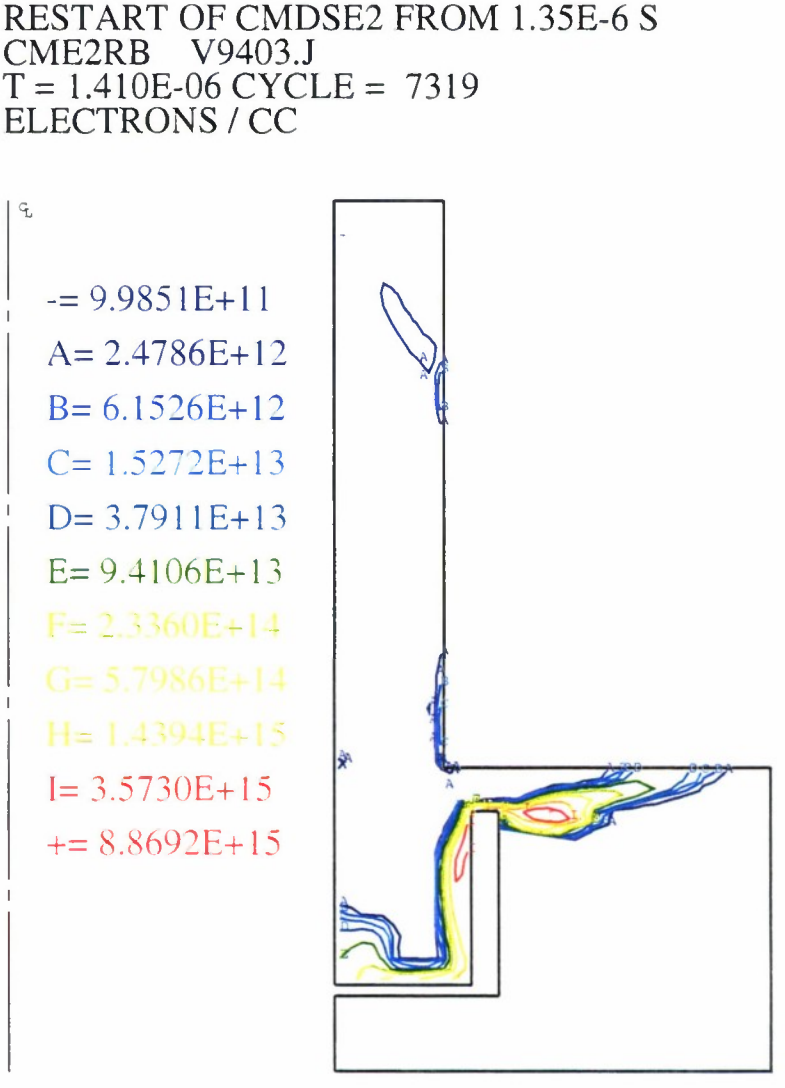

(b) t = 1.41 μs

Figure 3-4. Density contours following onset of current for case E2 (see text) (Continued).

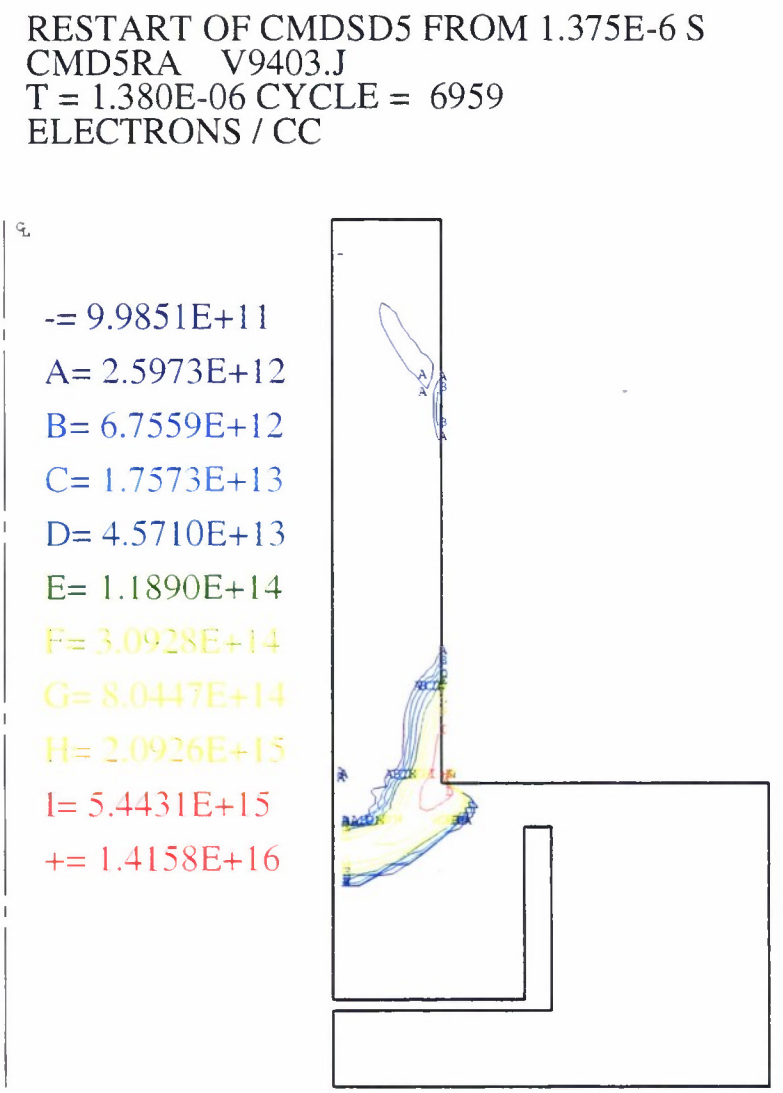

(a) t = 1.38 μs

Figure 3-5. Density contours following onset of current for case D5 (see text).

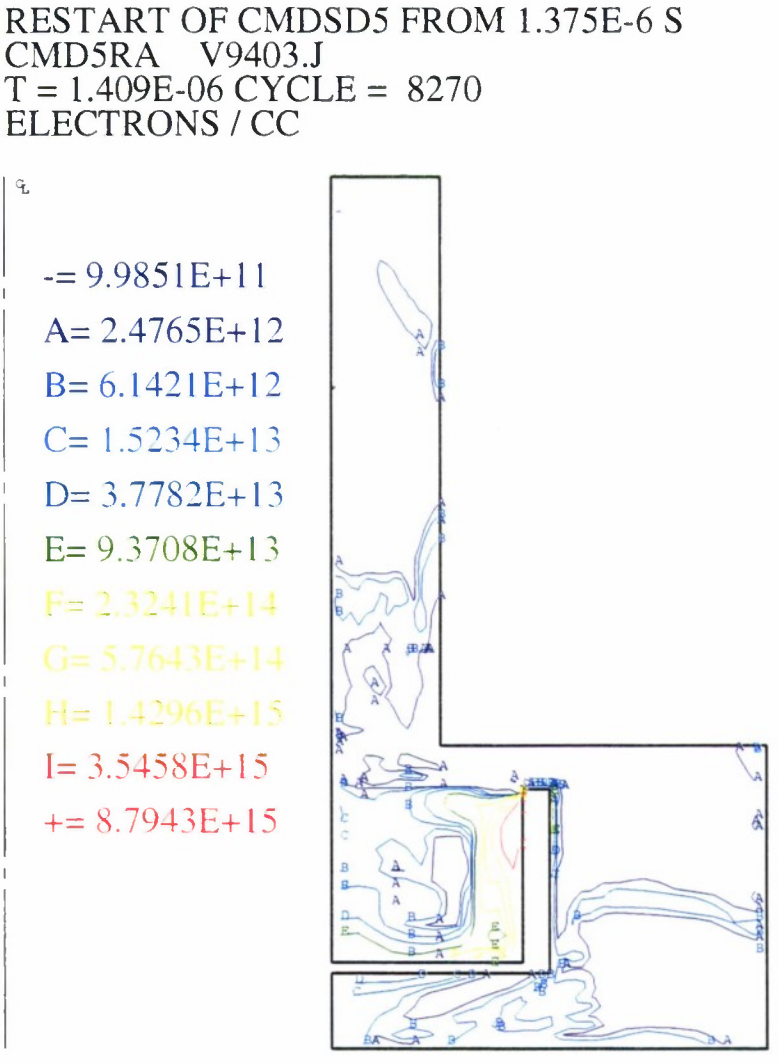

(b) t = 1.409 μs

Figure 3-5. Density contours following onset of current for case D5 (see text) (Continued).

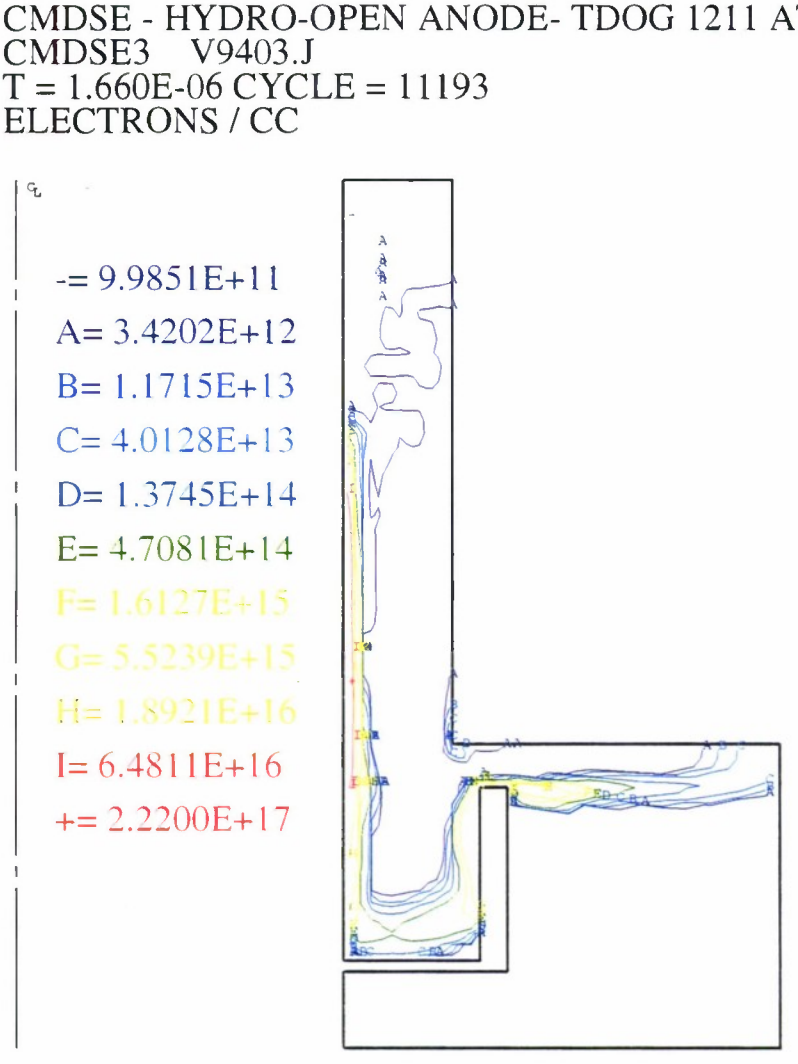

(a) t = 1.66 μs

Figure 3-6. Density contours following onset of current for case E3 (see text).

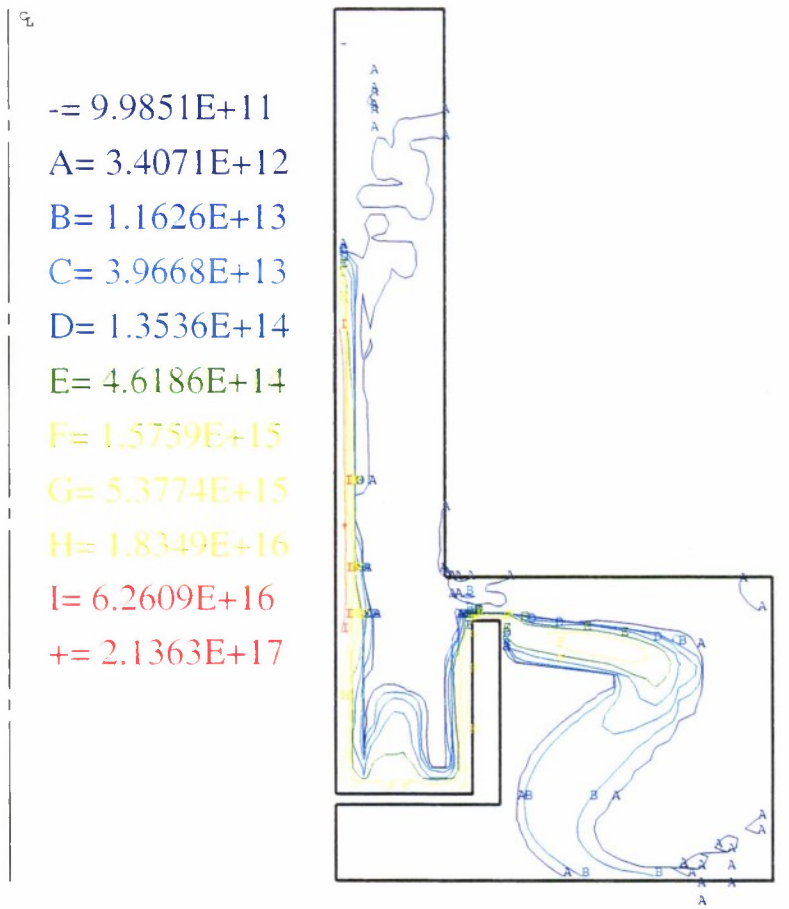

(b) t = 1.68 μs

Figure 3-6. Density contours following onset of current for case E3 (see text) (Continued).

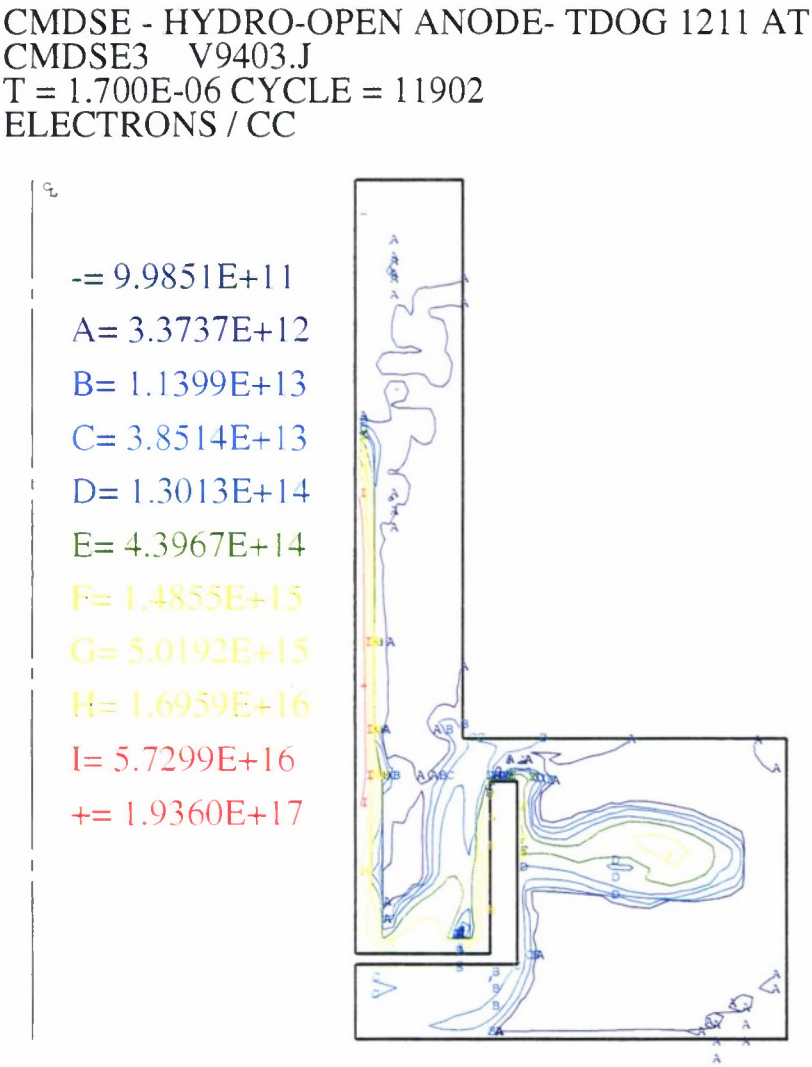

(c) t = 1.7 μs

Figure 3-6. Density contours following onset of current for case E3 (see text) (Continued).

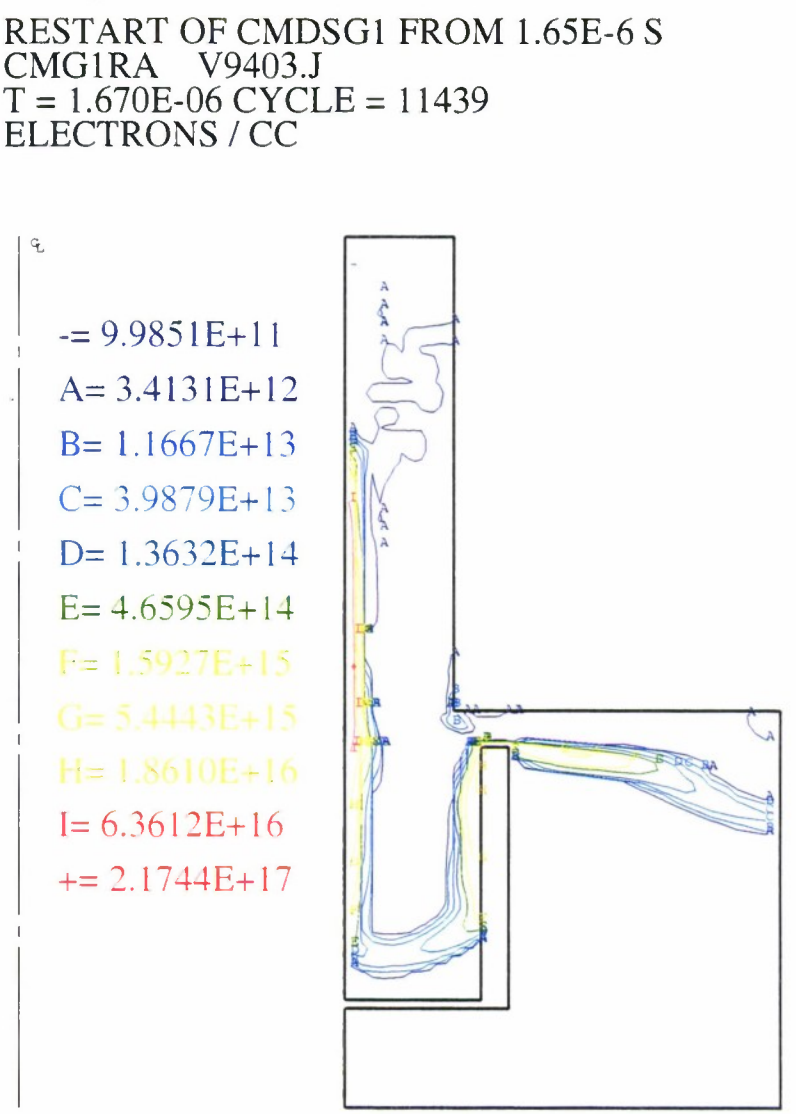

(a) t = 1.67 μs

Figure 3-7. Density contours following onset of current for case G1 (see text).

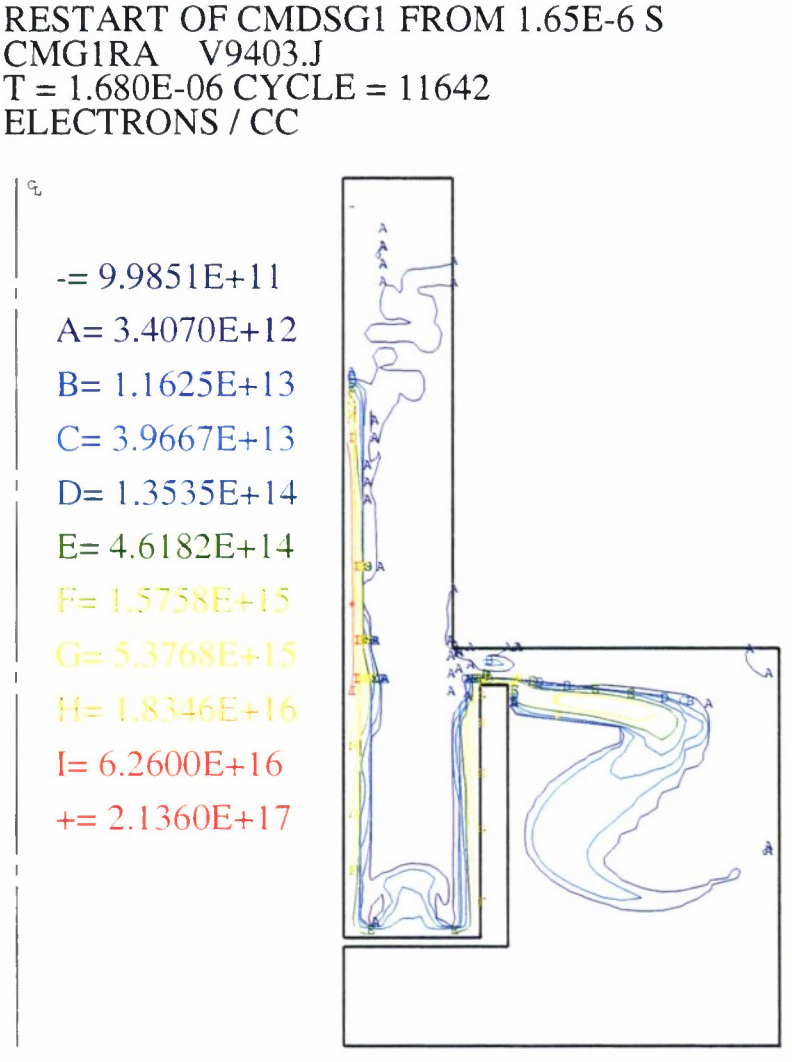

(b) t = 1.68 μs

Figure 3-7. Density contours following onset of current for case G1 (see text) (Continued).

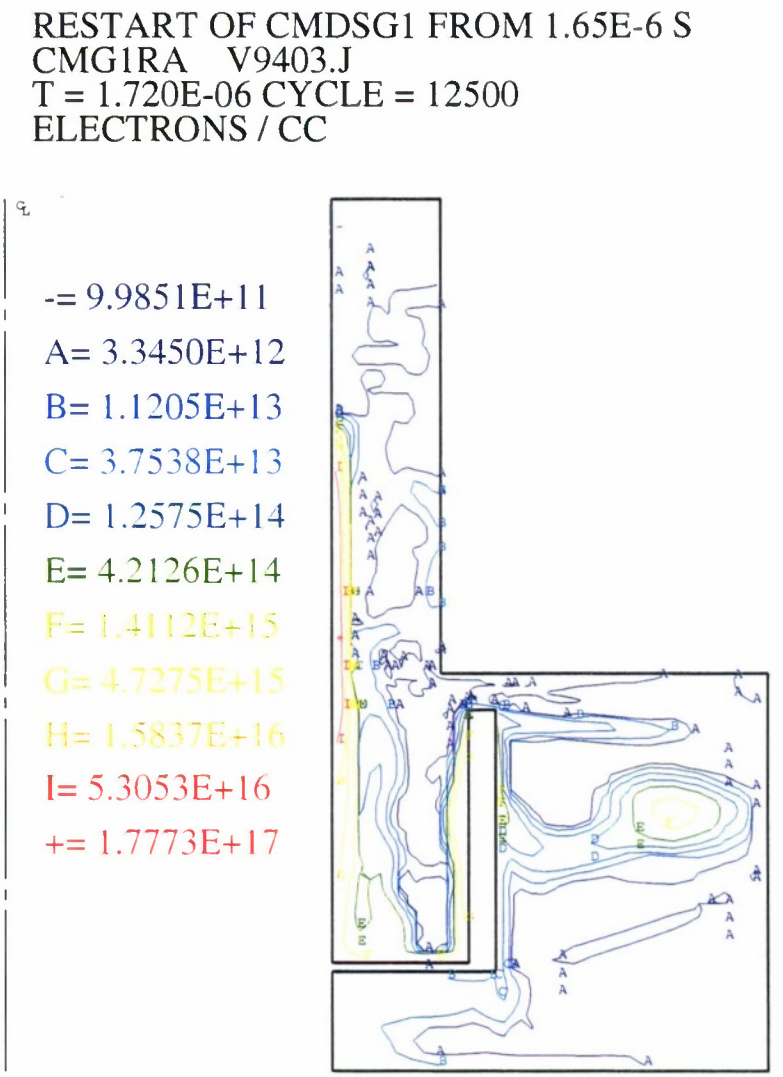

(c) t = 1.72 μs

Figure 3-7. Density contours following onset of current for case G1 (see text) (Continued).

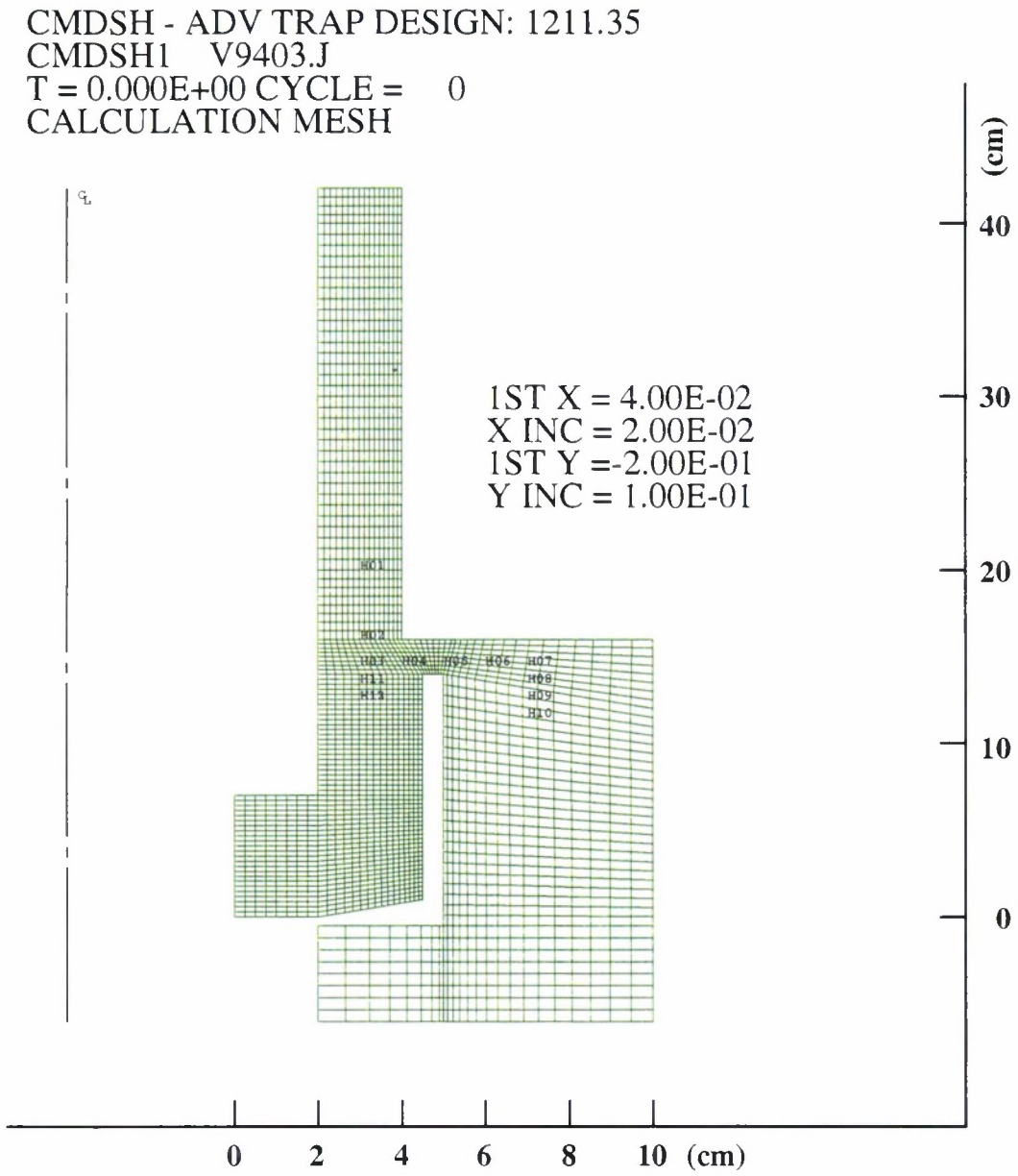

Figure 3-8. Computational grid used in the design study of modified Cather's Mitt concept.

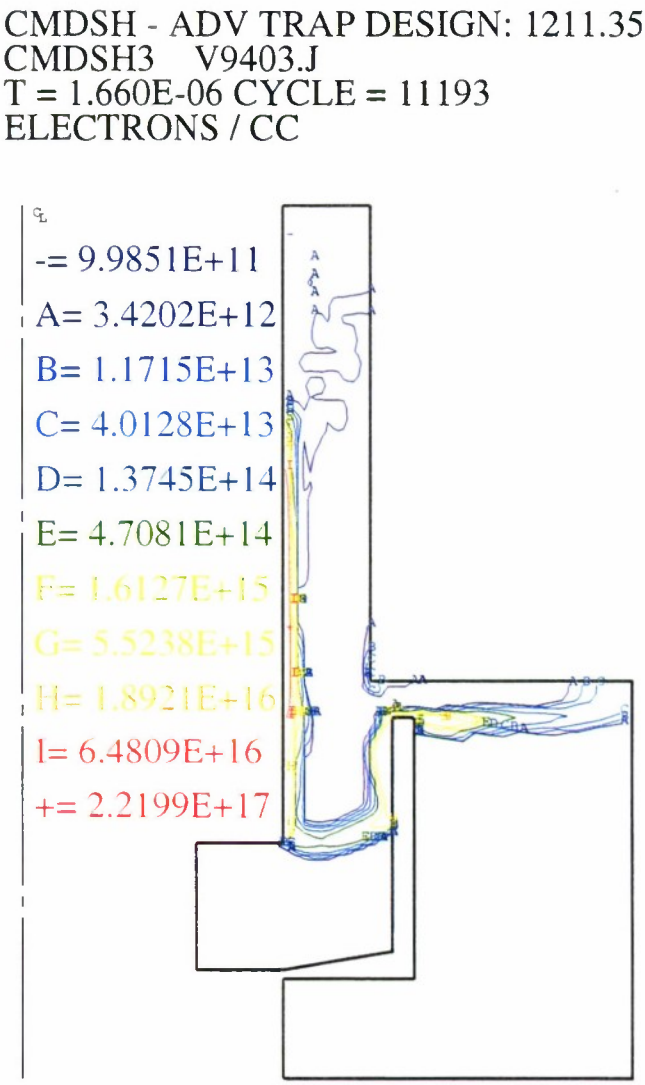

(a) t = 1.66 μs

Figure 3-9. Density contours following onset of current for modified Cather's Mitt and density profile 1211.35.

(b) t = 1.68 μs

Figure 3-9. Density contours following onset of current for modified Cather's Mitt and density profile 1211.35 (Continued).

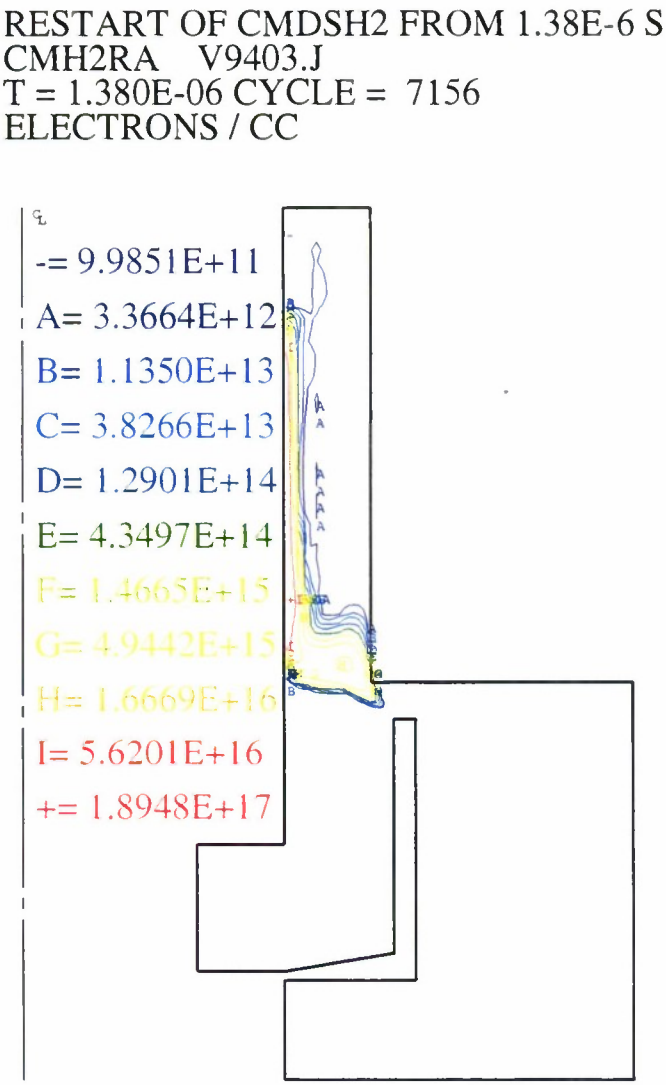

(a) t = 1.38 μs

Figure 3-10. Density contours following onset of current for modified Cather's Mitt and density profile 1466.30.

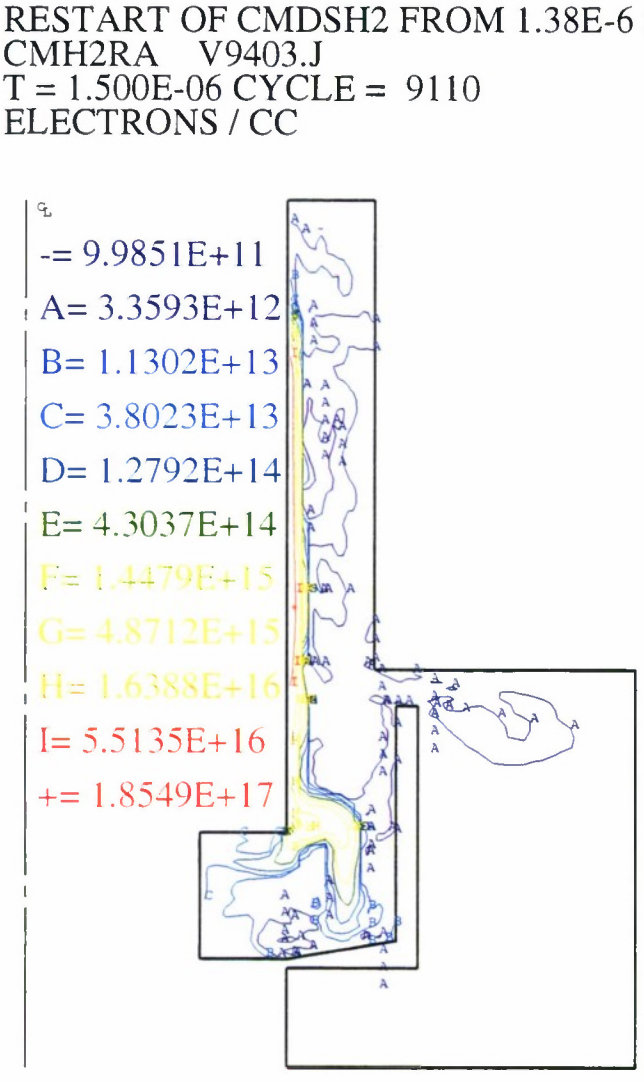

(b) t = 1.5 μs

Figure 3-10. Density contours following onset of current showing effect of trap design with initial density profile 1466.30 (Continued).

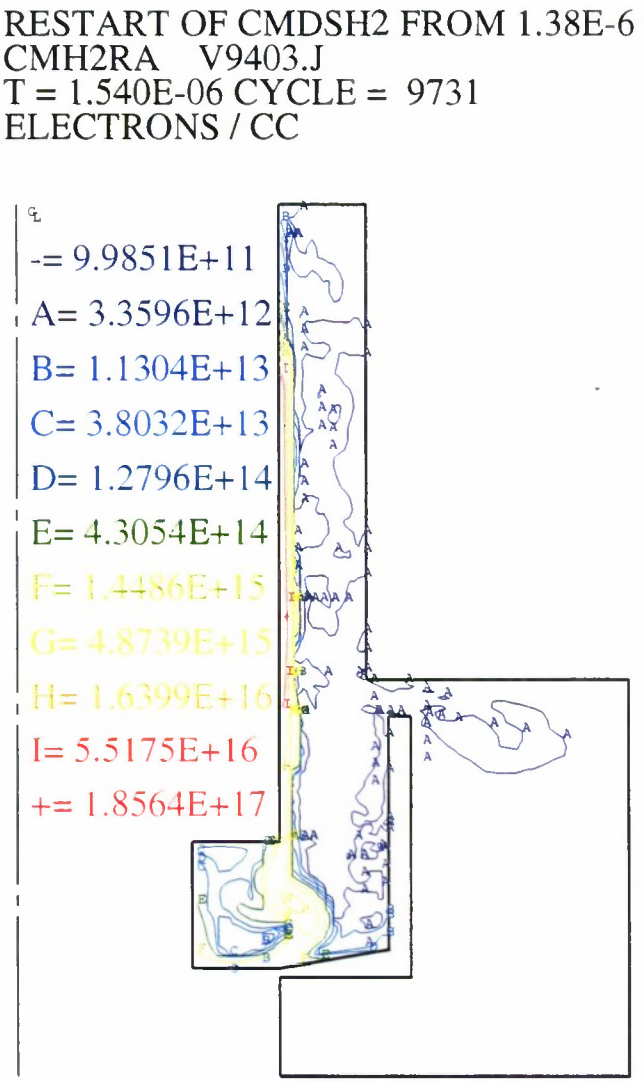

(c) t = 1.54 μs

Figure 3-10. Density contours following onset of current showing effect of trap design with initial density profile 1466.30 (Continued).

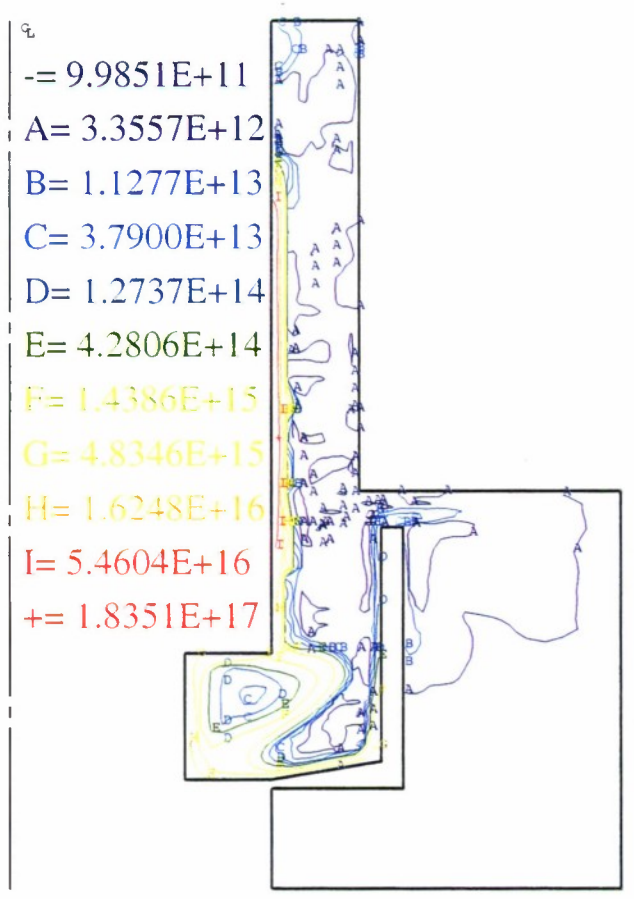

(d) t = 1.63 μs

Figure 3-10. Density contours following onset of current showing effect of trap design with initial density profile 1466.30 (Continued).

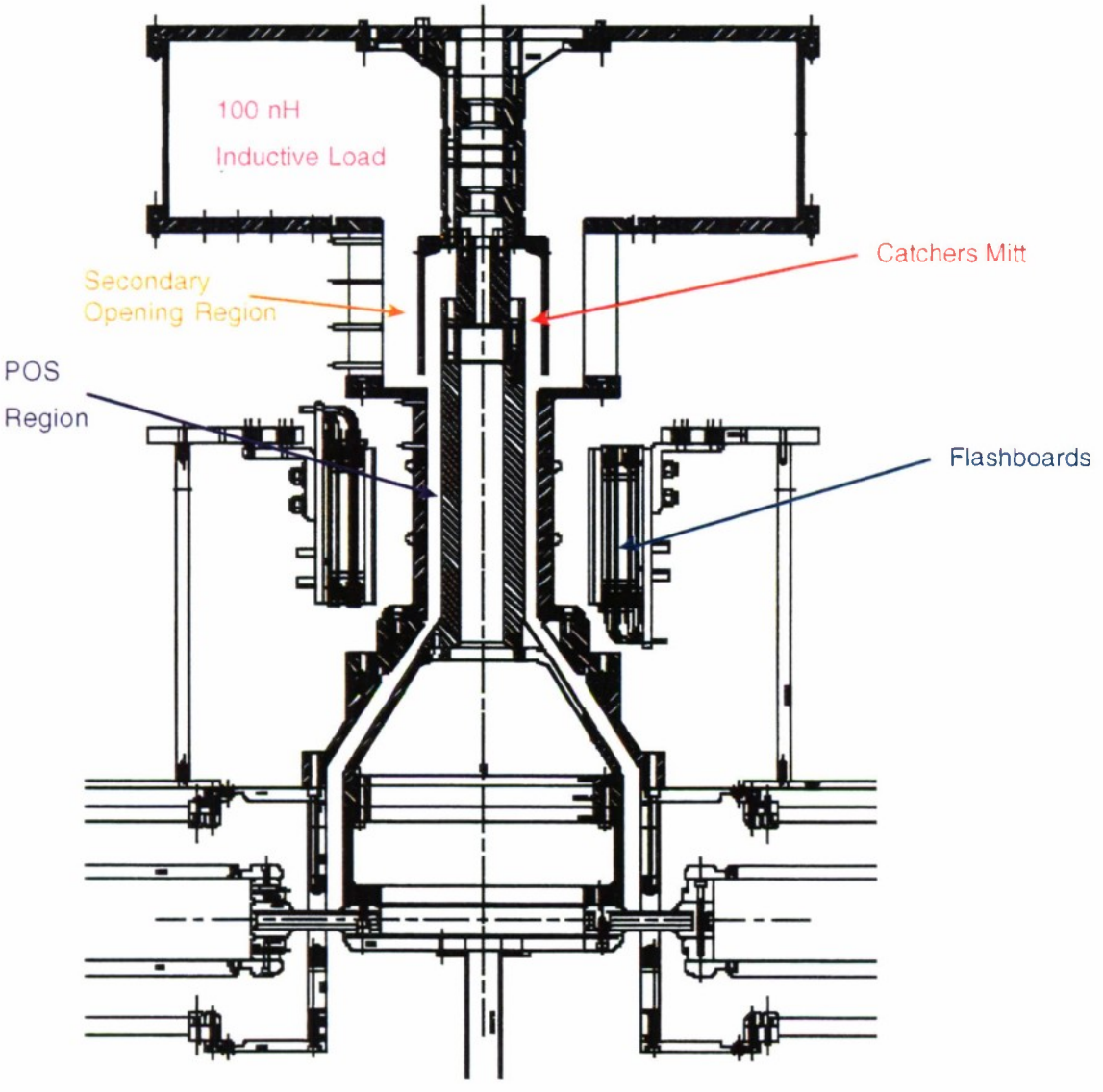

Figure 3-11. ACE 4 Cather's Mitt configuration.

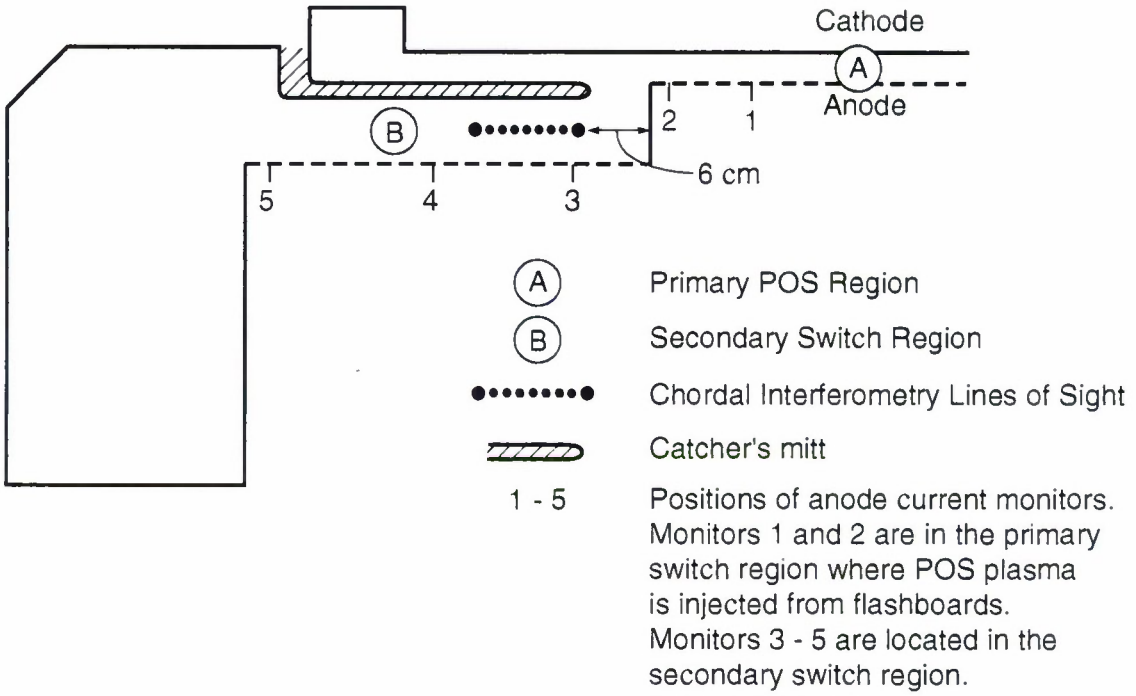

Figure 3-12. Detail of Cather's Mitt showing locations of current monitors and chordal interferometry lines of sight.

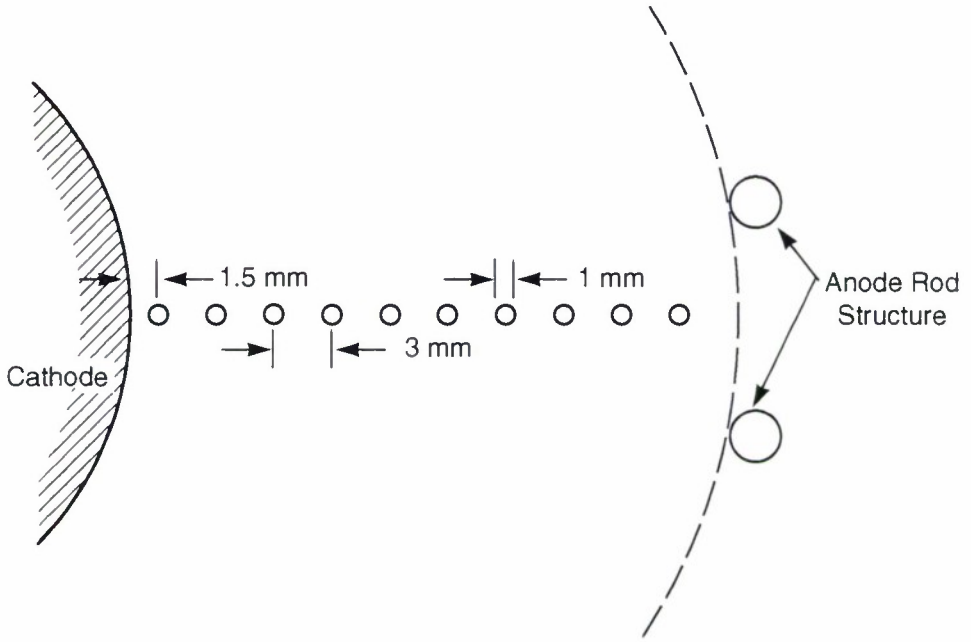

Figure 3-13. Locations of probe beams used in axial interferometry.

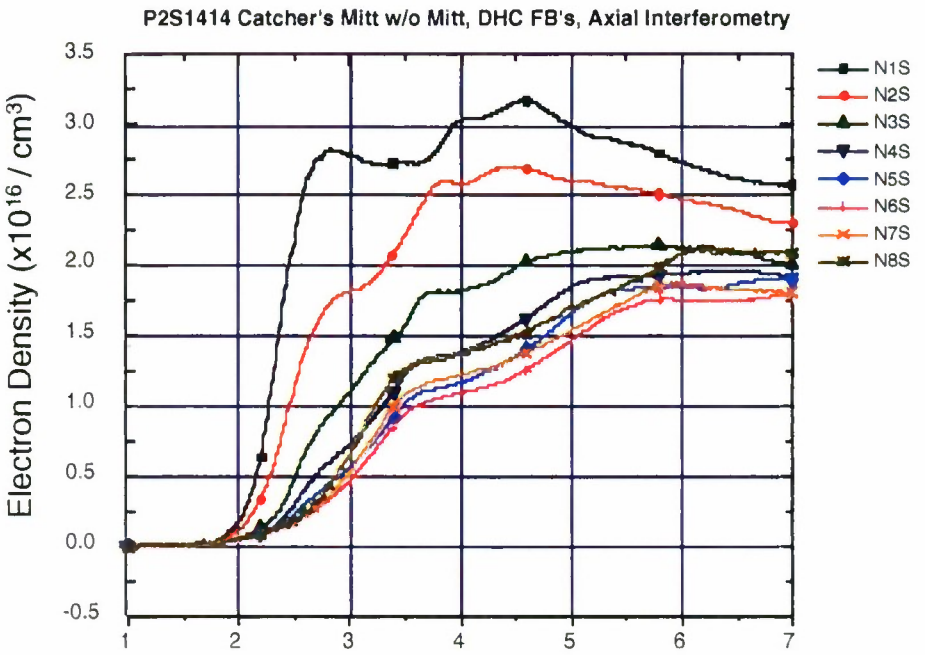

Figure 3-14. Electron density taken before firing Marx banks (shot 1414).

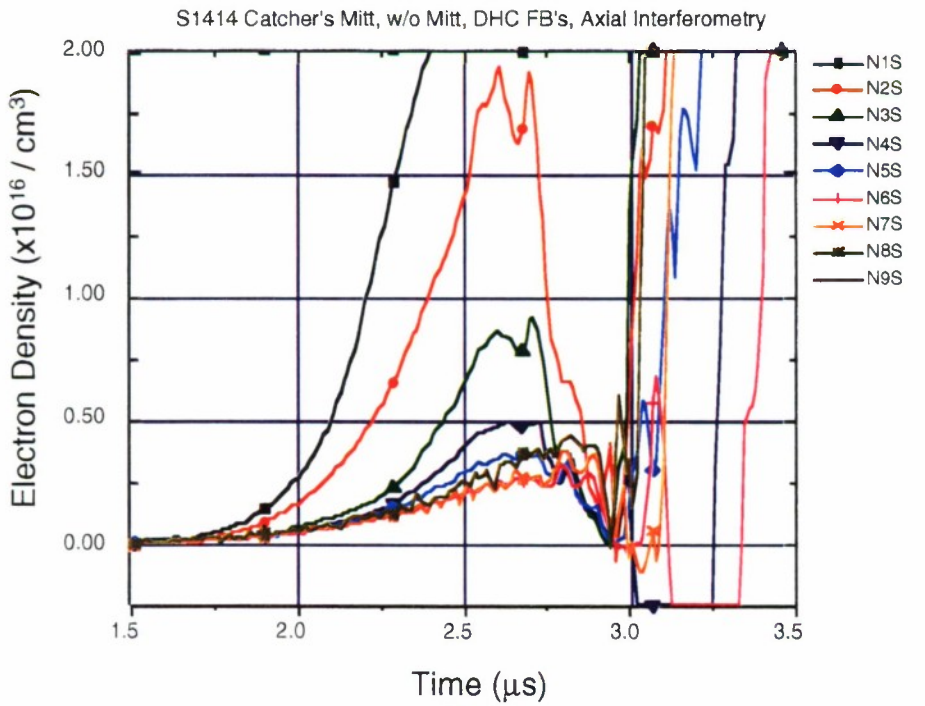

Figure 3-15. Electron density measured with pulsed power (shot 1414). Marx current rises at 2.5 μs.

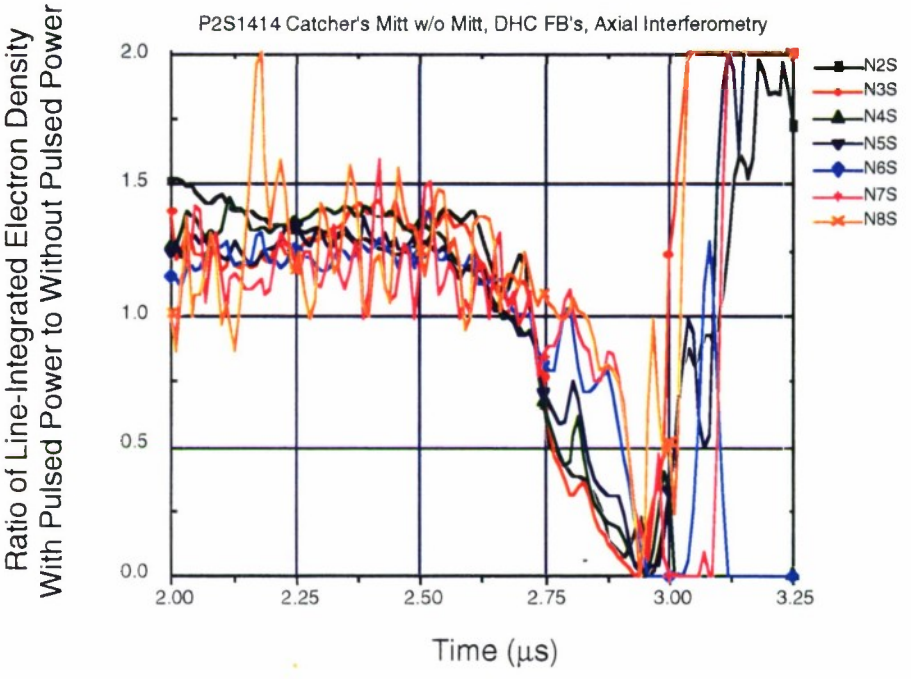

Figure 3-16. Ratio of measured line density with pulsed power to that without pulsed power (shot 1414).

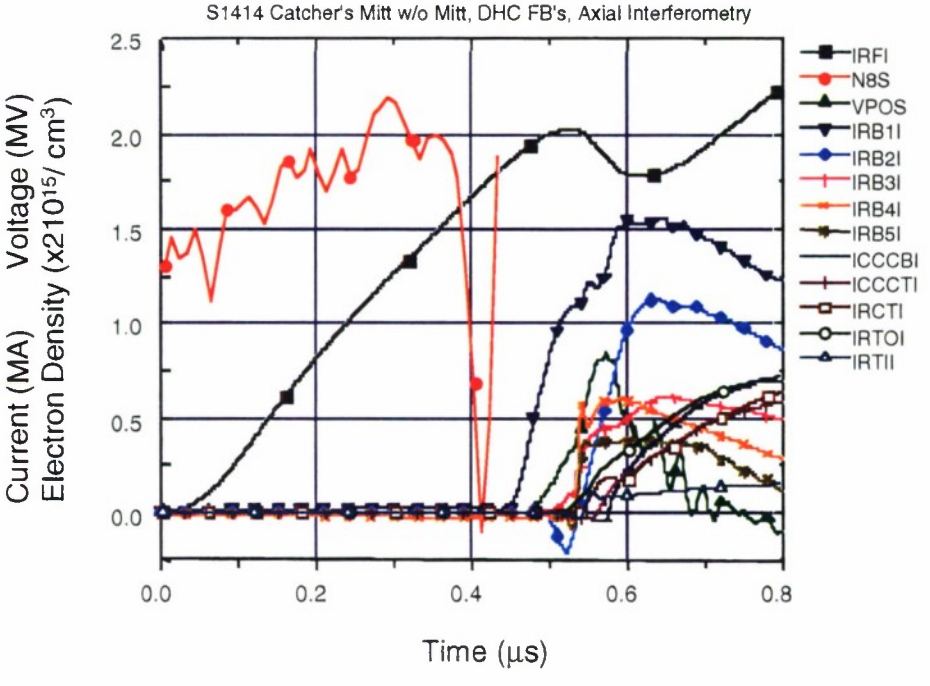

Figure 3-17. Current and voltage traces overlaid by density measured by axial probe 3.

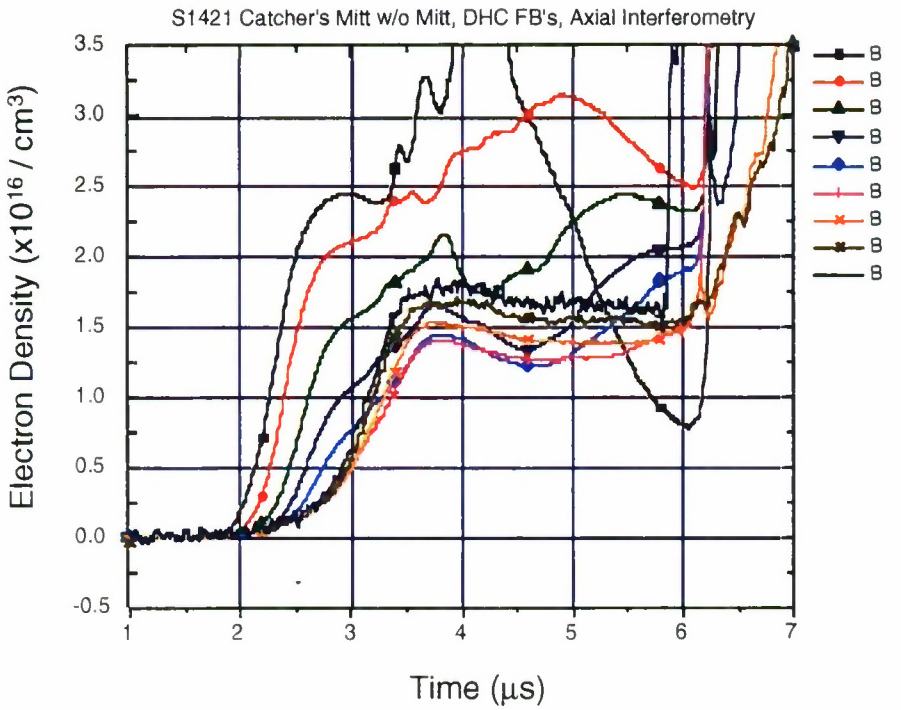

Figure 3-18. Electron density taken before firing Marx banks (shot 1421).

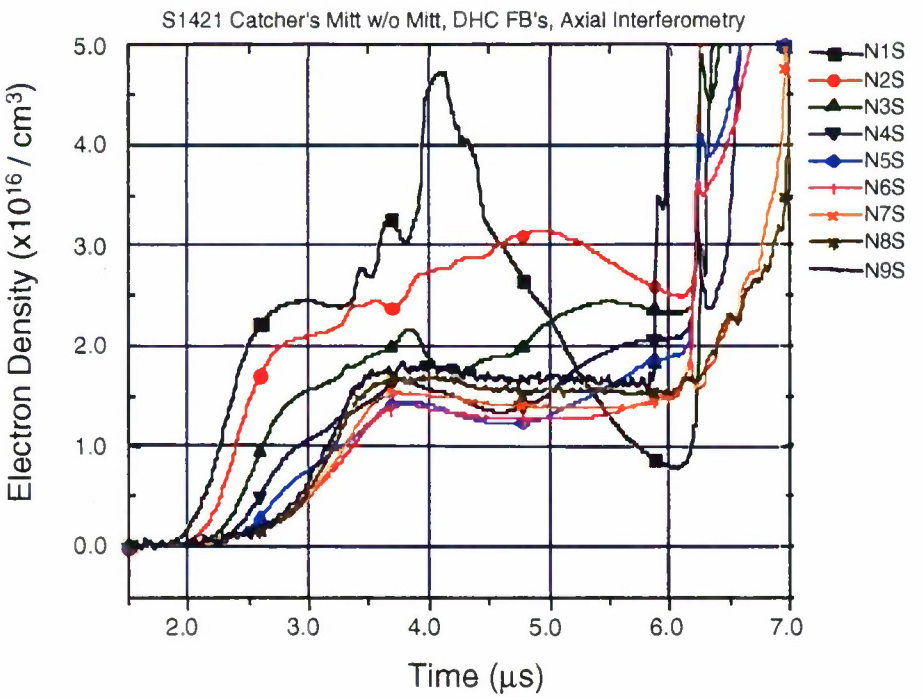

Figure 3-19. Electron density measured with pulsed power (shot 1421).

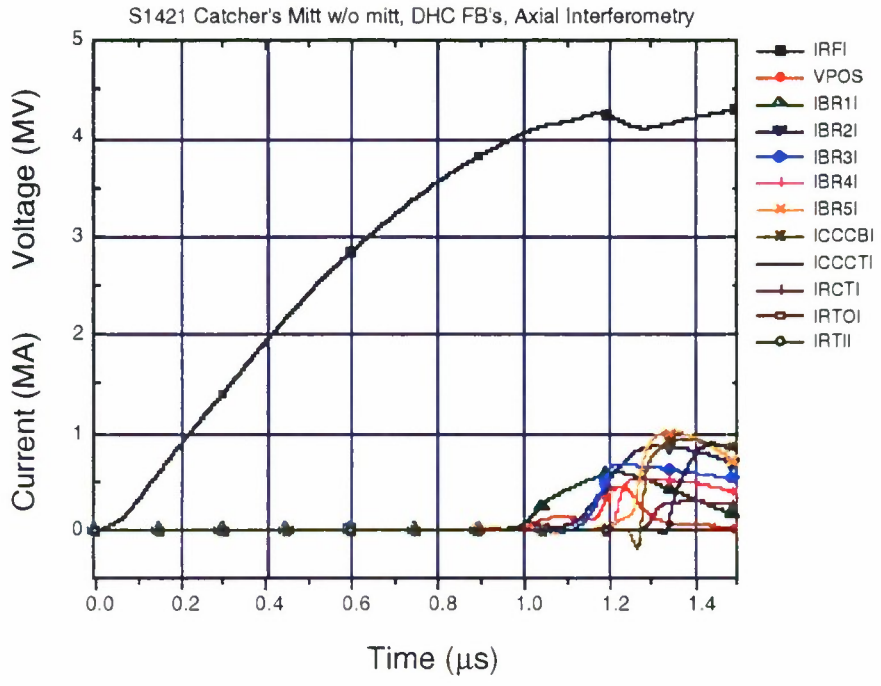

Figure 3-20. Current and voltage in downstream probes rise 1 μs after start of generator current.

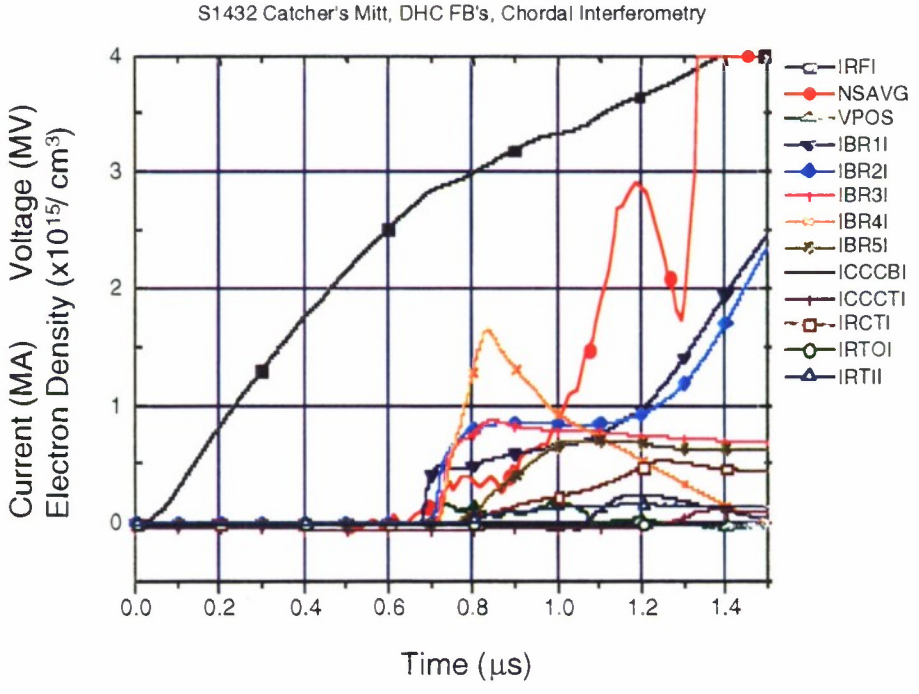

Figure 3-21. Current and voltage waveforms (shot 1432), and average densities in secondary switch region (see text).

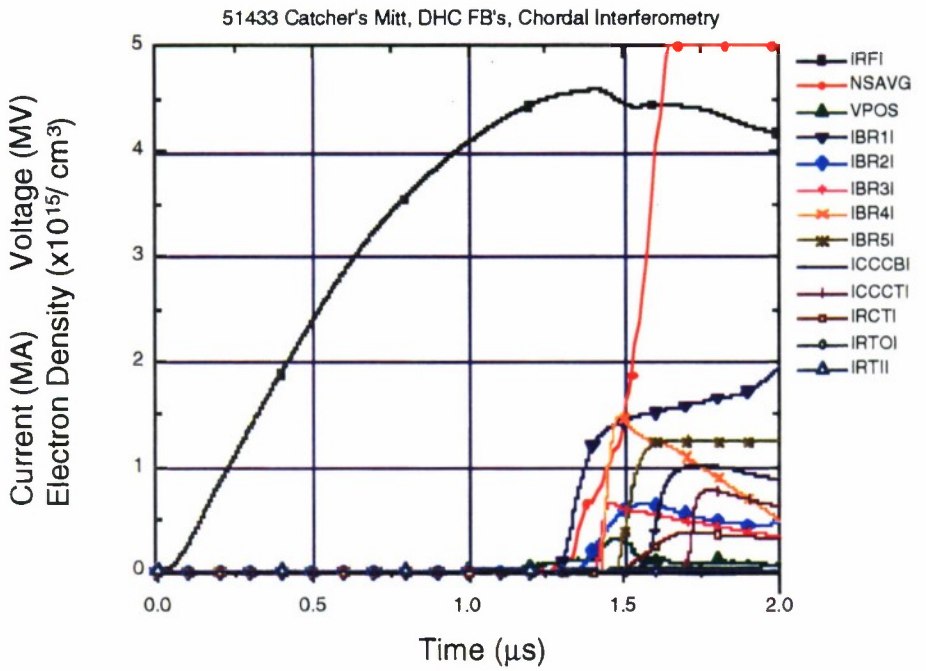

Figure 3-22. Current and voltage waveforms (shot 1433) and average densities in secondary switch region (see text).

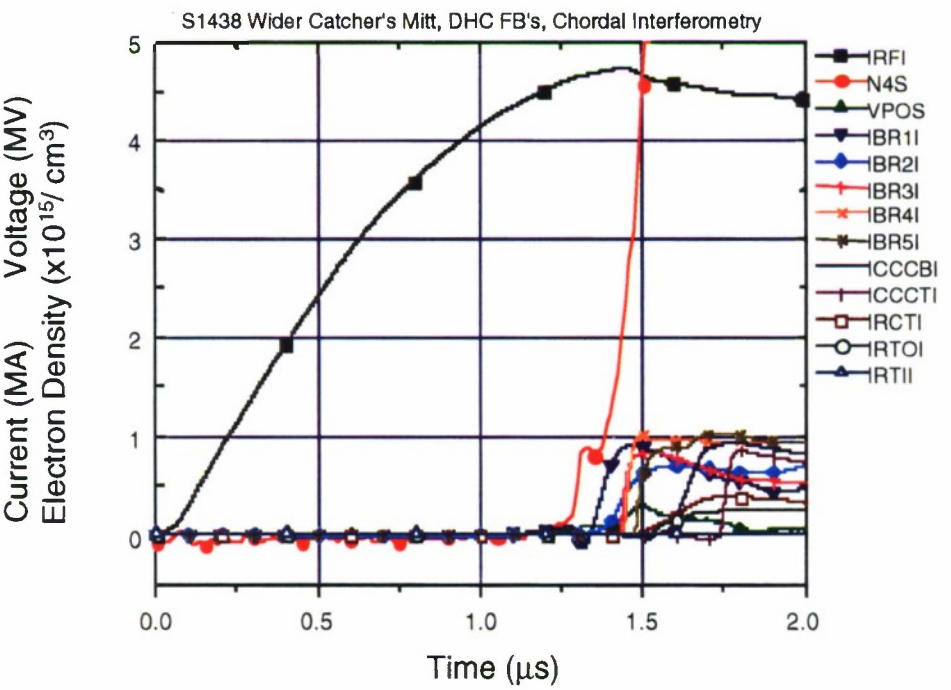

Figure 3-23. Current and voltage waveforms (shot 1438) and average densities in secondary switch region (see text).

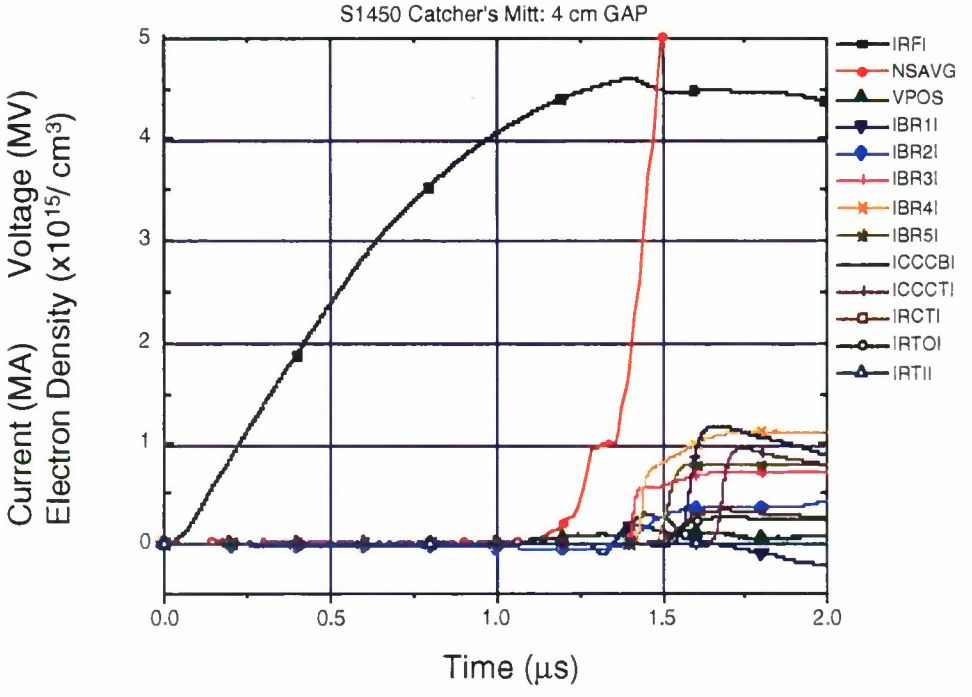

Figure 3-24. Current and voltage waveforms (shot 1450) and average densities in secondary switch region (see text).

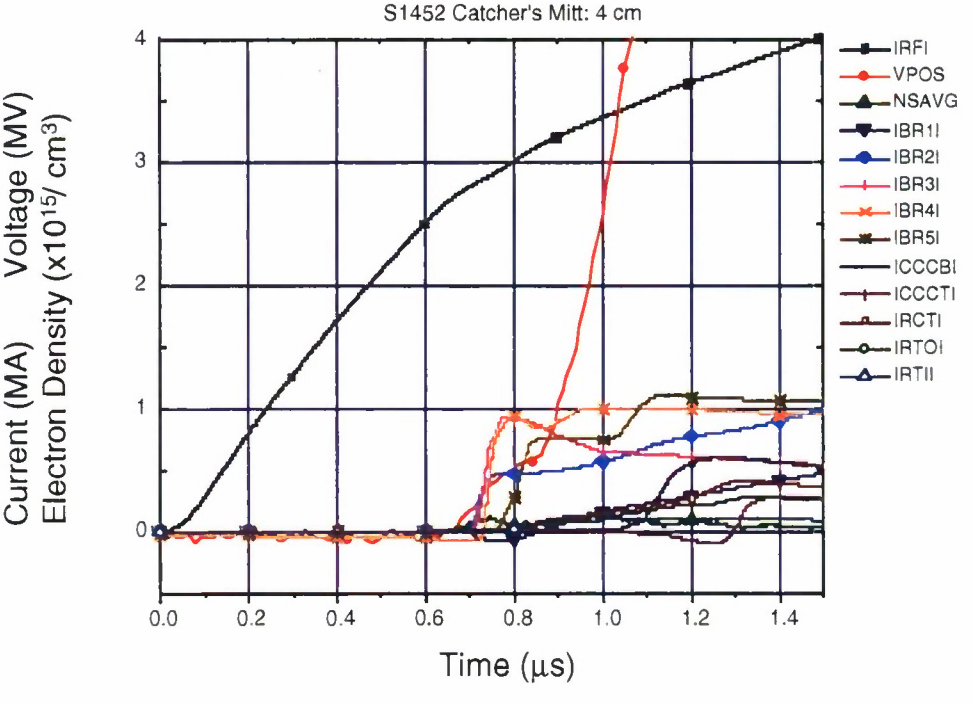

Figure 3-25. Current and voltage waveforms (shot 1452) and average densities in secondary switch region (see text).

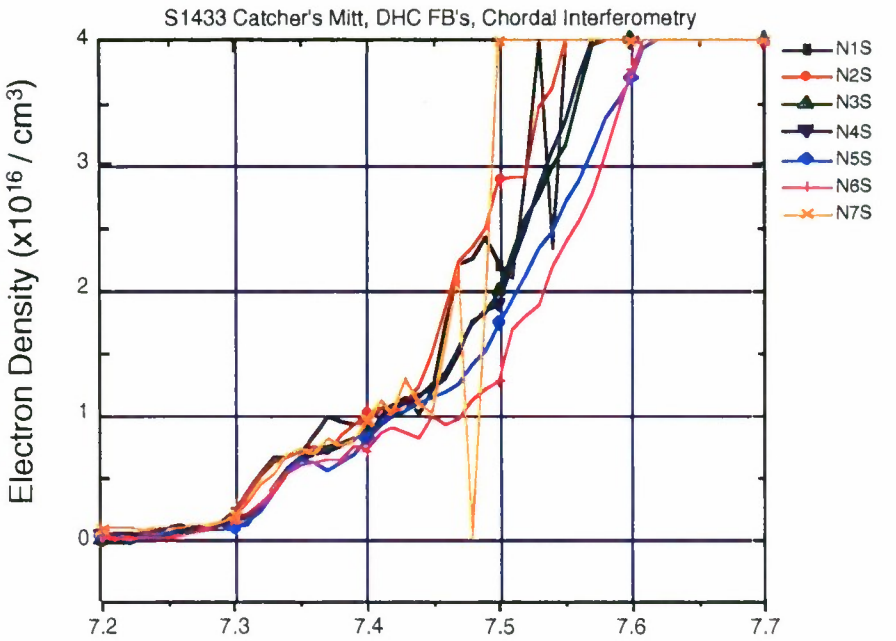

Figure 3-26. Densities in secondary switch region measured by chordal interferometry (see Figure 3-12) (shot 1433).

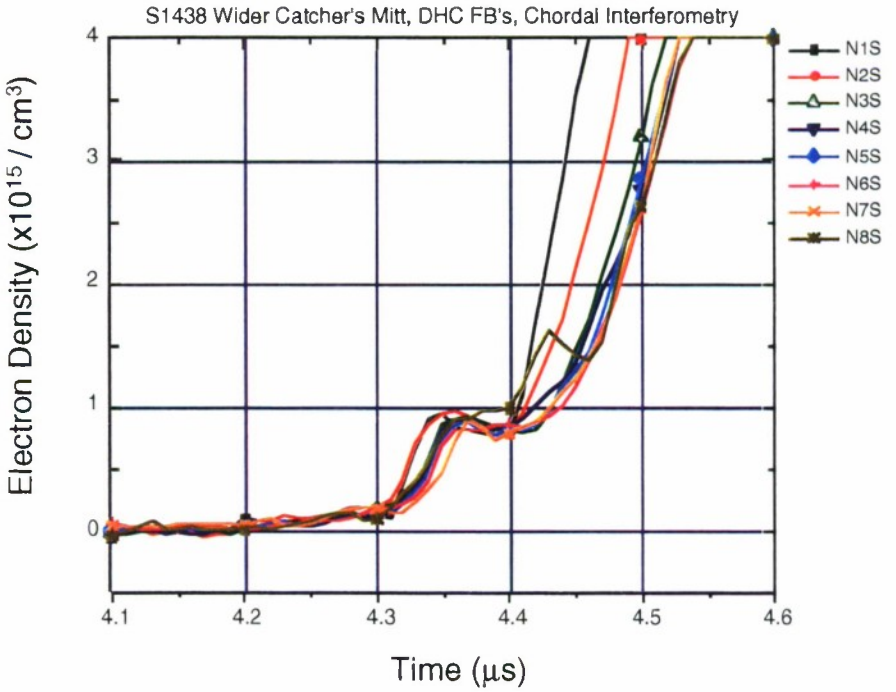

Figure 3-27. Densities in secondary switch region measured by chordal interferometry (see Figure 3-12) (shot 1438).

SECTION 4

ANALYSIS OF ACE-4 FLASHBOARD EXPERIMENTS

4.1 INTRODUCTION.

The primary justification of the modeling effort described here is to compare simulation results with experimental results, and in so doing, develop a greater understanding of the physics. To date, the comparison of experimental results to Mach2 simulations has resulted primarily in an understanding of some of the deficiencies in the model and in the development of improved modeling approaches.

Two basic areas have been identified where the simulation disagree significantly with the experiment. In both cases, the disagreement clearly is due to some essential incompleteness in the computational model. Due to the importance of these areas of disagreement, the business of simulating ACE-4 experiments was put on hold until it could be established whether the disagreements could be resolved in a reasonable manner.

The first general area of disagreement is in the relation between measured electron number density and mass density. In MHD, the mass density is far more important than the electron number density. The latter does effect transport properties, such as electrical resistivity and thermal conductivity, but these are secondary to the interaction between magnetic field and mass. The importance of the electron number density is in that it is the quantity which is measured in the experiments. In order to use these measurements to set up a simulation properly, information on how electron number density relates to mass density is required. Assuming a fixed ionization state is easy, and the assumed degree of ionization can be varied parametrically until some sort of match between experiment and simulation, say in the conduction time, is obtained. However, the electron measurements often exhibit changes at times early in the conduction phase when little rearrangement of mass has yet a chance to occur. This is strongly suggestive of ionization caused by heating as the snowplow begins to compress the plasma. This effect can be significant, amounting to as much as 30 to 50% changes in the measured electron number density. If the simulations are to be able to guide the experiments in any useful manner, then effects as large as this must be taken into account.

The second general area of disagreement concerns the initial distribution of plasma. This has some relation to the previous point of disagreement, but there is a distinction, as well. The experiments very often show a systematic increase in line-integrated electron number density moving across the gap from cathode to anode after the apparent end of the conduction phase. Among other possibilities, this suggests that a high-density layer of plasma was formed along the cathode at some time, and then is released somehow once the switch opens. Hypothetically, it is possible that the plasma from this conjectured layer is reaching across the A-K gap to short out the switch. An investigation of this effect requires a greater understanding of how the flashboard plasma behaves in the system, in particular, how it interacts with the cathode. Perhaps the in-flowing plasma stagnates against the cathode, and by virtue of its contact with the cathode, cools to form a dense layer. Thoughts along such lines have motivated a careful investigation of the flashboard plasma.

4.2 FLASHBOARD EXPERIMENTS.

In order to understand the nature of the flashboard plasma better, a series of experiments and simulations was undertaken in which a set of flashboards were operated in free-space, i.e. without the complications of the anode and cathode. Experimentally, these free-space shots were diagnosed with magnetic field probes and laser-interferometric measurements of the electron number density. From the simulation viewpoint, the goal was to match the experimental

measurements as well as possible, and from so doing, gain greater understanding of the nature of the plasma created by the flashboard.

The experiment consisted of five flashboards placed on the circumference of a 15 cm radius circle. The five boards subtended roughly one quarter of the circle's circumference; this is the same arrangement of flashboards used in ACE-4 experiments, except that normally the entire circle is covered and 18 flashboards are needed to do so. Thus, the freespace flashboard experiment was devised to look like a subset of the plasma source arrangement used in the ACE-4 experiments. Diagnostics were set-up to look at the plasma at various locations along the symmetry line as shown in Figure 4-1.

The first goal of the simulations was to attempt to match experimental measurements close to the flashboard. Within a few centimeters of the flashboard surface, the measurements should be strongly dominated by the behavior of only the closest flashboard; the other four more distant flashboards can be ignored safely. Once this goal is accomplished, the plan is to simulate all five flashboards and compare with experimental measurements. At the time of writing, we have not yet gotten to this second goal, but we have achieved some success in achieving the first goal.

As Mach2 is a two-dimensional code, a choice of what sort of symmetry to impose in order to model the experiments must be made. Two choices are possible. First, one can regard the flashboards as being infinitely long in extent, and model the current which drives the flashboards to flow in the direction normal to the plane of the simulation. This is called the poloidal geometry. The second choice is to regard the flashboards as being azimuthally uniform, and model the current as flowing in the axial direction. This is called the toroidal geometry. In the poloidal simulations, the magnetic field is in the plane of the simulation. In the toroidal simulations, the magnetic field is azimuthal, i.e. normal to the simulation plane. The poloidal simulations are much more difficult than the toroidal simulations. The magnetic field must be treated specially to avoid creation of divergence, and magnetic field boundary conditions are sometimes quite difficult to determine. For reasons involving these difficulties, the poloidal simulations have not yet had a chance to be of as much use as the toroidal simulations. However, the poloidal simulations are the only means available for simulating the discrete nature of the five flashboards used in the freespace experiments.

The basic strategy in the simulations, poloidal as well as toroidal, is to manipulate the boundary conditions to bring simulated probe responses in line with experimental probe responses. Boundary conditions for the density and magnetic field were varied, as was the boundary condition for the temperature. The greatest degree of success to date has been obtained with static boundary conditions for density and temperature, and a time-varying boundary condition for the magnetic field. The time-variation was chosen to match the experimentally observed temporal behavior of the current which drives the flashboards.

Figures 4-1 and 4-2 show the experimental measurements against which the simulations are to be judged and adjusted. Figure 4-1 shows magnetic field probe measurements taken at 1 cm intervals from the central flashboard. Figure 4-2 shows laser interferometric measurements of the electron number density taken at 0.30 cm intervals from the central flashboard. The response from the probe nearest the flashboard does not have the full confidence of the experimentalists, so it is not considered an important feature to match in the simulations. An important point to keep in mind when comparing the simulations to the experiments is that the definition of zero on the timeline differs. In the simulations, t=0 corresponds to the time at which current begins to flow. In the experiments, t=0 corresponds to the time at which voltage is first applied to the flashboards. The process of electric breakdown takes roughly half a microsecond, so it takes roughly that long before current begins to flow in the flashboards. Thus, the experimental time lags behind the simulation time by half a microsecond.

Figures 4-3 and 4-4 show the simulated electron and magnetic field probe responses from the first simulation. Because of the relatively coarse gridding used in these simulations, several of the probes lie within the same cells, thus causing their output to coincide with that of their cell-mates. The biggest discrepancy between simulation and experiment is the magnitude of the signals. The times at which peak values occur in the simulations are also systematically earlier than those observed experimentally. To seek closer agreement, both the boundary value used for density and the magnitude of the driving current were increased. The current was increased by a factor of 1/0.58; the density was increased by a factor of 6. Together, these two changes create a decrease in the Alfven scale-speed by 70%. Thus, the density and magnetic field should move toward the experimental values, and the times of peaks should also move in the right direction. Figures 4-5 and 4-6 show the simulated electron and magnetic field probe responses, respectively, from this second simulation. The peaks have arrived some 100 to 200 ns later, and the magnitudes are closer to the observed magnitudes.

A very revealing comparison is shown in Figures 4-7 and 4-8. Here, the simulated line-integrated electron as well as ion number densities are compared to the experimentally obtained line-integrated electron number density. In Figure 4-7, the simulated ion number density has been multiplied by a factor of 2. Before proceeding with the comparison, we must note that the simulation used the Saha equilibrium ionization model and ionization energy-corrected equation of state, which is described in detail below. For now, suffice it to say that the simulation uses a model for self-consistently incorporating energy and density dependent ionization for any given mixture. The mixture under consideration here is two fluorine atoms for every carbon atom. The simulation curves have been shifted 500 ns to the right to match the time required for current to begin flowing in the flashboards. Figure 4-7 shows very good agreement in the vicinity of the peaks between the experimental electron data and the simulated ion data, which, as noted above, has been multiplied by two. The striking agreement strongly suggest that the plasma in the experiment, at electron probe location 2, has an ionization state of 2. Figure 4-8 shows the simulated ion and electron probe responses in comparison with the experimental electron number density at probe 9. Here, the simulated ion data has not been multiplied by 2. The implication is that at electron probe location 9, the experimental plasma was in a charge state of Z=1.

The comparison between simulated density probe responses and magnetic field probes responses indicates that this simulation has matched the basic magnetohydrodynamics of the flowing flashboard plasma quite well. The magnetic field magnitudes and timing are in fairly good agreement, in particular, the drop in field magnitude across the first three probes observed in the simulation matches well with that seen experimentally. The agreement between experiment and simulation between both the field magnitudes and the timing suggests that the simulated ion density is in fair agreement with experiment, as well. If it were not, the Alfven speed would be different, and this would ruin the agreement in the timing. There are some discrepancies, particularly with how quickly response curves come up, but the agreement is still quite good. If the assumption is made that the simulated ion density is correct, i.e. provides a perfect match to what occurred in the experiment, and that the Saha model provides an accurate description of ionization effects, then the comparison between experiment and simulation suggests some interesting possibilities for the behavior of the flashboard plasma. At density probe location 2, the simulated ion density peaks at 1.8056×10^{16} per cc. But the experimental electron number density peaks at that probe with a value of 3.614×10^{16} per cc. This implies a charge state of Z=2. The Saha model implies that at the indicated ion number density, a CF2 mix will have a charge state of 2 if the temperature is 3.083 eV. The specific internal energy corresponding to this temperature and density is 6.068×10^{8} J/kG. At probe location 9, the simulated ion density peaks at 1.68×10^{16} per cc, and the experimental electron number density peaks at 1.8×10^{16}, implying an effective charge state of Z=1.07. The Saha model implies a temperature of 1.69 eV and an internal energy of 2.31×10^{8} J/kg. Thus, as the plasma moves from probe 2 to probe 9, it loses a substantial amount of energy. The cooling rate can be estimated by the difference in energies at the two locations divided

by the time-of-flight between the two probes. The time-separation between the experimental peaks at probes 2 and 9 is 0.65 x 10^{-6} s. Using this time to calculate a cooling rate, one obtains

$$de/dt = \left(6.068\times10^{8}\,J/kg - 2.31\times10^{8}\,J/kg\right)/0.65\times10^{-6} = 2.8\times10^{11}\,W/kg \quad . \qquad (4.1)$$

Thus, the suggestion is that the simulation is correctly calculating the flow of mass and magnetic field, but is not currently calculating the relation between electron density and ion density. The comparison between simulation and experiment suggests that there is some sort of heating mechanism near the surface of the flashboard, and that as plasma moves away from the flashboard, it loses energy according to the rate estimated above. This cooling rate is consistent with that to be expected from bound-bound radiation at these temperatures and densities. This leaves as the mystery the heating mechanism which increases the plasma's ionization state to the suggested levels in the immediate vicinity of the flashboard.

A hypothetical heating mechanism involves magnetic reconnection. The postulated mechanism is based on the fact that the flashboards consist of five parallel current paths. As the flashboard breaks-down, each of these paths might become a line-source of magnetized plasma. When the plasma expands away from the flashboard, the magnetic field in the plasma resistively decays to wash out the features of the five individual current paths. Whether or not such resistive reconnection is a plausible heat source has not yet been investigated in any detail.

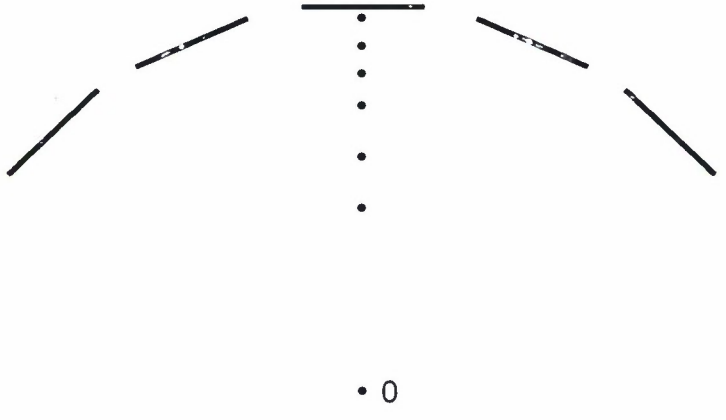

Figure 4-1. Schematic of arrangement of five flashboards on a circumference in measurement of line electron densities in direction perpendicular to plane of paper at various positions along symmetry line. Flashboard current is perpendicular to plane of paper. For infinitely long flashboards this geometry is called poloidal.

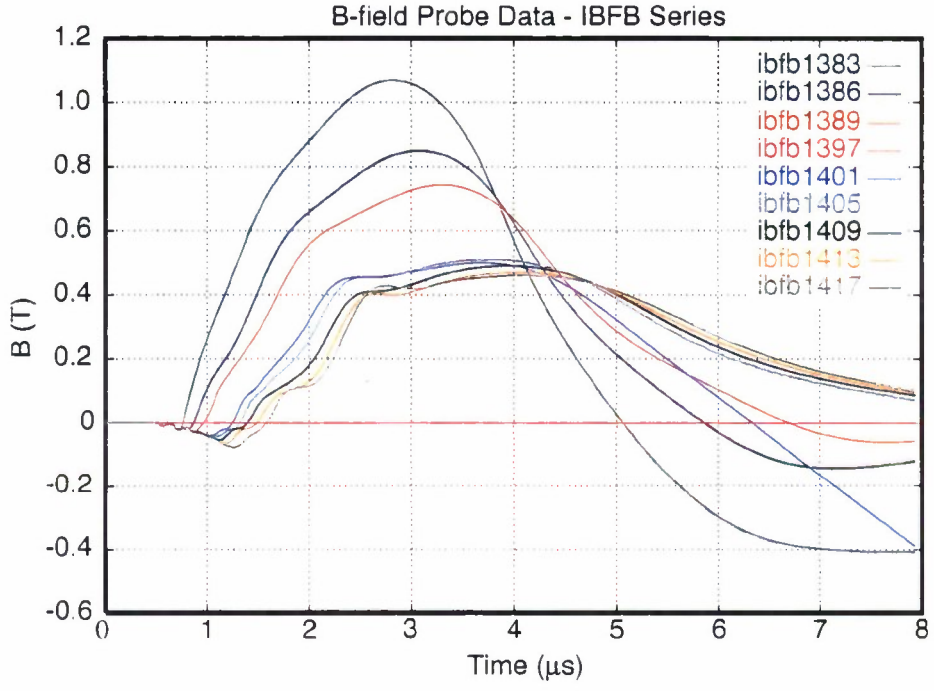

Figure 4-2. Measured magnetic field waveforms at 1 cm intervals from central flashboards.

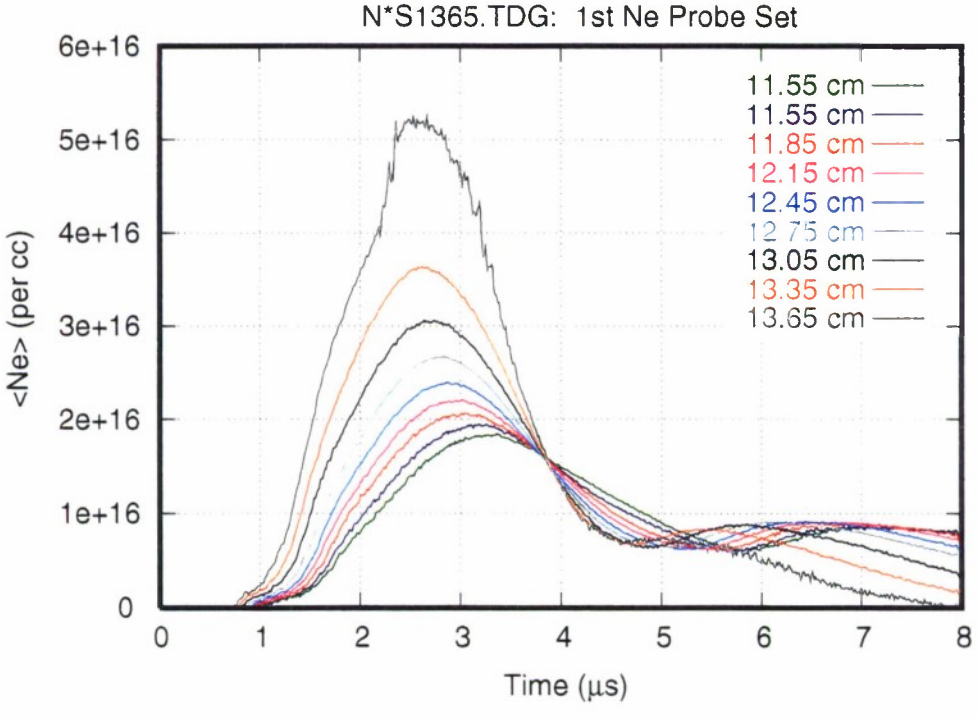

Figure 4-3. Measured electron number density at 0.3 cm intervals from the central flashboard.

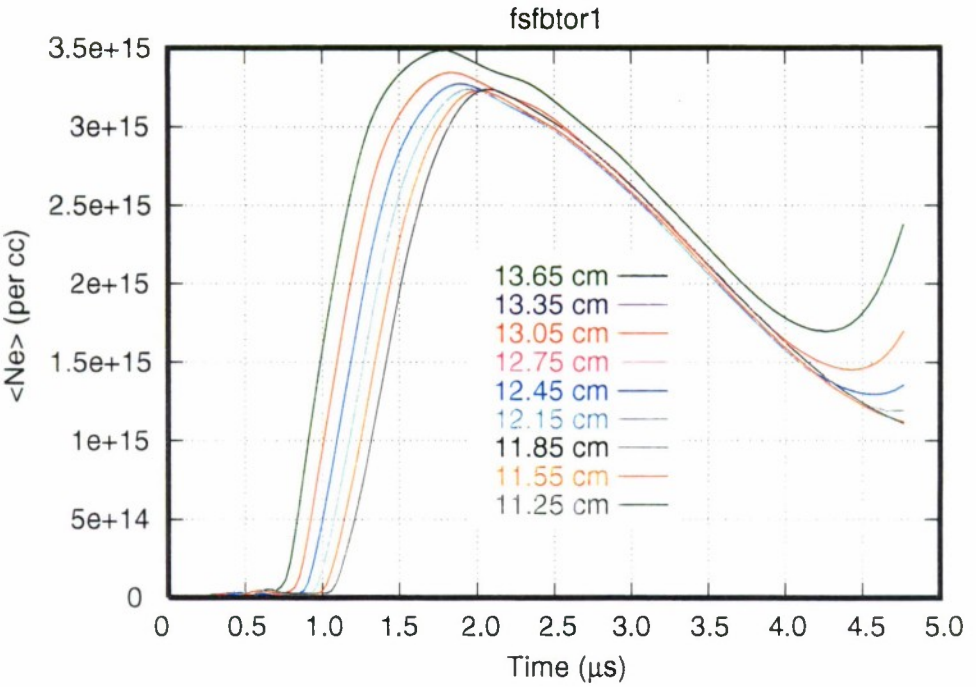

Figure 4-4. First Mach 2 simulation results for electron density.

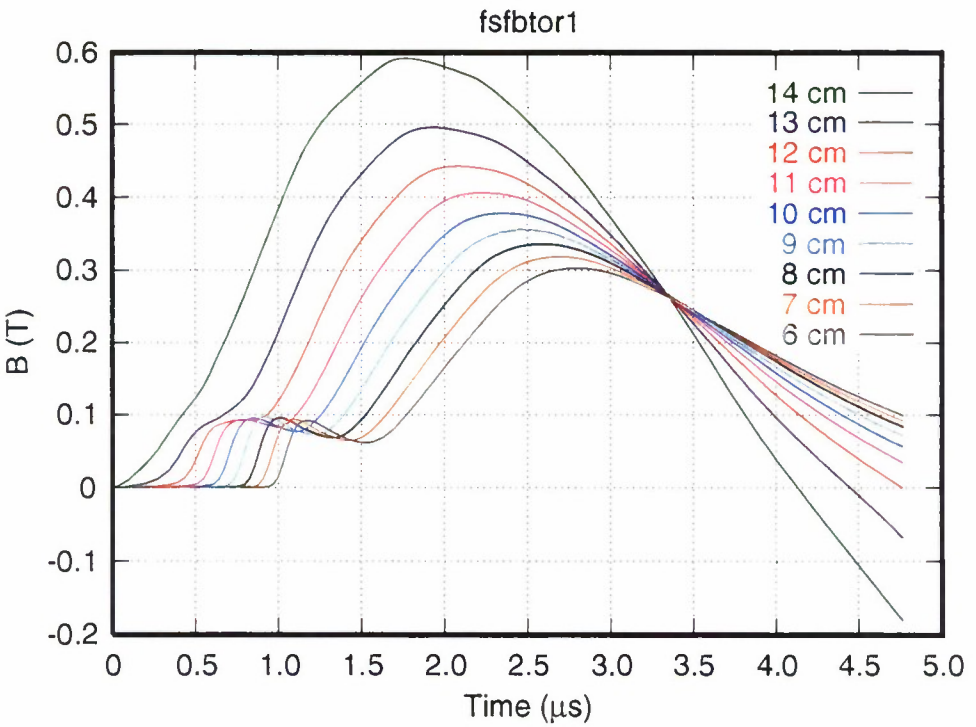

Figure 4-5. First Mach 2 simulation results for magnetic field.

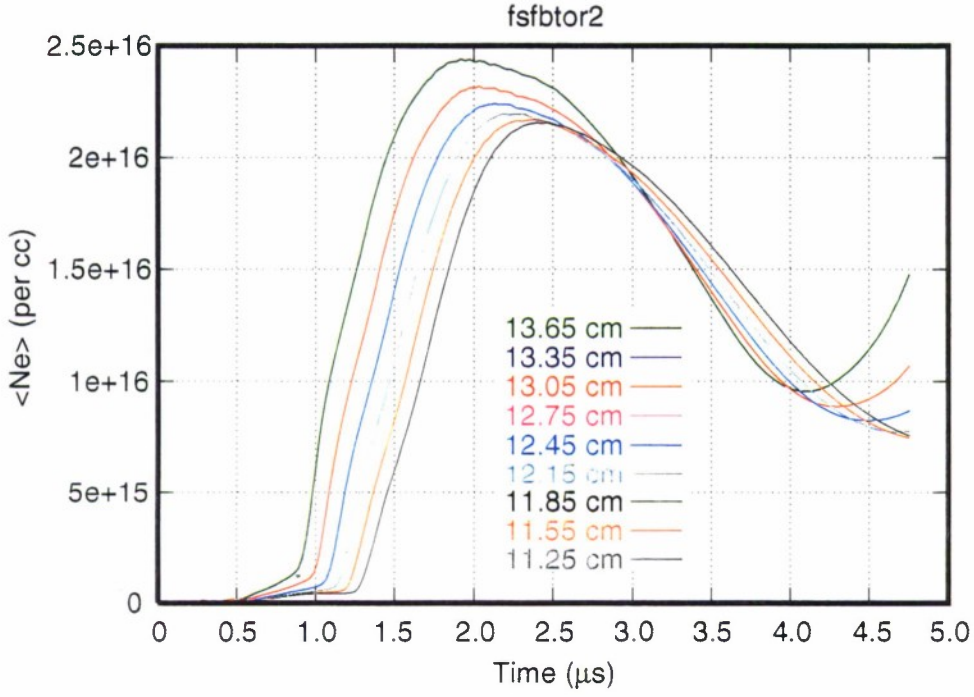

Figure 4-6. Second Mach 2 simulation results for electron density.

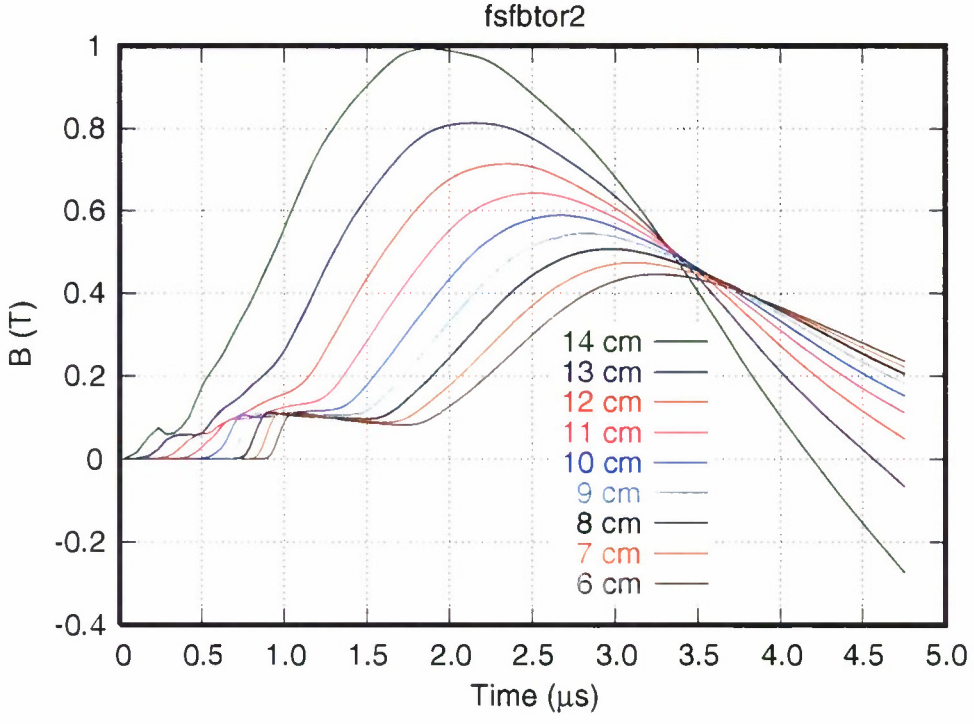

Figure 4-7. Second Mach 2 simulation results for magnetic field.

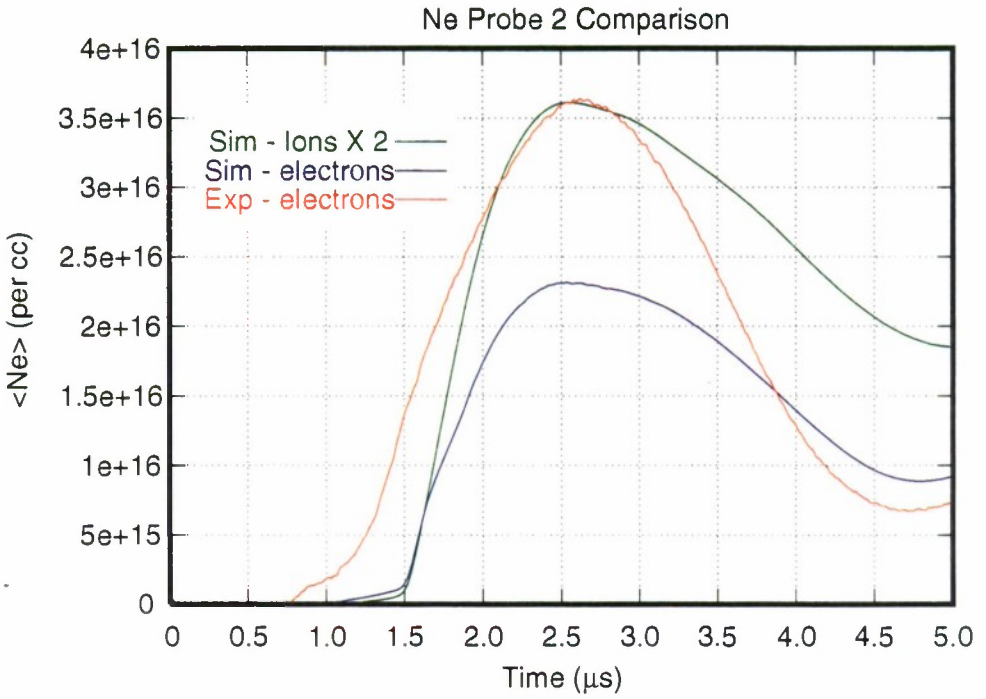

Figure 4-8. Comparison of measured and calculated electron densities at probe 2 location. The simulated ion density has been multiplied by a factor of 2.

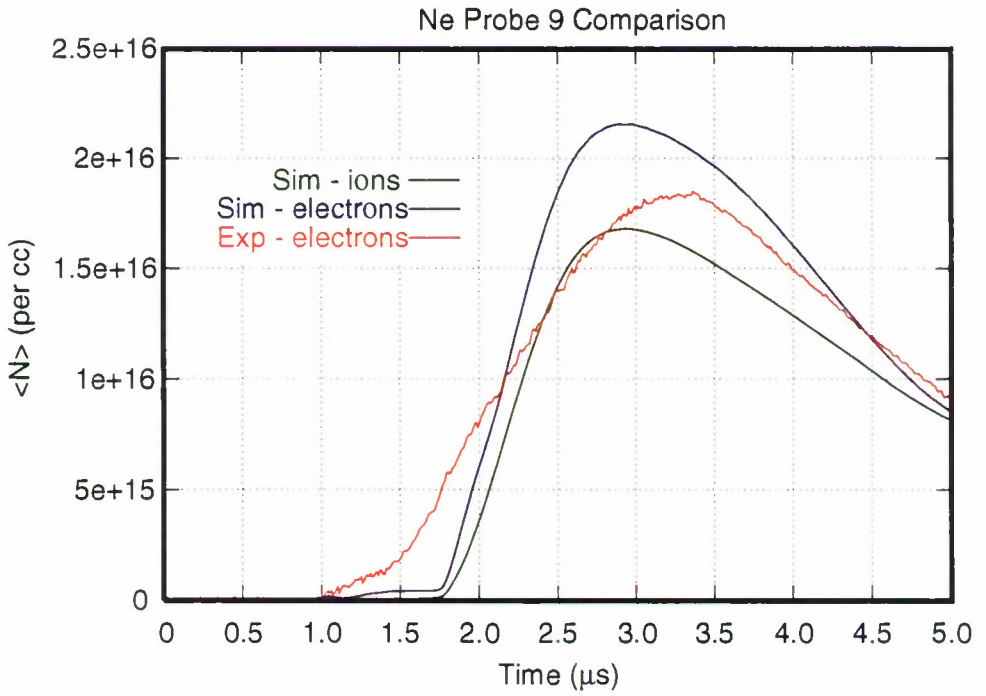

Figure 4-9. Comparison of measured and calculated electron densities at probe 9 location.

SECTION 5

IONIZATION EFFECTS IN POS PLASMAS

The preponderance of ionization effects observed in the ACE 4 POS experiments indicates that inclusion of a variable ionization capability in the modeling effort would be of great benefit. Mach2 already has two options for variable ionization, but these were deemed inappropriate for this effort. One option is a Saha model restricted to hydrogen. The other option is to use the SESAME equation of state tables. The first option is deficient since the switchboard plasma is dominated by carbon and fluorine. The second option has some points in its favor. First, it is an existing capability. Second, it allows ionization effects to be included in the equation of state automatically. Third, the SESAME tables allow radiative cooling effects to be included for most materials within the SESAME collection. The importance of radiative cooling was discussed above in conjunction with modeling the flashboard plasma. But the points against the SESAME option were judged to outweigh the proponent points. First, Mach2 does not have the proper coding to combine SESAME tables in order to get equations of state and ionization levels for mixtures of elements. Second, the SESAME tables were designed primarily for UGT applications - for the pulsed-power arena, they have applicability in such areas as imploding liners where accurate, reliable models of solids such as aluminum or copper are of prime importance. But for the relatively low density, low temperature regime of the plasma opening switch, the SESAME tables are of only infrequent accuracy. Thus, in order to allow for variable ionization in a self-consistent manner, and to do so in a way which would allow mixtures of elements to be treated, and further, to do so with a model of well-characterized applicability, the decision was made to institute in Mach2 the Saha equilibrium ionization model, referred to hereafter as the Saha model.

5.1 MODEL.

The Saha model is appropriate for describing situations in local thermodynamic equilibrium. It assumes that the rate of ionization is in balance with that of recombination. The Saha model loses applicability in cases where the timescale of interest is smaller than the timescale describing ionization rates. It also is not valid in optically thin systems where photonic processes become significant. We have not yet determined the bounds on temperature and density which characterize the validity of the Saha model. The timescales characterizing the flow of flashboard plasma and the conduction phase are probably not shorter than timescales reflecting the ionization rates. The plasma density may verge on being too low, in which case a non-LTE model could be used. However, a simple Saha model should be quite adequate for indicating the degree to which ionization effects are important.

A set of coupled, nonlinear algebraic equations, parameterized by electron temperature, describe the Saha model. For a plasma consisting of a single element, these equations are:

$$n = n(0) + n(1) + \ldots + n(Z) \tag{5.1}$$

$$ne = n(1) + 2n(2) + 3n(3) + \ldots + Z\,n(Z) \tag{5.2}$$

$$n(i+1)/n(i) = G_i\,(T^{3/2}/ne)\exp(-I(i+1)/T) \quad . \tag{5.3}$$

where n is the density of all neutrals plus ions, regardless of their charge state, ne is the number density of (free) electrons, and I(i) is the energy required to remove the ith electron from an ion from which (i-1) electrons have already been removed, and G_i is a constant independent of T and n_e. n(i) is the number density of ions with i electrons removed. Z is the number of protons in the nucleus of the species under consideration. T, of course, is the electron temperature. In (5.8), the

contribution of excited states is neglected. For simplicity, we assume that G_i, which is proportional to the ratio of internal partition functions of ions i + 1 and i, is independent of i.

Consider the situation wherein the temperature and n are known, and it is desired to determine ne. Equation (5.3) may be used repeatedly to rewrite equation (5.1) solely in terms of n(0) and ne. To do so, it is convenient first to write equation (5.3) as:

$$n(i+1)/n(i) = f(i)/ne \quad . \tag{5.3a}$$

Then, equation (5.6) becomes

$$n = n(0) * \{1 + f(0)/ne + f(0)f(1)/ne^2 + f(0)f(1)f(2)/ne^3 + \ldots$$

$$\ldots + f(0)f(1)\ldots f(Znuc)/ne^Z\} \quad . \tag{5.4}$$

This reduces the system of coupled equations to a single equation - the remaining task is to solve equation (5.4) for ne. This can be done analytically for Znuc = 1, 2, 3 and 4, but purely analytic means fail for Znuc ≥ 5. Thus, an iterative scheme is used wherein an initial guess is made for ne. This, with the known value for n, allows a value for n(0) to be calculated from equation (5.4). Then equation (5.3) is used to calculate each n(i). These results are then used in equation (5.2) to obtain a new value for ne. If this new value for ne is identical to the value initially assumed for ne, then the initial guess was correct. If the new value for ne differs from the initial guess, then the calculation is repeated until the difference between the new value for ne and the previous value for ne is less than some predetermined value. In practice, a scheme whereby the value to use for the new iteration is determined as a linear combination of the past value and newly calculated value has been found to speed the iteration process significantly.

Figure 5-1 shows some examples of this model. The effective charge state, i.e., the number of free electrons per ion, is plotted against temperature for a total ion density of 1×10^{16} per cc.

The procedure described above for a single element can be generalized easily for mixtures of elements. Suppose the mixture consists of M elements. Let a(k) denote the fractional composition of the kth element. The coefficients a(k) must sum to 1:

$$1 = a(1) + a(2) + \ldots + a(M) \tag{5.5}$$

The procedure described above is then used for each of the M mixture components with the following modifications: in equations (5.1) and (5.4), n is replaced by a(k)n, n(i) is replaced by n(i,k), and equation (5.3) is replaced by

$$\begin{aligned} ne = {} & \{n(1,1) + 2n(2,1) + \ldots + Z(1)n(Z(1),1)\} + \\ & n(1,2) + 2n(2,2) + \ldots + Z(2)\, n(Z(2),2)\} + \\ & \qquad \vdots \\ + {} & \{n(1,m) + 2n(2,m) + \ldots + Z(m)n(Z(m),m)\} + \end{aligned} \tag{5.6}$$

where n(i,k) is the number density of the i-times ionized ion of the kth species.

Figure 5-2 shows the results of the Saha/mixture calculation for carbon and fluorine in various concentrations. An interesting feature is the manner in which the "ledge" at Zeff=4 is altered as more and more fluorine is added to the carbon.

The ability to include self-consistent variable ionization states, in which the degree of ionization changes in response to the local state of the plasma, is crucial for comparing to experiments in which the main diagnostic measures electron number density. An example of the use of the Saha model in this conjunction is presented below.

5.2 MODIFICATIONS TO THE IDEAL GAS EQUATION OF STATE.

Calculating a density- and temperature-dependent charge state is an important step in improving the flashboard and conduction phase simulations. To make the model consistent, however, the equation of state must be modified. The ideal gas equation of state used in Mach2 includes only the translational degrees of freedom. Consistency with the Saha equilibrium ionization model requires that the equation of state include the energy required for ionization, as well. Ionization has an effect on the equation of state similar to that of a phase change. For a plasma undergoing ionization, the appropriate equation of state is:

$$E = (3/2)N(1 + Zeff)kT + \sum_{m=1}^{m} E_{ion}(m) \tag{5.7}$$

where

$$E_{ion}(m) = \sum_{k=1}^{Z(m)} n(k,m) \sum_{j=1}^{k} I(j,m) \quad . \tag{5.8}$$

The immediate question one might ask is to what degree does inclusion of the ionization energy effect the equation of state. Figure 5-3 gives an answer to this question for a CF2 mixture over the density and temperature ranges of relevance to ACE 4 modeling. In this plot, the ratio of the left-hand side of equation (5.6) to the first term on the right-hand side of equation (5.6), the thermal term, is shown. The thermal energy is thus an underestimate of the total energy by a factor ranging from 4 to 10. This means that the temperature obtained with the old equation of state, which included just the thermal or translation term, was several times higher than it is once the energy needed for ionization is properly accounted for. Figure 5-4 shows the relation between total (translational and ionization) specific internal energy and temperature for a CF2 mixture. Figure 5-5 shows the specific heat for the CF2 mix at a density of 1.e16 per cc. The complicated structure corresponds to the many ionization levels which occur in this temperature range.

This modification to the equation of state effects the hydrodynamics through the pressure. The pressure is depends on the temperature both directly as well as through the effective charge:

$$p = (1 + Z(n,T))nkT \quad . \tag{5.9}$$

The Saha model affects the pressure in two ways: through the (1+Z) factor and through the temperature. Both can be significant.

5.3 EFFECTS ON CONDUCTION PHASE.

The development of the Saha model and its incorporation into Mach2 has been too recent to allow more than an initial exercise of the capability on a few simple test cases. The prime motivation for creating this capability was the time-dependent ionization observed in the interferometric measurements of the electron number density during the conduction phase. So it was to this problem that the model was first applied.

For an initial test, a very simple situation was chosen. This was a coaxial geometry in which a given axial length was filled with plasma of uniform density. The geometry was that of the ACE 4

switch region, with a cathode radius of 5 cm and an anode radius of 7 cm. The plasma filled a region 20 cm in axial extent. The total length of the simulation domain was 62 cm, with vacuum occupying the downstream 42 cm. The switch was driven with an RLC circuit with parameters chosen to mimic the ACE 4 generator.

Two runs were performed: one with a constant degree of ionization, the second with the Saha equilibrium ionization model running. A CF2 mixture was used for the switch material; the ion density was 5×10^{15} per cc. The constant ionization run used Z=1 for the ionization state. The Saha ionization run was initialized with a temperature of 1.472 eV, which is the temperature for which the CF2 mixture has an effective ionization state of Z=1 at the given total ion density. The point was to examine the differences between the two runs' simulated interferometry readings to see whether the Saha model appeared to bring the simulation closer to the experimental observations.

Figure 5-6 shows the simulated interferometry readings of all nine probes from both runs. The difference is significant. Moreover, the results from the Saha run show much in common with the generic experimental results; the rise of all probes during the first 300-500 ns of the conduction phase, in particular, is similar both qualitatively and quantitatively to the behavior observed experimentally. This rise is due to the initial shocking of the plasma by the magnetic piston. As Figures 5-7 (a, b) indicate, the plasma has moved very little by 500 ns. But with the degree of ionization tied to the state of the plasma, the compression of the plasma during this early stage of acceleration results in heating and thus, an increase in the degree of ionization. This is shown in Figure 5-7(c), which shows ionization levels ranging from Z=1 to Z=4 in the snowplow front.

The primary cause for the observed difference between these runs is, of course, just the inclusion of variable ionization. But the equations of state are different, as well. This should be expected to be a small effect on the mass motion, since the dominating behavior in the problem is the magnetic piston pushing mass, and both the mass and the current are identical between the two simulations. However, careful inspection of the simulated interferometry responses shows a difference that is caused by the different equations of state.

The difference is the abrupt change in the slope of the curves in Figure 5-6 observed just before $t=1 \times 10^{-6}$ s in the Saha run, and the lack of such behavior in the constant ionization run. The break in the slopes for the Saha run do not occur simultaneously; the effect begins at the cathode and moves across the gap toward the anode. The increase in the rate at which the plasma density is decreasing suggested by this change in slope is of no great surprise. Given the initially uniform plasma density and the 1/r nature of the magnetic field this sort of "gating" action is to be expected. The question is why is it so clearly visible in the Saha run, but apparently absent in the constant ionization run.

The likely cause for this difference is how mass is transported radially as the snowplow front accelerates axially. Due to the 1/r nature of the magnetic field and the initially uniform mass loading, the snowplow front develops a tilt in which the cathode side races ahead of the anode side. This causes the snowplow to reach the loadside vacuum region earlier near the cathode than near the anode. This portion of the plasma is now able to cool by expanding into the vacuum, thereby lowering the degree of ionization in the case of the Saha model. We observe that at any given time during the conduction phase, not as much mass has been transported out of the system in the Saha run as has been in the constant ionization run. Figures 5-8 (a, b) compare the ion density in the two runs just as the snowplow front is about to break into the vacuum region. The snowplow in the Saha run clearly has a greater mass inventory.

The primary effect of the Saha model observed in the conduction phase is thus just the difference in line-integrated electron number density due to increased availability of free electrons. A minor secondary effect is due to a difference in how mass is pushed out of the system by the snowplow

front, and this is caused by the increase in pressure, again caused by the increased availability of free electrons.

5.4 EFFECTS ON FLASHBOARD PLASMA.

A second area in which the Saha model is hoped to be of significance is in modeling the flashboard plasma and its interaction with the electrode structure. The flashboard modeling discussed above has benefited significantly from this development, but we have not yet had time to use this new tool for studying the interaction of flashboard plasma with the cathode. However, preliminary calculations indicate that it will be helpful.

A series of calculations performed in the toroidal geometry was performed to test the significance of the Saha equilibrium ionization model and the effect of the new equation of state. These were simulations in the coaxial geometry with anode and cathode radii chosen to match those of the ACE 4 experiments. Other than these measurements, no attempt was made to match the simulation parameters to reality. The simulations used the resistive MHD model with Spitzer resistivity. Thermal conduction was included, again using the Spitzer model for transport. The cathode was treated as a constant temperature boundary, with a boundary temperature of 0.025 eV. Figures 5-9 (a, b, c, d) show fluid velocity, ion number density, magnetic field, and temperature from a run using the Saha ionization model and the improved equation of state. Quantities are shown at 1.9×10^{-6} s into the run. A low temperature layer along the cathode can be seen; this is a consequence of thermal conduction losses to the cold cathode. The magnetic field distribution shows that current flows from the anode through the plasma to the cathode, then back through the plasma to the anode. This sets up a JxB field that tends to pump plasma into the upstream and downstream regions. This is an effect which could have some influence on how the conduction phase begins as well and how it ends.

Figures 5-10 (a, b) and 5-11 (a, b) compare a simulation which used the Saha equilibrium ionization model and the ideal gas equation of state (no ionization energy correction) with a simulation which used the Saha ionization model in conjunction with the improved equation of state. The plots show axially integrated ion and electron number densities at various times throughout the simulations. The profiles are distributed in time from t = 0 to t = 4000 ns. Each profile is separated in time from its neighbors by 200 ns. The earliest times produce curves which lie along the x-axis. So time and signal magnitude are related, with the largest signals coming latest in time. The timing is the same for all four figures. The point in comparing axially integrated quantities is to see whether the different equations of state amount to a difference large enough to be seen experimentally. The plots indicate a significant difference does appear. The simulation using the improved equation of state shows greater ion density at the cathode and steeper gradients developing and persisting than in the simulation with the uncorrected equation of state. This is encouraging since it is in the direction needed to come into closer agreement with experimental observations.

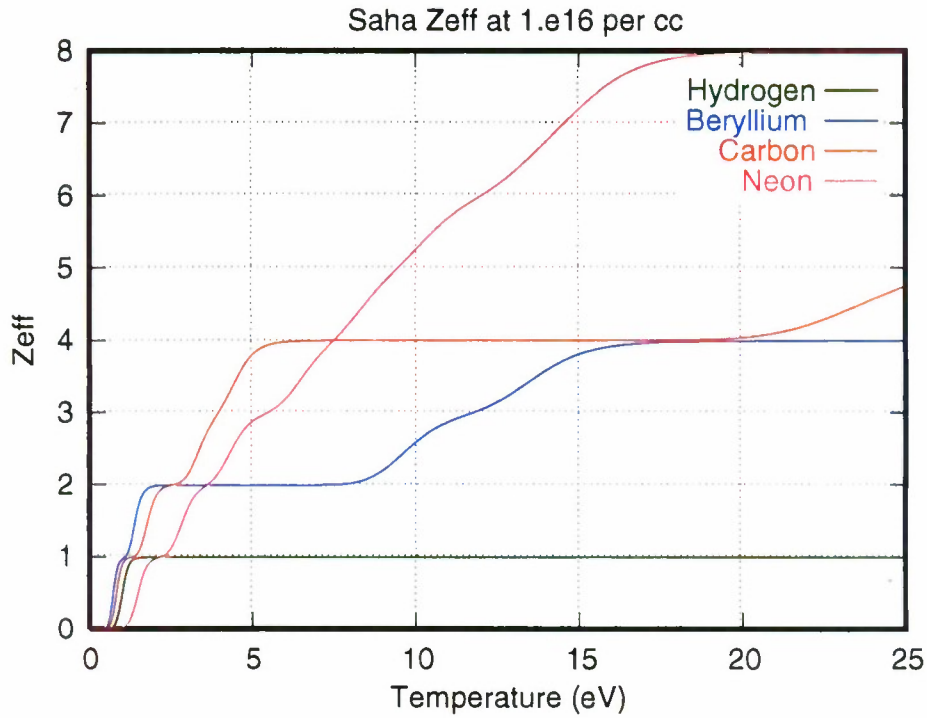

Figure 5-1. Average charge state of various elements for an ion density of $10^{16}/cm^3$.

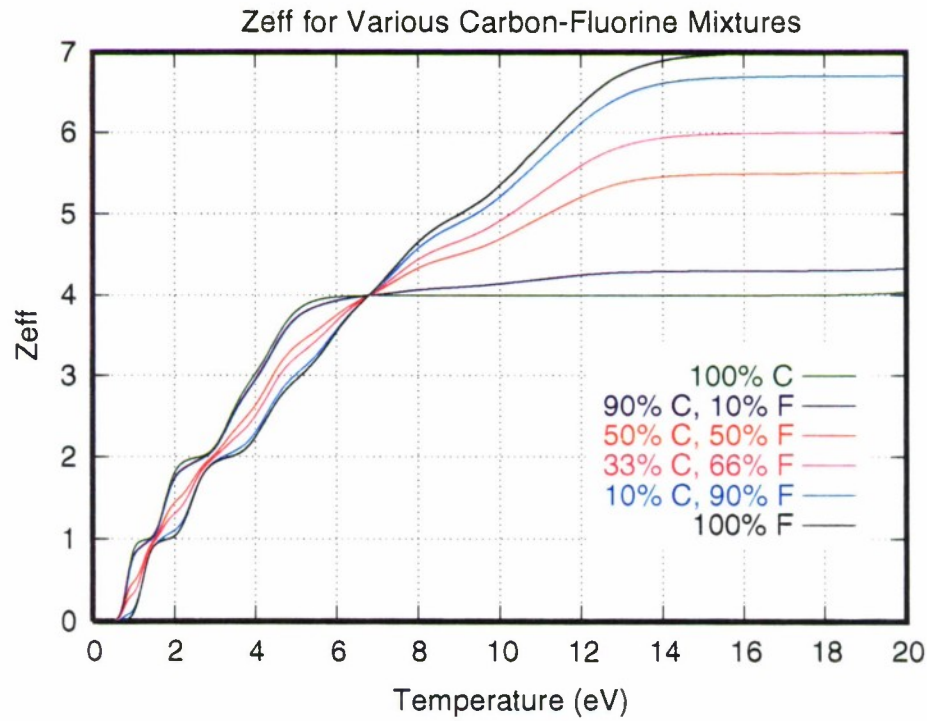

Figure 5-2. Average charge state of various mixtures of C and Z for an ion density of $10^{16}/cm^3$.

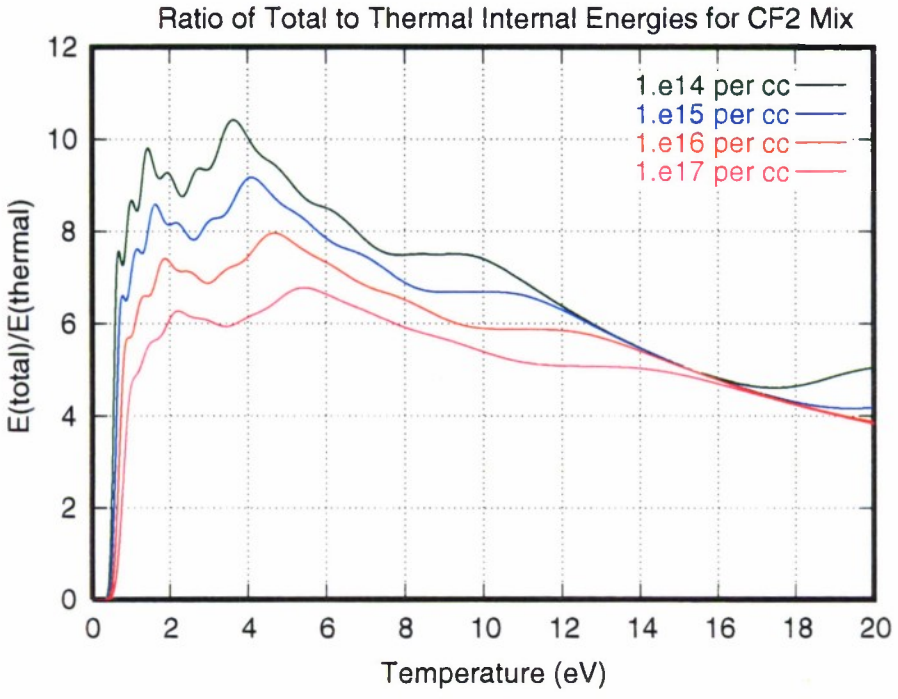

Figure 5-3. Ratio of total to thermal internal energies for CF_2 mix.

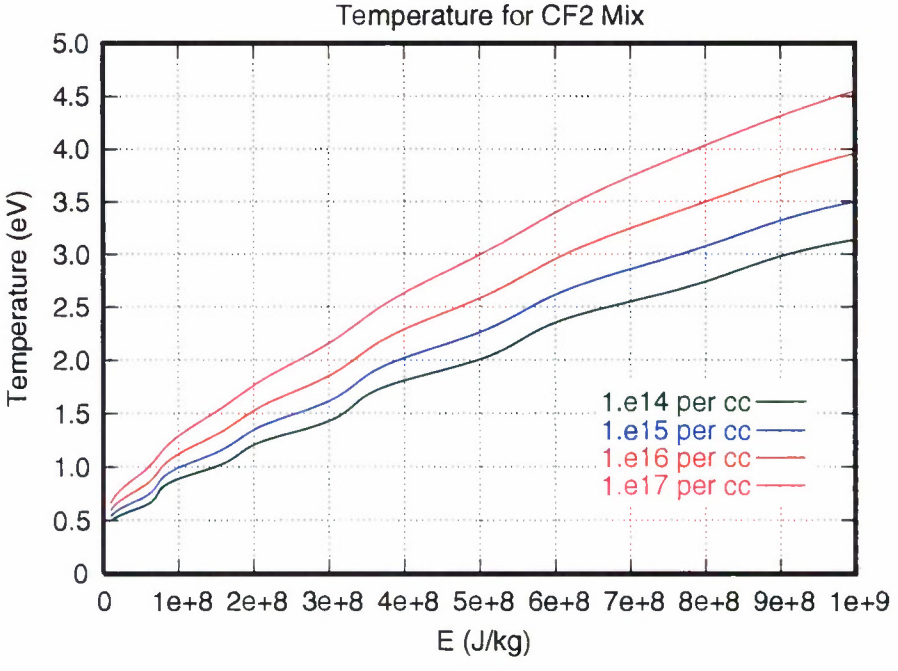

Figure 5-4. Temperature for CF_2 mix.

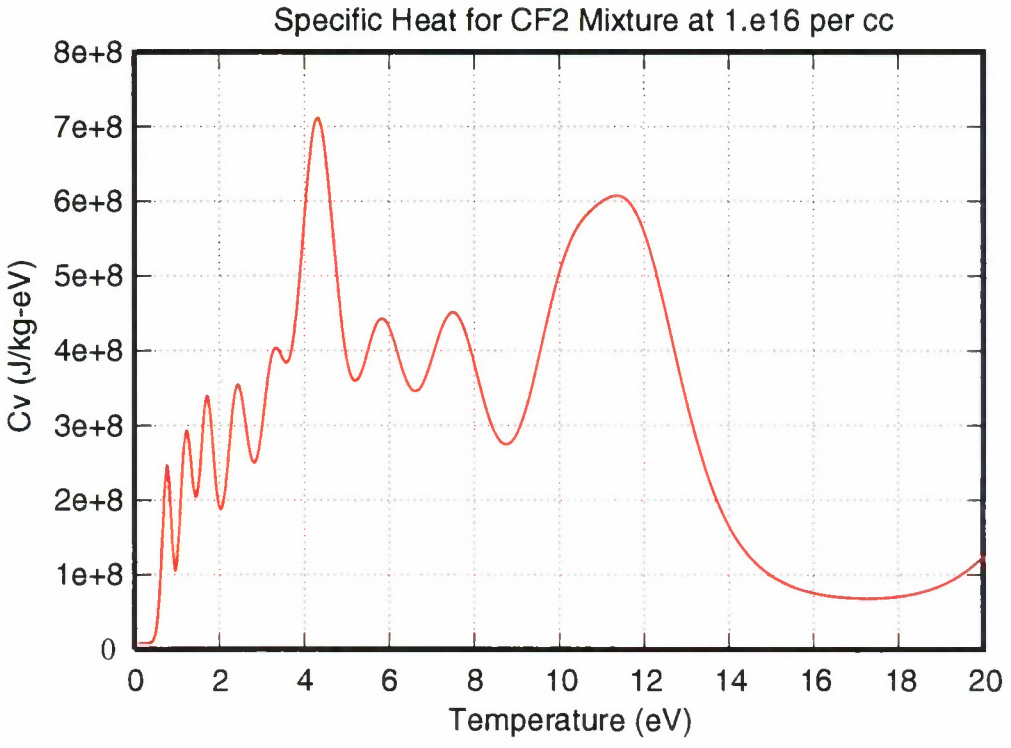

Figure 5-5. Specific heat for CF_2 mixture at 1.e16 per cc.

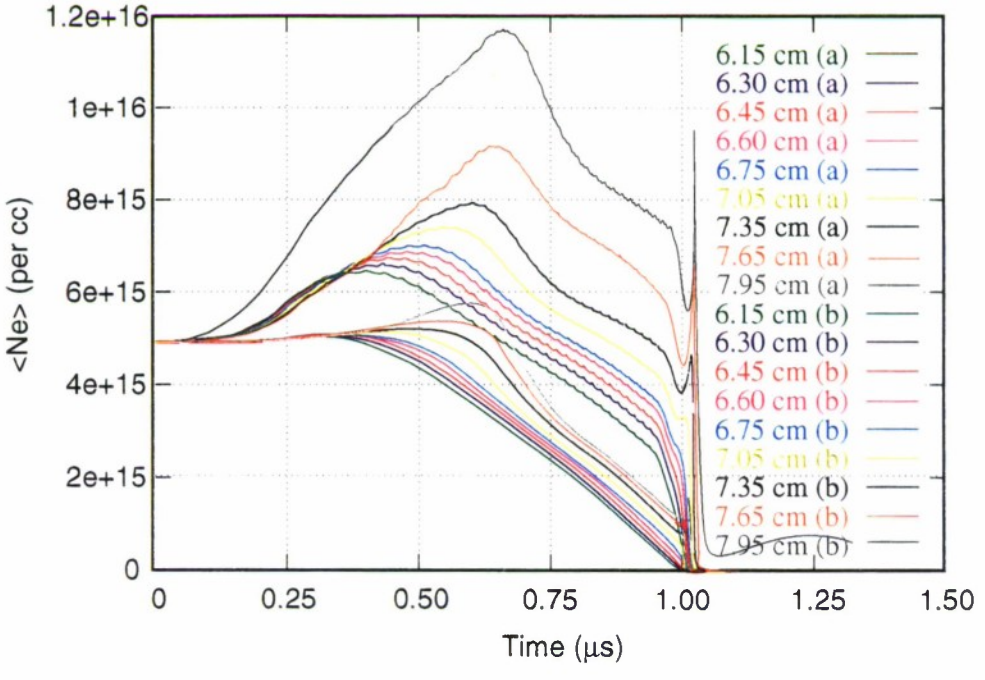

Figure 5-6. Mach2 simulated electron densities for Saha and constant (Zeff = 1) ionization models.

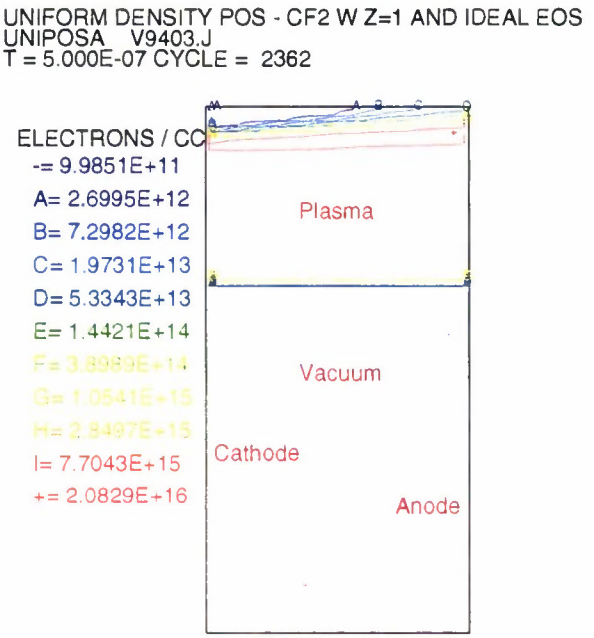

(a) Electron density contours - constant ionization model

Figure 5-7. Mach2 simulation for CF_2 at t = 0.5 μs.

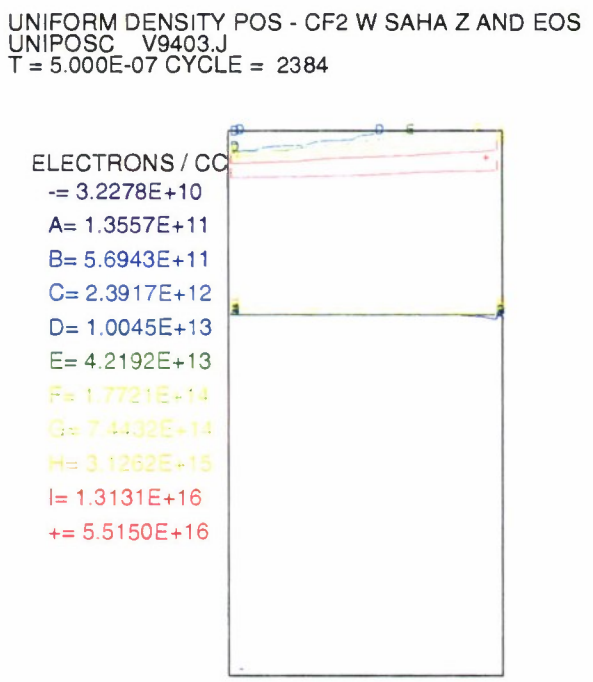

(b) Electron density contours - Saha model

Figure 5-7. Mach2 simulation for CF_2 at t = 0.5 μs (Continued).

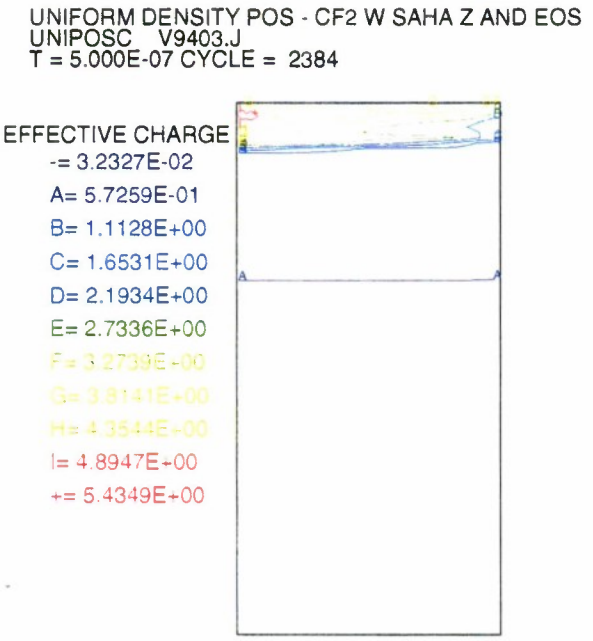

(c) Ionization level contours - Saha model

Figure 5-7. Mach2 simulation for CF_2 at t = 0.5 μs (Continued).

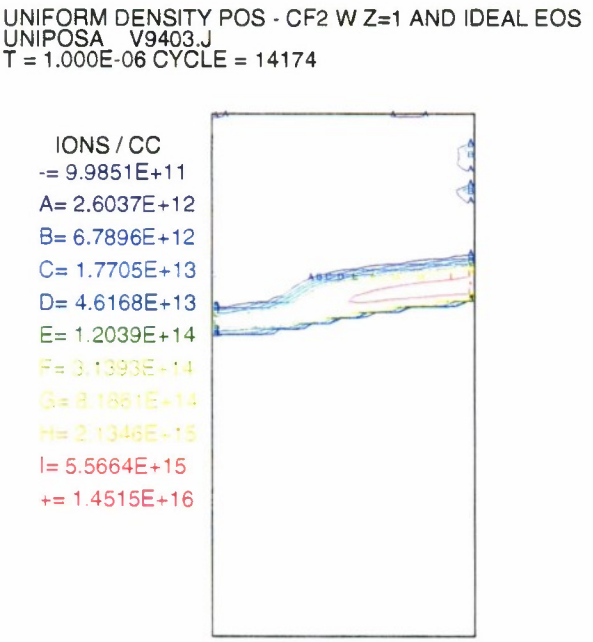

(a) Ion density contours - constant ionization model

Figure 5-8. Mach2 simulations for CF_2 at t = 1.0 μs.

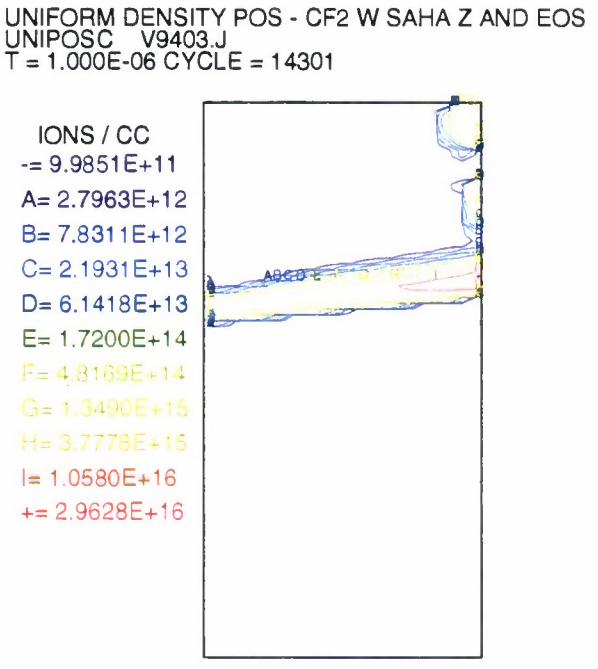

(b) Ion density contours - Saha model

Figure 5-8. Mach2 simulations for CF_2 at t = 1.0 μs (Continued).

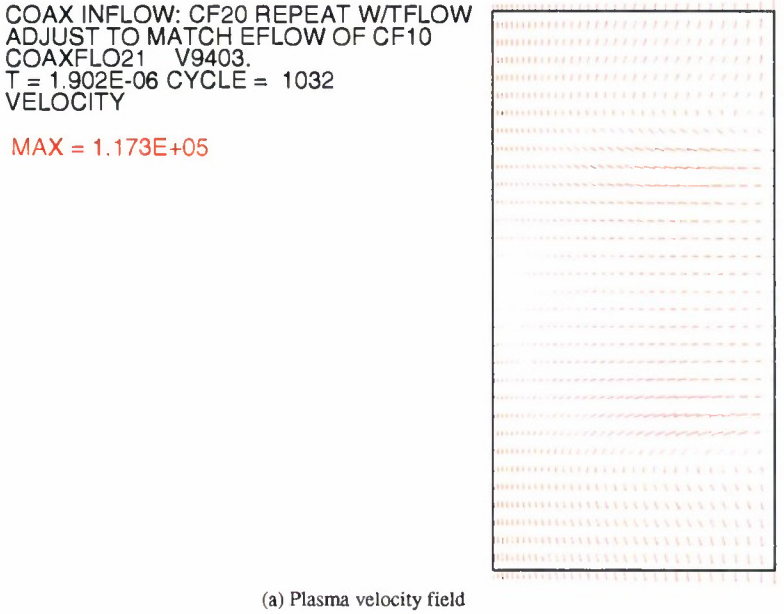

(a) Plasma velocity field

Figure 5-9. Mach2 simulation of inflowing flashboard plasma at t = 1.9 μs using the Saha ionization model.

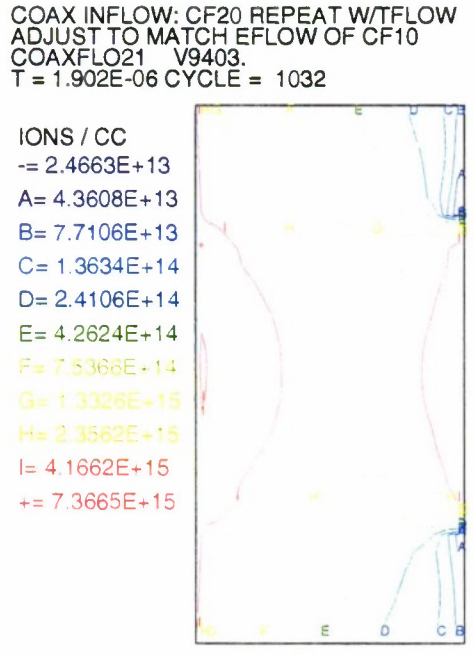

(b) Ion density contours

Figure 5-9. Mach2 simulation of inflowing flashboard plasma at t = 1.9 μs using the Saha ionization model (Continued).

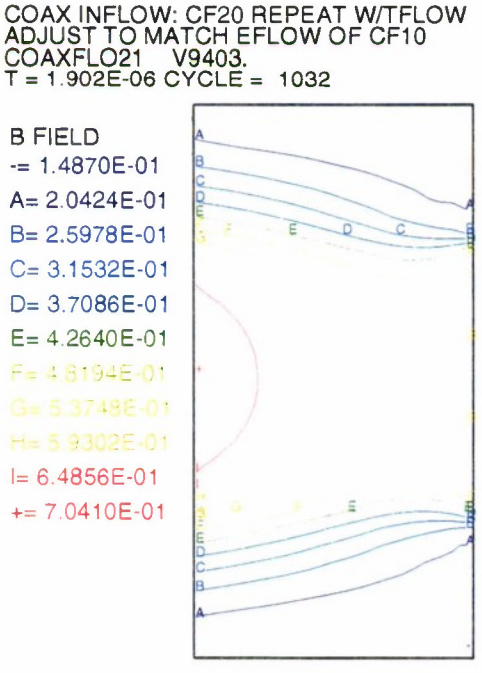

(c) Magnetic field contours

Figure 5-9. Mach2 simulation of inflowing flashboard plasma at t = 1.9 μs using the Saha ionization model (Continued).

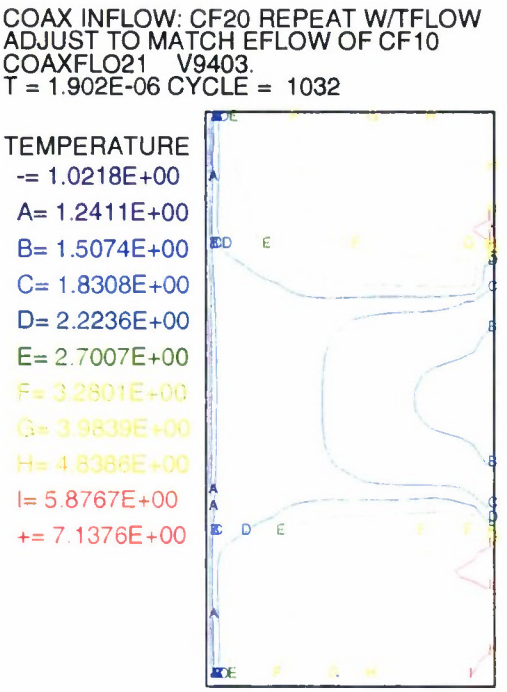

(d) Plasma temperature contours

Figure 5-9. Mach2 simulation of inflowing flashboard plasma at t = 1.9 μs using the Saha ionization model (Continued).

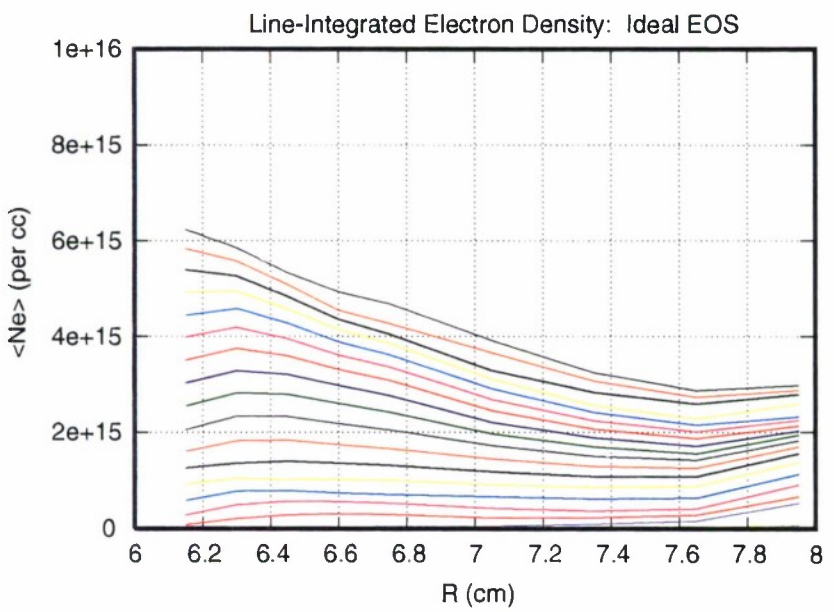

(a) Line-integrated electron density

Figure 5-10. Mach2 simulation showing the time dependence of the injected flashboard plasma radial profile for ideal EOS.

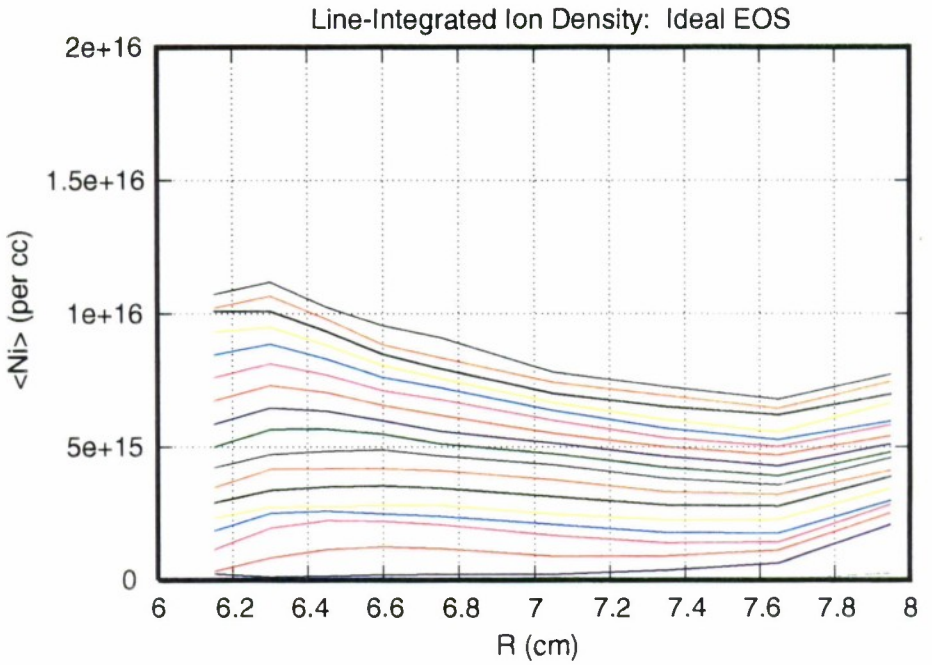

(b) Line-integrated ion density

Figure 5-10. Mach2 simulation showing the time dependence of the injected flashboard plasma radial profile for ideal EOS (Continued).

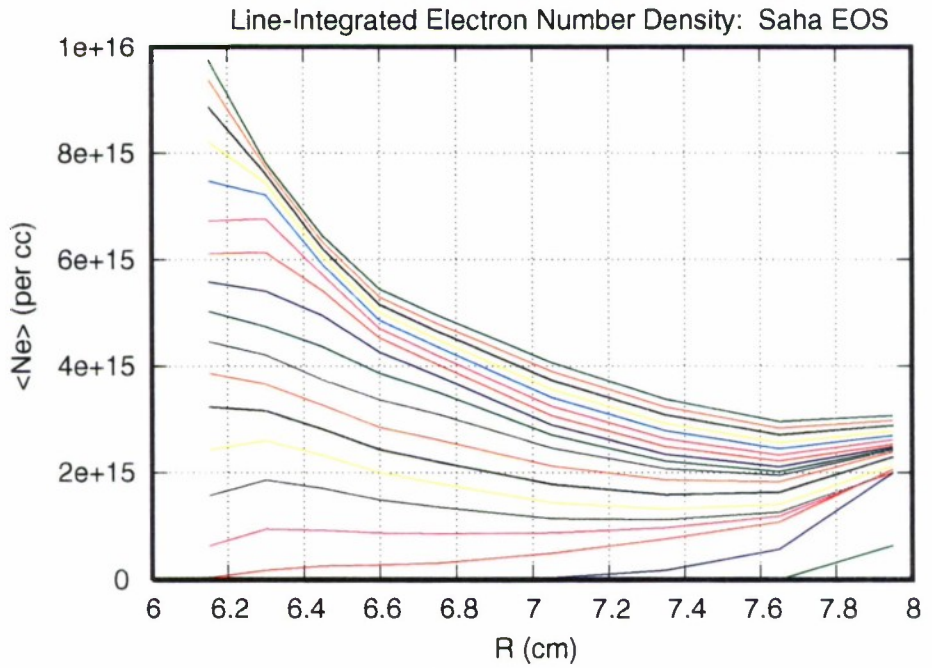

(a) Line-integrated electron density

Figure 5-11. Mach2 simulation showing the time dependence of the injected flashboard plasma radial profile for Saha EOS.

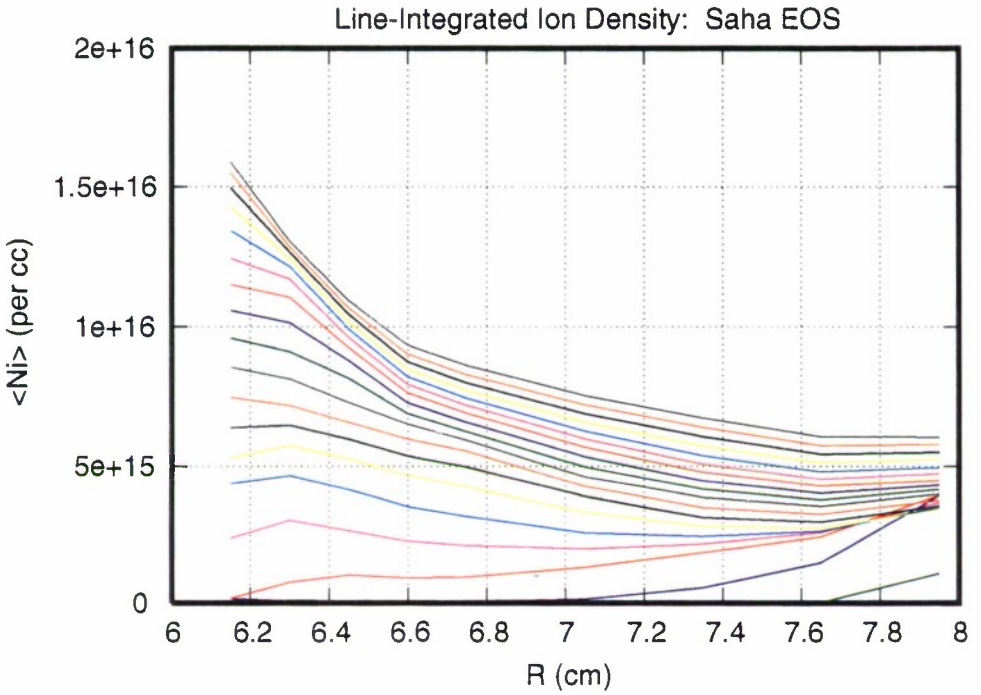

(b) Line-integrated ion density

Figure 5-11. Mach2 simulation showing the time dependence of the injected flashboard plasma radial profile for Saha EOS (Continued).

SECTION 6

TEST OF ALGORITHMS FOR THE HALL EFFECT

Theoretical investigations and, to a lesser degree, at least until recently, computational investigations, have indicated that the Hall effect can have a significant effect on the propagation of magnetic field into the switch plasma during the conduction phase. Mach2 has provisions for including the Hall effect on magnetic field evolution, but this provision has not been exercised to the extent more standard options in the code, such as resistive diffusion, have been. Recent efforts to include the Hall effect in conduction phase Mach2 simulations met with dismal failure. Efforts to determine the cause of failure and to rectify the situation have lead to a new algorithm for calculation the effect of the Hall field.

Mach2 makes use of a method called fractional timestep splitting to update all the physical variables being calculated. This method is quite simple, and has the very positive feature of admitting an open architecture with respect to the numerical algorithms used for the time-advance. The basic notion of fractional timestep splitting is if there is a physical quantity which evolves in response to a number of different effects, then numerically each of these effects may be treated separately and their contributions to the evolution of the quantity of interest summed to obtain the overall change to the quantity. As a particular example of this method, consider the magnetic field. From Faraday's Law, the magnetic field evolves according to the curl of the electric field:

$$dB/dt = - \text{curl}(E) \tag{6.1}$$

Ohm's Law relates the electric field to the magnetic field and the current density by:

$$E = \eta J - u \times B + (1/ene)\, J \times B \tag{6.2}$$

Putting this into Faraday's Law then gives an equation for the magnetic field evolution which is a prime candidate for treatment under the fractional timesplitting method:

$$dB/dt = -\text{curl}(\eta j) + \text{curl}(u \times B) - \text{curl}\left[(1/en_e) J \times B\right] \tag{6.3}$$

Symbolically, the fractional timestep splitting approach is

$$B_{new}(1) = B_{old} + dt\ \{\text{curl}(nJ)\}$$

$$B_{new}(2) = B_{new}(1) + dt\ \{-\text{curl}(u \times B)\}$$

$$B_{new}(3) = B_{new}(2) + dt\ \{\text{curl}[(1/en_e)J \times B]\} \tag{6.4}$$

The inductive ($u \times B$) portion of Faraday's Law is treated within the implicit hydrodynamics portion of Mach2. The resistive portion is solved with an implicit multigrid algorithm. The Hall contribution had been treated with a simple explicit treatment with subcycling provisions. Both the inductive and resistive algorithms have been exercised extensively – they are very well-known quantities whose numerical behavior has been tested against theory and experiment time and time again. The Hall treatment, however, has never received much attention.

The traditional lore surrounding Mach2's numerical treatment of the Hall effect is that the algorithm is unstable. For this reason, it has been supplied with an upstream averaging technique which is thought to provide stability. Because of the manner in which this upstream averager is used, the Hall effect is completely turned-off if the user chooses the incorrect polarity. When we attempted

to use the current Hall algorithm, we chose the incorrect polarity – the Hall electric field remained zero at all times and locations. Having recognized that the upstream averager was at fault, we removed it from the algorithm. This allowed the Hall electric field to be nonzero, but it also provided positive evidence of the legendary instability of the Hall effect algorithm. The magnetic field went wildly unstable, with the current density exhibiting the characteristic patterns of the checkerboard mode. Within a few hundred timesteps, the magnetic field had grown to unarguably nonphysical levels. The simplest fix would have been to restore the upstream averager and change the polarity of current in the problem. We chose, however, to attempt to determine the cause of the instability and to devise a stable algorithm.

Our first step in the process was to inspect the finite difference algorithm, looking for features which might excite the observed checkerboard instability. Some features of that nature were found, but the more interesting finding was made in comparing the finite difference algorithm used for the Hall effect with that used for the resistive diffusion part of the magnetic field advance. It turned out that they were identical. This was puzzling because the resistive diffusion solver had not exhibited the unstable behavior which the Hall effect solver had. A series of careful test problems were run to check and double check these observations.

Given that the spatial portion of the algorithms used for the Hall effect and the resistive diffusion solver were identical, we examined the finite difference technique used for the temporal portion of the algorithms. Here the two algorithms differed significantly. The Hall effect algorithm used a simple, explicit technique with a subcycling option. The subcycler merely allows the algorithm to compare the global timestep with the timescale associated with the Hall effect, and to use a timestep smaller than the global timestep. In contrast, the resistive diffusion algorithm used for its temporal portion an implicit multigrid technique. The multigrid technique is a convergence accelerator in which an iterative method of solution is applied to the given numerical grid and to a series of grids each of which is coarser than the original. For example, if the initial grid is 16×32 in terms of numbers of cells in each coordinate direction, then the coarser grids are 8×16, 4×8, 2×4, and 1×2. The errors for a given number of iterative steps on a given grid level are collected and used to form the source terms for application of the iterative scheme on the next coarser grid.

Since the only difference between the resistive diffusion and Hall effect algorithms was the manner in which the time-advance was treated, we were strongly tempted to apply the implicit multigrid technique to the Hall effect. While this seems a daunting task, it is truly quite simple by virtue that the spatial part of the algorithms was identical. This allowed the Hall electric field to be brought into the implicit multigrid algorithm merely by augmenting every appearance of the resistive electric field with the Hall electric field. Our implementation of the Hall effect in the existing implicit multigrid solver included a logical structure so that the user can select whether or not to enable the resistive effects as well as the Hall effect. Thus, the previous Hall effect algorithm was removed, and the existing resistive diffusion implicit multigrid algorithm was extended to include the Hall effect. The logical structure was altered so that by invoking the implicit multigrid algorithm, the user could select to include either the resistive electric field, the Hall electric field, or both.

The effort was only partially successful. It overcame the numerical instability which had previously prevented the code from executing as desired. On the other hand, the algorithm led to large negative fields in problems where no negative field at all should have occurred. Consequently we are abandoning the use of the implicit multigrid technique and in the future will seek an algorithm based on upwind differencing schemes.

SECTION 7

THE DELTA MHD RAD CODE AND ITS APPLICATION TO TANDEM PUFF EXPERIMENTS

During fiscal year 95 S-Cubed made two improvements in the DELTA code which substantially advanced its analysis capability in the area of coupled magnetohydrodynamic and radiation phenomena. The first improvement was the development of a capability to solve problems in r-z geometry, in addition to the extant capability in x-y geometry. The second improvement was achieved by wedding the CREMIT code with the two-dimensional DELTA MHD code. CREMIT is a stand alone code for calculating the non-equilibrium atomic level kinetics of a hot, optically thin radiating system. First developed in the 1970's to study the behavior of z-pinches, its content is described in several reports from that period.[3,4] The DELTA code is supported by S-Cubed MESH, an automatic mesh generator which spans the problem space of interest with a triangular array of mesh elements. The marriage of CREMIT, DELTA and S-Cubed MESH provides a formidable tool for the analysis of problems of interest to the pulsed power community.

Below we will summarize the method for extending the DELTA code to r-z geometry. Then we will give a brief description of the physics contained in CREMIT and the improvements that were added to this code and to DELTA during the period of resurrection. Following this we will describe the application of the code to the analysis of tandem puff experiments performed at Maxwell Laboratories during the past year.

7.1 R-Z GEOMETRY CAPABILITY.

The extension of DELTA to r-z geometry is desirable because geometrical modeling capabilities of DELTA are more powerful that those of Mach2. This power arises from the triangular grid on which the conservation equations are formulated and from the automatic mesh generator coupled to the code. The extension is non-trivial however and required an approach differing significantly from the standard finite volume approach used throughout DELTA to solve the fluid equations. The finite volume approach apparently leads to a nonsymmetric system of equations when applied to the solution of the r-z convective-diffusion equation for the magnetic field. This system of equations is not amenable to solution with Incomplete Cholesky Conjugate Gradient (ICCG) and Scaled-Conjugate Gradient (SCCG) algorithms presently available in the DELTA code. One possibility would be to implement a non-symmetric solver in DELTA. An alternative approach , which we follow here, is to employ a mixed finite- element finite-volume (FE-FV) technique. In our version of this approach the diffusion terms in the equation are treated implicitly with a Galerkin finite element methodology while the convective terms are treated explicitly using FRAM finite volume differencing. The system of equations resulting from implicit time integration in the Galerkin technique with linear trial and test space functions leads to a positive-definite symmetric matrix equation which can be solved using the existing ICCG or SCCG algorithms within DELTA.

We have implemented the magnetic field convection-diffusion equation in cylindrical coordinates with the mixed FE-FV technique. (An r-z capability for the non-MHD fluid equations already exists in DELTA so that this is the only extension needed to obtain full r-z MHD capability.) We have successfully tested the coding. In Sections 7.3 we analyze the tandem puff experiments recently conducted at ACE 4.

7.2 RADIATION MODEL.

CREMIT[3,4] is a multi-ion collisional-radiative model of atomic state populations in a hot, optically thin, radiating plasma. The code is applicable to light elements($Z \leq 40$). In each ion the electronic states are configuration based, that is they are described by giving the occupation numbers of the

one-electron states described by a principal quantum number n and an orbital quantum number l. The configurations counted for any given ion are the ground configuration and all excited configurations obtained by single excitation of the most loosely bound electron in the ground configuration, up to a maximum principal quantum number that is controlled by the user.

Energy levels are calculated using the large nuclear charge limit of screened hydrogenic wave functions developed by Layzer[5] and by Naqvi and Victor[6]. Einstein spontaneous emission coefficients are obtained using the Coulomb approximation. The results of this approximation, developed in the works of Bates and Damgaard[7] for bound -bound transitions and Burgess and Seaton[8] for bound-free transitions, have been conveniently summarized by Griem[9] and extended by Parks, et al.[10]

Cross sections for electronic ionization, recombination, excitation and deexcitation are obtained in the Bethe approximation.[11] This approximation gives nonvanishing results only for optically allowed electric dipole transitions, so that the Bates-Damgaard and Burgess-Seaton tables can be used for their evaluation. Dielectronic recombination is accounted for in the original CREMIT model but has not been implemented in the resurrection.

The population rate equations in CREMIT are solved according to assumptions introduced by Bates, Kingston, and McWhirter.[12] This assumption is that within any ion the excited state populations relax instantaneously to values determined by instantaneous values of ground state populations, electron density and electron temperature. This approximation leads to a set of rate equations involving the ground states alone, but with effective ionization and recombination coefficients which depend on excited state collision and emission properties.

The ground state population rate equations for an ion population density Nk(1) can be written in the form

$$\frac{dN_k(1)}{dt} = S_{k-1}N_{k-1} - (S_k + \alpha_{k-1})N_k + \alpha_k N_{k+1} \tag{7.1}$$

where S_k is the effective ionization rate coefficient for ionization from in charge state k to charge state k+1 and α_k is the rate of recombination on an ion in charge state k+1 to produce an ion in charge state k. This result is obtained by summing equation 6 of reference 3 over all levels p of the ion stage k subject to the constraint of equation 5 for the excited states, which are represented by state index values p >1.) Using the notation of that reference 3 the effective recombination rate coefficient is given by:

$$K_k(c,p)\,\alpha_k = N_e \sum_{p>1} (K_k(c,p)(1-r_0^k(p)) + \beta_k(p)) \quad , \tag{7.2}$$

and the effective ionization coefficient by:

$$S_k = N_e \sum_{p>1} \frac{N_k^*(p)}{N_k^*(1)} r_1^k(p) K_k(p,c) \quad . \tag{7.3}$$

Here $K_k(p,c)$ is the collisional ionization rate coefficient from level p in the ion k to the continuum and $K_k(c,p)$ the inverse three body recombination rate coefficient. The quantity $\beta_k(p)$ is the rate coefficient for radiative recombination to the level p in the ion species k. The quantity $N_k^*(p)$ is defined to be the equilibrium value of the level population corresponding to the electron temperature θ, electron density N_e, and the ground state density $N_{k+1}(1)$ in the species k;

$$N_k^*(p) = N_{k+1}(1)\frac{w_k(p)}{w_{k+1}(1)}\frac{\exp(I_k(p)/\vartheta)}{\Gamma} \tag{7.4}$$

The electron degeneracy factor Γ is given by:

$$\Gamma = 2(2\pi\, m\vartheta\, /h^2)^{3/2}. \tag{7.5}$$

where m is the electron mass and h is Planck's constant.

The quantities r_0^k and r_1^k are obtained as solutions of matrix equations as described in Harvey, et al.[3] They depend on the temperature and density of electrons, and on the collisional and radiative cross sections of the electron-ion system. From the r_0^k and r_1^k the level populations and radiative emission rates can be expressed in terms of the ground state populations obtained from the solution of the rate equations. For example,

$$\begin{aligned} N_k(p) &= N_k^*(p)r_0^k(p) + \frac{N_k^*(p)}{N_k^*(1)}r_1^k(p)N_k(1) \\ &= \frac{w_k(p)}{w_{k+1}(p)}\exp(\frac{I_k(p)}{\vartheta})\Gamma^{-1}r_0^k(p)N_{k+1}(1) + \frac{N_k^*(p)}{N_k^*(1)}r_1^k(p)N_k(1) \end{aligned} \tag{7.6}$$

Equations (7.1) can be solved in either the fully time dependent mode where the time derivatives are retained, or in the quasi-steady mode where the derivatives are set to zero. The latter is justified when ground state populations adjust rapidly to changes of temperature and density induced by hydrodynamic motions or by heating and cooling; this case presents no particular difficulties. However, in the former case we must recognize that it is the total number of ions that is conserved in a given mass, not the total number of ground state ions. The excited state contribution may be negligible in some cases but, in general, it is not. Thus instead of making the approximation that excited state populations are negligible, we have solved the rate equations in a least squares sense subject to the constraint that the total ion density

$$N = \sum_{k,p} N_k(p) \tag{7.7}$$

is prescribed.

7.3 ANALYSIS OF TANDEM PUFF EXPERIMENTS.

7.3.1 Tandem Puff Experimental Configurations.

Figures 7-1 and 7-2 illustrate the tandem puff geometry and ACE 4 vacuum chamber. The geometric details common to all PRS loads investigated are:

1. a 17.8 cm. diameter cathode
2. an array of 16 anode rods whose centerlines are located 13 cm. from the axis of symmetry
3. a 20 cm Teflon plasma conduction region
4. an 11 cm annular gas nozzle 17.8 cm. above the cathode
5. cm from load end of conduction plasma to top of cathode

6. a 9.5 degree nozzle tilt
7. fixed B-dot probes at three positions along the anode rods.

7.3.2 Calculations with Ideal Gas Model.

The calculations in this section were performed with an ideal gas equation of state. The primary purpose of these preliminary studies is to calculate the time of arrival of signals at the various $\dot{B}$-probes and the time of pinching at various positions on the symmetry axis. These calculated quantities can be compared with experimental results and used later to initialize more complex calculations containing radiation models for describing neon and argon implosions.

The calculations used a prescribed current waveform measured on ACE 4 shot 1102, Figure 7-3, and a POS density profile measured on ACE 4 shot 1082, Figure 7-4. In all calculations the anode rods extended 7 cm in the axial direction beyond the termination of the cathode. The initial plenum pressure and temperature were 200 psi and 300 degrees Kelvin.

The two-dimensional computational space containing approximately 30,000 DELTA code triangular fluid elements is shown in Figure 7-5. The region between the anode rods and the flashboards was zoned as part of the calculation and contained a uniform initial density equal to that measured at the radial location nearest the anode rods. Electrically, however, the region occupied by the anode rods is a region of high conductivity (see below). Conducting surfaces also defined the radial and axial boundaries of the computational space, except for the axial boundary at z = -45 cm, where the magnetic field (current) was prescribed.

The DELTA runs on this tandem puff configuration employed a bilevel resistivity model. To simulate vacuum the resistivity is assumed to be 2×10^{-8} sec (esu) for ion densities less than 10^{15} cm^{-3}, permitting rapid diffusion for the magnetic field. For densities above the threshold value and in the annular region containing the anode rods the resistivity is set to a low value, $\eta = 2\times10^{-18}$ sec so that the plasma emulates a perfect conductor. Lower values of the density floor were attempted; these values led to inconveniently small time steps and appeared not to affect the results. In the first set of calculations given below the plasma is treated as a fully ionized gamma-law gas with two electrons per ion. The purpose of these preliminary calculations is to calculate the time of arrival of current at the B-dot probes, and to estimate the time at which maximum on-axis density and temperature occur at various axial locations. The comparison of the timing of B-dot probes with experimental values then permits us to adjust the densities, which are not measured, to achieve agreement with experiment. The timing of the onset of high temperature and density at various axial locations defines the axial propagation speed of the pinch, that is, the zippering speed. Later calculations, in section 7.4 will invoke a more realistic model of the pinch which includes a non-LTE model of ionization, excitation and radiation.

Figure 7-6 is representative of the evolution of density for a neon puff gas and POS fill. The current is initiated at the lower axial boundary of the computational space 300 μs after the opening of the puff valve. The conduction time to the end of the cathode is about 2 μs and the pinch occurs on axis near the cathode about one microsecond later. However, the timing characteristics calculated for this run do not agree with those observed. Table 7-1 gives typical timing data from the three B-dot probes and Table 7-2 gives zippering data from a one-dimensional imaged array of XRD x-ray sensors.

Table 7-1. Times of arrival at B-dot probes (nanoseconds measured from start of current) and of start of x-rays.

Shot Number	IBFBD	IBNED	IBPD	Start of X-rays
1098	1250	1451	1621	2004
1099	1226	1375	1583	1981
1100	1238	1381	1583	1995
1102	1214	1351	1595	1976

Table 7-2. Time at 10% of peak x-ray signal and FWHM of pulse (ns).

	Sensor	1	2	3	4	5	6
cm above cathode		0.96	1.75	2.54	3.33	4.12	4.91
z		-16.82	-16.03	-15.24	-14.45	-13.66	-12.87
Shot No.							
1100	Time	14	6	0	6	20	36
	FWHM	22	19	22	24	47	49
1102	Time	16	9	0	3	15	24
	FWHM	21	18	24	19	31	74

Figure 7-7 compares B-dot probe data for two runs, labeled 7a and 7b. Run 7b differs from 7a by the reduction in delay time between puff valve opening and generator firing from 300 to 225 μs. The arrival times of the current pulse at the probes exceed measured times by a few hundred microseconds. This disparity between calculation and measurement is removed in run 7c, Figure 7-8, by reducing the POS density by half. The arrival times reflected in the onset of magnetic field at the three probe locations is also apparent in the jumps in fluid density and temperature indicated in Figure 7-9.

The arrival times of the pinch at various axial locations is apparent in the temperatures and density data presented in Figure 1-10. The timing results of theory agree with those of experiment in many but not all respects;

1. The probe at 2.54 cm (probe 3) comes on first in theory and experiment.
2. Apart from the apparent simultaneity of onset of two pairs of computational indicators, the ordering in which theory and measurement probes come on is the same.
3. The time difference between probe 3 (the first to light up) and probe 1 (nearest the cathode) is 10 μs computationally, 15 μs experimentally.
4. The time difference between probe 3 and probe 6 (farthest from the cathode) is 20 ns computationally, 33 μs experimentally.

Despite the differences between theory and experiment, the extent of the agreement is rather remarkable. We cannot state however, that the differences are insignificant, or what adjustments in physics or computational technique are required to remove them.

The rise time of temperature or density in Figure 7-10 amounts to approximately 20 ns, comparable to the FWHM's observed at the four probes nearest the cathode. However, a valid comparison should be based on calculations of the radiation pulse itself, not on time profiles of temperature calculated for the g - low gas assumed here. The results with a collisional radiative model of the plasma appear in Section 7.4.

The geometry for the next set of calculations, run set 12, differ from the previous ones by including an annular baffle as indicated in Figure 7-11. This figure shows the internal energy per unit volume at a puff valve delay time of 300 μs, the instant when current begins to flow. Figure 7-12 displays the same quantity at 302.6 μs, the instant when on-axis temperatures begin to increase sharply.

The primary purpose of runset 12 was to assess the effect of the baffle on zippering in an experimental configuration proposed to block off some of the gas flow that drifts onto the cathode. As Figure 7-13 shows, the baffle indeed affected the zippering, but not in a manner that could be considered an improvement over the results obtained without the baffle.

Perhaps the particle trajectory plots of Figure 7-14 display the most interesting results from run 12. The question has been raised as to whether or not the single fluid MHD simulations of the tandem puff actually implode puff gas on-axis or if they just push the gas out of the way and implode the POS plasma on-axis instead. To attempt to answer this question Lagrangian marker particles were created along a 15 cm axial length (starting on-axis at the cathode) at 4 different radii extending out to r=7 cm. The particles were created at 302 μs (the time that the POS plasma snowplow just starts to round the cathode corner). We claim this is sufficient to insure the particles are initially created at points which still lie within the puff gas. The particles were then followed until the end of the calculation (a few implosion bounce times). The positions of all the particles were plotted as dots (once each 5 ns) forming a composite time integrated plot. The resulting picture allows one to see where an individual particle starting out in the puff gas winds up. Use of this new diagnostic in the calculations has dramatically demonstrated that the MHD simulations indeed implode the puff gas. In general, particles within an initial 7 cm radius of the axis are seen to implode (bounce) if they are initially within approximately 5 cm (axially) of the cathode. Particles further than this also move inward but they tend to 'toothpaste' away from the cathode, exhibiting a laminar axial flow type of motion rather than imploding (bouncing on-axis).

7.3.3 Analysis of Tandem Puff Neon and Argon Implosions.

The objective of the following calculations is the determination of the radiative properties of pinched neon and argon plasmas in a realistic mock-up of the tandem puff configuration. Comparison of the results with measurements will give valuable insights into what processes are affecting the experimental results.

The sequence of runs included the full CREMIT radiation package described in Section 7.2. The geometry is the same as for Figure 7-11. The calculations are performed for a single fluid, so that the POS (flashboard) plasma is treated as neon (argon) if the puff gas is neon (argon). In addition, rather than the bilevel resistivity model, the resistivity was calculated self-consistently from the Spitzer model. For ion densities below 10^{15} cm^{-3}, however, the resistivity was set to the artificially high value of $h=2 \times 10^{-8}$ sec in order to simulate the instantaneous propogation of magnetic field through vacuum.

7.3.3.1 **Neon.** Figures 7-15 through 7-17 present results for neon with a delay of 225 μs between the initiation of gas flow and current. Figures 7-18 through 7-23 show similar quantities for the increased delay times, 275 and 300 μs. The quantities on the axes of ordinates include the mass per unit length contained within a radius of 9 cm. from the symmetry axis and the mean radial location of the mass. The plotted linear mass density includes not only the mass injected by the

puff valve but also the plasma mass injected by the flash boards when it enters the PRS region. The energy and kinetic energies labeled "puff" include all energy contained in the PRS region, namely the region bounded by the end of the cathode stalk (z=17.8 cm in Figure 7-5), the exit plane of the gas nozzle (z = 0), r = 0 and the cathode radius (r=9 cm). The energy plots labeled "all" include the contributions from the entire mass of flashboard plasma and puff gas. The total radiative energy is always calculated as if the plasma were optically thin, even at early times when the plasma temperature is low and the assumption of an optically thin plasma is a poor one; in this circumstance however the radiated energy is a small part of the overall and radiated energy budgets. The kinetic energy plots show the axial, radial and total kinetic energies. The axial components of kinetic energy are clearly a substantial fraction of the total kinetic energy. The on-axis radiative power includes radiation only from zones which border the axis of symmetry. The mass and volumes contained in these zones is not given, as our primary interest is the time at which these zones begin to radiate above 1 keV.

The quantities presented in Figure 7-17 describe the characteristics of the physical state of the imploded plasma on axis. Calculated temperatures are substantially lower than in previous figures because ionization, excitation and radiation have been included in the energy budget. The results for Z-bar show that neon spends up to 250 ns ionized to the K-shell at most axial locations.

The characteristics of the curve of X-ray yield for energies greater than 1 keV warrant some discussion. Two notable features are the foot rising to about 6 kJ between 1.6 and 2 μs, and the increasing yield above about 2.1 μs, features which appear not to be present in experimental results. The former is believed to be caused by radiation produced when the compressed POS plasma turns the corner at the end of the cathode stalk and interacts with the gas in the PRS volume. This interpretation is consistent with the jump in linear mass density and $\bar{r}$ just beyond 1.2 μs. The foot on the radiation pulse may be an artifact attributable to treating the POS plasma as neon in the one-fluid DELTA code. In fact the components of the POS plasma are carbon and fluorine, elements which do not radiate a line spectrum above 1 keV. The steadily increasing yield beyond 1.7 μs is believed caused by the heating of puff valve gas at distances from the cathode greater than about 6 or 7 cm, which define the field of view in the experiments. It is also possible that this continued compressional and joule heating does not in fact occur because current, rather than continuing to flow through the gas, is shorted in a region where the anode-cathode gap is narrow and does not contain a significant amount of radiating plasma. This speculation remains to be tested, but it is consistent with a computational approach used by Whitney, et al.[13] whereby the current driving the collapsing plasma is ignored following the development of a prescribed radial kinetic energy. Taking into account only the energy in the sharply rising part of the pulse, the energy radiated beyond 1 kV is about 20 kJ in about 200 ns, compared with measured values of 3 to 20 kJ and about 100 ns. In any case, substantial improvements are required in our understanding of the physics of the pinch and the physical content of the code before unambiguous comparisons with experiment can be made.

The discussion of the results for a 300 μs delay time, shown in Figures 7-21 through 7-23, closely mirror those for the 225 μs case. The steady rise of the yield ($\rangle$ 1 keV) is now more pronounced and the energy contained in the steeply rising part of the pulse at about 2 μs is now only about 10 kJ, compared with ~20 kJ for the 225 μs case. The reduced yield in this part of the pulse is attributed to the greater mass of neon participating in the implosion.

Figure 7-24 shows the spectral features of the radiation produced by the implosion for the 275 μs delay time. The quantities plotted contain the contributions from the early foot and the late time compression at axial distances greater than 6 cm from the cathode, as well as the contribution from the main pulse.

The results in Figures 7-25 and 7-26 are for a run containing neon only in the POS region, with no gas initially in the PRS region. This configuration resulted in little compression, little mass density on axis, and no significant radiation above 1 kV, indicating that in previous figures the gas injected by the puff valve is the principal source of radiation produced by the pinch.

7.3.3.2 Argon. The final set of calculations were for argon. Figures 7-27 and 7-28 show the results with a valve delay of 225 μs. The discussion for this case runs parallel to that for neon.

Again the prominent features in the curve for X-rays with photon energy greater than 1 kV are the early time foot, the main pulse and the late time slow, but steady, increase in the yield. The foot is now smaller in magnitude, presumably because of the greater energy required for argon than for neon to strip to the K-shell, where line photons with energies in excess of 1 kV can be radiated.

The next set of results, exhibited in Figures 7-29 through 7-31, were obtained to check the hypothesis that the late time radiation comes from the puff region beyond the field of view of the measurements. The volume over which energy is accumulated in the calculations now extends only 5 cm in the axial direction from the end of the cathode. The main pulse contains about 8 kJ in a pulse of about 100 ns, and does not exhibit the late time rise observed in previous runs. The calculated energy, about 8 kJ, far exceeds the less than 1 kJ of energy at greater than 1 keV observed in the experiments, further prompting the speculation that there is less current driving the pinch than that used in the calculations. Data from the B-dot probes suggest that this is indeed the case.

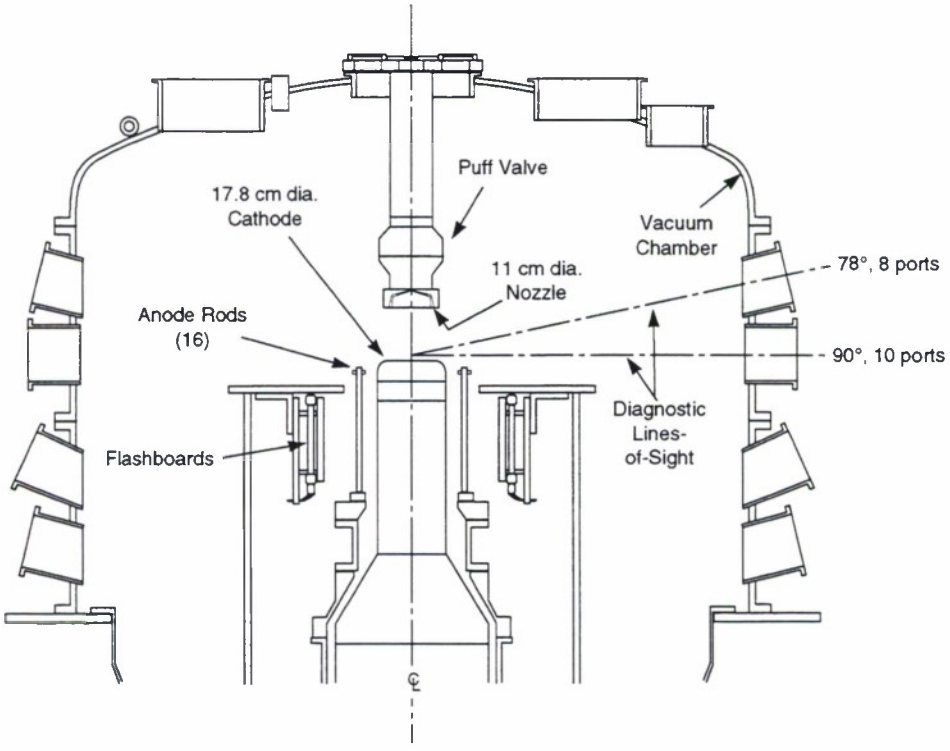

Figure 7-1. The ACE 4 vacuum chamber with tandem puff experimental arrangement.

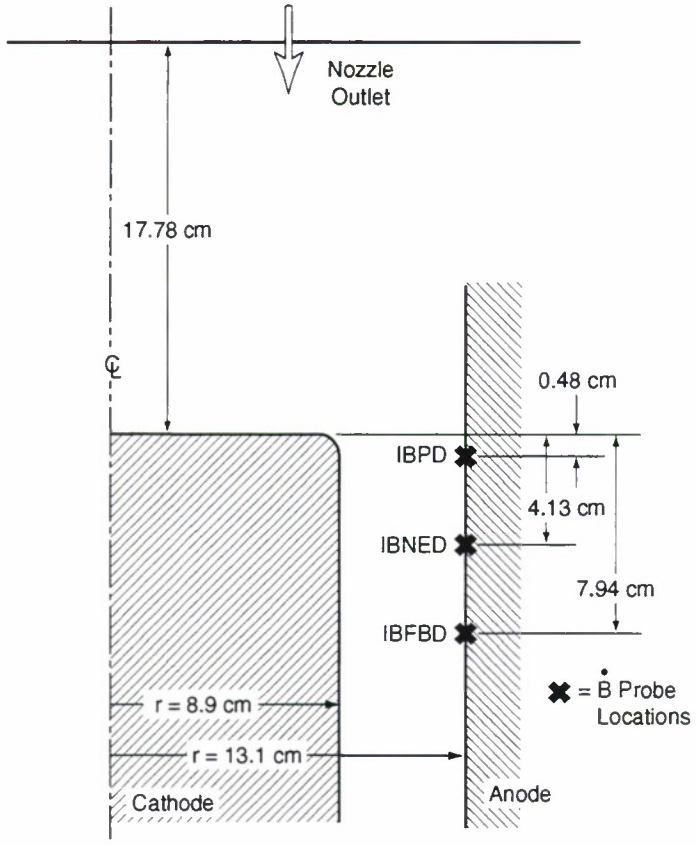

Figure 7-2. Schematic of PRS load region showing geometric details and location of $\dot{B}$-probes.

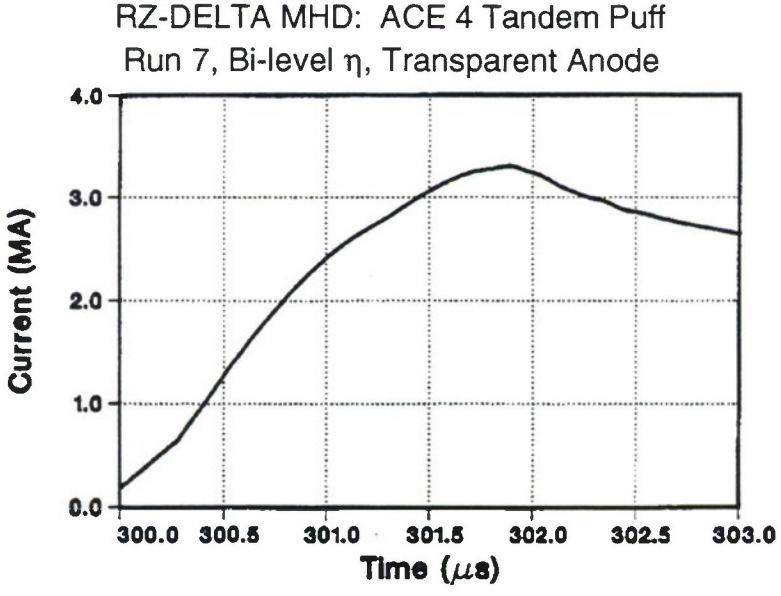

Figure 7-3. Current wave form used in the analysis (ACE 4 shot 1102). The absolute time is for a 300 μs delay time. The same waveform is used for all delay times.

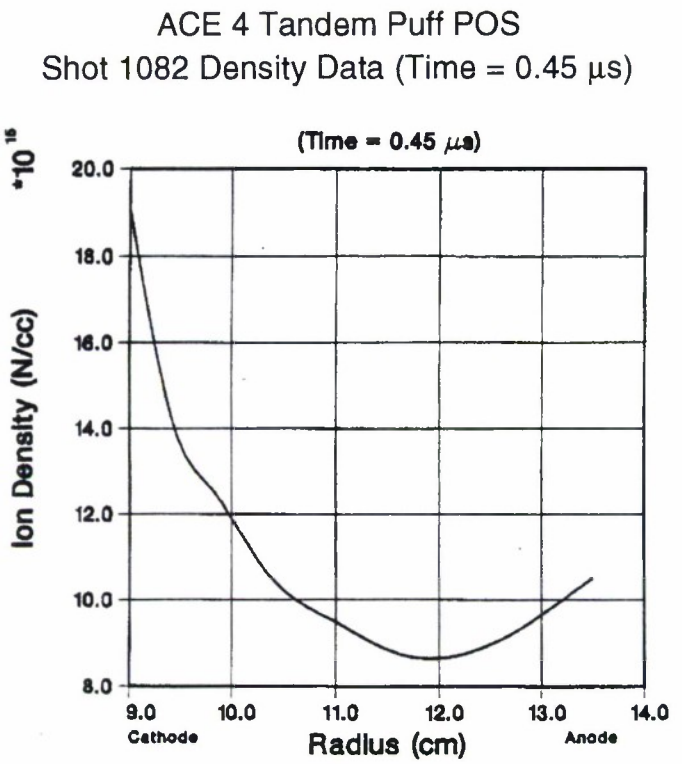

Figure 7-4. Density profile, ACE 4 shot 1082.

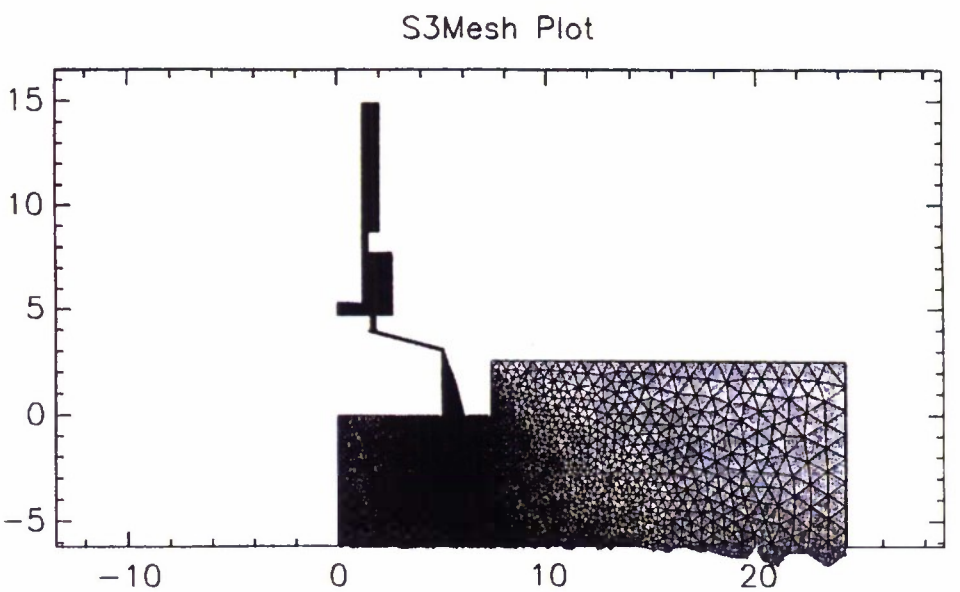

Figure 7-5. The 2-dimensional computational space includes the plenum, the PRS load region, and the POS plasma region. The entire mesh contains approximately 30,000 triangular cells.

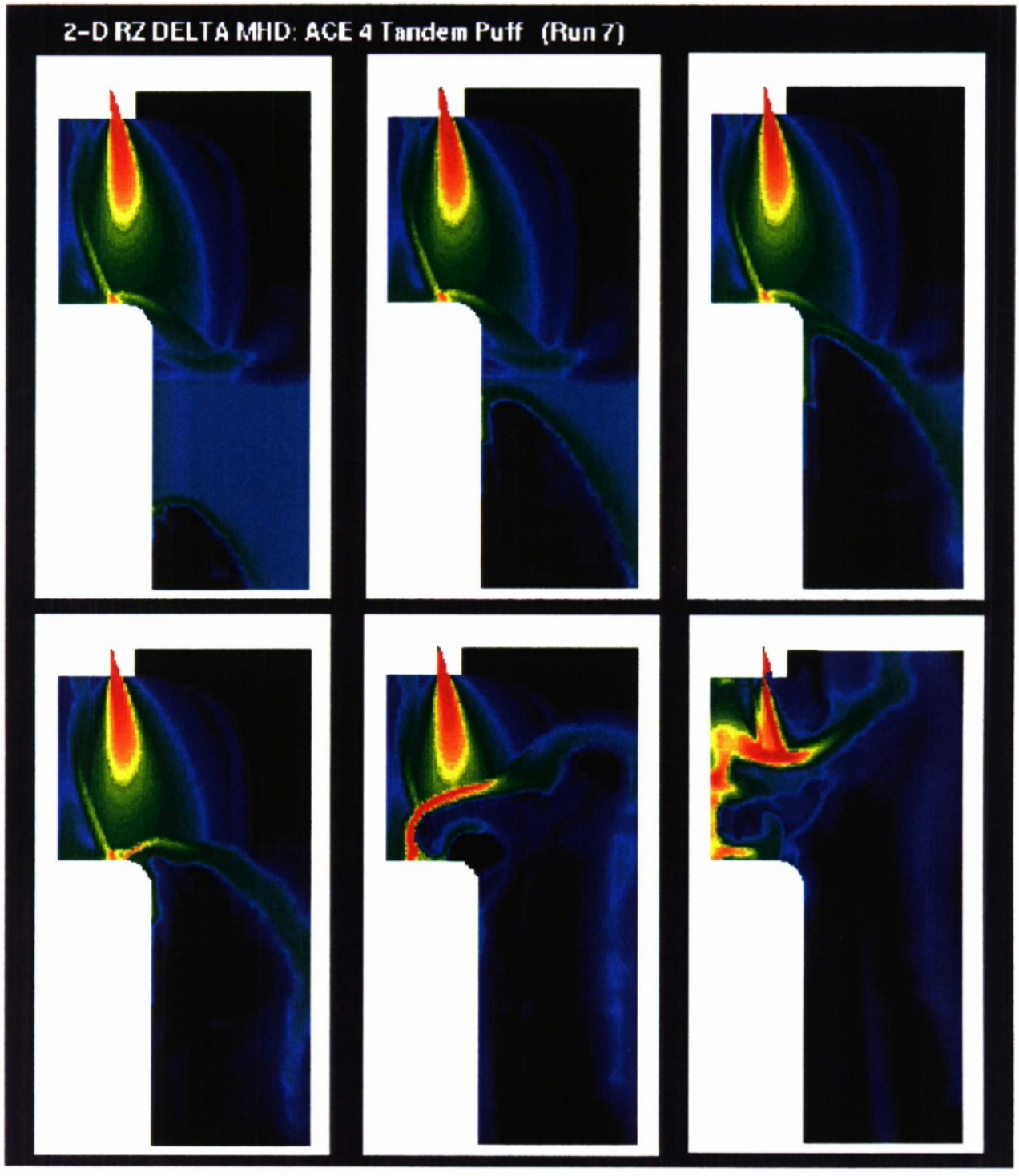

Figure 7-6. Evolution of density for a neon puff gas and POS fill.

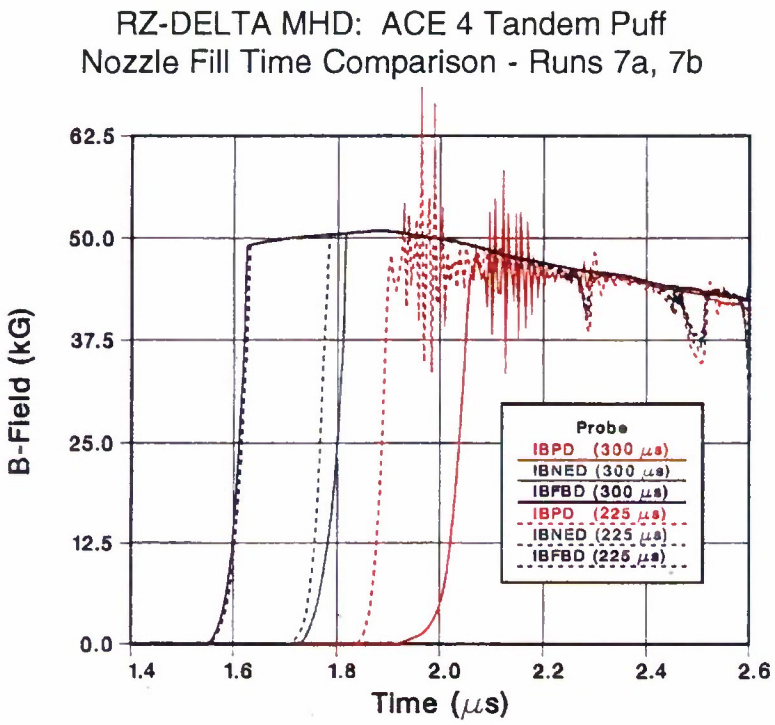

Figure 7-7 Calculated $\dot{B}$-probe timing data and their dependence on valve delay time.

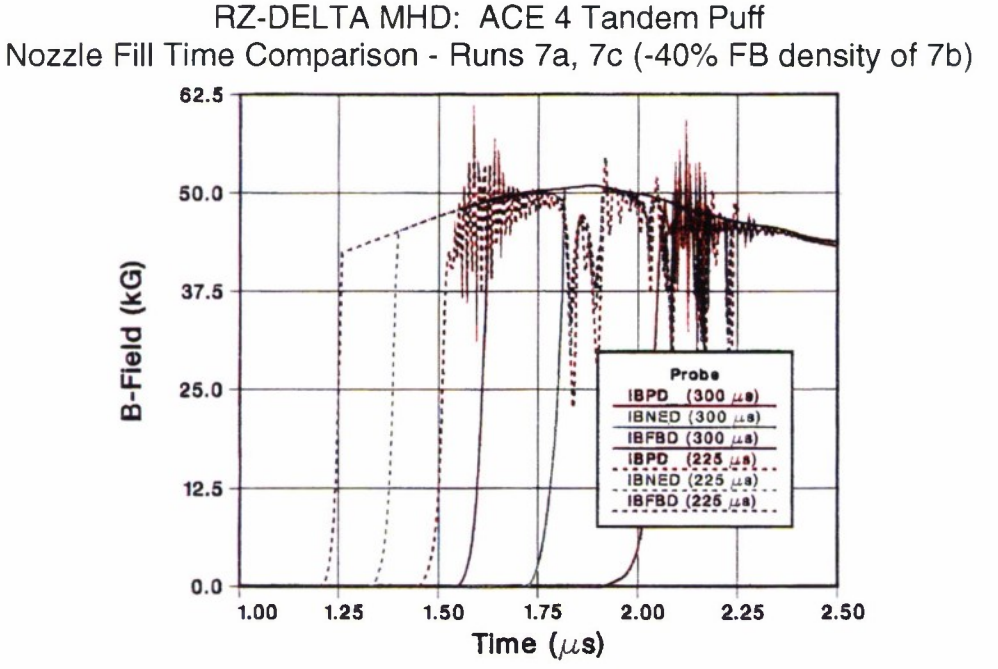

Figure 7-8. The POS density is scaled to yield observed timing indicated by $\dot{B}$-probes. The density is 0.58 times that in Figure 7-4. The zero time corresponds to the start of current flow from the generator.

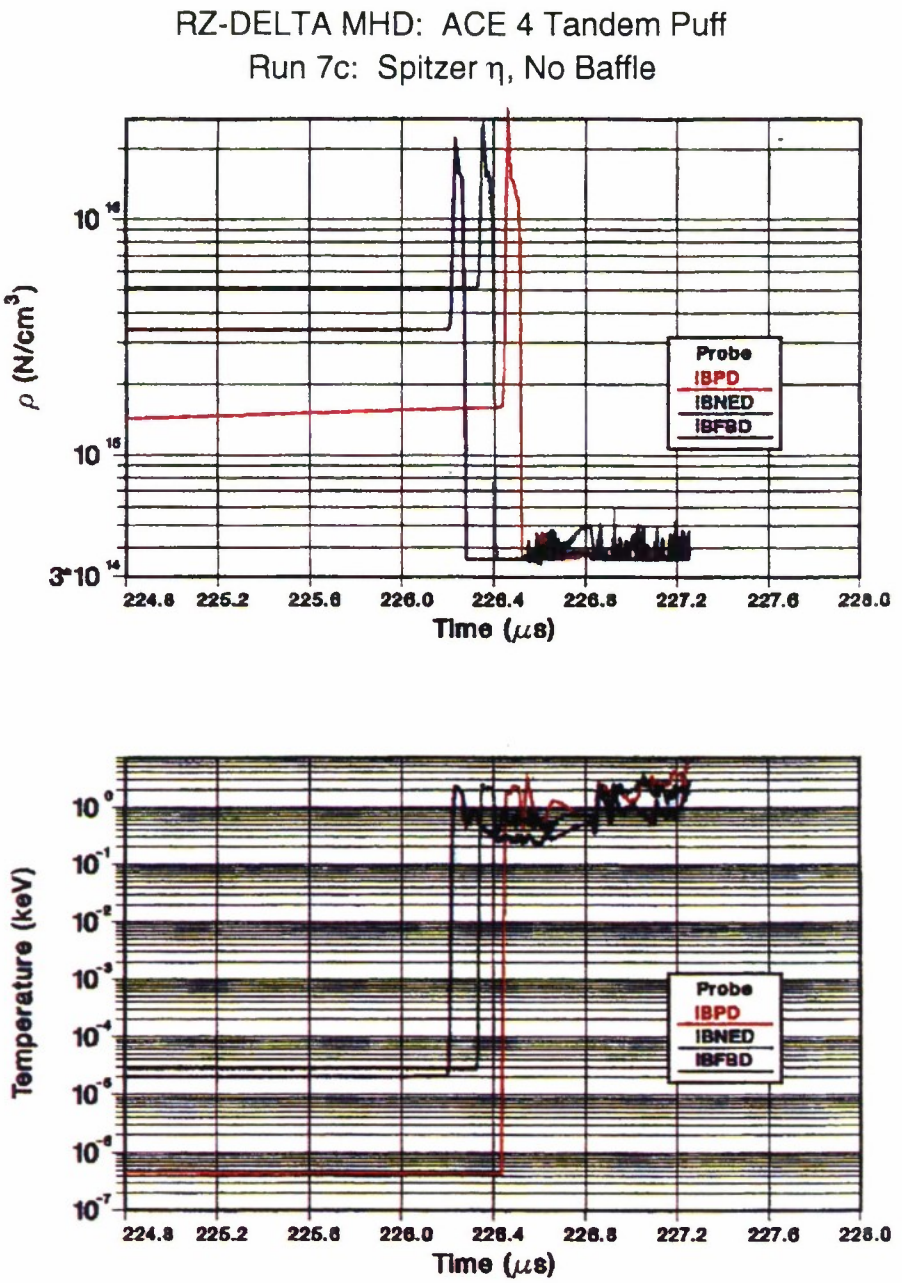

Figure 7-9. The temperature and density disturbances at the probe locations are simultaneous with the arrival of current at these locations.

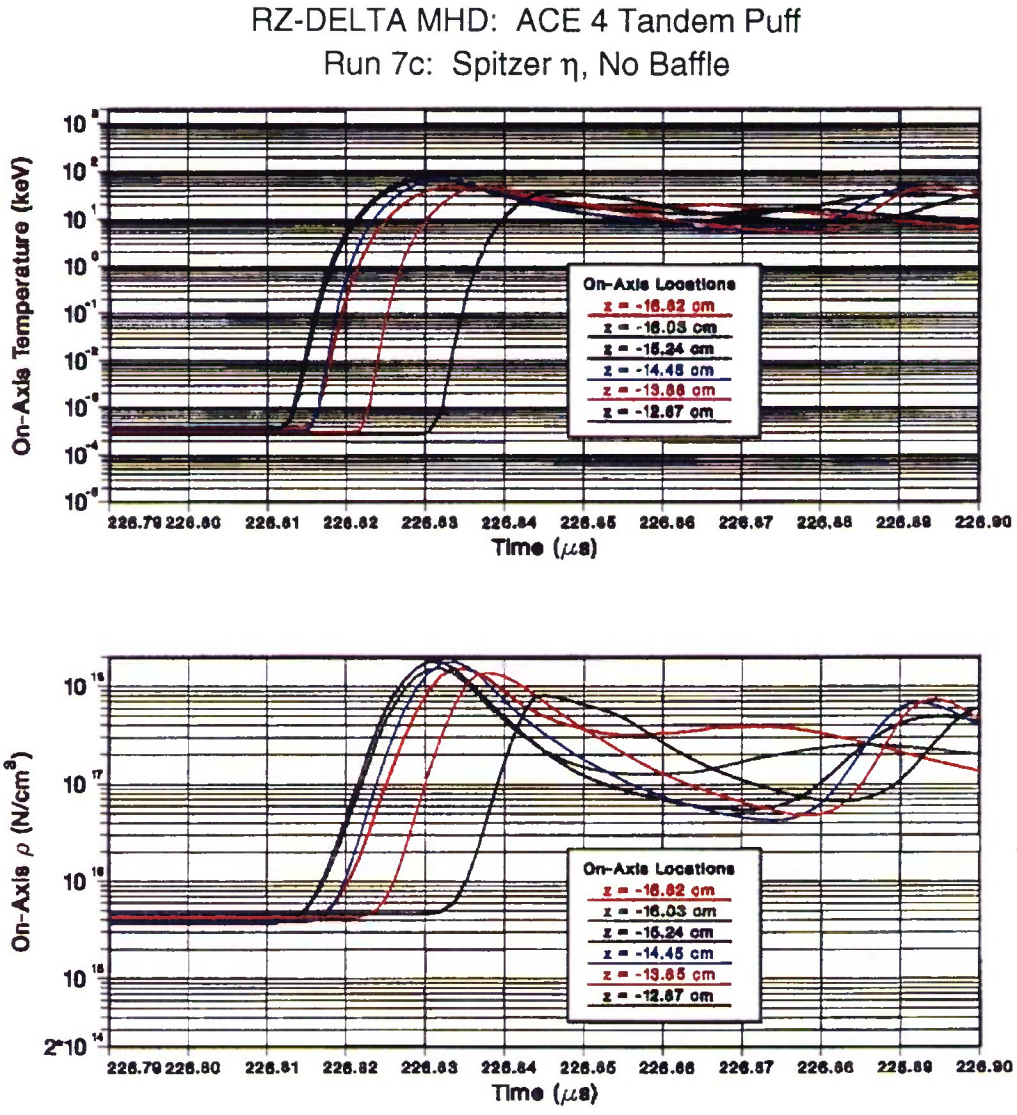

Figure 7-10. On axis temperature and density at various axial locations. These times can be compared with the onset of signal in XRD probes. The high temperatures on axis are the result of neglecting ionization, excitation and radiation. Temperatures are strongly reduced when account is taken of these effects. See Section 7.4.

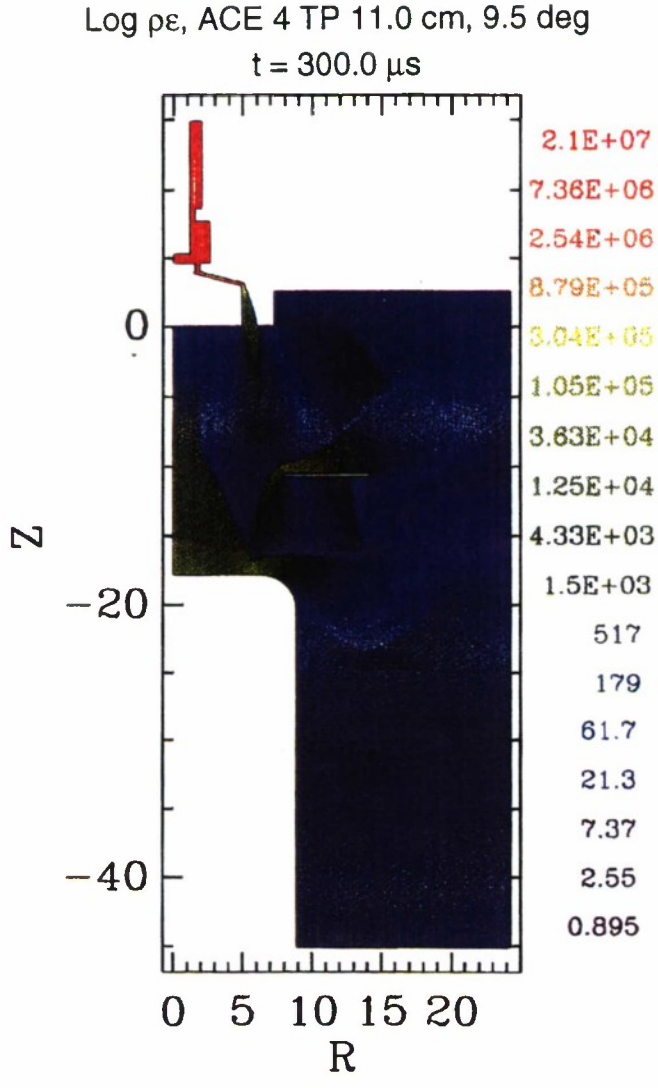

Figure 7-11. The effect of an annular baffle in zippering is to be studied. The colored graphic shows the internal energy per unit volume just before the onset of current flow.

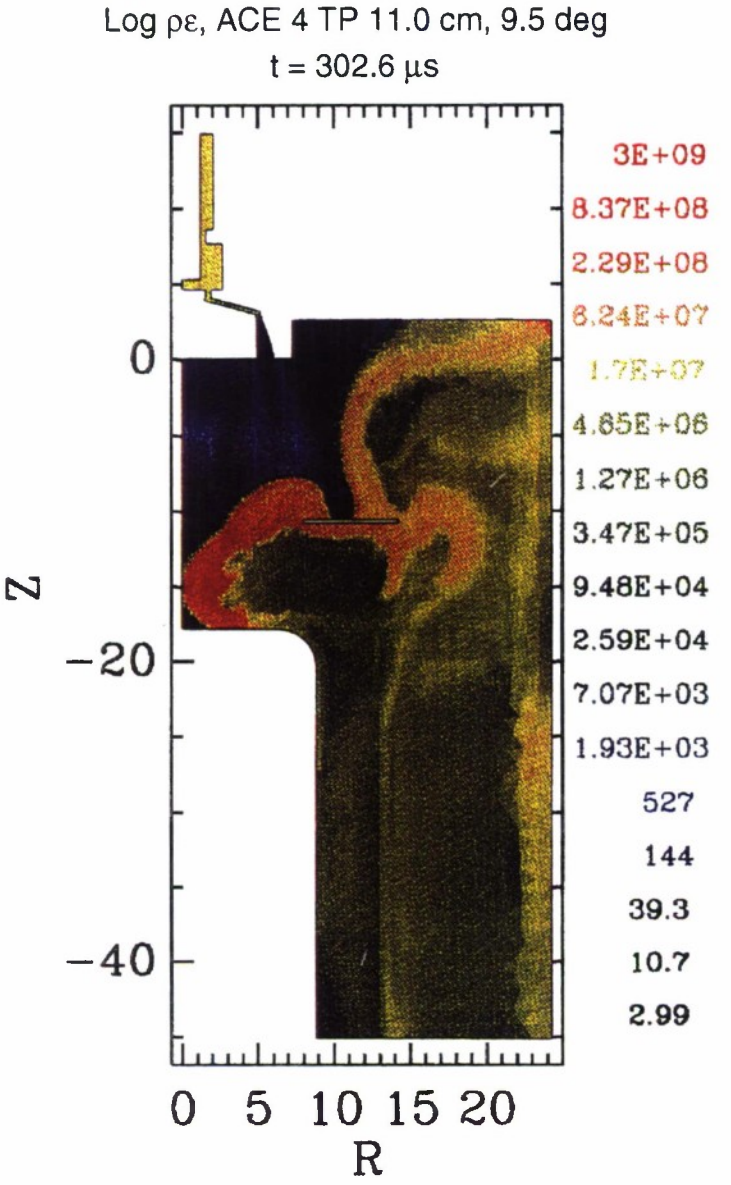

Figure 7-12. Internal energy per unit volume at the instant when on axis temperatures begin to rise.

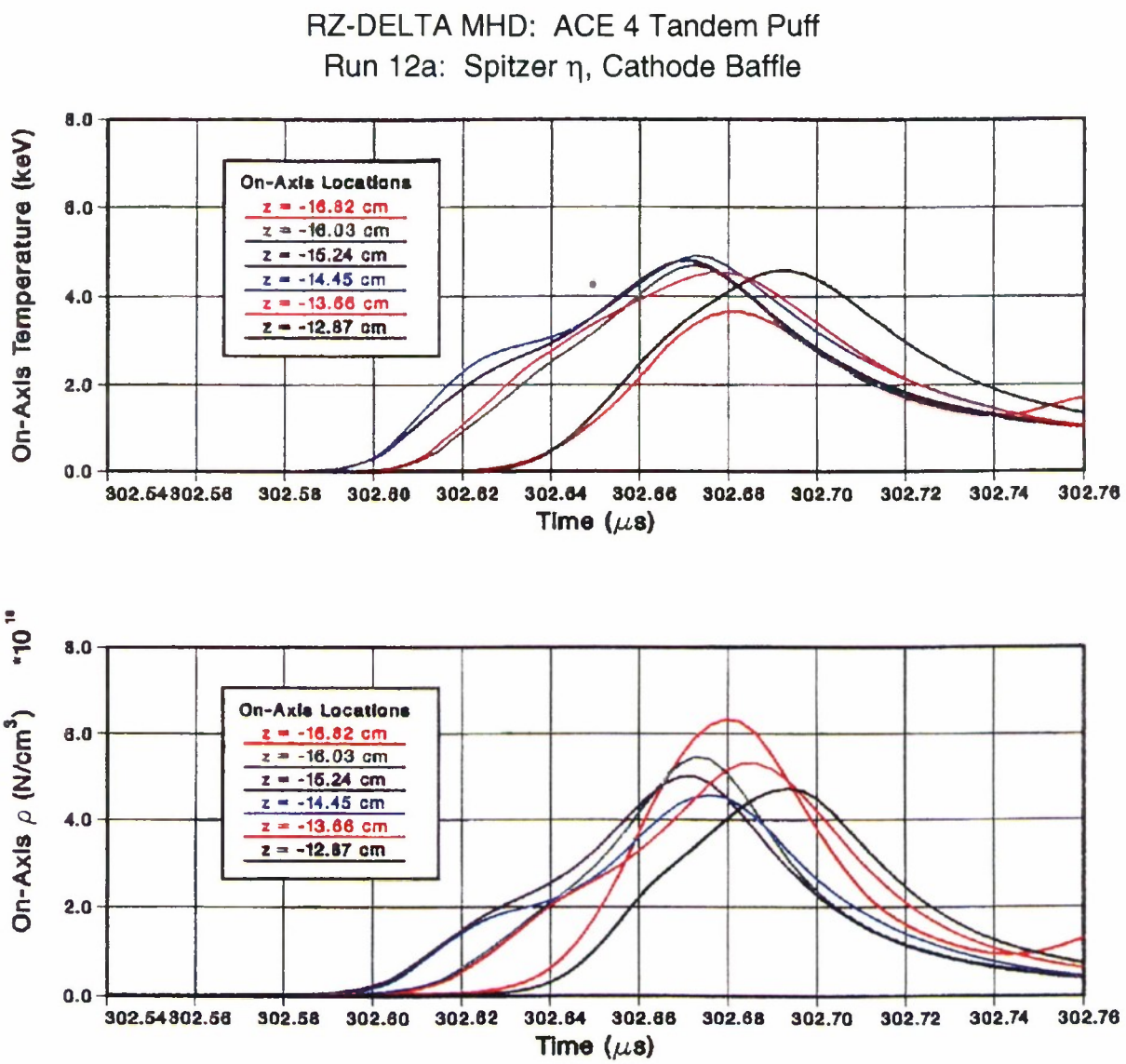

Figure 7-13. Zippering calculations to be compared with those of Figure 7-10 (not at the same delay as in Figure 7-10).

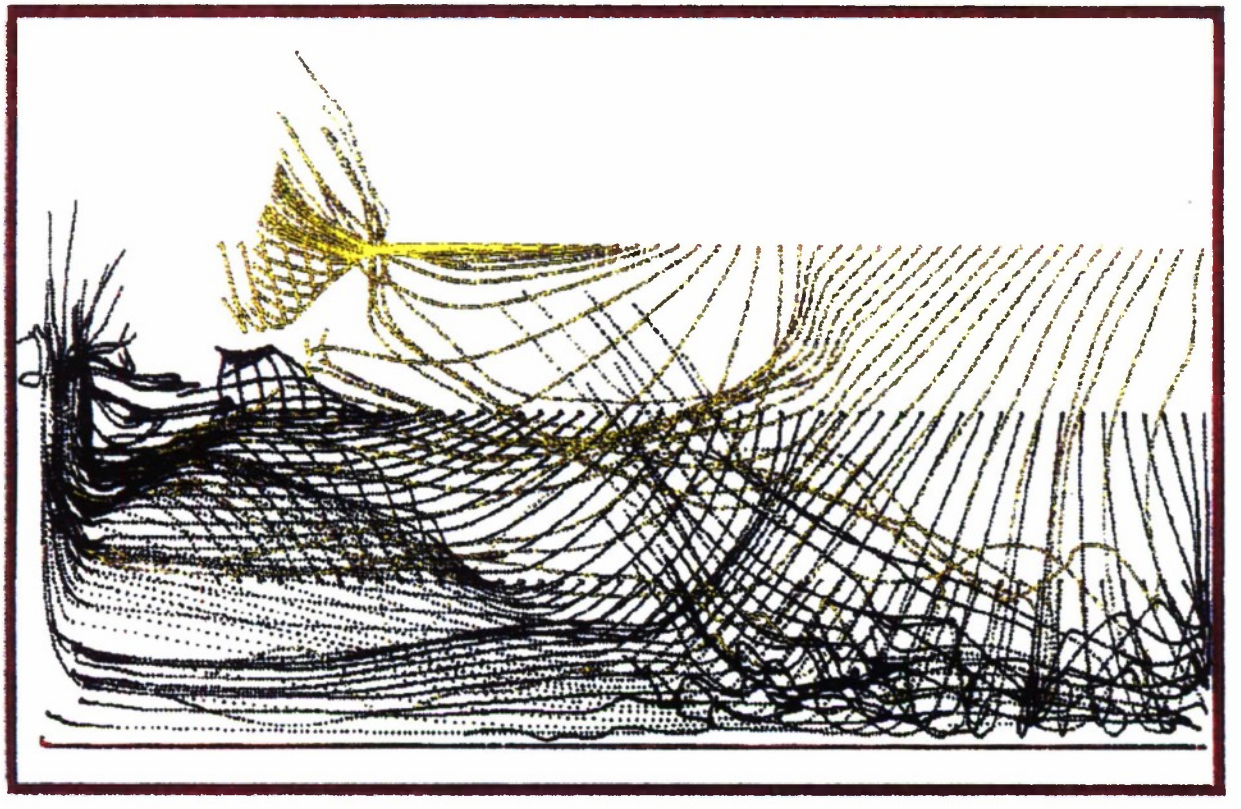

Figure 7-14. Fluid particle trajectories in the PRS region (see text for discussion).

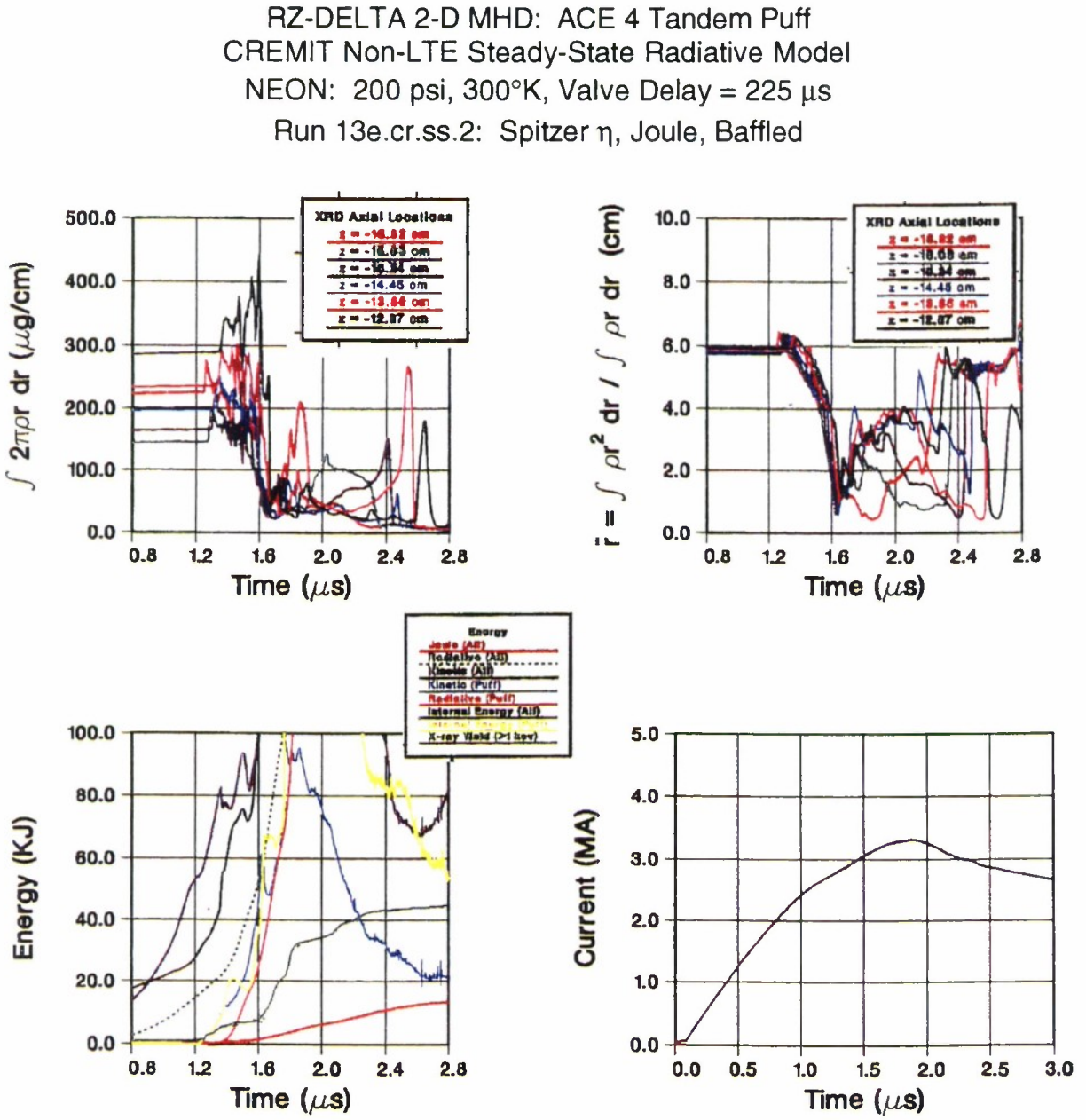

Figure 7-15. Top: Linear mass density and mean radius at various axial locations vs. time. Bottom: Energy partition and generator current vs. time.

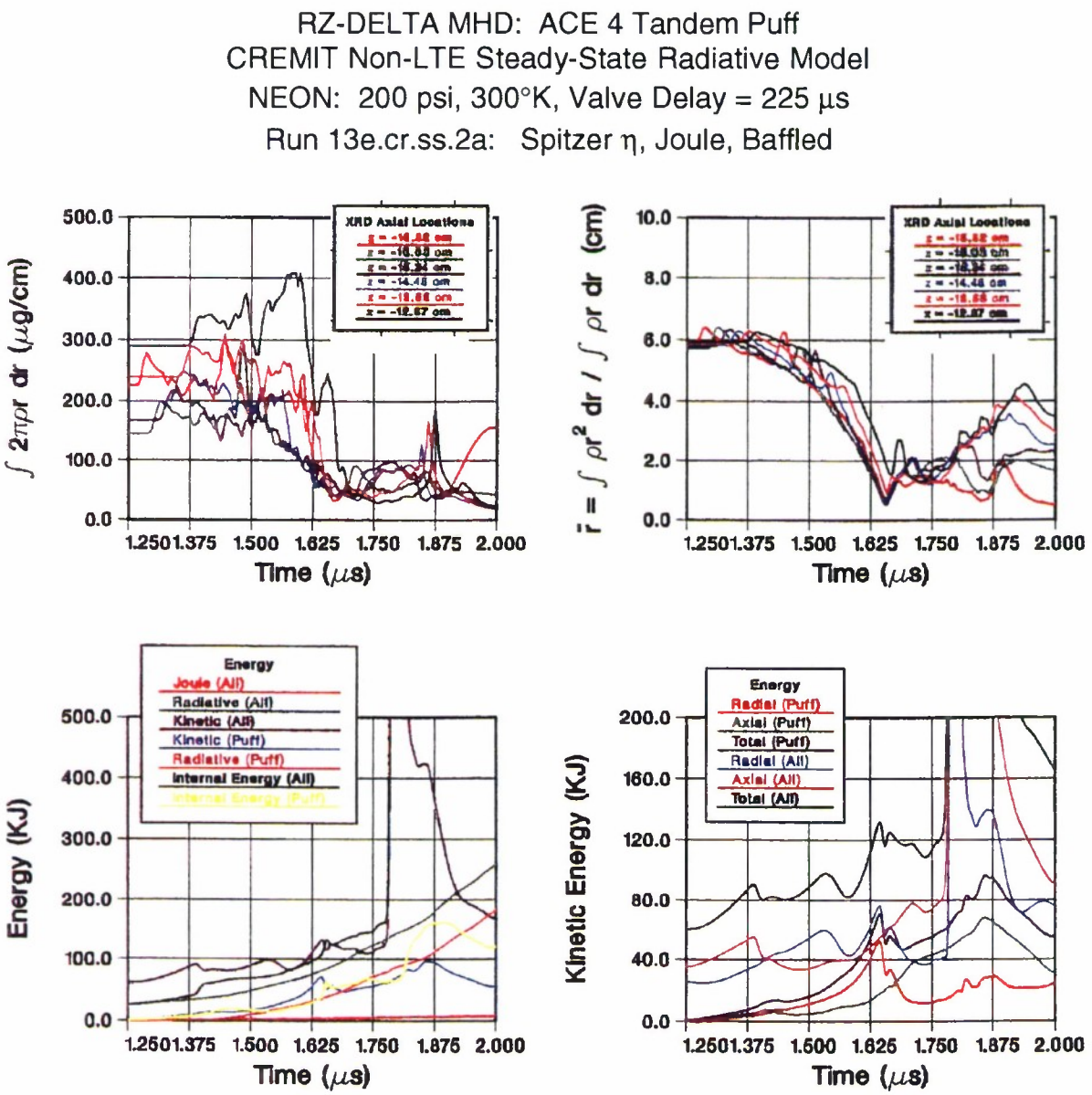

Figure 7-16. Same calculations as in previous figure shown on a finer time scale. Top: Linear mass density and mean radius at various axial locations vs. time. Bottom: Energy partition vs. time.

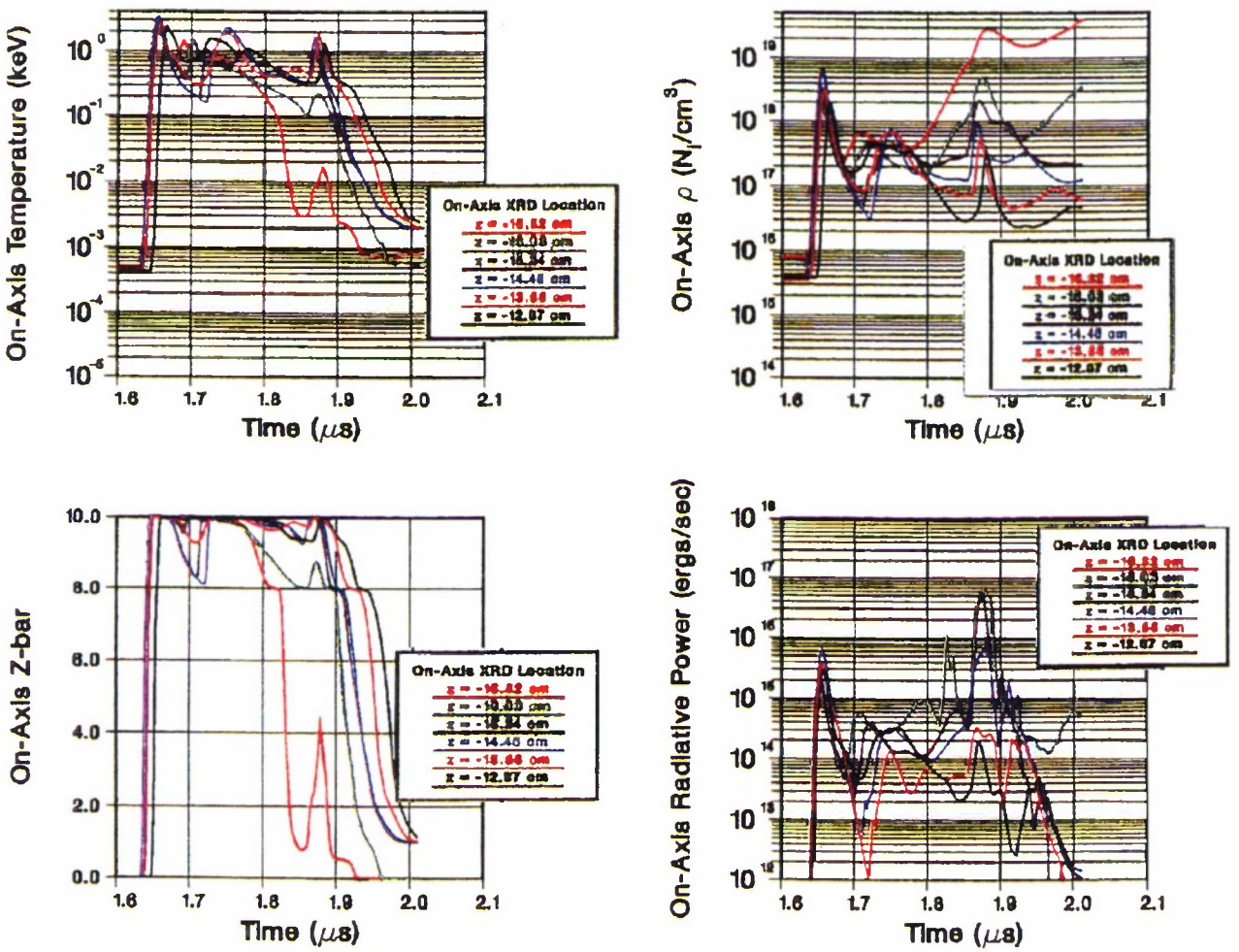

Figure 7-17. On-axis properties of pinched plasma.

RZ-DELTA MHD: ACE 4 Tandem Puff
CREMIT Non-LTE Steady-State Radiative Model
NEON: 200 psi, 300°K, Valve Delay = 275 μs
Run 13e.cr.ss.4: Spitzer η, Joule, Baffled

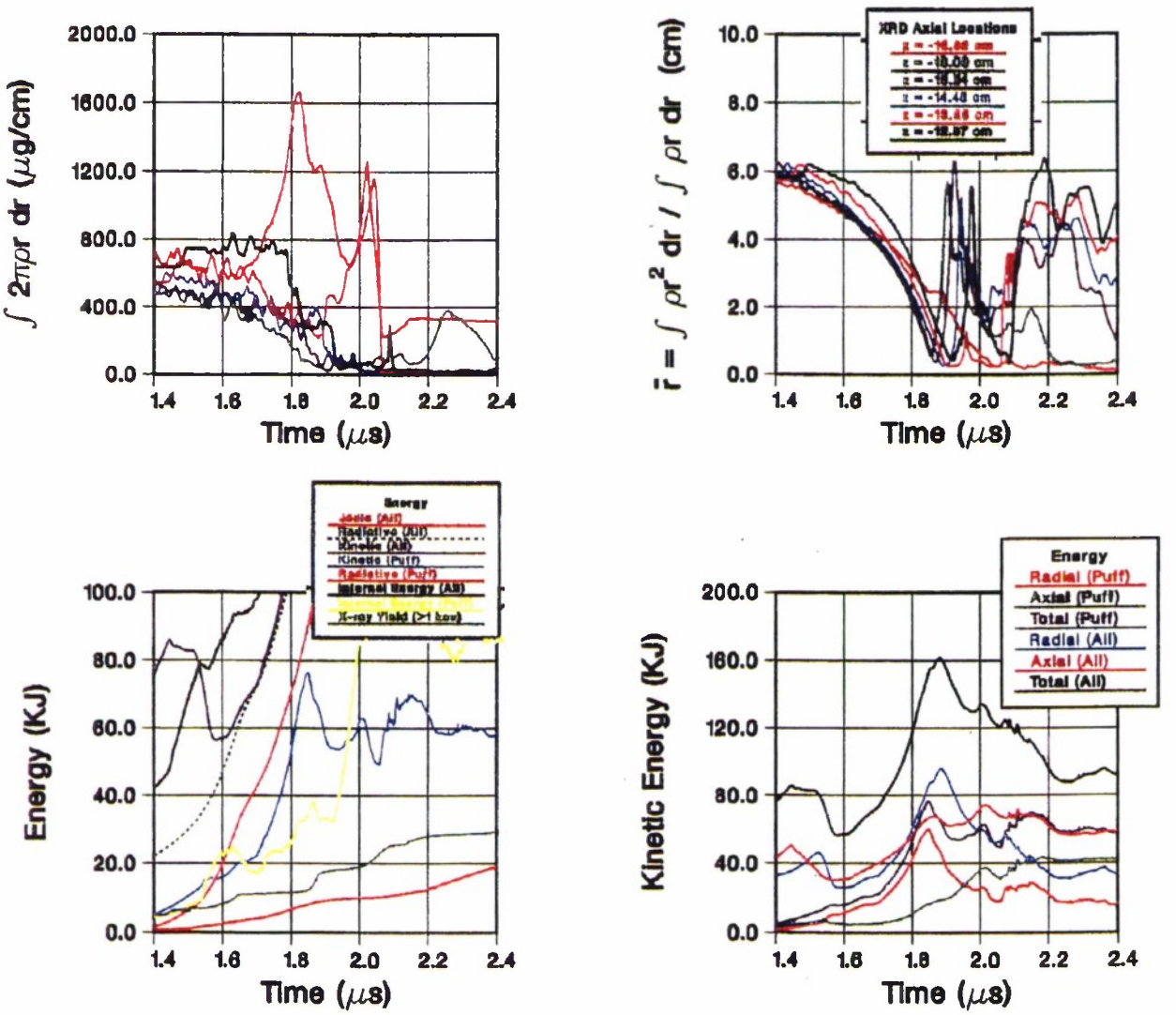

Figure 7-18. Top: Linear mass density and mean radius at various axial locations vs. time. Bottom: Energy partition vs. time.

RZ-DELTA MHD: ACE 4 Tandem Puff
CREMIT Non-LTE Steady-State Radiative Model
NEON: 200 psi, 300°K, Valve Delay = 275 μs
Run 13e.cr.ss.4: Spitzer η, Joule, Baffled

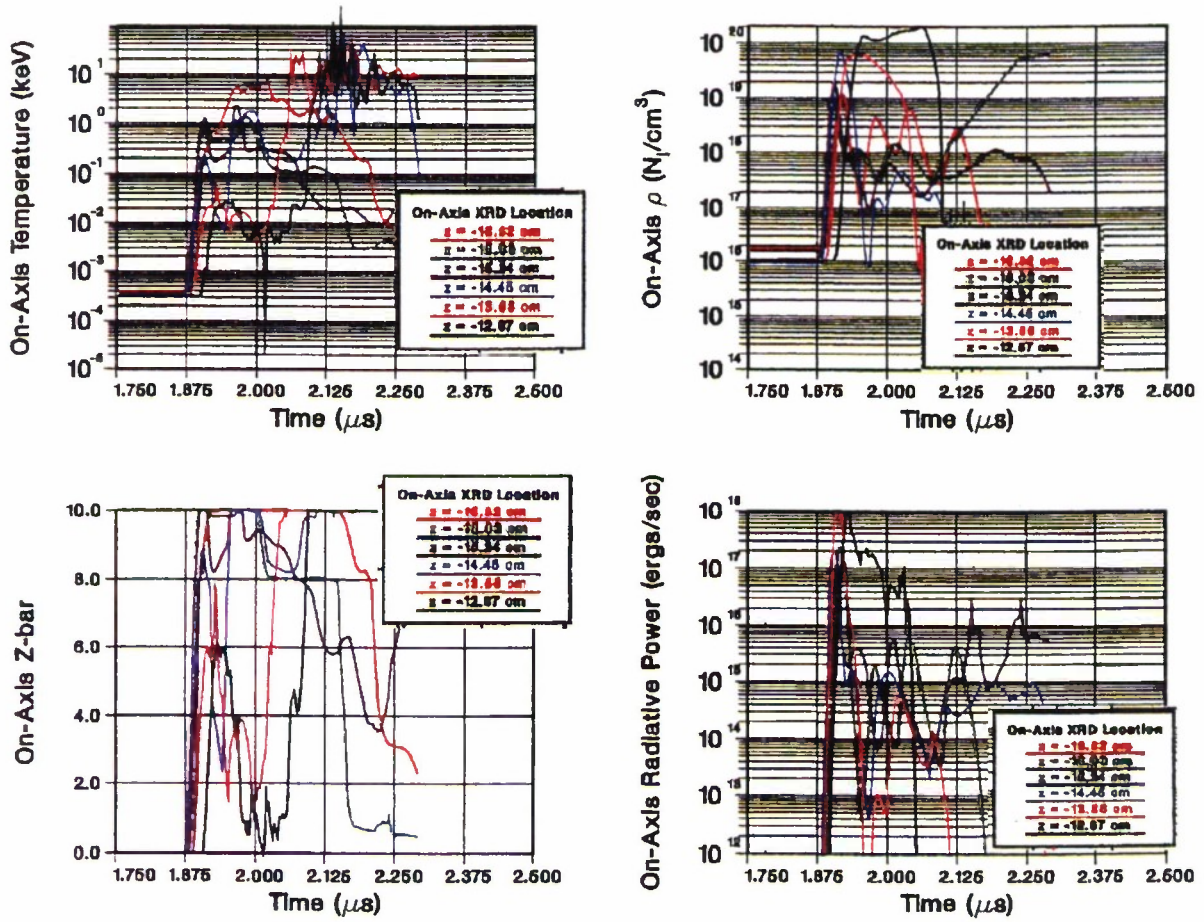

Figure 7-19. On-axis properties of pinched plasma.

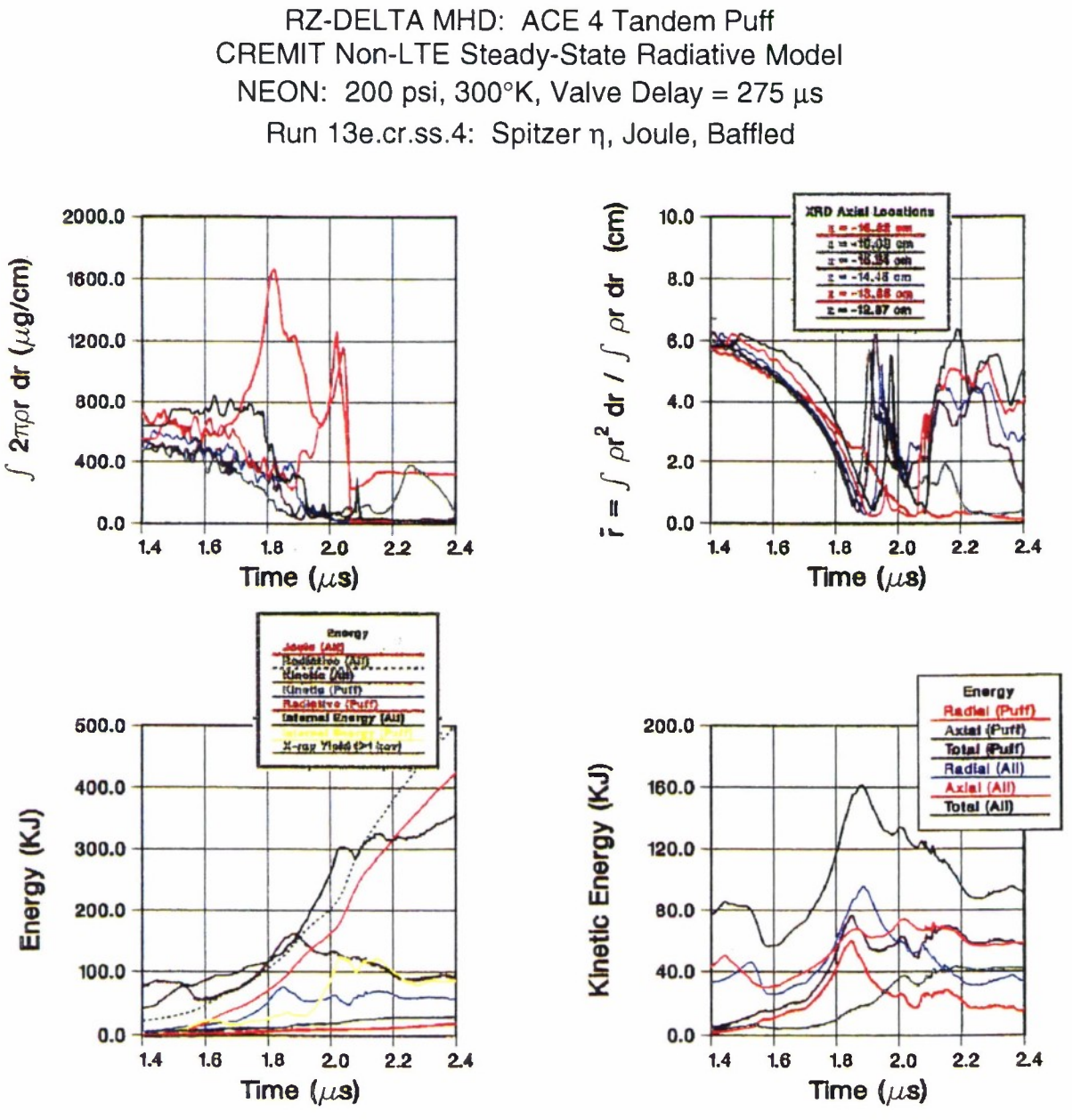

Figure 7-20. Top: Linear mass density and mean radius at various axial locations vs. time. Bottom: Energy partition vs. time.

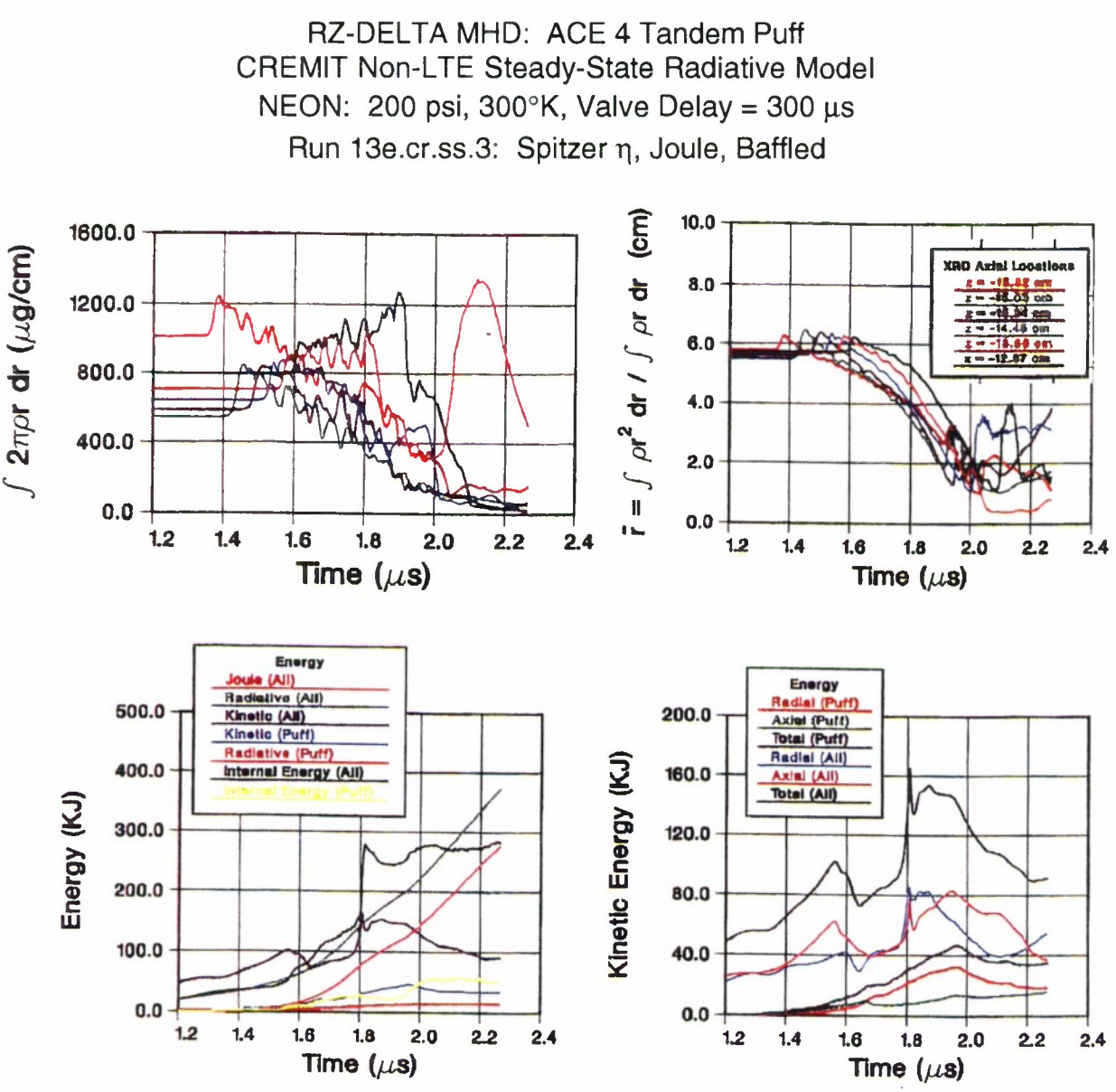

Figure 7-21. Top: Linear mass density and mean radius at various axial locations vs. time. Bottom: Energy partition vs. time.

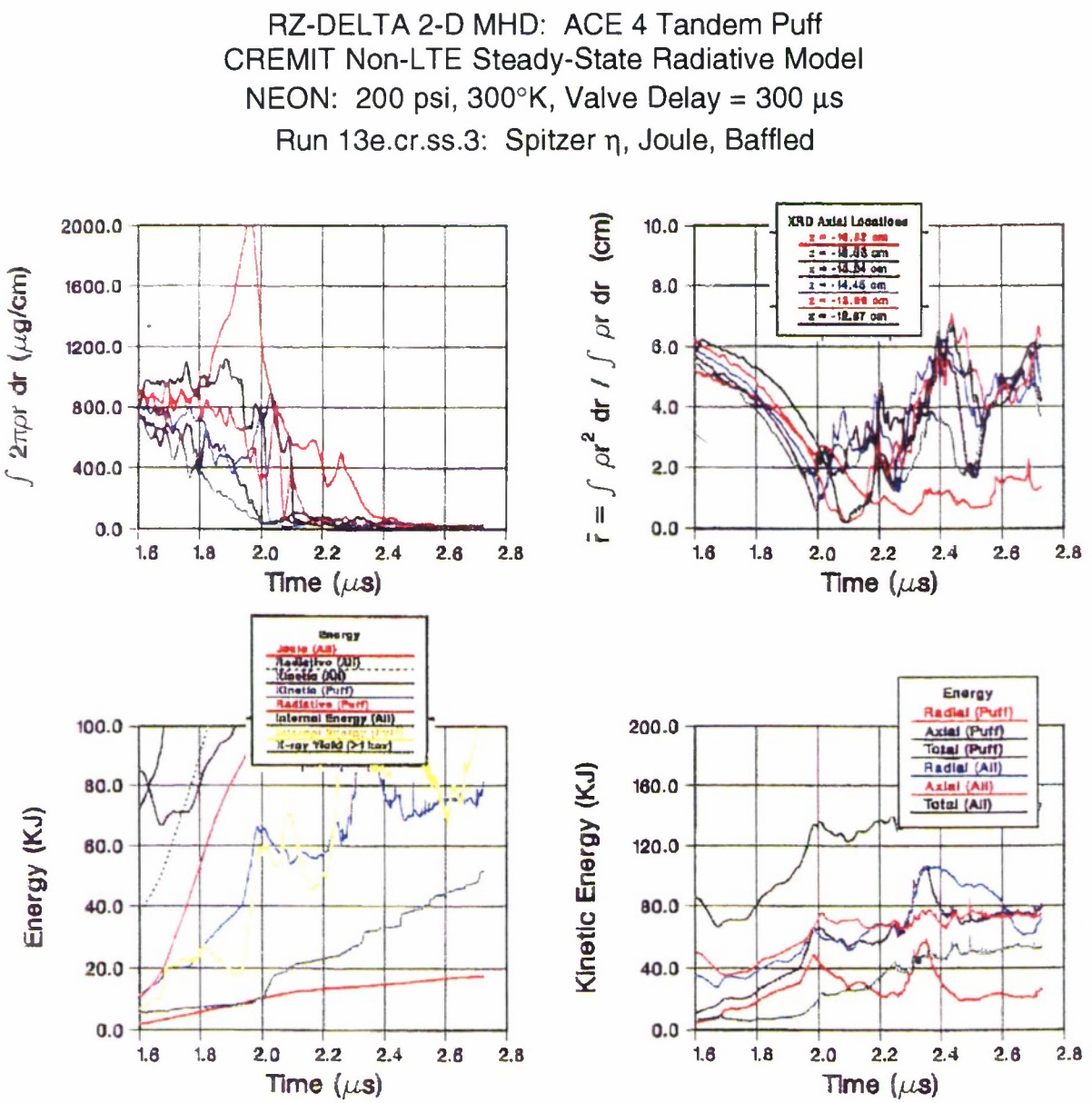

Figure 7-22. Top: Linear mass density and mean radius at various axial locations vs. time. Bottom: Energy partition vs. time.

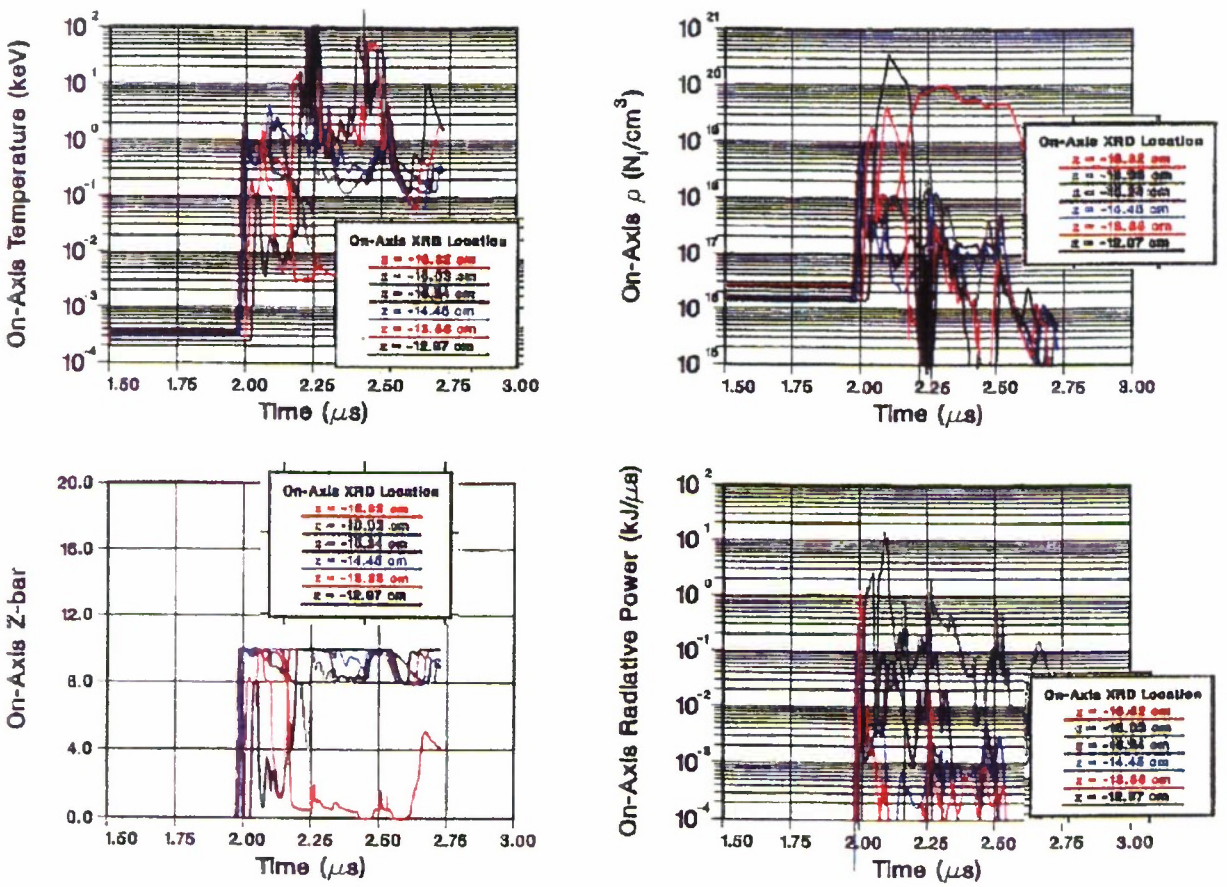

Figure 7-23. On-axis properties of pinched plasma.

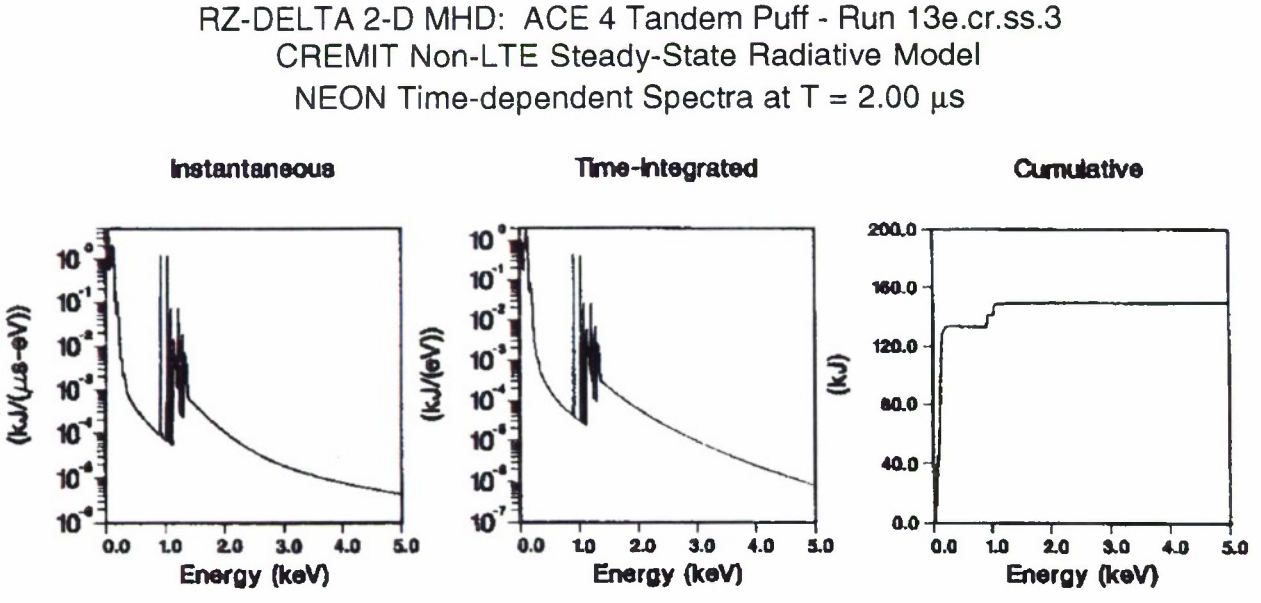

Figure 7-24. Spectral features for the 275 μs delay time.

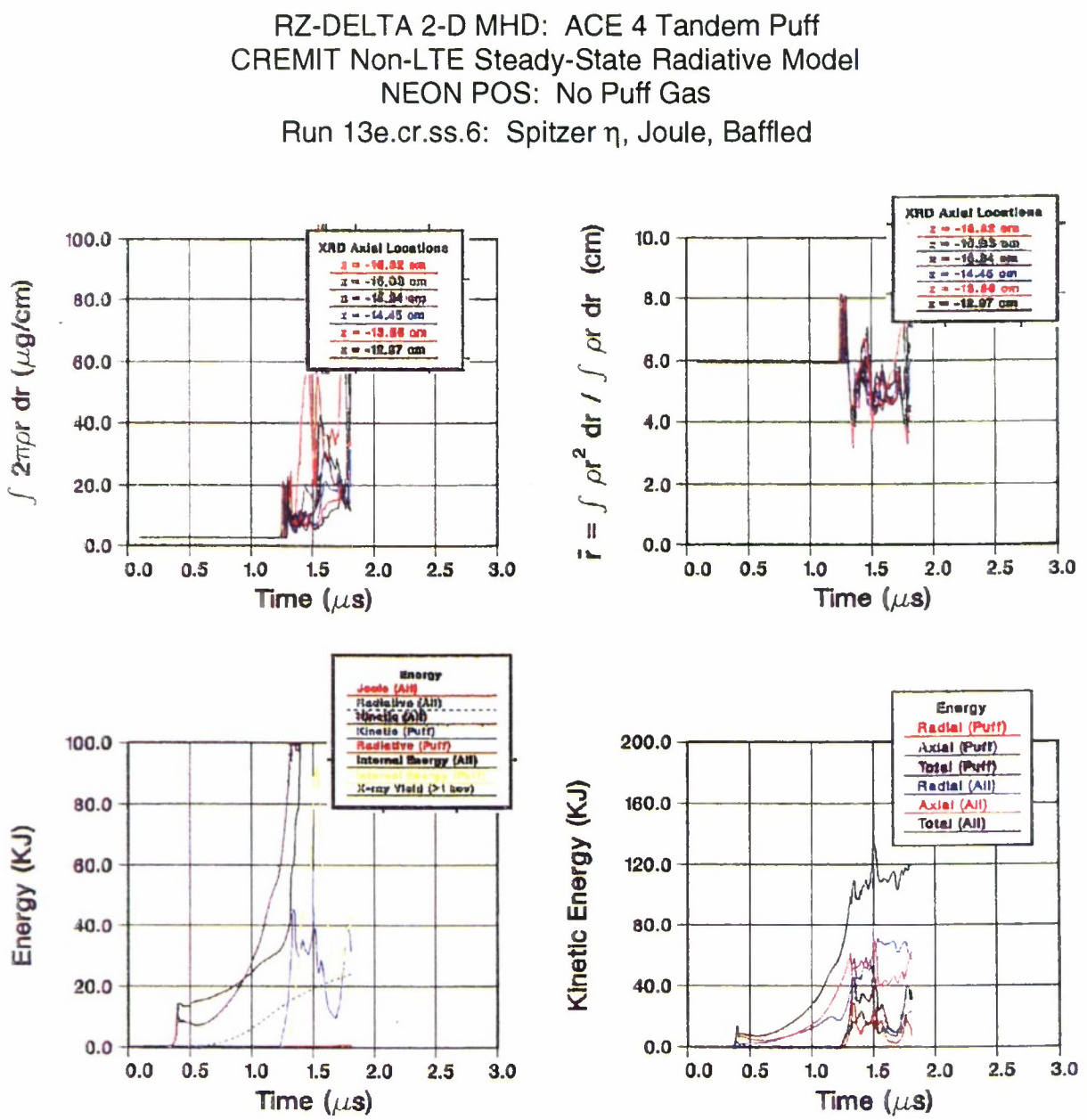

Figure 7-25. Results for no puff gas. Top: Linear mass density and mean radius at various axial locations. Bottom: Energy partition vs. time.

RZ-DELTA 2-D MHD: ACE 4 Tandem Puff
CREMIT Non-LTE Steady-State Radiative Model
NEON POS: No Puff Gas
Run 13e.cr.ss.6: Spitzer η, Joule, Baffled

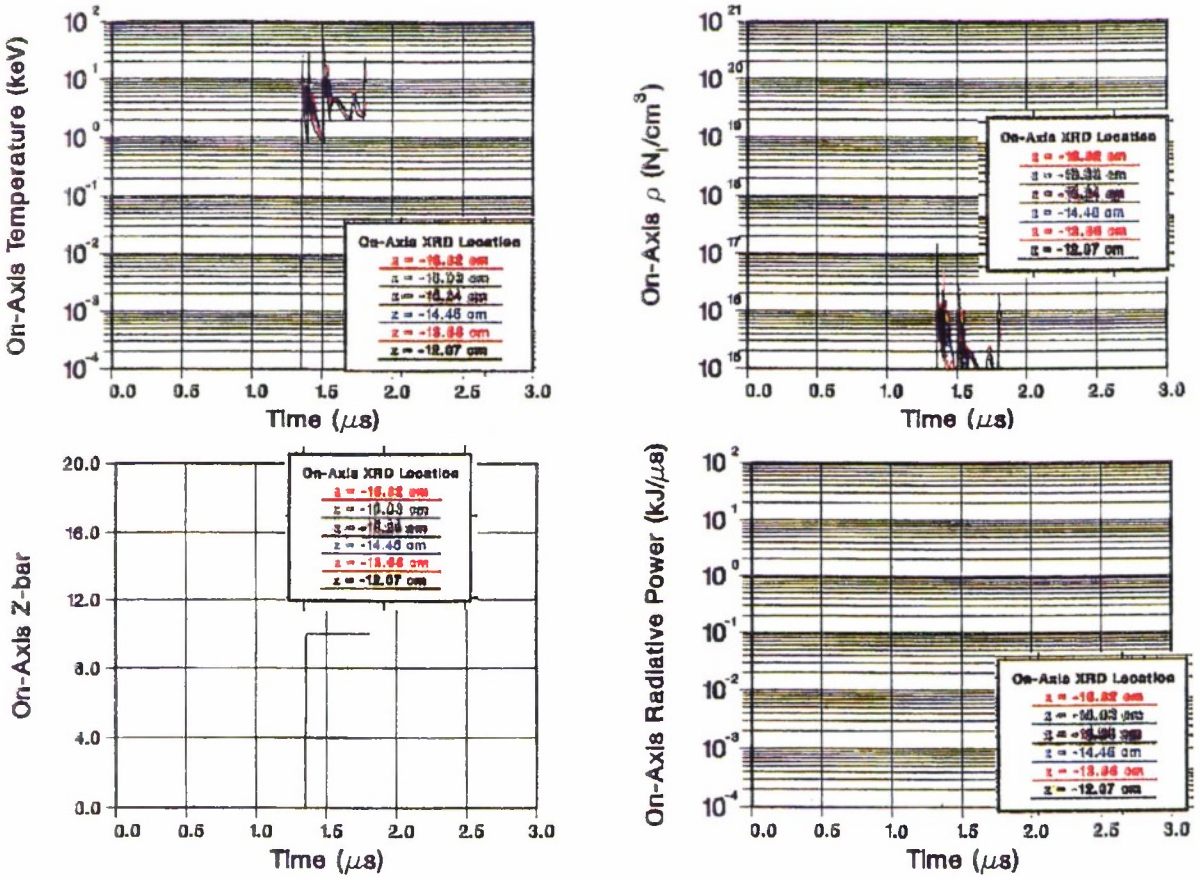

Figure 7-26. Results for no puff gas. On-axis properties of pinched POS plasma.

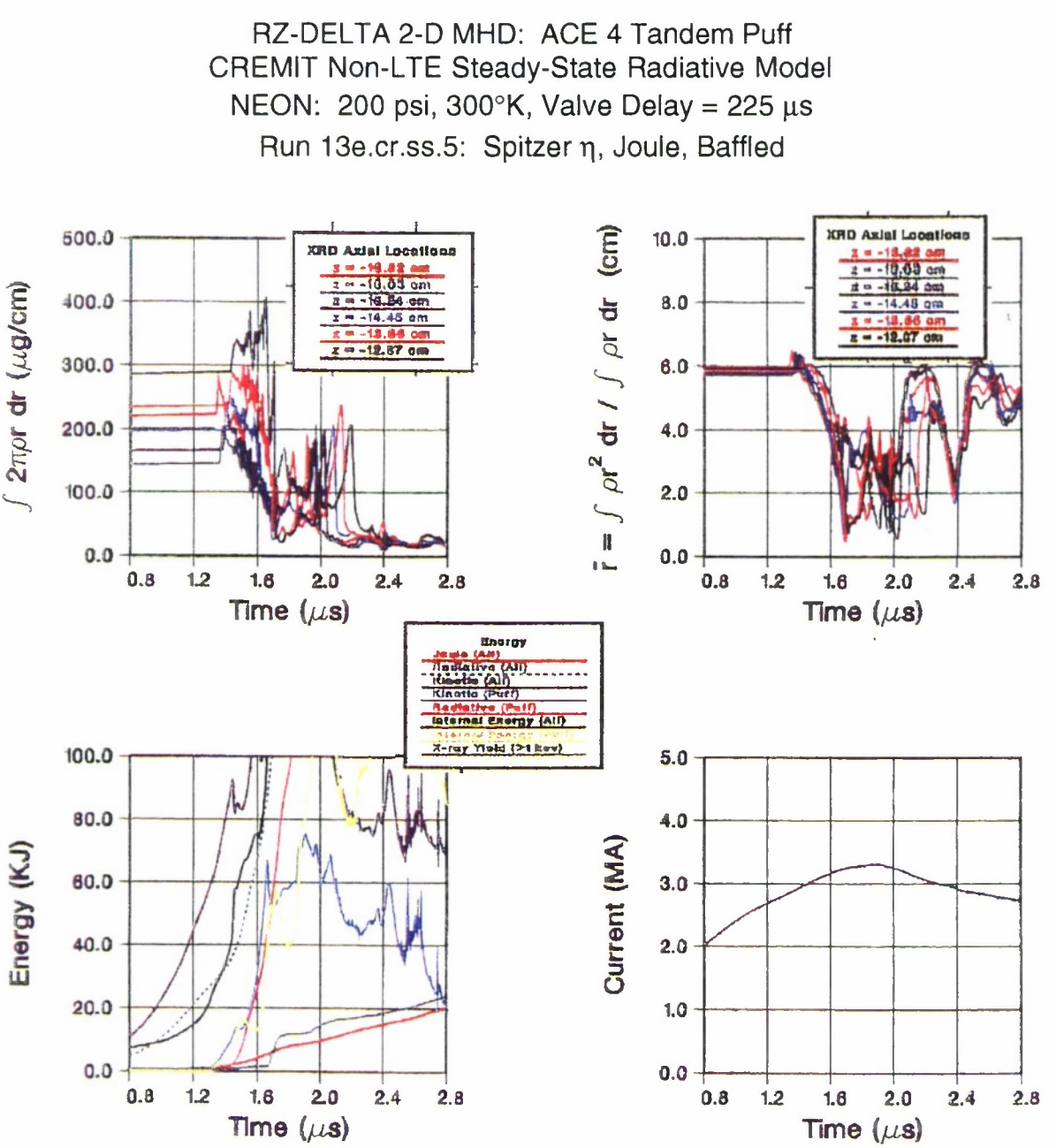

Figure 7-27. Top: Linear mass density and mean radius at various axial locations vs. time. Bottom: Energy partition and generator current vs. time.

RZ-DELTA 2-D MHD: ACE 4 Tandem Puff
CREMIT Non-LTE Steady-State Radiative Model
NEON: 200 psi, 300°K, Valve Delay = 225 μs
Run 13e.cr.ss.5: Spitzer η, Joule, Baffled

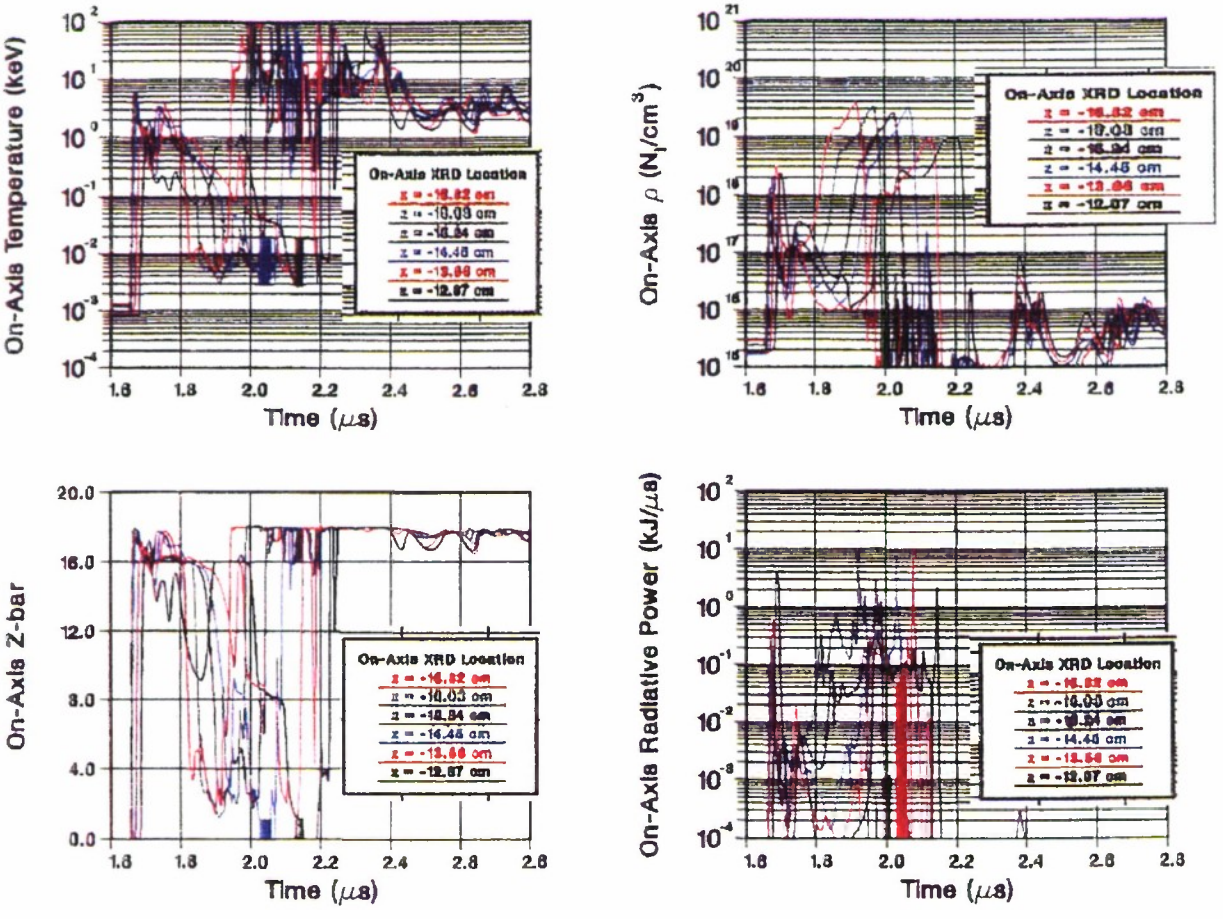

Figure 7-28. On-axis properties of pinched plasma.

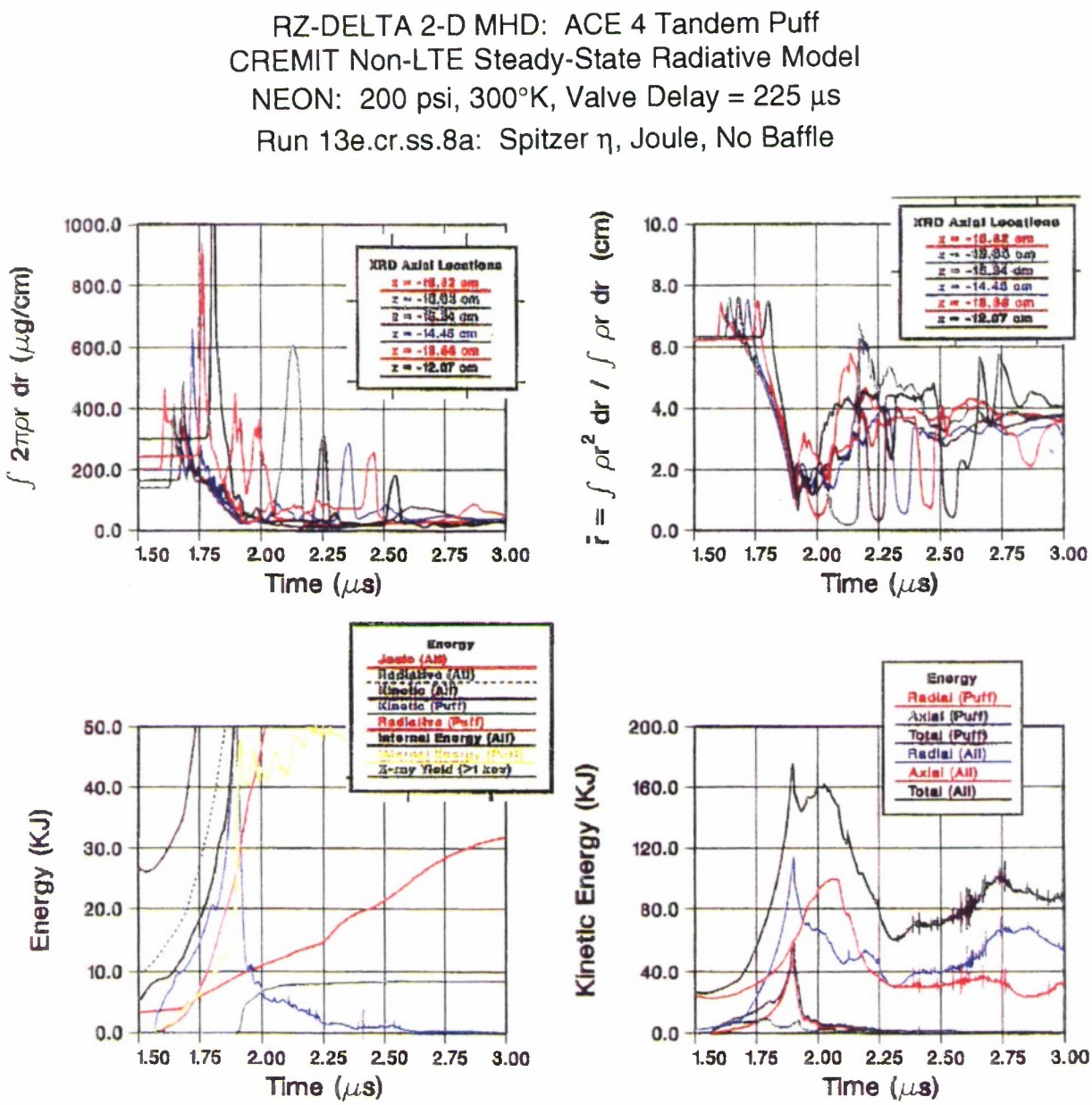

Figure 7-29. Top: Linear mass density and mean radius at various axial locations vs. time. Bottom: Energy partition vs. time.

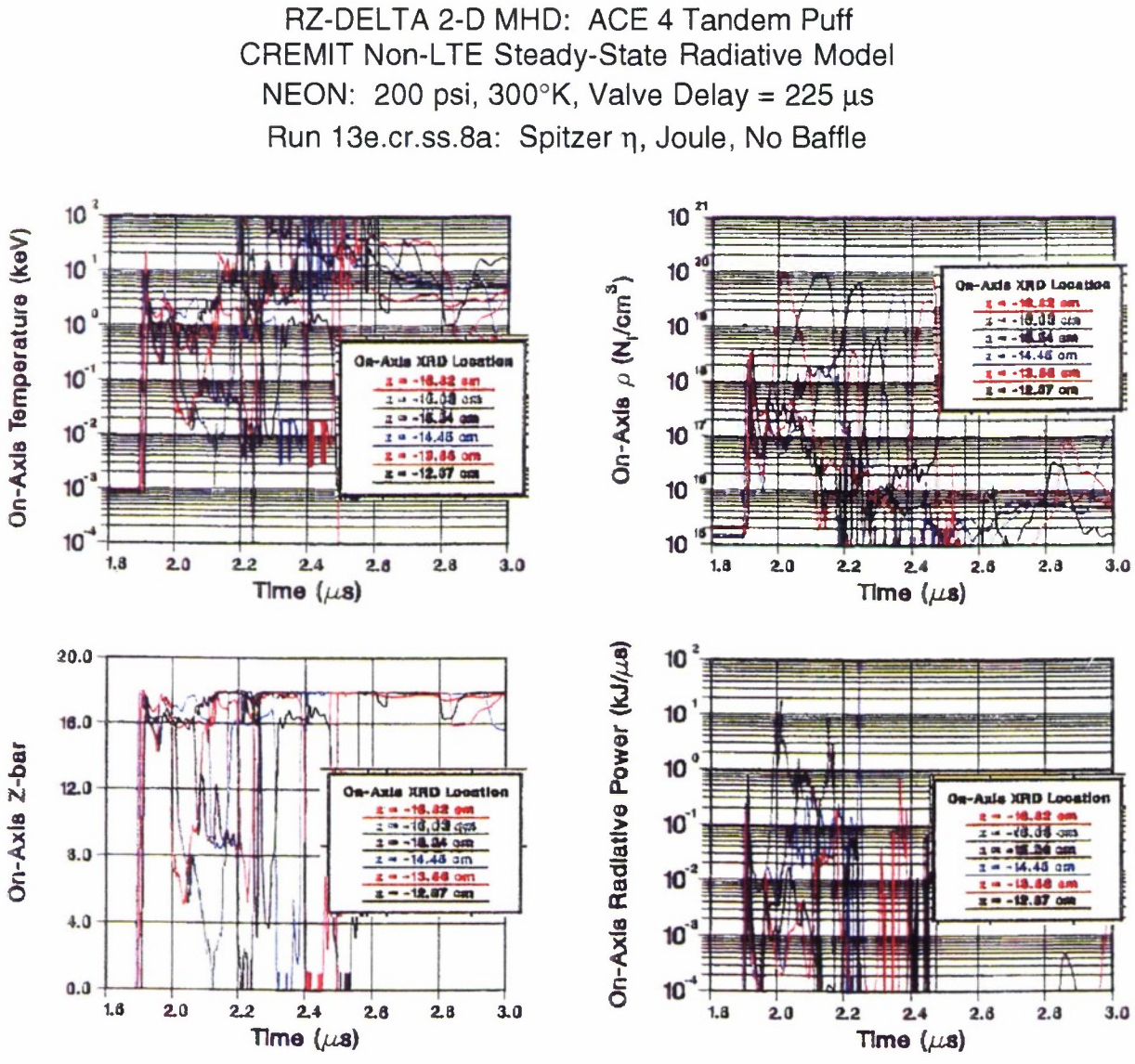

Figure 7-30. On-axis properties of pinched plasma.

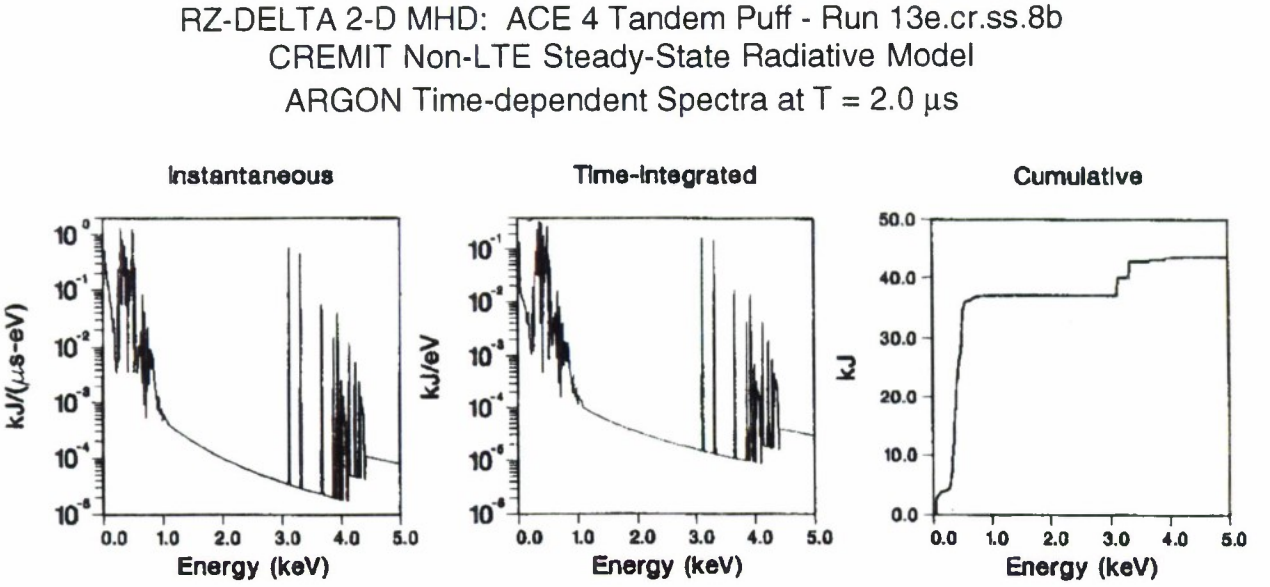

Figure 7-31. Spectral features of pinched argon plasma.

SECTION 8

CIRCUIT CODE DEVELOPMENT

8.1 OVERVIEW.

Work was begun on a general circuit code that will incorporate our best models of the POS and various loads. The components of the code are as follows:

1. The industry standard circuit-modeling code SPICE, developed over the last twenty years at the University of California at Berkeley. SPICE comes with a very clumsy user interface and some rudimentary plotting facilities. It has a large number of devices defined, including resistors, capacitors, inductors, lossless and lossy transmission lines, current and voltage sources, ideal switches, and diodes, as well as an impressive array of semiconductor components that are not of interest to the pulsed-power community.

2. Several new SPICE devices, representing such components as a POS, a PRS, a MITL, a bremsstrahlung diode, and a plasma-filled diode. These are being developed by us, using the recipe spelled out in the SPICE documentation for defining new devices. We are incorporating models of the conduction and opening phases of the POS and of bremsstrahlung and PRS loads. We developed a one-dimensional PRS slug model, a bremsstrahlung diode, a one-dimensional snowplow model of the POS, a simple plasma source device for the POS, and two models of the opening phase of the POS - an R-dot model and a Z-flow model.

3. A SPICE preprocessor with a graphical user interface for easy setup of circuits. A number of these are available as freeware, shareware, or payware.

4. The MIRIAD technology developed at S-Cubed over the last several years. MIRIAD allows the easy integration of many codes, and allows for quick setup of parameter studies.

In this report, we will focus on component 2 above, the new SPICE devices, since this contains the real physics, and also presents the greatest challenge in terms of software development.

8.2 NEW SPICE DEVICE DEVELOPMENT.

The general steps for creating a new SPICE module are as follows:

1. Develop an idealized physical representation of the device

2. Write a mathematical model of the physics

3. Embed these equations into the SPICE circuit equations

4. Linearize any nonlinear terms in the equations of motion to allow for an iterative Newton-Raphson solution

5. Write computer code to implement these equations

6. Incorporate the new module into SPICE

Of these, only steps 1 through 4 are described in this report. We will give a detailed description for the first device we constructed, a 1-D slug model of the PRS. The other devices will be documented in less detail.

8.3 PHYSICAL IDEALIZATION OF THE PRS.

An idealized representation of the PRS is shown in Figure 8-1. This representation is suitable for a one-dimensional model, due to symmetry in the axial direction.

We assume in this model that the plasma is concentrated in a slug of negligible thickness. In future work, we will consider the more general case of finite distribution functions of the mass.

We assume that current initially starts flowing along the plasma surface at some radius r_i that is less than the cage radius r_c. The current induces a magnetic field which causes the current sheath to move inward, accelerating until it implodes on the Z-axis. The implosion is characterized by an implosion radius r_f, which is typically about a tenth of the initial radius. The region upstream of the current sheath has the usual inductance associated with a coaxial volume.

This model says nothing about the radiation produced by the implosion. However, it gives us two useful pieces of information:

1. The inductance of the device causes a voltage which feeds back upstream, modifying the dynamics of the driver circuit.

2. The material in the current sheath carries kinetic energy, which is thermalized at the implosion. If Joule heating can be neglected, this gives an upper bound on the energy yield of the PRS. This upper bound may not be realized, of course, due to instabilities, zippering, or other effects which are not in the model.

8.4 MATHEMATICAL MODEL OF 1-D PRS.

It is straightforward to reduce the above physical idealization into a set of equations. The voltage across the device is given by:

$$V_A - V_C = \frac{d\Phi}{dt} + IR \tag{8.1}$$

where V_A is the anode voltage in volts
V_C is the cathode voltage
Φ is the flux LI in the device
L is the time-varying inductance in Henries
I is the current through the PRS in amps
R is the joule resistance of the PRS plasma in Ohms.

The inductance of the PRS region is given by:

$$L = \left(2x10^{-9}\right)\ell \quad \log \quad \left(\frac{r_c}{r}\right) H \tag{8.2}$$

where ℓ is the length of the current sheath in cm
r_c is the cage radius in cm
r is the position of the current sheath in cm.

The current sheath follows the 1-D snowplow equations of motion:

$$\frac{dr}{dt} = \frac{p}{M} \tag{8.3}$$

$$\frac{dp}{dt} = \frac{-\ell I^2}{100r} \tag{8.4}$$

$$\frac{dM}{dt} = 0 \tag{8.5}$$

where p is the momentum of the plasma in cgs units
M is the mass of the plasma in gm.

Equation 8.5 is not really necessary in the present formulation. We have included it with an eye toward future upgrades, in which the mass is distributed over a shell of finite thickness, in which case material will be snowplowed as the current sheath implodes.

8.5 EMBEDDING THE MODEL INTO SPICE.

SPICE was developed by a collaboration of electrical engineers and computer scientists at the University of California at Berkeley. It is normally used by engineers for the analysis of large integrated circuits with hundreds or thousands of nodes and branches. The techniques used in SPICE for assembling the circuit equations are probably unfamiliar to the reader, so we will outline them here.

Simple devices, such as resistors, inductors and capacitors, have two nodes. Physically, they can be characterized by the current I_b going through them and the voltage difference V_b across their nodes. These quantities are called the branch current and branch voltage. Mathematically, the branch current can be related to the branch voltage by some simple relation such as:

$$V_b = I_b R \quad . \tag{8.6}$$

The fact that the devices are connected in a circuit implies a number of topological relations which can be summarized by the two Kirchhoff laws:

1. The sum of all currents entering a node is zero

2. The sum of all branch voltages in any loop is zero.

The mathematical problem is that the combination of the branch relations and the Kirchhoff laws generally yields more equations than unknowns. For small circuits, one can simply begin writing down equations until there are enough to solve the problem. Most physicists develop an instinct for this that they cannot easily reduce to an algorithm.

For large circuits that must be solved on a computer, one needs an automated algorithm that is simple and robust. The technique developed for SPICE is called Modified Nodal Analysis.

A full description of this method would take a number of pages. The following description is therefore a stripped down version. In this method, one takes the voltages at nodes as the basic set of unknowns. For each inductor or voltage source in the problem, one adds the branch current to

the list of unknowns. It turns out that this produces exactly one more equation than is needed to solve the problem. But one must always specify one of the nodes as ground. In doing so, one of the equations can be trivially eliminated, and the rest yield a set of N equations in N unknowns.

This formulation automatically satisfies the Kirchhoff voltage law, since each branch voltage is the difference of two nodal voltages. In going around any loop, summing branch voltages, one adds and subtracts each nodal voltage in the loop exactly once, which yields zero.

To get the circuit equations, one constructs a matrix equation of the form:

$$\begin{bmatrix} \cdots & \vdots & \cdots \\ \cdots & \cdots & \cdots \end{bmatrix} \begin{bmatrix} V_I \\ \vdots \\ V_n \\ \cdots \\ I_I \\ \vdots \\ I_m \end{bmatrix} = \begin{bmatrix} J_I \\ \vdots \\ J_n \\ \cdots \\ E_I \\ \vdots \\ E_m \end{bmatrix} \tag{8.7}$$

The upper block of this matrix represents currents entering each node. Each line of this block is calculated using the appropriate branch relations to determine the current coming into the node. By setting the RHS of this equation to any current sources entering the node, one satisfies the Kirchhoff current law. The lower block of the matrix represents branch relations for inductors or voltage sources.

The above formulation is sufficient for purely electrical devices. However, the PRS also has mechanical equations of motion for mass, radius, and velocity. To embed the PRS in SPICE, we therefore have to add new variables for these quantities. It is convenient to also add auxiliary variables for the inductance and flux.

To show how this works out in practice we consider the case of a current driver dumping current into a PRS, as shown in Figure 8-2.

The equations of motion for this system are given in the matrix below:

$$\left[\begin{array}{c|ccc|cc} 0 & 1 & 0 & 0 & 0 & \\ & -1 & 0 & 0 & & \\ \hline I & -1 & -R & 0 & -d/dt & \\ 0 & 0 & 0 & 1 & 0 & 0 \\ 0 & 0 & 0 & 0 & 1 & \\ \hline 0 & & 0 & & d/dt & -1/M \\ & & & & 0 & d/dt \end{array}\right] \left[\begin{array}{c} V_A \\ V_C \\ \hline I \\ L \\ \Phi \\ \hline r \\ p \end{array}\right] = \left[\begin{array}{c} I_s \\ -I_s \\ \hline 0 \\ 2\times10^{-9}\ell\log(r_c/r) \\ LI \\ \hline 0 \\ -\ell I^2/100r \end{array}\right] \tag{8.8}$$

The first two equations are not independent. However, by grounding the cathode, we can eliminate the second, yielding a set of six independent equations.

These equations involve the time derivatives of dynamical quantities. SPICE has some sophisticated control features to integrate these equations forward in time. Assuming that we have

computed a quantity X at some time t, SPICE needs us to give a formula for computing X at a time (t + dt). A convenient notation is the following:

$$X_0 \text{ denotes } X(t)$$
$$X \text{ denotes } X(t+dt) \quad .$$

SPICE maintains a history of previously computed values of X at earlier timesteps, and provides a routine to linearize the time derivative of X using an implicit integration scheme. The result is that one approximates the derivative by:

$$\frac{dX}{dt} = D_0 X + (DX)_0 \tag{8.9}$$

where D_0 and $(D\,X)_0$, are constants which depend on the approximation representing the derivative. In the backward Euler integration scheme, for example:

$$D_0 = \frac{1}{\Delta t}$$

$$(D\,X)_0 = \frac{-x_0}{\Delta t} \quad . \tag{8.10}$$

We can now linearize the equations. As an example, the flux equation becomes:

$$\Phi = L_0 I_0 + L_0 (I - I_0) + I_0 (L - L_0) \tag{8.11}$$

or

$$\Phi = L_0\, I + I_0\, L - L_0\, I_0 \quad . \tag{8.12}$$

The current equation becomes:

$$V_A - V_C - RI - D_0 \Phi = (D\Phi)_0 \tag{8.13}$$

The full linearized matrix equation becomes:

$$\left[\begin{array}{cc|ccc|cc} 0 & & 1 & 0 & 0 & 0 & \\ & & -1 & 0 & 0 & & \\ \hline 1 & -1 & -R & 0 & -D_0 & 0 & 0 \\ 0 & 0 & 0 & 1 & 0 & 2\times10^{-9}\ell/r_0 & 0 \\ 0 & 0 & -L_0 & -I_0 & 1 & 0 & 0 \\ \hline & 0 & 0 & 0 & 0 & D_0 & -1/M \\ 0 & & \ell I_0/50r_0 & 0 & 0 & -\ell I_0^2/100r_0^2 & D_0 \end{array}\right] \left[\begin{array}{c} V_A \\ V_C \\ \hline I \\ L \\ \Phi \\ \hline r \\ p \end{array}\right] = \left[\begin{array}{c} I_s \\ -I_s \\ \hline (D\Phi)_0 \\ 2\times10^{-9}\ell[\log(r_0/r_c)-1] \\ -L_0 I_0 \\ \hline (Dr)_0 \\ (Dp)_0 \end{array}\right] \tag{8.14}$$

When the PRS device is embedded in a circuit, this matrix is placed into a large matrix describing the full circuit. The first two lines of (14) will be modified for this case. SPICE provides a sparse matrix solver to solve the system. At each timestep, the linearized equations of motion are solved. This serves as the starting place for a Newton-Raphson solution of the full nonlinear equations of

motion. If the solution converges, SPICE saves the results in a history buffer and moves on to the next timestep, until the end of the calculation is reached.

It remains only to code up the above equations and embed them in SPICE. We will exhibit some results of sample runs at the end of this section. First, however, it is appropriate to sketch the equations of motion for a number of other devices, since the most interesting calculations will involve several of our newly developed SPICE devices.

8.6 BREMSSTRAHLUNG DIODE.

We modeled the brems diode using the following simplified 1-D model. The diode has some initial gap d_o and an effective area A. When a voltage is applied to the device, it initially has some high vacuum impedance R_o. As the voltage rises, it eventually reaches the threshhold for Child-Langmuir emission. A further increase in current ultimately causes the diode to switch to the magnetic limited regime. The diode's effective gap begins decreasing exponentially with the onset of Child-Langmuir emission. For simplicity, we assume the following behavior for the gap size:

$$d(t) = d_0 \exp\left(\frac{-v_0(t-t_0)}{d_0}\right) \tag{8.15}$$

where d_0 = initial gap size
t_0 = onset time of Child-Langmuir emission
v_0 = velocity of gap at time t_0.

The voltage-current relations for the three regimes are shown below. For the benefit of SPICE, these have been cast into an admittance form, current as function of voltage.

$$I_{vac} = \frac{V}{R_0}$$

$$I_{CL} = \frac{Z_0 A V^{3/2}}{d^2}$$

$$I_{ML} = I^* \sqrt{\left(\frac{V}{V^*}+1\right)^2 - 1} \tag{8.16}$$

where

$$Z_0 = 2.33\times10^{-6}\,\text{amp}(\text{volt})^{3/2}$$

$$V^* = 5.11\times10^5\,\text{volts}$$

$$I^* = \frac{\alpha f r}{d}$$

$$\alpha = 8500$$

$$f = 1.6 \quad . \tag{8.17}$$

The regime is chosen as follows: If $V < 0$, then $I = I_{vac}$. Otherwise,

$$I = \max\left(I_{vac}, \min\left(I_{CL}, I_{ML}\right)\right) \quad . \tag{8.18}$$

To linearize the equations of motion, we note that the voltage V in the above equations is:

$$V = V_A - V_C \tag{8.19}$$

where V_A = anode voltage
V_C = cathode voltage.

The linearized form of all three regimes takes the general form:

$$g\begin{pmatrix} 1 & -1 \\ -1 & 1 \end{pmatrix}\begin{pmatrix} V_A \\ V_c \end{pmatrix} = j\begin{pmatrix} 1 \\ -1 \end{pmatrix} + \text{source terms} \tag{8.20}$$

where j is the intercept of the tangent curve of I vs. V_A - V_c on the current axis, and "source terms" represent the contribution to the nodal matrix from other devices in the circuit.

For the vacuum case,

$$g = \frac{1}{R_0}$$

$$j = 0 \quad . \tag{8.21}$$

For the Child-Langmuir case,

$$g = \frac{3I_0}{2V_0}$$

$$j = \frac{I_0}{2} \tag{8.22}$$

For the magnetic-limited case,

$$g = \frac{I_0\left(V_0 + V^*\right)}{V_0^{\,2} + 2V_0V^*}$$

$$j = gV_0 - I_0 \tag{8.23}$$

8.7 PLASMA OPENING SWITCH.

The plasma opening switch is a very complicated device. A number of different models have been developed to describe the conduction and opening phases. In addition, the switch is controlled by the plasma density, which may vary in all three dimensions and in time. A single model to characterize this device would be enormous and unwieldy.

The solution we have chosen is to break the POS into three logical components - a plasma source, a conduction-phase device, and an opening switch device (see Figure 8-3).

Our plan is to create several SPICE devices to model each of these components. The full POS can then be constructed by connecting these components together like Lego to custom-build a POS device. We anticipate having nine plasma source devices, two conduction-phase devices, and at least three opening-phase devices. This will allow the user freedom to build at least 54 different POS configurations.

We built at least one of each type of component. Our goal was to verify that no insurmountable problems might lurk in our approach. We achieved this goal. The method works, thanks to the object-oriented approach used by SPICE. In the following sections, we present the equations for the example POS components.

8.8 1-D SNOWPLOW MODEL OF POS CONDUCTION PHASE.

The device has two nodes, labeled 'upstream' and 'downstream'. The voltage across the device is:

$$V_u - V_d = \frac{d\Phi}{dt} \tag{8.24}$$

$$\Phi = LI \tag{8.25}$$

where
- V_u = the upstream voltage
- V_d = the downstream voltage
- F = the flux through the device
- L = the inductance of the POS
- I = the current through the switch.

The current is assumed to flow in a thin sheath which moves into the plasma due to JxB forces, steadily scooping up more and more mass. The equations of motion are:

$$\frac{dx}{dt} = v \tag{8.26}$$

$$\frac{dM}{dt} = \dot{M} \tag{8.27}$$

$$v = \begin{cases} \dfrac{p}{M} & \text{if } M \neq 0 \\ \dfrac{\sigma B}{\sqrt{8\pi\rho(x,t)}} + U(x,t) & \text{if } M = 0 \end{cases} \tag{8.28}$$

$$\dot{M} = \sigma A \rho(x,t)\left(v - U(x,t)\right) \tag{8.29}$$

$$\frac{dp}{dt} = \frac{\sigma B^2 A}{8\pi} + \dot{M}U(x,t) \tag{8.30}$$

where x = position of the snowplow front

v = velocity of the snowplow front

M = mass in the snowplow

$\dot{M}$ = rate of accretion of mass into the snowplow front

p = momentum of the snowplow front

B = magnetic field at the position of the snowplow front

A = area of the snowplow front

σ is the sign ± 1 of the velocity of the snowplow front

$\rho(x,t)$ is the plasma mass density immediately ahead of the snowplow front

U(x,t) is the plasma velocity immediately ahead of the snowplow front.

Note that $\rho(x,t)$ and U(x,t) are functions of position and time. They are specified by SPICE function devices, one example of which we will detail in the next section.

Equations 8.26 - 8.30 are independent of the particular POS geometry (coaxial, radial, or X-Y-Z). They must be supplemented with the following geometry-dependent equations for σ, A, B, and L:

8.9 COAXIAL GEOMETRY, AXIAL MOTION.

$$\sigma = 1$$

$$A = \pi \left| r_a^{\,2} - r_c^{\,2} \right| \tag{8.31}$$

$$B = \frac{I}{5\bar{r}} \tag{8.32}$$

$$L = \left(2 \times 10^{-9}\right)(x - x_i) \log \left| \frac{r_a}{r_c} \right| \tag{8.33}$$

where r_a = anode radius

r_c = cathode radius

$\bar{r}$ = the "mean radius" of the snowplow

x_i = initial snowplow front position

8.10 COAXIAL GEOMETRY, RADIAL MOTION.

$$\sigma = -1$$

$$A = (2\pi\Delta Z)\,x \tag{8.34}$$

$$B = \frac{I}{5x} \tag{8.35}$$

$$L = \left(2\times10^{-9}\right)\Delta Z \log\left(\frac{x_i}{x}\right) \tag{8.36}$$

where ΔZ = gap size of the switch

x_i = initial snowplow front position.

8.11 X-Y-Z GEOMETRY.

$$\sigma = 1$$

$$A = \Delta Y\,\Delta Z \tag{8.37}$$

$$B = \frac{4f}{\Delta Z}\tan^{-1}\left(\frac{\Delta Z}{\Delta Y}\right)I \tag{8.38}$$

$$L = \frac{\left(16\times10^{-9}\right)f^2\,\Delta Y}{\pi\,\Delta Z}\left[\tan^{-1}\left(\frac{\Delta Z}{\Delta Y}\right)\right]^2(x - x_i) \tag{8.39}$$

where ΔY = gap size of the switch

ΔZ= width of the switch in the ignorable dimension

f = fudge factor to account for the approximations inherent in equations 8.39 and 8.40. f is nominally 1.0.

x_i = initial snowplow front position.

In linearizing the equations of motion given above, one needs not only the values of ρ and U at arbitrary positions and time, but one also needs spatial derivatives of both of these quantities. This leads naturally to the next section, which describes a very general function device, and one specific implementation.

8.12 CONSTANT FUNCTION FOR POS PLASMA SOURCE.

As we saw in the previous section, we require a function device that can provide to the conduction-phase device a density function ρ (x,t), a velocity function U(x,t), and their derivatives. While we could implement a special purpose function device which does exactly this and no more, it is just as easy to build a general function device that returns a function f(x,y,t), as well as derivatives in

x, y, and t. Then, we need only specify one such device for the density ρ and another device for the velocity U.

The advantage of using general 2+1 dimensional function devices with derivatives defined with respect to x, y, t is easy to see. We can imagine building a 2-D snowplow model for a POS conduction device. For that, we'll obviously need a function to define ρ, U_x, and U_y, all on a 2-dimensional space, and possibly time-varying. It costs very little to write a completely general function device now.

In fact, we will do something slightly better. We will define an abstract general function device. Then, we will build a number of interchangeable implementations of this device, each having the same capabilities: to provide on demand a function at arbitrary x, y, and t, and also to provide derivatives of that function at arbitrary x, y, and t. The function will be allowed to restrict itself to some arbitrary domain, and to specify a "backup function" for values of (x,y) outside this range.

In equations,

$$f(x,y,t) = \begin{cases} \text{some function } f_{in}(x,y,t) \text{ for } (x,y) \text{ within range} \\ g(x,y,t) \text{ otherwise, where g is an optional "backup function" device} \\ f_0 \quad \text{if } (x,y) \text{ is out of range and g is not specified} \end{cases}$$

Here, g(x,y,t) is a function just like f(x,y,t), which means it can also specify its own domain, backup function, and backup value. A chain of backup functions can be specified of virtually infinite length (i.e., limited only by the amount of memory and virtual memory on the computer.)

For the purposes of this project, we will not need more than this. The computer-savvy reader will immediately see that we are merely defining an "interface for an abstract superclass," which all of its subclasses must implement. This is one feature of object-oriented programming.

Having defined the requirements for a general function class, it is pretty trivial to implement the simplest case, the constant function. We need only specify how f_{in} (x,y,t) and its derivatives are defined. This is chosen as follows:

$$f_{in}(x,y,t) = \text{a constant}$$

$$\text{all derivatives of } f_{in}(x,y,t) \text{ vanish} \quad .$$

The above device can be written in a couple of hours, and we can have confidence that the device will not only be useable for defining a constant plasma density or velocity, but that it will also be interchangeable with other devices that define spatially and/or temporally varying function devices. Any code that uses our constant function device will also be able to use any of these other more interesting function devices without change. This is a principle feature of object-oriented programming—the production of reusable and interchangeable code.

8.13 R-DOT MODEL OF THE POS OPENING PHASE.

This device was the first one we developed with more than two nodes. It has very simple equations of motion. Physically, it behaves like the device pictured in Figure 8-4. The variable resistance takes the form displayed in Figure 8-5.

The resistance is initially some low value during the conduction phase of the POS. The device knows the identity of the conduction phase device, and keeps checking to see if the conduction phase has terminated. When it detects the end of the conduction phase, it begins ramping up the resistance at a constant rate until it reaches some maximum value.

To implement this in SPICE, we assign currents and voltages to the three nodes as shown in Figure 8-6.

Then the equations of motion for the device are:

$$V_1 - V_2 = 0 \tag{8.40}$$

$$I_1 - I_2 - I_3 = 0 \tag{8.41}$$

$$V_1 - V_3 - R(t) I_3 = 0 \tag{8.42}$$

SPICE automatically sets up equations for the voltages V_1, V_2, V_3. In order to implement this device, we allocate space in the sparse matrix for the three currents I_1, I_2, I_3. The above three equations then provide a set of constraints on the three voltages and three currents, sufficient to solve the problem. These equations are already linearized, and it is very simple to write a SPICE device to incorporate them.

8.14 Z-FLOW MODEL OF THE POS OPENING PHASE.

This device is very similar to the R-dot model. It has the same topology and the same watchdog to check for the end of the conduction phase in the conduction-phase device. And two of the equations of motion 8.41 and 8.42 are identical to the R-dot case. The difference is in equation 8.43, which now becomes:

$$V_1 - V_3 = \sigma Z \sqrt{\left| I_1^2 - I_2^2 \right|} \tag{8.43}$$

where Z(t) is the flow impedance of the POS, assumed to take the following idealized form:

$$Z(t) = Z_F \left[1 - \exp\left(\frac{-\left[t - T_{open} \right]}{\tau} \right) \right] \tag{8.44}$$

$$\exp\left(\frac{-\left[t - T_{open} \right]}{\tau} \right) \tag{8.45}$$

$$\sigma = \text{sign}\left(I_1 - I_2 \right) \tag{8.46}$$

where Z_F is the asymptotic flow impedance of the device

T_{open} is the time at which the conduction phase ended

τ is the characteristic time to open.

The above equations can be linearized with very little trouble, providing us with a second POS opening-phase device.

8.15 EXAMPLE CIRCUIT.

As an example of the circuits that can be simulated using the devices we have developed so far, consider the model of ACE 4 shown in Figure 8-7. By adjusting the POS plasma density to achieve a conduction time of 1 μs, we can compute the current and voltage waveforms at the POS and PRS shown in Figures 8-8 through 8-10.

8.16 PROJECT STATUS.

We have created a code capable of computing anything that could be done in the old circuit code. But the new code is infinitely more flexible, since the circuit topology can now be changed at will, adding or deleting new components or new loops without limit. This contrasts starkly with the old circuit code, where each modification in the circuit topology required a painful reprogramming of the equations of motion for the circuit.

Furthermore, new devices can be added to the code with only a small incremental effort. Adding new devices to the old circuit code caused an exponential increase in the code complexity. The reason that the new code is easy to upgrade is that it uses the techniques of object-oriented programming, a set of methods for managing complexity.

8.17 FUTURE WORK.

Future work will advance on two fronts: a new interface, and more SPICE devices. Currently, the code exists only in a user-unfriendly version, suitable for prototyping the new ideas being introduced, but unsuitable for the average user. We will shortly embed our work into the MIRIAD framework, which has a user friendly graphical interface, better plotting capabilities, and tools for performing parameter studies.

A number of SPICE devices remain to be written. Most of these are new function devices representing time and space dependent functions in various combinations needed for detailed analysis of the POS. We will also develop a 2-D snowplow model of the conduction phase of the POS. Interestingly enough, because of the way we have factored the POS into conduction phase and opening phase, this device can also serve as a 2-D model of the implosion phase of the PRS.

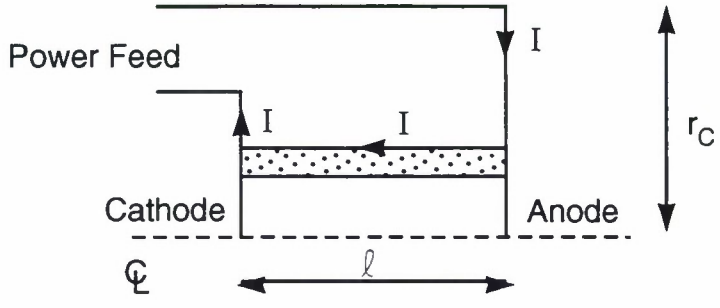

Figure 8-1. Idealized physical model of the PRS. Current flows through the plasma from anode to cathode, creating a magnetic force which causes the plasma to implode on axis. ℓ is the length of the pinched plasma. r_c is the cage radius.

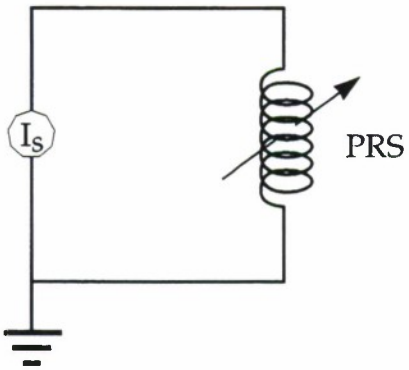

Figure 8-2. Lumped PRS circuit element driven by a current source.

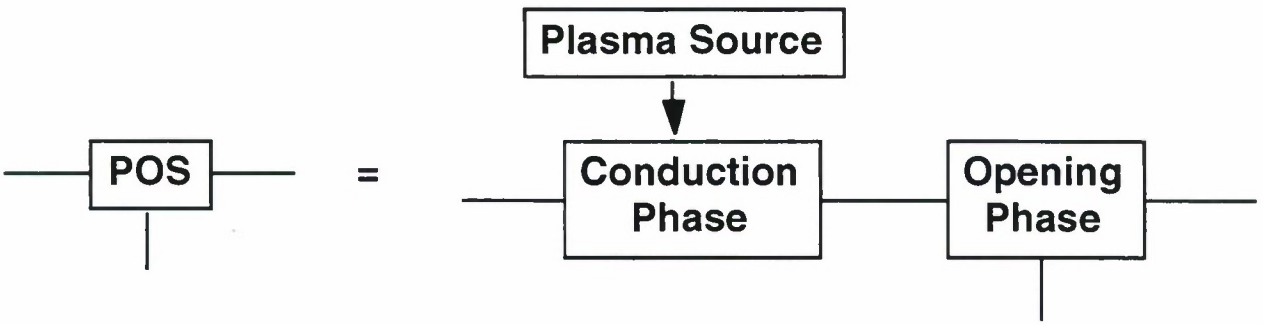

Figure 8-3. Generic form of a plasma opening switch. A POS model is build up from components that model the plasma source, conduction phase, and opening phase.

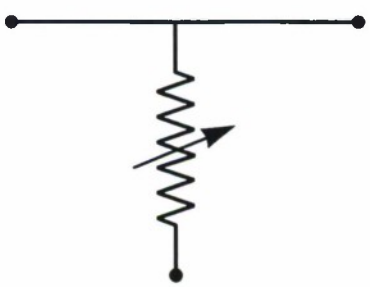

Figure 8-4. Effective circuit diagram of R-dot POS opening model.

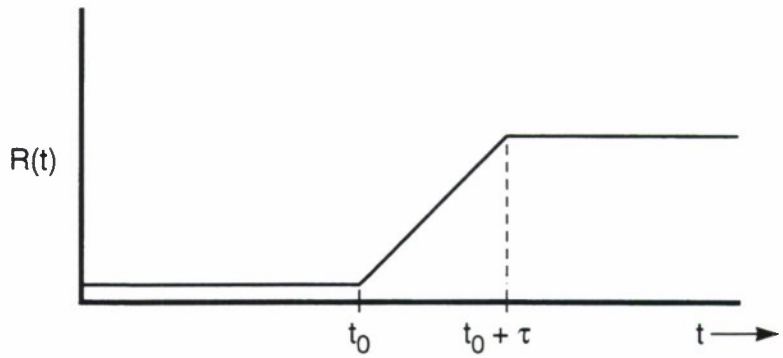

Figure 8-5. Time-dependent behavior of resistance in R-dot POS opening model.

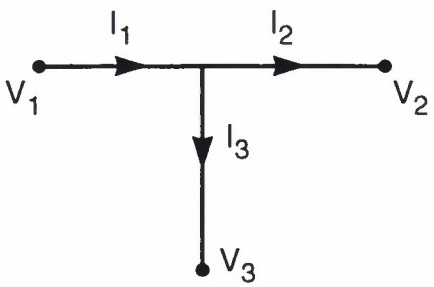

Figure 8-6. Voltage and current notation for the nodes and branches of any POS opening model.

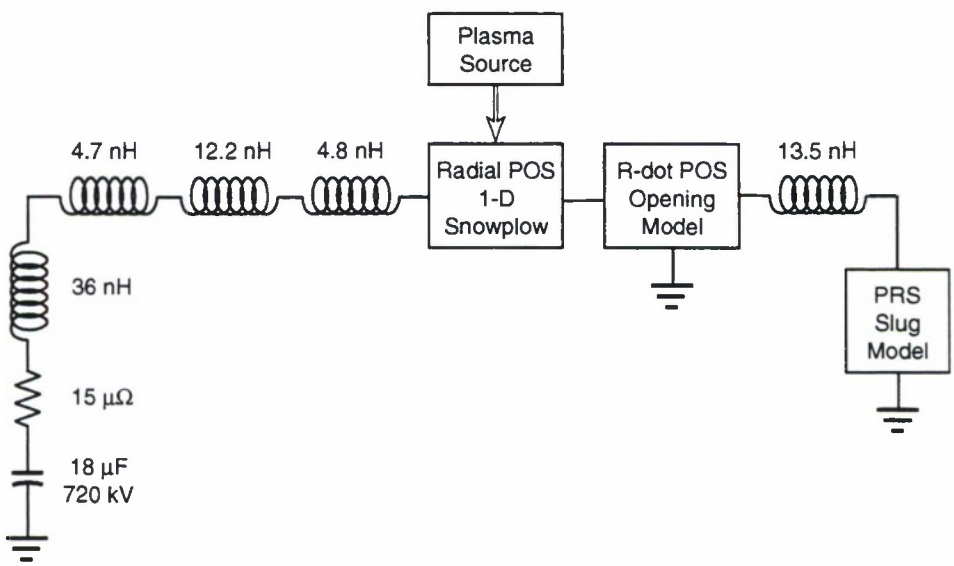

Figure 8-7. A simple model of ACE 4, using SPICE components. The plasma source is adjusted to give a microsecond conduction time. The opening model opens to 1 Ω in 100 ns. The PRS has 20 μg/cm of mass imploding from an initial radius of 2.5 cm.

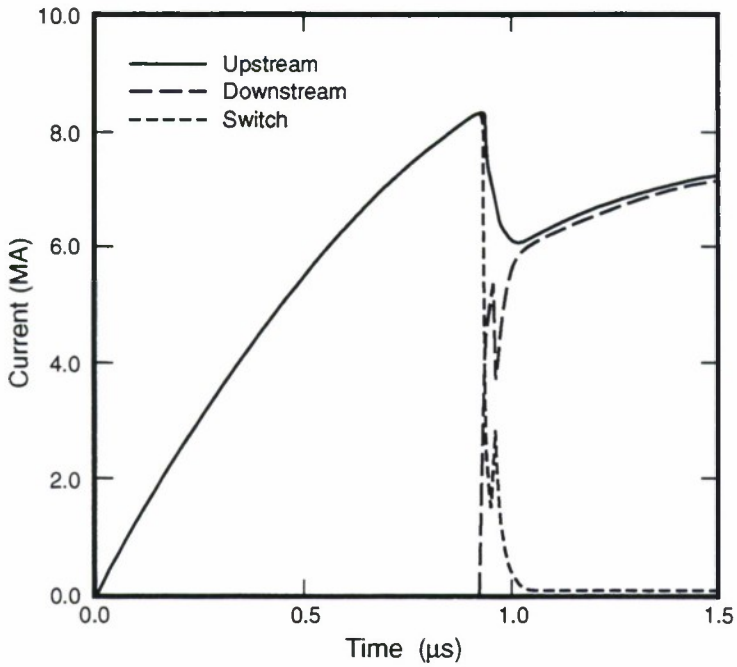

Figure 8-8. Plot of upstream current, downstream current, and switch current for the POS in Figure 8-7. Currents are in MA, time in μsec.

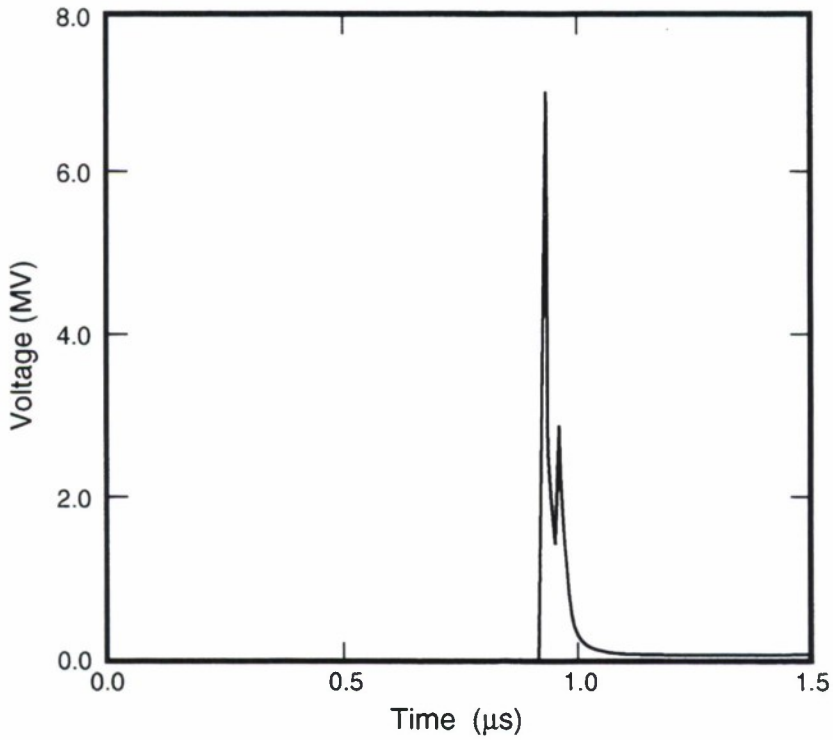

Figure 8-9. Plot of POS voltage for the circuit shown in Figure 8-7.

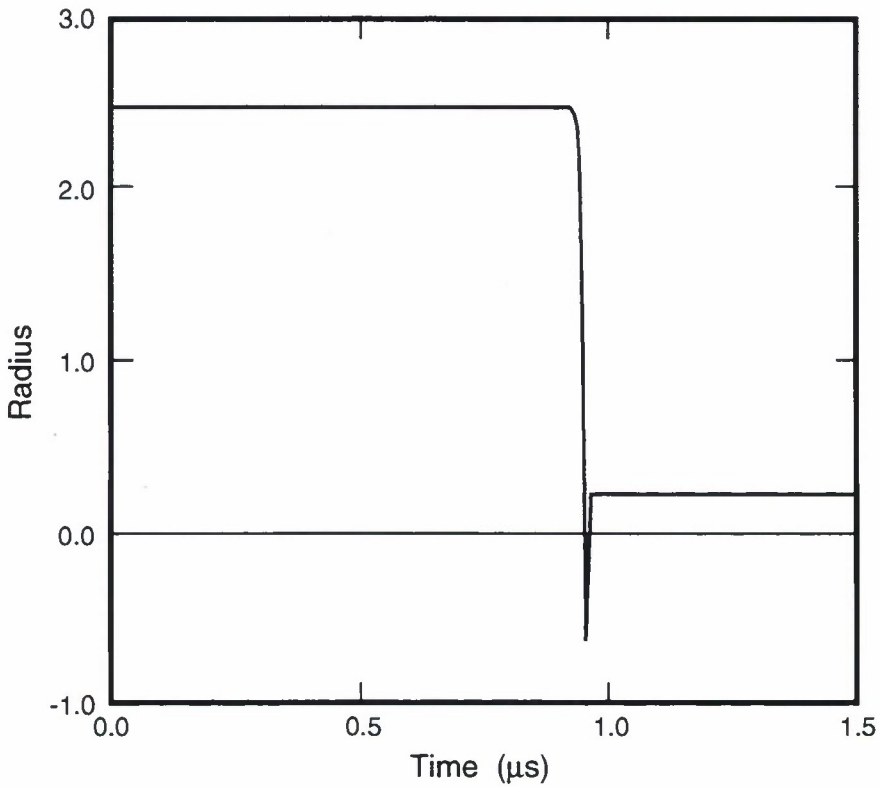

Figure 8-10. Plot of slug radius for the PRS slug model shown in Figure 8-7. The slug radius overshoots at implosion, a numerical artifact which needs to be corrected.

SECTION 9

SNOWPLOW MODEL

9.1 CODE IMPROVEMENTS.

We have upgraded the two-dimensional snowplow code S3Snow[14] to account for the energy equation. Previously, the code solved only the mass and momentum equations. Addition of energy conservation equations permits us to estimate heretofore inaccessible features of the snowplowed plasma, such as its temperature and thickness.

We start with the continuum equations of motion for a compressible inviscid fluid in three dimensions:

$$\frac{\partial \rho}{\partial t} + \vec{\nabla} \cdot (\vec{v}\rho) = 0 \tag{9.1}$$

$$\frac{\partial}{\partial t}(\rho\vec{v}) + \vec{\nabla} \cdot (\vec{v}\rho\vec{v}) + \vec{\nabla} p = 0 \tag{9.2}$$

$$\frac{\partial}{\partial t}\left(u + \frac{1}{2}\rho v^2\right) + \vec{\nabla} \cdot \left[\vec{v}\left(u + \frac{1}{2}\rho v^2\right)\right] + \vec{\nabla} \cdot (\vec{v}p) = 0 \tag{9.3}$$

where ρ = mass density

$\vec{v}$ = fluid velocity

u = energy density

p = pressure.

We also assume an equation of state that relates the pressure and energy density:

$$p = (\gamma - 1)u \tag{9.4}$$

Normally, we would integrate these equations over a control volume to get a discretized set of equations to be solved on a computer. However, the lesson we have learned from the snowplow model is that there is a singular surface (the snowplow front) which must be treated carefully. The snowplow approximation states that all the interesting physics happens on this surface. Furthermore, we can use physical symmetry to reduce this to a line in two dimensions.

We therefore look for a formulation that takes account of this simplification. We proceed in two steps:

1. Integrate over a control area to reduce the 3-D fluid equations to a 1-D fluid model, where the "dimension" is arc-length along the snowplow front.

2. Discretize this 1-D fluid model to obtain the equations of motion for the snowplow front.

This is illustrated in Figure 9-1. It is convenient to define three local unit vectors, $\hat{s}, \hat{n}$, and $\hat{z}$. $\hat{s}$ is tangent to the snowplow front; $\hat{n}$ is normal to it $\hat{z}$ points in the "ignorable" dimension (in the coaxial case, this would be the $\hat{\theta}$ unit vector). The control area to be integrated lies in the $\hat{n} - \hat{z}$ plane. In the z-direction, one integrates over the full ignorable dimension (for the coaxial case, this would be an integration over $d\theta$). In the $\hat{n}$ direction, one integrates only across the snowplow front, which is presumed to be finite but small compared to all other lengths in the problem.

We now define three new quantities along the snowplow front. These are functions of arc-length s, and time t:

$$\mu = \int_{\text{plane}} \rho \, dA \tag{9.5}$$

$$\vec{\pi} = \int_{\text{plane}} \rho \vec{v} \, dA \tag{9.6}$$

$$\psi = \int_{\text{plane}} u \, dA \tag{9.7}$$

The integration assumes that the plasma ahead of the snowplow front is unaffected until the front arrives, at which time it is scooped up into the front, adding in mass, momentum, and energy. We therefore define the undisturbed plasma quantities:

ρ_0 = mass density of undisturbed plasma

$\vec{v}_0$= velocity of undisturbed plasma

u_0 = energy density of undisturbed plasma

p_0 = thermal pressure of undisturbed plasma.

The result of integrating over the control area is easily understood as a 1-D fluid model with source terms. In general

$$\frac{\partial \mu}{\partial t} + \frac{\partial}{\partial s}(v_s \mu) = \dot{\mu}_0 \tag{9.8}$$

$$\frac{\partial \vec{\pi}}{\partial t} + \frac{\partial}{\partial s}(v_s \vec{\pi}) + \vec{p} = \dot{\vec{\pi}}_0 + \vec{f} \tag{9.9}$$

for an axisymmetric geometry

$$\frac{\partial \psi}{\partial t} + \frac{\partial}{\partial s}(v_s \psi) = \dot{\psi}_0 + (\gamma - 1)\psi \left[\frac{\vec{v} \cdot \hat{\gamma}}{r} + \frac{\partial v_s}{\partial s} \right] \tag{9.10}$$

where

$$\vec{v} = \frac{\vec{\pi}}{\mu} \tag{9.11}$$

$$\vec{v}_s = \vec{v} \cdot \hat{s} \tag{9.12}$$

$$\vec{p} = (\gamma - 1)\left[\frac{-\psi \hat{r}}{r} + \left(\frac{\partial \psi}{\partial s}\right)\hat{s}\right] \quad . \tag{9.13}$$

The terms proportional to $\hat{r}$ term should be taken to be zero in a rectangular geometry.

The equations contain source terms that represent mass, momentum and energy scooped up by the front:

$$\dot{\mu}_0 = \rho_0 \Delta Z (\vec{v} - \vec{v}_0) \cdot \hat{n} \tag{9.14}$$

$$\dot{\vec{\pi}} = \dot{\mu}_0 \vec{v}_0 \tag{9.15}$$

$$\Psi_0 = \left(\frac{u_0}{\rho_0} + \frac{1}{2}(\vec{v} - \vec{v}_0)^2 + \frac{p_0}{\rho_0}\right)\dot{\mu}_0 \tag{9.16}$$

where ΔZ is the length of the ignorable dimension. They also contain a source term that represents the external magnetic force applied at the snowplow front:

$$\vec{f} = \Delta Z \left(\frac{B^2}{8\pi} - p_0\right)\hat{n} \quad . \tag{9.17}$$

These equations are easily discretized. The result is a generalized version of the original snowplow equations of motion.

9.2 RESULTS FROM THE IMPROVED SNOWPLOW MODEL.

After coding up the discretized equations of motion, one can compute the time-evolution of the temperature of the snowplow front. Consider the following analytically soluble configuration.

Let a cold plasma be uniformly distributed across a gap, as in Figure 2-2.

Assume that the magnetic field increases linearly in time. Since the plasma is cold, its thermal pressure vanishes, and we have the following simplified equations of motion:

$$B = \dot{B}\, t \tag{9.18}$$

$$\frac{d\mu}{dt} = \Delta Z \rho_0 \frac{dx}{dt} \tag{9.19}$$

$$\frac{d\pi}{dt} = \Delta Z \frac{\dot{B}^2 t^2}{8\pi} \tag{9.20}$$

$$\frac{d\Psi}{dt} = \frac{\Delta Z \rho_0 v^3}{2} \quad . \tag{9.21}$$

Integrating (19) and (20), we find:

$$\mu = \Delta Z \, \rho_0 \, x \tag{9.22}$$

$$\pi = \frac{\Delta Z \dot{B}^2 t^3}{24\pi} = \frac{d}{dt}\left(\mu \frac{dx}{dt}\right) \quad . \tag{9.23}$$

Substituting (22) into (23) and integrating, we find:

$$x = \frac{\dot{B}\, t^2}{\sqrt{48\pi\rho_0}} \tag{9.24}$$

$$v = \frac{\dot{B}\, t}{\sqrt{12\pi\rho_0}} \tag{9.25}$$

These are the equations of a uniformly accelerating front:

$$x = \frac{1}{2} g\, t^2 \tag{9.26}$$

$$v = g\, t \tag{9.27}$$

$$g = \frac{\dot{B}}{\sqrt{12\pi\rho_0}} \tag{9.28}$$

One then integrates (21) to find the energy as a function of time. This assumes, of course, that no ionization takes place, and that no energy is lost due to radiation.

$$\Psi = \frac{\Delta Z \rho_0 g^3 t^4}{8} \tag{9.29}$$

It is interesting to recast these results slightly. Often, one knows the length ℓ (in cm) of the conduction region and the conduction time τ (in microseconds).

Then the directed velocity, thermal velocity, and temperature at the end of the conduction phase are:

$$v = \frac{2\ell}{\tau} \quad \text{cm}/\mu\text{sec} \tag{9.30}$$

$$v_{th} = \frac{\sqrt{2\ell}}{\tau} \quad \text{cm}/\mu\text{sec} \tag{9.31}$$

$$\theta = \frac{25}{3}\left(\frac{\ell}{\tau}\right) \quad \text{eV} \tag{9.32}$$

These formulae are useful for back-of-the-envelope calculations. For ACE 4, for example, with a POS length of 20 cm and a conduction time of 1 μs, we find:

$v = 20$ cm/μs

$v_{th} = 14$ cm/μs

$\theta = 3.3$ keV.

The very high temperature leads us to suspect that some ionization must be going on, and possibly also some radiative cooling. The snowplow model can easily be applied to this sample problem, and one finds precisely the analytic result. This is not surprising, since the snowplow code merely solves the problem numerically.

However, we should note that 2-D fluid codes such as DELTA and Mach2 have considerably more trouble within this problem. If run in Lagrangian mode with high spectral resolution, they come within fifty percent of the temperature estimated by equation 2-2 (see Section 2.3). In Eulerian mode, they get the correct velocity, but are typically short in temperature by one to two orders of magnitude as a result of too coarse zoning. This is a difficulty, because nontrivial problems must generally be run in Eulerian mode to avoid tearing the zones apart.

The Eulerian mode is unable to resolve the short distance scales in the snowplow unless an excessively large number of zones cover the problem space. On the other hand, because of its zero thickness feature the snowplow model overestimates the temperature relative to finely resolved Mach2 Lagrangian calculations by about fifty percent.

We note that the energy equation as formulated here is obviously incomplete. It should be clear that at the high temperatures predicted by the naive model given above, the snowplow front will ionize rapidly. In future work, it would be worthwhile to try to account for this ionization. It is unclear at this time whether radiation should also play an important role in the energy equation.

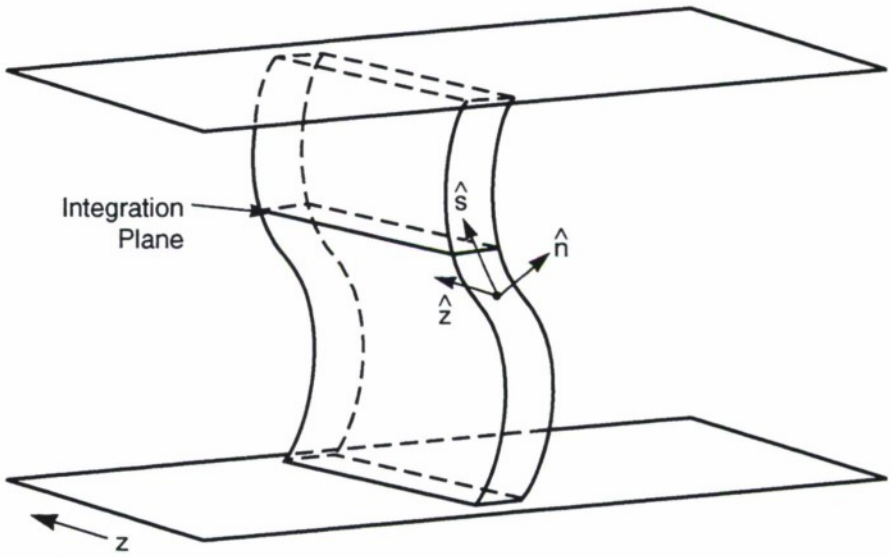

Figure 9-1. 3-D snowplow front. The symmetry in the ignorable direction, here labeled z, can be integrated out. The three unit vectors $\hat{s}$, $\hat{n}$, and $\hat{z}$ are shown at one point on the surface.

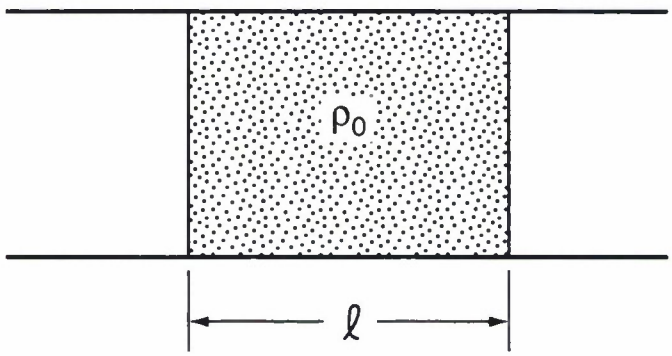

Figure 9-2. Plasma distributed uniformly in a POS region of length ℓ. The ignorable dimension has length ΔZ. Plasma velocity and temperature are assumed to be zero.

SECTION 10

CONVOLUTE CURRENT LOSSES IN THE ACE 4 COAXIAL CONFIGURATION

In June of 1994, measurements were made of current losses in the ACE 4 coaxial configuration. The losses are believed to be associated with the convolute transition between the radial triplate feed and the coaxial sections. Figure 10-1 shows a circuit diagram of the configuration and indicates the positions of current monitors and the location of the convolute.

We focus attention on shot 895, which was taken with no plasma opening switch; thus on Figure 10-1 the branch marked POS is an open circuit to ground. The results for shot 895 are given in Figures 10-2 through 10-4. The Rogowski coils labeled IRISI and IROSI measure the currents near the insulator stack in oil and in vacuum, respectively, while the ICOSI monitor measures currents just upstream of the convolute (with respect to the directions of power flow). The IRFI Rogowski, on the other hand, measures current just downstream of the convolute. The ICCTI and IRCT monitors measure current at various locations within the 200 nH inductor at the end of the coaxial feed section. For the first microsecond of current flow, that is for 0.5×10^{-6} sec $< t < 1.5 \times 10^{-6}$ sec, the current measured by IRFI is roughly one-half of that measured by the upstream monitors. This is interpreted to mean that half of the current is lost at the convolute. The nearly constant current recorded by IRFI for $t > 5 \times 10^{-7}$ sec indicates shorting of the convolute at $t \approx 1.5\ \mu s$. We interpret this to indicate that an electrode plasma, formed near the convolute structure early in the current pulse, moves across the anode-cathode gap in about 1.0 μs following the onset of current.

Let us assume for the moment that the convolute leakage results from electrons locally emitted in regions of the null or weak magnetic fields associated with the twelve post convolute structure. This requires the existence of a cathode plasma in these regions. The voltage V across the 2.5 cm A-K gap of the convolute is $V = L\dot{I} = 248 \times 10^{-9} H \times 1 \times 10^{12} \text{amps/sec}$ $V \approx 248$ kV. The voltage computed in this manner is consistent with that determined by inductively correcting the voltage VCOT measured in the oil. The electric field across the D = 2.5 cm A-K gap at the convolute location, approximately 100 kV/cm, is probably sufficient to generate the cathode plasma.

The Child-Langmuir Law give us an estimate of the current density at the beginning of the current pulse in the neighborhood of magnetic nulls

$$j = 2.3 \times 10^{-6} \frac{V^{3/2}}{D^2}$$

$$= 46 \text{ amp/cm}^2 \ . \qquad (10.1)$$

The total current loss, I_{loss}, would be j x 2 (a cathode on each side of the anode ring) x A, where A is the effective emission area. Taking $A = 2\pi Rh$ where $R \approx 20$ cm is the radius of the anode ring and $h \approx 7.5$ cm is its height, give $I_{loss} = 87$ kA at the time t~0.6 μs (Figure 10-3) when the voltage was 250 kV. To say that the estimates and the observations agree would be an overstatement, but considering uncertainties in the effective emission area, the comparison is close enough to justify proceeding further on the basis of the hypothesized mechanism. We

make this assertion fully cognizant of the impact that magnetic fields should have on transport of electrons.

We ask now whether the current density, 46 amp/cm^2 at the measured voltage is enough to generate an anode plasma. The rate of energy deposition at the anode surface is

$$\begin{aligned} j\frac{dE}{dx} &= 46\times 1.81\times 10^6 \text{watts/gm} \\ &= 83\times 10^6 \text{watts/gm} \end{aligned} \tag{10.2}$$

Here dE/dx = 1.81 MeV - cm^2/gm is the stopping power of iron at 250 KeV. At this energy the stopping power of iron does not differ substantially from that of the stainless steel anode. In one microsecond the surface dose amounts to about 83 j/gm, corresponding to a temperature increase of about 200°C. According to Sanford, et al this is short of the ~400°C temperature increase required to generate an anode plasma.[15]

We assume therefore that the only relevant electrode plasma is the cathode plasma. The leakage current as a function of time can now be estimated as

$$I(t) = 87\left(\frac{V(t)}{250}\right)^{3/2}\left(\frac{D}{D-vt}\right)^2 \text{kA} \tag{10.3}$$

where I is in kA, V(t) in kV, D in cm, t, the time from onset of current, in μs, and V the cathode plasma expansion velocity in cm/μs. Since the D = 2.5 cm gap shorts in 1 μs, we take v = 2.5 cm/μs. Equation 10.2 fits the observed leakage current for the first one-half microsecond or so; clearly the theory is an inadequate description of the current leakage during the last one-half of gap closure.

In summary, the calculations presented here are based on a model of local Child Langmuir electron emission in regions of the magnetic nulls near the anode ring. The theory assumes that the emission law applies over the entire area of the anode ring. No account is taken of the effects of magnetic fields arising from currents in metallic conductors; for this reason the effective area must be considered highly uncertain.

In view of the strong magnetic fields that are expected to exist beyond the immediate neighborhoods of the magnetic nulls, it is surprising, as the model suggests, that an emission area equal to the area of the entire anode ring should be involved in the flow of leakage current. On the other hand if we assume that the observed leakage current flows over a small area around the location of an unperturbed magnetic null, we would be forced to conclude that one parasitic current channel leads to the formation of two nulls at positions half way between the convolute posts and the parasitic channel. Continuing this line of reasoning forms a semi-empirical justification for the appearance of the entire area in the calculation of leakage currents. It is also possible that the correct explanation lies elsewhere; perhaps the leakage currents crossing the convolute are not locally emitted, but originate remotely from the convolute, for example near the insulator stack.

Currents were also measured with a plasma opening switch located just down stream of the convolute. In this case, with the large inductor shorted by the POS, little voltage should occur at the convolute during the conduction phase of the switch, and current should not be lost through the convolute.

Losses were observed in the first experiments conducted with a POS in place, but these losses were believed to be caused by POS plasma invading regions of the diode upstream of the convolute. This belief was subsequently verified and no losses observed when flashboard plasma was localized by baffles to the intended region downstream of the convolute.

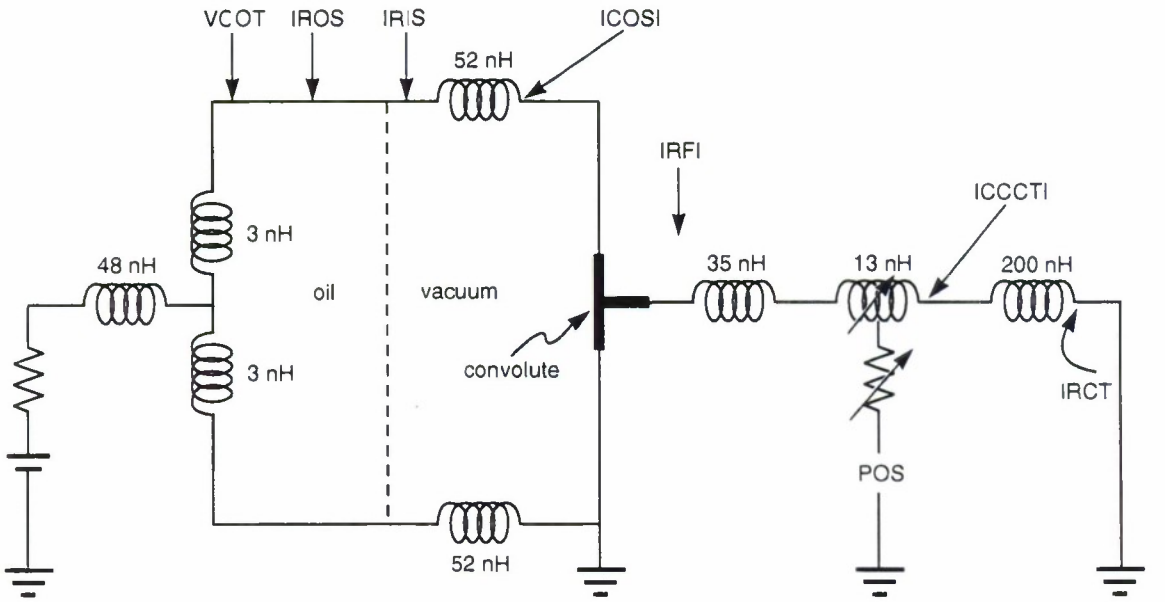

Figure 10-1. Circuit representation of ACE 4 coaxial configuration showing location of current and voltage monitors.

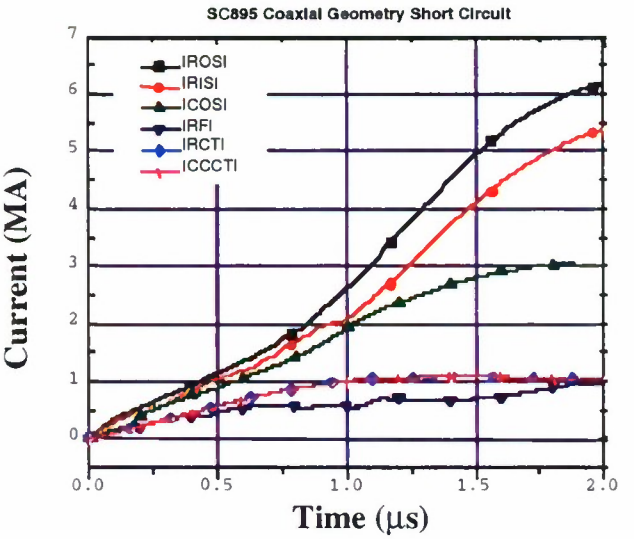

Figure 10-2. Currents for shot 895 measured at locations indicated in Figure 10-1.

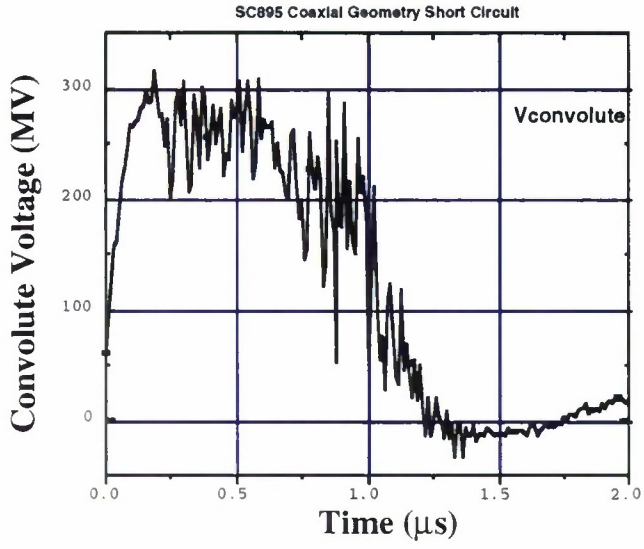

Figure 10-3. Voltage at convolute obtained by inductive correction of measured voltage VCOT.

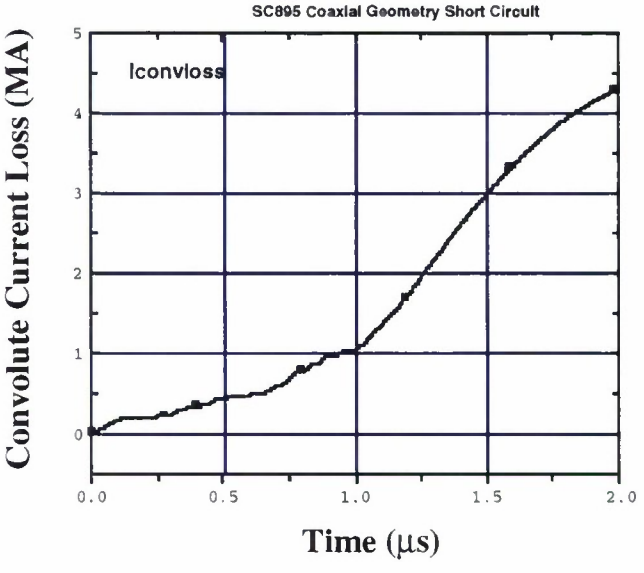

Figure 10-4. The measured current loss at the convolute.

SECTION 11

ELECTRODE POWER LOSSES IN HIGH MAGNETIC FIELDS

In pulsed power generators where currents converge to levels of megaamps per centimeter before passing through a load, dissipation of power in the metallic electrodes can become a substantial fraction of the power delivered to the load. The losses can be important, for example, for plasma radiating source and ion beam loads. Hussey[6] has performed magneto hydrodynamic calculations of resistive, shock, and ablative losses for a cylindrical convergence of power between two parallel planes. The losses follow simple scaling laws to a high degree accuracy. This fact permits the predominantly resistive dissipation to be described by a simple analytical model for arbitrary current wave forms. The description of the losses in terms of a dynamic resistance depending on current is especially convenient for incorporation of the effect into effective circuit models of the pulsed power system.

As magnetic field diffuses into a metallic conductor, the heating of the metal by the current leads to an increase of the resistivity and eventually to melting and vaporization of the metal. Significant power losses can occur however even before vaporization becomes significant, that is even before there has been a substantial change in the specific volume of the heated material. Then the most important physical process is the enhanced magnetic diffusion associated with the increasing resistivity of the heated electrodes.

The one-dimensional nonlinear diffusion of magnetic field into a heated, incompressible conductor has been considered by Knoepfel.[17] He found a self-similar solution for a material whose resistivity is proportional to its specific internal energy. Specifically,

$$B(x,t) = kt^{1/2}(1 - x/vt)^{1/2} \quad , \tag{11.1}$$

where B is the magnetic field at the distance x from the vacuum interface, the time t is measured from the instant at which the surface field is turned on, and v is the constant velocity at which the diffusion front moves into the medium. The constant prefactor k and v depend on material constants. The manner of dependence can be found in Knoepfel, but it is also given in the developments that follow. It is apparent from the preceding equation that a requirement for the validity of self similarity is that the boundary field should increase as the square root of time.

In the following we shall develop approximate solutions of the magnetic diffusion equation for an arbitrary dependence of the boundary field on time. For this purpose we assume a resistivity

$$\eta = \eta_0(\varepsilon/\varepsilon_0)^n \tag{11.2}$$

where e is the specific internal energy, ε_0, η_0, and n are material constants. We look for approximate solutions of the form

$$\frac{\varepsilon}{\varepsilon_0} = A(t)\left(1 - \frac{x}{X(t)}\right)^r \tag{11.3}$$

$$B(x,t) = B(0,t)(1 - x/X(t))^s \tag{11.4}$$

where B(0,t) is the prescribed surface field and where X(t), the position of the advancing diffusion front, A(t), and the exponents r and s are to be determined. The governing equations are the magnetic diffusion equation

$$\frac{\partial}{\partial x}\left(\eta\frac{\partial B}{\partial x}\right)=\frac{4\pi}{c^2}\frac{\partial B}{\partial t} \tag{11.5}$$

and the first law of thermodynamics for a stationary medium with mass density ρ.

$$\rho\frac{\partial \varepsilon}{\partial t}=\eta j^2=\eta\left(\frac{c}{4\pi}\frac{\partial B}{\partial x}\right)^2 \tag{11.6}$$

Substituting the trial solutions into the governing equations and demanding that the resulting equations be satisfied for $(1-x/X)<<1$ leads to the required values of the exponents r and s,

$$s = 1/2n \tag{11.7}$$

$$r = 1/n \tag{11.8}$$

The time dependent quantities A(t) and X(t) are obtained by demanding balance between volume integrated rates of joule heating and increase of internal energy in addition to overall energy conservation. The first condition is expressed by integrating equation 6 between x = 0 and x = X(t). Using equation 2, this condition gives:

$$\frac{\rho\varepsilon_0}{r+1}\frac{\partial(AX)}{\partial t}=\frac{1}{2}\left(\frac{c}{4\pi}\right)^2\eta_0 sB(0,t)^2\frac{A^n}{X} \tag{11.9}$$

Total energy follows from multiplying equation 5 by B(x,t) and integrating over x. Since B(X,t) vanishes, we get

$$-\left(\frac{c}{4\pi}\right)^2\eta B\frac{\partial B}{\partial x}(0,t)=\left(\frac{c}{4\pi}\right)^2\int\eta\left(\frac{\partial B}{\partial x}\right)^2 dx+\frac{1}{8\pi}\frac{\partial}{\partial t}\int_0^X B^2 dx \quad . \tag{11.10}$$

Substituting equations 2, 3, 4 and 9 into the latter result gives:

$$\frac{1}{8\pi(2s+1)}\frac{\partial}{\partial t}\left(B(0,t)^2X\right)=\frac{\rho\varepsilon_0}{r+1}\frac{\partial}{\partial t}(AX) \quad . \tag{11.11}$$

The solution to equations 9 and 11 follow easily. They are

$$A(t)=\frac{B(0,t)^2}{8\pi\rho\varepsilon_0}$$

$$\frac{B(0,t)^4X(t)^2}{8\pi}=\frac{n+1}{2n^2}\left(\frac{c}{4\pi}\right)^2\frac{\eta_0}{(8\pi\rho\varepsilon_0)^n}\int_0^t B(0,t)^{2n+4}dt \quad . \tag{11.12}$$

Following Singer,[18] we now specialize to the case n = 1 in equation 2, that is, where the resisting of the material varies linearly with the specific energy density. Energy is lost to unit area of the electrodes at a rate:

$$-\left(\frac{c}{4\pi}\right)^2\left(\eta B\frac{\partial B}{\partial X}\right)(0,t)=\frac{1}{2}\left(\frac{c}{4\pi}\right)^2\eta_0 A(t)B(o,t)^2/x(t)$$

$$=\frac{1}{2}\left(\frac{c}{4\pi}\right)^2\left(\frac{\eta_0}{8\pi\rho\varepsilon_0}\right)\frac{B(o,t)^4}{x(t)}$$

$$=\frac{c}{16\pi^{3/2}\sqrt{2}}\left(\frac{\eta_0}{8\pi\rho\varepsilon_0}\right)^{1/2}\frac{B(o,t)^6}{\left[\int_0^t B(o,t)^6dt\right]^{1/2}} \quad . \tag{11.13}$$

In an axial geometry at a distance r from the axis, where

$$B\ (\text{gauss}) = I(\text{amps})/5r\ (\text{cm}),$$

the power loss is given by:

$$\frac{P}{A}=\frac{1.27x10^{-11}}{r^3}\left(\frac{\eta_0}{\rho\varepsilon_0}\right)^{1/2}I^6(t)/\left[\int_0^t I^6dt\right]^{1/2}\ \text{watts/cm}^2 \quad , \tag{11.14}$$

where r is in cm, ρ in grams/cm^3, ε_0 in joules/gm. The total power loss to both electrodes between the initial load radius r = a and the outer radius of the diode at $r = R_0 >> a$ is given by the integral

$$P=2\int_a^\infty\frac{P}{A}2\pi rdr$$

$$=\frac{1.59x10^{-10}}{a}\left(\frac{\eta_0}{\rho\varepsilon_0}\right)^{1/2}I^6(t)/\left[\int_0^t I(t)^6dt\right]^{1/2}\ \text{watts} \tag{11.15}$$

The equivalent resistance R(t) for circuit calculations is

$$R(t) = P/I^2(t)\ \text{ohms} \quad . \tag{11.16}$$

The energy lost to the electrodes in time t is

$$E=\frac{3.18x10^{-10}}{a}\left(\frac{\eta_0}{\rho\varepsilon_0}\right)^{1/2}\left[\int_0^t I^6(t)dt\right]^{1/2}\ \text{joules} \tag{11.17}$$

For a linearly ramped current

$$E(t)=\frac{1.20x10^{-10}}{a}\left(\frac{\eta_0}{\rho\varepsilon_0}\right)^{1/2}I^3(t)t^{1/2} \quad . \tag{11.18}$$

Choosing

$$\left(\frac{\eta_0}{\rho\varepsilon_0}\right)^{1/2} = 7.27\text{x}10^{-4}\left(\frac{\Omega - \text{cm}^4}{\text{joule}}\right)^{1/2} \tag{11.19}$$

leads to the results shown in Figure 11-1 for a current rising linearly to a value I_m at $t = 10^{-7}$ sec

$$E(I_m, a) = 2.76\text{x}10^{-17}\,\frac{I_m^3}{a} \tag{11.20}$$

The results, plotted in Figure 11-1, should be compared with the corresponding numerical results calculated by Hussey[16] in Figure 11-2, using an MHD code that incorporates equations of state and resistivity routines.

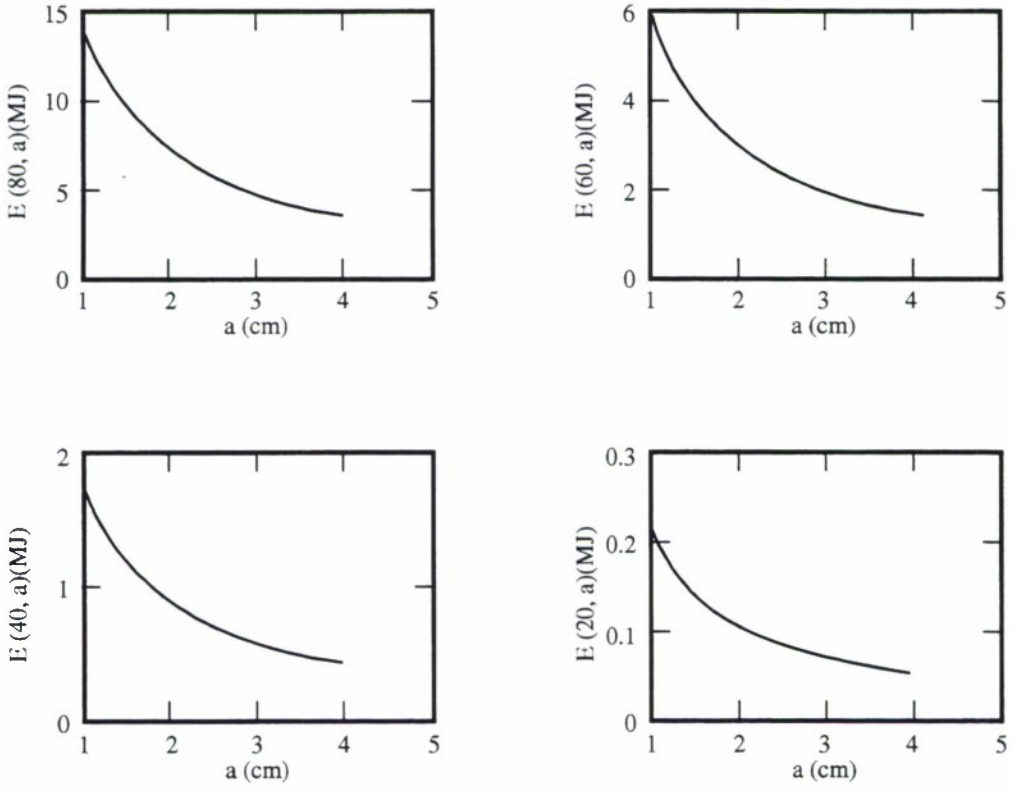

Figure 11-1. Analytical model calculations of energy loss in megajoules versus initial foil radius for several values of final current in megaamps (at $t = 10^{-7}$ sec)

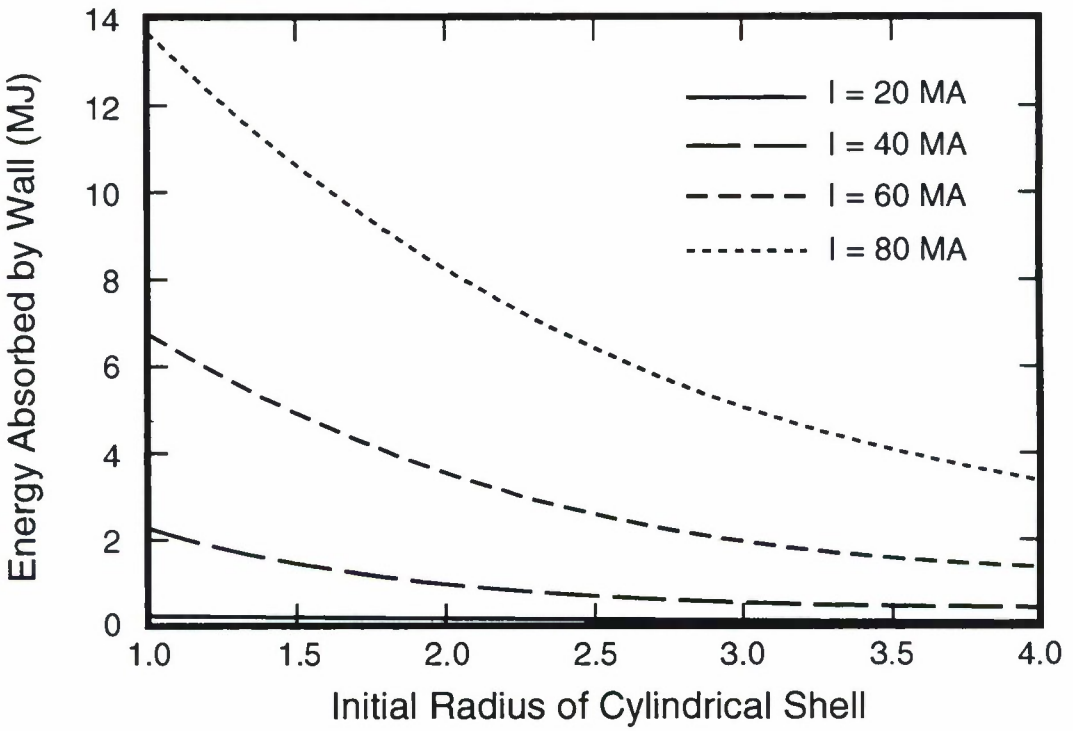

Figure 11-2. Numerical calculations of electrode energy loss in megajoules versus initial foil radius for several values of final current in megaamps (at $t = 10^{-7}$ sec).[16]

SECTION 12

REFERENCES

1. Goodrich, P.J., R.J. Commisso, J.M. Grossmann, D.D. Hinshelwood, R.A. Riley, S.B. Swanekamp, and B.V. Weber, "High Power Plasma Opening Switch Operation on HAWK," proceedings from the 10th International Conference on High Power Particle Beams, pp. 299-302, San Diego, California, June 20-24, 1994 (Unclassified).

2. Parks, D., R. Ingermanson, E. Salberta, P. Steen and J. Thompson, "Advanced Simulator Power Flow Technology/Advanced Radiation Simulation," Maxwell Laboratories, Inc., S-Cubed Division, Annual Report 555-DTR-94-14855, May 1995 (Unclassified).

3. Harvey, J.M., I. Katz, and R.C. Vik, "A Study of Equations of State/Opacity of Ionized Gases," DNA 3278F, October 1973 (Unclassified).

4. Cohen, H.D., D.E. Parks, and A.G. Petschek, "A Study of Equations of State/Opacity of Ionized Gases," DASA 2597-1, April 1971 (Unclassified).

5. Layser, D., "On a screening Theory of Atomic Spectra," Ann. Phys. 8, 271 (1959) (Unclassified).

6. Naqvi, A.M. and G.A. Victor, "Screened Hydrogenic Orbitals for Lithium to Cesium Isoelectronic Sequences, with Selected Calculations of Energies and Transition Probabilities," Air Force Weapons Laboratory No. RTD-DTR-63-3118, Vol I, November 1963 (Unclassified).

7. Bates, D.R., and A. Damgaard, "The Calculation of the Absolute Strengths of Spectral Lines," Phil. Trans. Roy. Soc. London A242, 101 (1949) (Unclassified).

8. Burgess, A., and M.F. Seaton, "A General Formula for the Calculation of Atomic Photo-Ionization Cross Sections," Monthly Notices Roy. Astron. Soc. 120, 121 (1960) (Unclassified).

9. Griem, H.R., "Plasma Spectroscopy," p. 52f, 109f, McGraw-Hill, New York (1964) (Unclassified).

10. Parks, D.E., G. Lane, J.C. Stewart, and S. Peyton, "Optical Constants of Uranium Plasma," NASA Report No. CR-72348 (GA-8244) (1967) (Unclassified).

11. N.F. Mott and H.S. Massey, "The Theory of Atomic Collisions," p. 497 Oxford, (1965) (Unclassified).

12. Bates, I.R., A.E. Kingston and R.W.P. McWhirter, "Recombination Between Electrons and Atomic Ions, Vol. I. Optically Thin Plasmas," Prov. Roy. Soc. A267 p. 297, (1962) (Unclassified).

13. Whitney, K.G., J.W. Thornhill, J.P. Apruzese, and J. Davis, "Basic Considerations for Scaling Z-pinch X-ray Emission with Atomic Number," J. Appl. Phys. 67 (4) 172S, (February 1990) (Unclassified).

14. Parks, D., E. Waisman, R. Ingermanson, E. Salberta, "Above Ground Test (AGT) Evaluation Support Program, Maxwell Laboratories Final Report, Defense Nuclear Agency DNA-TR-94-102 (Unclassified).

15. Sanford, T.W.L. et al., "Measurement of Electron Energy Deposition Necessary to Form an Anode Plasma in Ta, Tu, and C for Coaxial Bremstrahlung Diodes," J. Appl. Phys. 66 (1) 1989 pp. 10-22 (Unclassified).

16. Hussey, Thomas, Air Force Phillips Lab, Private Communication, May 1994 (Unclassified).

17. Knoepfel, Heinz, Pulsed High Magnetic Fields, North-Holland Publishing Company, Amsterdam, London, (1970) (Unclassified).

18. Singer, S. and Hunter, R.O., "Energy Losses in Conductors Carrying Very High Currents," 3rd IEEE International Pulsed Power Conference, p. 351, (1981) (Unclassified).

DISTRIBUTION LIST

DEPARTMENT OF DEFENSE

DEFENSE TECHNICAL INFORMATION CENTER
8725 JOHN J KINGMAN RD., SUITE 0944
FORT BELVOIR, VA 22060-6218
ATTN: DTIC/OCP

DEFENSE THREAT REDUCTION AGENCY
45045 AVIATION DRIVE
DULLES, VA 20166-7517
ATTN: NSSA, W SUMMA
ATTN: NSSS, K WARE
ATTN: TRC

DEFENSE THREAT REDUCTION AGENCY
ALBUQUERQUE OPERATIONS
1680 TEXAS ST. SE
KIRTLAND AFB, NM 87117-5669
ATTN: SWP, G BALADI

DEPARTMENT OF DEFENSE CONTRACTORS

BERKELEY RSCH ASSOCIATES, INC.
P O BOX 241
BERKELEY, CA 94701-0241
ATTN: R KARES
ATTN: S BRECHT

ENERGY COMPRESSION RESEARCH CORP
6355 NANCY RIDGE DRIVE
SAN DIEGO, CA 92121
ATTN: D S WEIN

FORD MOTOR COMPANY CORPORATION
4800 EAST RIVER ROAD
MINNEAPOLIS, MN 55421
ATTN: M MOSBROOKER

GA TECHNOLOGIES, INC.
P O BOX 85608
SAN DIEGO, CA 92138-5608
ATTN: DOCUMENT CONTROL

ITT INDUSTRIES
ITT SYSTEMS CORP
ATTN: AODTRA/DASIAC
1680 TEXAS ST SE
KIRTLAND AFB, NM 87117-5669
ATTN: DASIAC
ATTN: DASIAC/DARE

ITT SYSTEMS CORP
2560 HUNTINGTON AVENUE
ALEXANDRIA, VA 22303
ATTN: D MOFFETT

JAYCOR
1410 SPRING HILL ROAD
SUITE 300
MCLEAN, VA 22102
ATTN: DR CYRUS P KNOWLES

LOCKHEED MARTIN VOUGHT SYSTEMS
P O BOX 650003
DALLAS, TX 75265-0003
ATTN: LIBRARY EM-08

MAXWELL FEDERAL DIVISION INC.
8888 BALBOA AVENUE
SAN DIEGO, CA 92123
ATTN: D PARKS
ATTN: J WATROUS
ATTN: P COLEMAN
ATTN: P STEEN
ATTN: R INGERMANSON

MAXWELL TECHNOLOGIES
8888 BALBOA AVE., BLDG. 1
ATTN: J THOMPSON
ATTN: WILLIAM H RIX

MINNESOTA MINING &
MANUFACTURING COMPANY
3 M FEDERAL SYSTEMS DEPARTMENT
3 M CENTER BUILDING 224-2S-25
ST. PAUL, MN 55144-1000
ATTN: D REDMOND
ATTN: E HAMPL

MISSION RESEARCH CORP.
P O BOX 542
NEWINGTON, VA 22122-0542
ATTN: B GOPLEN

PRIMEX TECHNOLOGIES, ORDNANCE
& TACTICAL SYSTEM
1840 FAIRWAY DRIVE
P O BOX 2055
SAN LEANDRO, CA 94577-0205
ATTN: C STALLINGS
ATTN: P SINCERNY

PULSE SCIENCES, INC.
600 MCCORMICK STREET
SAN LEANDRO, CA 94577
ATTN: P W SPENCE

TETRA CORP
3701 HAWKINS ST, NE
ALBUQUERQUE, NM 87109
ATTN: W MOENY

DISTRIBUTION LIST

DEPARTMENT OF DEFENSE CONTRACTORS

TEXAS TECH UNIVERSITY
P O BOX 5404
LUBBOCK, TX 79417
ATTN: DR M KRISTIANSEN

UNIVERSAL VOLTRONICS CORP
27 RADIO CIRCLE DRIVE
MT KISCO, NY 10549
ATTN: W CREWSON

UNIVERSITY OF MISSOURI-COLUMBIA
W 1025 ENGINEERING BLDG EAST
COLUMBIA, MO 65211
ATTN: DR W NUNNALLY

W J SCHAFER ASSOCIATES, INC.
1901 NORTH FT MYER DRIVE
SUITE 800
ARLINGTON, VA 22209-1681
ATTN: E ALCARAZ

WESTINGHOUSE STC
1310 BEULAH ROAD
PITTSBURG, PA 15235
ATTN: DR A H COOKSON

DEPARTMENT OF ENERGY

SANDIA NATIONAL LABORATORIES
ATTN: MAIL SERVICES
P O BOX 5800
ALBUQUERQUE, NM 87185-0459
ATTN: J HARRIS/MS 0523
ATTN: J MARTIN/MS 0523
ATTN: M BUTTRAM/MS-1153
ATTN: V HARPER-SLABOSZEWICZ
ATTN: W BEEZHOLD\MS-1155

DEPARTMENT OF THE AIR FORCE

AIR FORCE OFFICE OF SCIENTIFIC RSCH
BLDG 410
BOLLING AFB, DC 20332-6448
ATTN: DR. R. BARKER

AIR WEATHER SERVICE, MAC
DEPARTMENT OF THE AIR FORCE
SCOTT AFB, IL 62225
ATTN: AWS TECH LIBRARY, FL4414

ARNOLD ENGINEERING DEVELOLPMENT CENTER
1099 AVENUE C
ARNOLD AFB, TN 37389-9011
ATTN: MAJ J ROWLEY/DOT

DEPARTMENT OF THE NAVY

NAVAL POSTGRADUATE SCHOOL
411 DYER ROAD
MONTEREY, CA 93943-50002
ATTN: CODE 61SW F SCHWIRZKE

NAVAL RESEARCH LABORATORY
4555 OVERLOOK AVE, SW
WASHINGTON, DC 20375-5000
ATTN: CODE 6700 S OSSAKOW
ATTN: CODE 6750/R MEGER
ATTN: CODE 6770 G COOPERSTEIN
ATTN: CODE 6770/R COMMISSO

NAVAL SURFACE WARFARE CENTER
17320 DAHLGREN ROAD
DAHLGREN, VA 22448-5000
ATTN: CODE B-20

DIRECTORY OF OTHER (LIBRARIES AND UNIVERSITIES)

AUBURN UNIVERSITY
231 LEACH SCIENCE CENTER
AUBURN, AL 36849
ATTN: M ROSE

CALIFORNIA-DAVIS, UNIVERSITY OF
DEPARTMENT OF APPLIED SCIENCES
DAVIS, CA 95616
ATTN: J S DEGROOT

NEW YORK-BUFFALO,
STATE UNIVERSITY OF
BONNER HALL, ROOM 312
BUFFALO, NY 14260
ATTN: R DOLLINGER

OTHER GOVERNMENT

CENTRAL INTELLIGENCE AGENCY
WASHINGTON, DC 20505
ATTN: OSWR, J PINA

NATIONAL AERONAUTICS AND
SPACE ADMINISTRATION
LANGLEY RESEARCH CENTER
HAMPTON, VA 23681-0001
ATTN: MS-493 J LEE

NATIONAL INSTITUTE OF STANDARDS AND
TECHNOLOGY
PHYSICS BLDG., RM B157
GAITHERSBURG, MD 20899
ATTN: R HEBNER, BLDG 220, 8344